Karlsruhe Institute of Technology

Characterisation of the KATRIN tritium source and evaluation of systematic effects

Zur Erlangung des akademischen Grades eines
Doktors der Naturwissenschaften
von der KIT-Fakultät für Physik
des Karlsruher Instituts für Technologie
genehmigte
Dissertation

von

Hendrik Seitz-Moskaliuk, M. Sc.
geb. Seitz

aus Frankenberg (Eder)

Referent:	Prof. Dr. Guido Drexlin Institut für Experimentelle Teilchenphysik
Korreferent:	Prof. Dr. Ulrich Husemann Institut für Experimentelle Teilchenphysik
Korreferentin:	Dr. Kathrin Valerius Institut für Kernphysik

Tag der mündlichen Prüfung: 01.02.2019

Erklärung der Selbstständigkeit

Ich versichere wahrheitsgemäß, die Arbeit selbstständig verfasst, alle benutzten Hilfsmittel vollständig und genau angegeben und alles kenntlich gemacht zu haben, was aus Arbeiten anderer unverändert oder mit Abänderungen entnommen wurde, sowie die Satzung des KIT zur Sicherung guter wissenschaftlicher Praxis in der gültigen Fassung vom 24.05.2018 beachtet zu haben.

Karlsruhe, den 16.01.2019, _____

Hendrik Seitz-Moskaliuk

Contents

List of Figures

List of Tables

1. Introduction

Neutrinos are the most abundant massive elementary particles in the Universe known today. At the same time, they are the most mysterious ones: since they do not carry electric charge, they are hard to detect – which is the reason why they are called "ghost particles" in popular science. They can change their flavour on their way from the source to the detector in neutrino oscillations. And finally, they are much lighter than any other massive elementary particle. The fact that neutrinos do have mass is the first confirmed deviation from the Standard Model of Elementary Particle Physics, in which they are assumed to be massless. Based on this motivation, neutrino physics has grown into a vital field of research today. The quest is on to find answers to some of the fundamental questions of particle physics, cosmology and astrophysics in the properties of neutrinos: What is dark matter? Why do we observe more matter than antimatter in the Universe? How are the masses of the elementary particles adjusted to the values we observe and why is there this huge gap between the neutrinos and the fermions which carry an electric charge?

Since the neutrino mass is the door opener to physics beyond the Standard Model, it is of utmost importance to determine its absolute scale. A neutrino mass measurement will be a huge step on the way to answering the big questions mentioned above, as it will help to discriminate between several of the theories that have been proposed as extensions of the Standard Model. The first experiments seeking to determine the neutrino mass were performed in the 1940s. Despite all efforts, even today only an upper limit on the effective electron antineutrino mass of $m_\nu < 2\,\mathrm{eV}/c^2$ (95 % C. L.) has been set by the Troitsk and Mainz experiments [Kra05; Ase11]. Based on their experience, the next-generation experiment KATRIN has been set up in Karlsruhe.

The Karlsruhe Tritium Neutrino (KATRIN) Experiment is designed for a sensitivity to the effective mass of the electron antineutrino of $0.2\,\mathrm{eV}/c^2$ (90 % C. L.) [Ang05]. It is a 70 m long setup, performing high-precision spectroscopy of the beta electrons from molecular tritium decay. It will start regular operation in 2019 for at least five years of measurements. The neutrino mass will manifest as a small deviation in the shape of the beta-electron spectrum close to the kinematic endpoint. To be able to measure a sub-eV neutrino mass, KATRIN has pushed technical limits to a new level: key achievements are the high-luminosity windowless gaseous tritium source (WGTS) with an activity of 100 GBq stabilised on the per mille level, one of the largest ultra-high vacuum vessels built by mankind, and a high-voltage system with a ppm[1] stability.

Besides the technical challenges, a precise understanding and modelling of the tritium beta-decay spectrum is crucial for the success of KATRIN. While the basic principles of beta decays are well understood through Fermi's model of weak interactions [Fer34], every distortion of the spectral shape due to systematic effects has to be investigated, quantified

[1] ppm = parts per million.

and included as far as possible into the analysing model. It has to be ensured that a detected distortion of the shape near the kinematic endpoint of the tritium beta-decay spectrum is caused by the neutrino mass and not mimicked by an experimental effect.

The scope of the thesis at hand comprises the evaluation of the systematic effects which have been studied in over 15 years of research by the KATRIN Collaboration. This thesis aims to draw a comprehensive picture of KATRIN systematic uncertainties and to review the total systematic uncertainty budget. Since many of the systematic effects are linked to the tritium source, the second part of the thesis characterises the operational parameters of the WGTS in stand-alone commissioning measurements and in a spectroscopy campaign with ^{83m}Kr. The thesis is structured as follows:

In chapter 2, a brief overview of neutrino physics is given. Starting with a short historical review, the current status of research is outlined and the properties of neutrinos are discussed in detail.

Chapter 3 presents the KATRIN experiment. It starts with a description of the setup and the features of the components of KATRIN, followed by an introduction to the data-taking and analysis software. The chapter ends with a discussion of the KATRIN measurement procedure and the objectives of this thesis.

In chapter 4, the systematic effects in KATRIN are discussed. First, different ways of implementing the systematic uncertainties in the neutrino mass analysis are introduced. Second, each systematic effect known at this point is described, including the experience gathered by former neutrino mass experiments, wherever available. For each systematic effect, its determination in KATRIN is presented and the impact on the neutrino mass measurement is calculated. The section ends with a list of systematic effects including their evaluation according to relevance and the conclusions for the upcoming regular operation.

In chapter 5, the results of a measurement campaign with gaseous ^{83m}Kr are reported. Conversion electrons produced by de-excitations of metastable ^{83m}Kr atoms are an important nuclear standard for various calibration purposes and for the determination of several systematic effects in KATRIN. Since the operation of the WGTS with gaseous ^{83m}Kr mode is technically challenging, a dedicated measurement campaign for the commissioning of the system was necessary. Several systematic effects, such as the ones related to stability and linearity of the energy scale, were tested, demonstrating the outstanding capabilities of KATRIN in high-resolution spectroscopy of keV-scale electrons.

Chapter 6 is dedicated to an in-depth characterisation of the performance of the WGTS cryostat. It is investigated whether the design specifications for the magnetic fields and the temperatures have been achieved. Recommendations for the standard operation are developed and outlined.

Final conclusions and an outlook are given in chapter 7.

2. Neutrino Physics

Neutrino physics is a vital section of modern physics with a lot of links and connections to other areas of physics. This chapter gives an overview of this research field starting with some historical remarks on the Standard Model properties of neutrinos in section 2.1. In section 2.2, theoretical aspects of neutrino oscillations are described and important experiments are reviewed. The last section of this chapter, section 2.3, covers extensions of the Standard Model to include a non-vanishing neutrino mass and experimental efforts to determine this mass.

2.1. Neutrinos in the Standard Model of Elementary Particle Physics

The story of the neutrino began at the end of the 19th century, when Becquerel discovered radioactivity [Bec96]. In the following years, large progress was made on this new research field, and when Bragg found α rays being monoenergetic [Bra04], the same was expected for β rays. Although Chadwick measured a continuous electron spectrum in the β decay of lead-214 and bismuth-214 [Cha14], some scientists like Meitner still believed that the electrons leaving the nucleus are monoenergetic, but that their energy is smeared out by secondary effects [Mei23]. By measuring the whole energy emitted by β electrons in a calorimetric setup, Ellis and Wooster ruled out Meitner's hypothesis and demonstrated that the continuous β-decay spectrum is a physical reality [Ell27]. Meitner confirmed their results in 1930 [Mei30]. Nevertheless, the scientific debate was not over then, because the β decay was to the best of knowledge assumed as being a two-body decay. If one of the decay products, the electron, has a continuous energy distribution, the conservation of energy and momentum is violated. Thus, two fundamental principles of physics seemed to be overthrown. Bohr even suggested to accept that energy and momentum are not conserved, with all the unfathomable consequences [Boh32]. Finally, in 1930, Pauli found a "desperate" solution for the problem, which he described in a famous letter [Pau30]. At that time, only three "elementary" particles were known, being the electron, the proton, and the photon. He postulated a new electrically neutral particle that we know today as the neutrino. Taking part in β decay and turning it into a three-body decay, this new particle explained the continuous energy spectrum of the electrons without violating the conservation of energy. Furthermore, Pauli assigned a spin of $1/2\,\hbar$ to the particle to satisfy the angular momentum conservation in the decay. In his letter, he already suspected that an experimental detection of the neutrino would be extremely difficult.

Based on Pauli's idea, Fermi developed a theory of β decay in 1934 [Fer34]. This theoretical treatment is still valid for β emitters with comparably low energy like e. g. tritium (see section 2.3.3). Fermi invented the term "neutrino" and included this particle in his considerations:

$$ {}^{\mathrm{A}}_{\mathrm{Z}}\mathrm{X} \longrightarrow {}^{\mathrm{A}}_{\mathrm{Z+1}}\mathrm{Y} + \mathrm{e}^{-} + \overline{\nu}_{\mathrm{e}} \; . \tag{2.1} $$

Table 2.1.: Neutrinos in the Standard Model of Elementary Particle Physics. The table lists all relevant properties of neutrinos in the Standard Model of particle physics. For details, the reader is referred to the main text.

Attribute	Property
Particle group	Leptons
Flavours	3 (ν_e, ν_μ, ν_τ)
Interactions	only weak interactions
Electric charge	0
Spin	$1/2\,\hbar$ (Fermion)
Helicity	100 % left-handed neutrinos, 100 % right-handed antineutrinos
Mass	0

The theory inspired Bethe and Peierls to think of processes to detect neutrinos. They suggested the so-called inverse β decay

$$\mathrm{p} + \overline{\nu}_\mathrm{e} \longrightarrow \mathrm{n} + \mathrm{e}^+ \ , \tag{2.2}$$

in which an antineutrino hits a proton, and a neutron and a positron are created. They calculated the cross-section for this process to be below $10^{-44}\,\mathrm{cm}^2$ and concluded that "there is no practically possible way of observing the neutrino" [Bet34].

It took about 20 more years and the invention of nuclear reactors to disprove this statement. First hints pointing towards a neutrino detection were published by Cowan and Reines in 1953 [Rei53] and they could confirm these results in 1956 at the Savannah River Site [Cow56]. Their multiple-layer neutrino detector consisted of two target chambers with a cadmium chloride solution in water (200 ℓ each) surrounded by three liquid-scintillator chambers, each of them equipped with 110 photomultiplier tubes. When an electron antineutrino coming from a close-by nuclear reactor hits a proton of the water molecules in the target tanks, according to the inverse β decay (see equation 2.2) a positron and a neutron are produced. The positron quickly annihilates with an electron to two γs of 511 keV energy each. The neutron is moderated by the water before it is captured by the cadmium. In this process, again γs are emitted with 3-11 MeV energy. The γs are detected by the scintillators. The γ pulse of the neutron is delayed by up to 17 µs in comparison to the γ pulse of the positron depending on the cadmium concentration. This coincidence signal enabled Cowan and Reines to discriminate the signal from background resulting in a neutrino detection rate of about 3 events per hour and confirming roughly the cross-section calculations by Bethe and Peierls [Bet34]. For their achievements in neutrino physics, Reines was awarded the Nobel prize in 1995.[1]

In the decades after the discovery of the neutrino, more and more of its properties have been investigated and today's picture of neutrinos as part of the Standard Model of Elementary Particle Physics has been deployed. Figure 2.1 shows all particles of the Standard Model and some of their basic characteristics. The neutrino properties are summarised in table 2.1 and discussed in the following:

Number of neutrino flavours: In 1962, the muon neutrino was discovered [Dan62]. With the detection of the tau lepton in 1975 [Per75], physicists also expected the corresponding tau neutrino, whose existence was demonstrated in 2001 by the DONUT

[1] see `https://www.nobelprize.org/nobel_prizes/physics/laureates/1995/` (accessed on Dec 21, 2018).

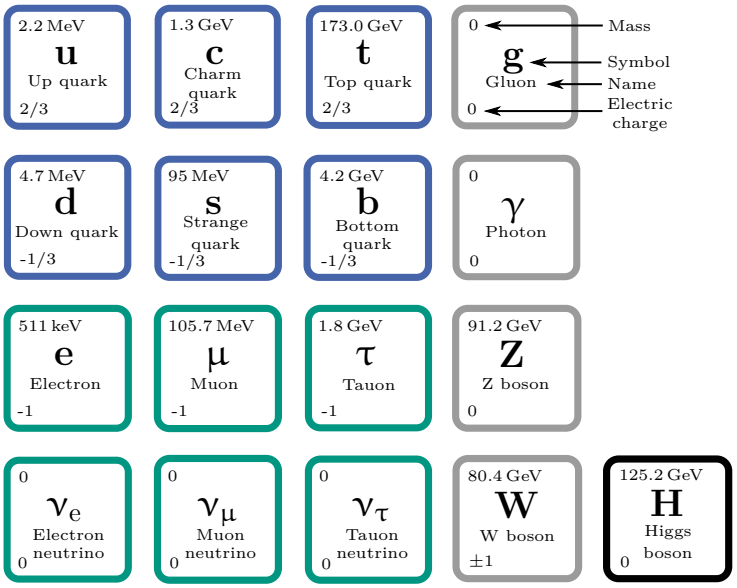

Figure 2.1.: The Standard Model of Elementary Particle Physics. The chart shows the masses, symbols, names, and electric charges of all known particles of the Standard Model of particle physics. The quark sector is marked in blue, the lepton sector marked in green. All particles of the two sectors are fermions with a spin of $1/2\,\hbar$. The bosons mediating the strong, weak, and electromagnetic forces with spin $1\,\hbar$ are marked in grey. The Higgs boson with spin 0 is marked in black. The masses and electric charges are taken from [Tan18]. It should be noted that in the original Standard Model the neutrino mass is considered to be zero as listed here [Gla61; Wei67; Sal68]. The observation of neutrino oscillations (see section 2.2) hints towards physics beyond the Standard Model. Some possible extensions to explain a non-vanishing neutrino mass are discussed in section 2.3.2.

collaboration [Kod01]. In the 1990s, precision measurements at the Large Electron Positron Collider (LEP) at CERN of the width of the Z-boson resonance showed, that the number of light neutrinos with $m_\nu < \frac{m_Z}{2}$ is consistent with $N_\nu = 3$ [Dec90a; Acc98].

Helicity: As Lee and Yang discussed in their famous paper from 1956, no experiment sensitive on the parity of β decay had been performed up to then [Lee56]. Since there was already a debate ongoing on a possible parity violation in weak interactions, they suggested in their paper four different experiments to test it. All four experiments were performed within the following year, demonstrating the parity violation of weak interactions [Wu57; Gar57; Sch57; Cra57] and making Lee and Yang Nobel laureates in 1957.[2] The parity nonconservation in weak interactions indicated already that neutrinos have to be left-handed and antineutrinos right-handed or vice versa. Goldhaber measured the neutrino helicity

$$H = \frac{\vec{s} \cdot \vec{p}}{|\vec{s} \cdot \vec{p}|} \,, \tag{2.3}$$

with $\vec{s}$ being the spin and $\vec{p}$ being the momentum, in his famous experiment in 1958 [Gol58]. His result of $H = -1$ confirmed that only left-handed neutrinos (and right-handed antineutrinos) participate in weak interactions. Until today, there is no evidence of right-handed neutrinos (or left-handed antineutrinos).

[2] see `https://www.nobelprize.org/nobel_prizes/physics/laureates/1957/` (accessed on Dec 21, 2018).

Mass: The helicity plays also an important role for the mass of the neutrinos in the Standard Model. Already in 1957, one year before Goldhaber's experiment, Lee and Yang, Landau and Salam independently suggested a two-component neutrino theory as a consequence of parity nonconservation [Lee57; Lan57; Sal57]. Other Dirac particles can be described as a four-component spinor (Dirac spinor), with two components describing the left- and right-handed particle and the two other components describing the left- and right-handed antiparticle. For each, the neutrino and the antineutrino, only one component is necessary. This two-component theory is only possible for a massless neutrino, otherwise a helicity of ± 1 cannot be obtained. The two-component theory also became part of the electroweak unification in the Standard Model [Gla61; Wei67; Sal68], so that the neutrino mass in the minimal version of the Standard Model is assumed to be zero.

Soon after the formulation of the Standard Model in the 1960s, first experimental hints of neutrino oscillations (see next section 2.2) indicated that neutrinos have a non-vanishing mass. Neutrinos are therefore keys to physics beyond the Standard Model, and learning more about their features and properties is crucial for the progress of many different fields of physics today.

2.2. Neutrino Oscillations

Neutrino oscillations describe the effect of flavour changes of neutrinos during propagation. This effect occurs because the mass eigenstates of neutrinos are not equivalent to the flavour eigenstates. The first who thought about neutrino oscillations was Pontecorvo in 1958 [Pon58]. He considered neutrino-antineutrino oscillations. Maki, Nakagawa and Sakata expanded this mechanism to flavour oscillations in 1962 [Mak62]. In both publications, neutrino oscillations are introduced as a hypothetical consideration without any experimental evidence. This changed when Davis reported first results of the Homestake Experiment, indicating that the measured flux of solar neutrinos is about a factor of three less than predicted by calculations [Dav68]. The so-called solar neutrino problem was born. Pontecorvo argued that such a result can be interpreted as neutrino oscillation signal [Pon68], and he started to work out the theory [Gri69]. The solar neutrino problem survived the next three decades, and at the end of the Homestake Experiment the measured neutrino flux [Cle98] was still a factor of three less than predicted by solar models [Bah01]. Finally, the Sudbury Neutrino Observatory (SNO) collaboration solved the problem [Ahm01; Aha13]: Davis' experiment was only sensitive to electron neutrinos since they are the only kind of neutrinos predicted to be emitted in solar fusion reactions by solar models. However, SNO could measure the flux of all three neutrino types, and this result was in perfect agreement with the predictions, demonstrating that solar neutrinos change their flavour on their way to Earth.

Since neutrino oscillations have also been observed elsewhere, e. g. by the Super-Kamiokande collaboration in atmospheric neutrinos from cosmic ray air showers [Fuk98], they are nowadays well-established in physics. Arthur McDonald for SNO and Takaaki Kajita for Super-Kamiokande received the Nobel prize in physics in 2015 for the discovery "that neutrinos have mass"[3], which is an important hint towards physics beyond the Standard Model. The experiments are described in more detail in subsection 2.2.2 after the following description of the underlying theory.

[3] see `https://www.nobelprize.org/nobel_prizes/physics/laureates/2015/` (accessed on Dec 21, 2018).

2.2.1. Theory of Three-Flavour Oscillations

The following overview on the theory of neutrino oscillations is mainly based on [Zub11] and [Bil10].

The neutrino mass eigenstates do not coincide with the eigenstates of the weak interaction, a characteristic which is also known from the quark sector. There, the mixing of the quarks is described by the unitary 3×3 Cabibbo-Kobayashi-Maskawa matrix (CKM matrix) [Kob73]. The analogue for the neutrinos is the Pontecorvo-Maki-Nakagawa-Sakata matrix (PMNS matrix $U_{\alpha i}$) which mixes the mass eigenstates ($i = 1, 2, 3$) to flavour eigenstates ($\alpha = \mathrm{e}, \mu, \tau$)

$$|\nu_\alpha\rangle = \sum_i U_{\alpha i} |\nu_i\rangle \tag{2.4}$$

with

$$U = \begin{pmatrix} U_{\mathrm{e}1} & U_{\mathrm{e}2} & U_{\mathrm{e}3} \\ U_{\mu 1} & U_{\mu 2} & U_{\mu 3} \\ U_{\tau 1} & U_{\tau 2} & U_{\tau 3} \end{pmatrix} . \tag{2.5}$$

The PMNS matrix is often parametrised in the following way:

$$U = \begin{pmatrix} 1 & 0 & 0 \\ 0 & \cos\theta_{23} & \sin\theta_{23} \\ 0 & -\sin\theta_{23} & \cos\theta_{23} \end{pmatrix} \begin{pmatrix} \cos\theta_{13} & 0 & \sin\theta_{13}\mathrm{e}^{\mathrm{i}\delta} \\ 0 & 1 & 0 \\ -\sin\theta_{13}\mathrm{e}^{\mathrm{i}\delta} & 0 & \cos\theta_{13} \end{pmatrix} \begin{pmatrix} \cos\theta_{12} & \sin\theta_{12} & 0 \\ -\sin\theta_{12} & \cos\theta_{12} & 0 \\ 0 & 0 & 1 \end{pmatrix} . \tag{2.6}$$

Here, the θ_{ij} denote the Euler angles of the mass eigenstates, and δ denotes the CP-violating phase. Two additional phases, so-called Majorana phases, have to be included in the PMNS matrix if neutrinos are Majorana particles, i. e. if neutrinos are their own antiparticles. They play an important role in the description of neutrinoless double β decay (see section 2.3.3).

Neutrinos are created and detected through weak interactions as flavour eigenstates, i. e. as a mixture of mass eigenstates. Due to this mixture, flavour eigenstates oscillate on their way to the detector. The most important experimental parameter is the transition probability from one flavour to another and its derivation is sketched in the following.

The time dependence of a neutrino created with flavour eigenstate ν_α ($\alpha = \mathrm{e}, \mu, \tau$) at $t = 0$ is

$$|\nu_\alpha(t, x)\rangle = \sum_i U_{\alpha i} \mathrm{e}^{-\mathrm{i}(E_i t - p_i x)} |\nu_i\rangle \tag{2.7}$$

with $c = \hbar = 1$. For the neutrinos being relativistic with $p \gg m$ and $E \approx p$, the energy of the mass eigenstates can be written as

$$E_i = \sqrt{p^2 + m_i^2} \approx E + \frac{m_i^2}{2E} . \tag{2.8}$$

Combining equations 2.7 and 2.8, the time-dependent transition amplitude for a neutrino of flavour α ending up in flavour β can be calculated to be

$$\langle \nu_\beta | \nu_\alpha(t, x) \rangle = \sum_i U^*_{\beta i} U_{\alpha i} \exp\left(-\mathrm{i} \frac{m_i^2}{2} \frac{L}{E} \right) . \tag{2.9}$$

The oscillation length $L = x = ct$ denotes the distance between source and detector for neutrinos travelling at the speed of light in the assumed relativistic case. The transition probability P, finally, is defined as the transition amplitude squared with $\Delta m_{ij}^2 = m_i^2 - m_j^2$:

$$\begin{aligned} P_{\alpha\to\beta} = |\langle \nu_\beta | \nu_\alpha(t,x)\rangle|^2 &= \sum_i \sum_j U_{\alpha i} U_{\alpha j}^* U_{\beta i}^* U_{\beta j} \exp\left(-\mathrm{i}\frac{\Delta m_{ij}^2}{2}\frac{L}{E}\right) \\ &= \delta_{\alpha\beta} - 4\sum_{i>j=1}^{3} \mathrm{Re}\left(U_{\alpha i} U_{\beta i}^* U_{\alpha j}^* U_{\beta j}\right) \sin^2\left(\frac{\Delta m_{ij}^2}{4}\frac{L}{E}\right) \\ &\quad + 4\sum_{i>j=1}^{3} \mathrm{Im}\left(U_{\alpha i} U_{\beta i}^* U_{\alpha j}^* U_{\beta j}\right) \sin\left(\frac{\Delta m_{ij}^2}{4}\frac{L}{E}\right) \cos\left(\frac{\Delta m_{ij}^2}{4}\frac{L}{E}\right) \ . \end{aligned} \tag{2.10}$$

If there is no CP-violation ($\delta = 0$), U becomes real and the transition probability simplifies to

$$P_{\alpha\to\beta} = \delta_{\alpha\beta} - 4\sum_{i>j=1}^{3} \left(U_{\alpha i} U_{\beta i} U_{\alpha j} U_{\beta j}\right) \sin^2\left(\frac{\Delta m_{ij}^2}{4}\frac{L}{E}\right) \ . \tag{2.11}$$

Equations 2.10 and 2.11 are relevant for so-called appearance experiments, in which the detector is sensitive to a different neutrino flavour as the one dominantly emitted by the source. However, there are also disappearance experiments looking for the same neutrino flavour in the final state as in the initial state. The probability not to change the flavour is

$$P_{\alpha\to\alpha} = 1 - \sum_{\beta\neq\alpha} P_{\alpha\to\beta} \ . \tag{2.12}$$

For current and planned precision experiments (see section 2.2.2), the outlined three-neutrino oscillation picture is mandatory. However, for former experiments, the data analysis has normally been based on the two-component picture. If, for instance, only electron and muon neutrinos are considered, the mixing matrix reduces to

$$U = \begin{pmatrix} \cos\theta & \sin\theta \\ -\sin\theta & \cos\theta \end{pmatrix} \ , \tag{2.13}$$

with only one mixing angle θ and without CP-violating phase. In this picture, the transition probability simplifies to

$$P_{\mathrm{e}\to\mu} = \sin^2 2\theta \sin^2\left(\frac{\Delta m_{21}^2}{4}\frac{L}{E}\right) \ . \tag{2.14}$$

Looking at equations 2.14, 2.10 and 2.11 it is obvious that neutrino oscillation experiments are only sensitive to relative mass differences, but not to the absolute neutrino mass (see section 2.3). To measure these mass differences with the highest possible count rates in the appearance or disappearance channel, the oscillation length has to be chosen in the ideal case to

$$L \approx \frac{E}{\Delta m_{ij}^2} \ . \tag{2.15}$$

However, in practice there are some limitations in optimising the experiment in that way. If the source is extended over a large volume and/or emits neutrinos with a continuous energy spectrum like the sun, which is an example of both, L cannot be adjusted that well.

Up to this point, only neutrino oscillations in vacuum have been considered. In areas with a large electron density the Mikheyev-Smirnov-Wolfenstein effect (MSW effect) influences the transition probabilities of the electron neutrino [Mik86; Wol78]. While tauon and muon neutrinos only undergo neutral current interactions, electron neutrinos can additionally perform charged current interactions with the surrounding electrons in a coherent forward scattering process. The electron neutrinos perceive an additional potential

$$V = \sqrt{2} G_{\mathrm{F}} n_{\mathrm{e}} \tag{2.16}$$

with the Fermi constant G_{F} and the electron density n_{e}. This additional potential is treated as an effective mass, changing the mixing angle, oscillation length and probability with respect to the vacuum case.

The MSW effect is normally only a small modification, but for very high electron densities as in the sun it has a large influence. The electron density in the sun decreases from the inner to the outer region. In the fusion processes of the sun, only electron neutrinos are produced (see equation 2.17), and their effective mass is in the inner regions of the sun larger than the one of muon and tauon neutrinos. At a critical electron density, the masses are equal, so that the electron neutrinos convert into muon or tauon neutrinos in a resonant process. For larger radii, the flux of electron neutrinos is significantly suppressed and in this region, vacuum oscillations are dominant already. It should be noted that the resonant MSW effect is energy dependent and this energy dependence is again connected to the vacuum mixing angle and the mass difference squared. Therefore, the resonant MSW effect was very important for the correct determination of $\sin\theta_{12}$ and Δm^2_{21} from solar neutrinos, which is described in more detail in the following section on neutrino oscillation experiments.

2.2.2. Neutrino Oscillation Experiments

As discussed in the previous section, the basic parameters which are probed by neutrino mass experiments are the differences Δm^2_{ij} of the squared neutrino mass eigenvalues, the neutrino mixing angles $\sin\theta_{ij}$ and the CP-violating phase δ of the unitary PMNS matrix (see equation 2.6). Since the combination of selected distance L from the source to the detector and the neutrino energy E fixes the sensitivity on those parameters (see equation 2.15), a huge variety of neutrino oscillation experiments has been conceived. As one can see in figure 2.2, these experiments can also make use of different kinds of natural and artificial neutrino sources. In the following, the achievements in measuring the oscillation parameters are reviewed. Based on precision measurements of these parameters in planned future experiments, also presently unsolved questions like the correct mass ordering of the mass eigenstates or additional (sterile) neutrino flavours will be addressed. These prospects are also discussed in this section. All parameters and their currently best values are summarised in table 2.2.

$\sin\theta_{12}$, Δm^2_{21}: Solar Neutrinos

The sun is an ideal neutrino source to study $\nu_{\mathrm{e}} \to \nu_{\mu}$ oscillations and to determine $\sin\theta_{12}$ and Δm^2_{21}. The main fusion reaction in the sun producing energy and neutrinos can be summarised as [Zub11]

$$4\mathrm{p} \to {}^4\mathrm{He}^{2+} + 2\mathrm{e}^+ + 2\nu_{\mathrm{e}} + 26.73\,\mathrm{MeV}\ . \tag{2.17}$$

In reality, this reaction takes place in different steps of the so-called pp cycle [Bet38]. The neutrinos have energies up to about 11 MeV depending on the production sub-reaction (see figure 2.2). The total flux of solar neutrinos at Earth is $6.5 \times 10^{10}\,\mathrm{cm}^{-2}\mathrm{s}^{-1}$ [Bah01].

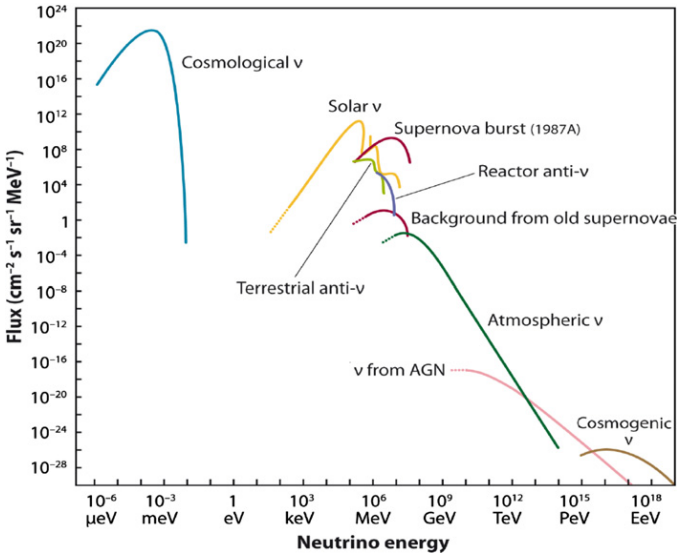

Figure 2.2.: Neutrino fluxes from artificial and natural sources. Shown are the neutrino fluxes over the energies of artificial and natural neutrino sources. So far it is not possible to detect relic neutrinos from the cosmic neutrino background with meV energies. Also the significant detection of AGN neutrinos has not been successful yet. All the other sources have been detected. Especially solar, atmospheric and reactor neutrinos are important sources for precision experiments on neutrino oscillation parameters. Not shown in this plot are neutrinos produced in accelerators which allow the precision measurement of neutrino properties (see the main text). Reprinted from [Kat12] with permission from Elsevier.

Table 2.2.: Overview of neutrino oscillation parameters. The table lists the parameters and open questions addressed by neutrino oscillation experiments and the currently best values. IH means inverted hierarchy, NH normal hierarchy. For $\sin^2\theta_{23}$, four values are given depending on the hierarchy and the octant ($\theta_{23} < 45°$ or $\theta_{23} > 45°$). For details and the related literature, the reader is referred to the corresponding paragraph of the main text. The values are taken from [Tan18].

Observable	Value
$\sin^2\theta_{12}$	$0.307^{+0.013}_{-0.012}$
$\sin^2\theta_{23}$	$0.417^{+0.025}_{-0.028}$ (NH, octant I)
$\sin^2\theta_{23}$	$0.597^{+0.024}_{-0.030}$ (NH, octant II)
$\sin^2\theta_{23}$	$0.421^{+0.033}_{-0.025}$ (IH, octant I)
$\sin^2\theta_{23}$	$0.592^{+0.023}_{-0.030}$ (IH, octant II)
$\sin^2\theta_{13}$	0.0210 ± 0.0011
Δm^2_{21}	$(7.53 \pm 0.18) \times 10^{-5}\,\mathrm{eV}^2/c^4$
Δm^2_{32}	$(2.51 \pm 0.05) \times 10^{-3}\,\mathrm{eV}^2/c^4$ (NH)
Δm^2_{32}	$(2.56 \pm 0.04) \times 10^{-3}\,\mathrm{eV}^2/c^4$ (IH)
δ	unknown
hierarchy (NH vs. IH)	unknown
4th generation (steriles)	unknown

In order to detect solar neutrinos, the radiochemical method first proposed by Pontecorvo [Pon83] turned out to be very useful and was elaborated on by Davis in the Homestake Experiment mentioned already above [Cle98]. In a tank of 615 t of tetrachloroethylene solar electron neutrinos underwent the following reaction:

$$\nu_e + {}^{37}\mathrm{Cl} \rightarrow {}^{37}\mathrm{Ar} + e^- \ . \tag{2.18}$$

The resulting ^{37}Ar decays via electron capture and the emitted Auger electrons were detected. After about two months of operating time, the argon atoms were extracted and counted. Due to the low count rate of about 800 detected solar neutrinos in roughly three decades, the experiment had to be located deep underground in the Homestake mine to reduce background processes. The threshold of the chlorine reaction is 0.814 MeV, thus enabling the detection of (^{3}He, p), (^{8}B), (p, e$^-$, p) and (^{7}Be, e$^-$) neutrinos from the pp fusion chain of the sun [Cle98].

A smaller threshold of 0.224 MeV and the detection of (p, p) neutrinos is possible with gallium in the reaction

$$\nu_e + {}^{71}\mathrm{Ga} \rightarrow {}^{71}\mathrm{Ge} + e^- \ . \tag{2.19}$$

The three experiments GALLEX/GNO and SAGE confirmed the results of the Homestake experiment demonstrating a solar neutrino deficit as outlined above [Kir99; Alt05; Abd09].

In order to solve the solar neutrino problem, the already mentioned SNO Experiment was designed [Aha13]. 2000 m underground near Sudbury (Ontario, Canada), a vessel of 1000 t heavy water D_2O was set up. The neutral-current reaction

$$\nu_\alpha + d \rightarrow p + n + \nu_\alpha \tag{2.20}$$

with $\alpha = e, \mu, \tau$ allows the detection of the total solar neutrino flux in real time, and the results were found to be consistent with the solar model. With the charged-current reaction

$$\nu_e + d \rightarrow p + p + e^- \tag{2.21}$$

the survival probability only of the electron neutrinos was measured. Photomultiplier tubes (PMTs) detected the Cherenkov radiation of the electron and the neutrons were detected in proportional counters, among other methods. The energy threshold of 3.5-6 MeV was sufficient to measure the high-energy flux due to ^{8}B neutrinos.

At the end of the SNO measurements, still two parameter regions were left for $\sin\theta_{12}$, one with a small angle, one with a large angle. Both solutions made predictions at which energies of the solar neutrino spectrum the MSW effect becomes important. Precise measurements of $\sin\theta_{12}$ and Δm^2_{21} can be done with antineutrinos from nuclear reactors, since the vacuum oscillation length of solar neutrinos is on the scale of 100 km. Such an experiment was KamLAND in Japan, which was surrounded by 55 reactors in an averaged distance of 180 km [Abe08]. The antineutrinos were detected with a liquid scintillator in the inverse β-decay reaction (see equation 2.2). The result of KamLAND pointed towards the large mixing angle solution. After the ground-breaking investigations by KamLAND using reactor neutrinos at long distances, the liquid scintillator experiment BOREXINO, located in the Gran Sasso Laboratory, directly confirmed the KamLAND results in 2011 with a precision measurement of solar neutrinos of the ^{7}Be part of the pp chain [Bel11]: the large mixing angle solution was demonstrated, which was not expected from the small angles of the CKM matrix in the quark sector.

The combined analysis of the solar neutrino observatories and KamLAND under the assumption of three-flavour mixing and CPT invariance lead to the currently best fit values of $\sin\theta_{12}$ and Δm^2_{21} [Gan13; Abe16b]:

$$\sin^2\theta_{12} = 0.307^{+0.013}_{-0.012}\ , \tag{2.22}$$

$$\Delta m^2_{21} = (7.53 \pm 0.18) \times 10^{-5}\,\mathrm{eV}^2/c^4\ . \tag{2.23}$$

$\sin\theta_{23}$, Δm^2_{23}: Atmospheric Neutrinos

Atmospheric neutrinos are a second very important natural source for the determination of neutrino oscillation properties. They are especially well-suited for the determination of $\sin\theta_{23}$ and Δm^2_{23}. The atmospheric neutrinos are produced in interactions of cosmic rays with the air in secondary processes. The most important production reactions are [Zub11]

$$\pi^+ \to \mu^+ + \nu_\mu \quad \Rightarrow \quad \mu^+ \to e^+ + \nu_e + \overline{\nu}_\mu\ , \tag{2.24}$$

$$\pi^- \to \mu^- + \overline{\nu}_\mu \quad \Rightarrow \quad \mu^- \to e^- + \overline{\nu}_e + \nu_\mu\ . \tag{2.25}$$

From these reactions a flavour ratio of muon to electron neutrinos of approximately 2 is deduced as expectation value. Experiments detecting atmospheric neutrinos deal with neutrino energies in the GeV range [Zub11] and oscillation lengths between 10 km and 12.700 km if the neutrinos are produced on the other side of the Earth and have to pass it to reach the detector (see figure 2.2).

The Kamioka Nucleon Decay Experiment (KamiokaNDE) started as a search for proton decay events before it was recognised as a very good instrument to investigate atmospheric neutrinos at the end of the 1980s. It was a 4.5-kiloton water Cherenkov detector equipped with PMTs which were able to detect muons or electrons produced in atmospheric neutrino reactions with the water molecules. Muon events could be distinguished from electron events due to a sharper Cherenkov ring pattern imaged through the PMTs. The threshold for electron detection was about 10 MeV and for muons about 200 MeV. Therefore, KamiokaNDE was also suited to the detection of solar neutrinos. First results showed that the observable muon neutrino flux is much less than expected while the electron neutrino flux agreed well with predictions [Hir88]. In the 1990s, the detector was upgraded to Super-KamiokaNDE, now comprising 50 kt of water and a much larger number of PMTs. Soon, the earlier results were confirmed and the oscillations from muon to tauon neutrinos were established [Fuk98].

Today, the Super-KamiokaNDE detector is also part of the T2K experiment, in which a muon neutrino beam produced in proton-on-target collisions is sent from a distance of 295 km to the detector. T2K [Abe17] and the similar NOνA experiment [Ada17b] together with the ice-based Cherenkov detector IceCube [Aar15] have performed the most precise measurements so far of $\sin\theta_{23}$ and Δm^2_{32}. All results of the different experiments are summarised by the Particle Data Group [Tan18] to be

$$\sin^2\theta_{23} = 0.417^{+0.025}_{-0.028}\ (\text{Octant I}), \tag{2.26}$$

$$\sin^2\theta_{23} = 0.597^{+0.024}_{-0.030}\ (\text{Octant II}), \tag{2.27}$$

$$|\Delta m^2_{32}| = (2.51 \pm 0.05) \times 10^{-3}\,\mathrm{eV}^2/c^4\ , \tag{2.28}$$

for normal hierarchy (see paragraph below) and

$$\sin^2\theta_{23} = 0.421^{+0.033}_{-0.025}\ (\text{Octant I}), \tag{2.29}$$

$$\sin^2\theta_{23} = 0.592^{+0.023}_{-0.030}\ (\text{Octant II}), \tag{2.30}$$

$$|\Delta m^2_{32}| = (2.56 \pm 0.04) \times 10^{-3}\,\mathrm{eV}^2/c^4\ , \tag{2.31}$$

for inverted hierarchy. The question of the octant of θ_{23}, i. e. if $\theta_{23} < 45°$ (octant I) or $\theta_{23} > 45°$ (octant II), is still not yet solved [Est17] and will be addressed by future precision experiments described further below.

$\sin\theta_{13}$: Reactor Antineutrinos

Antineutrinos from nuclear reactors turned out to be an ideal source to study the 13-transition of neutrino oscillations. For each fission reaction, 6 $\overline{\nu}_e$ are emitted in average, summing up to a total neutrino flux of about $2 \times 10^{17}\,\mathrm{s}^{-1}\mathrm{MW}^{-1}$. The electron antineutrinos have energies up to 8 MeV [Zub11] (see figure 2.2).

Three major disappearance experiments have been built to determine $\sin\theta_{13}$: the Double Chooz Experiment [Abe16c], the Daya Bay Experiment [An16a; An17] and the Reactor Experiment for Neutrino Oscillation (RENO) [Cho16]. All three of them make use of the inverse β decay as detection reaction (see equation 2.2). The detectors used in the three experiments are also very similar. In order to detect the antineutrinos, liquid scintillators doped with gadolinium are in operation. The scintillation light is collected by PMTs. The positron delivers a fast signal, while the neutron capture of gadolinium gives a signal about 30 µs later [Cho16]. Since the effect of θ_{13} mixing is small, and to reduce systematics, at least two identical detectors per experiment are needed, one near detector at a few hundreds of metres distance to the detector to measure the flux without oscillations and one far detector at about 1-2 km distance to measure the reduced flux due to oscillation effects [Zub11].

An average over the recent results for $\sin^2\theta_{13}$ of all described experiments (RENO [Cho16], Double Chooz [Abe16c], Daya Bay [An16a; An17]) is given by the Particle Data Group [Tan18]:

$$\sin^2\theta_{13} = 0.0212 \pm 0.0008\ . \tag{2.32}$$

CP-Violating Phase δ

CP violation is one of the Sakharov conditions to explain the asymmetry of matter and antimatter in the Universe [Sak67]. It means that the laws of physics are slightly different for particles and antiparticles. CP violation was first observed in the Kaon system in 1964 by James Cronin and colleagues [Chr64]. Further observations in the quark sector are coming from B mesons, see e. g. [Ger17]. Therefore, many efforts are put into experiments to measure this effect in form of the CP-violating phase δ also in the neutrino sector (see equation 2.6).

Currently, two experiments are taking data, the aforementioned NOνA and T2K long-baseline experiments. As described above, both experiments use a muon neutrino beam from proton-on-target collisions. In order to reduce systematic effects, the beam is analysed by a near detector at a distance of several hundreds of metres and a far detector at a distance of several hundreds of kilometres. Both experiments can change their operating mode from muon neutrinos to muon antineutrinos. A difference of the oscillation rates for the two operation modes is directly connected to the value of δ. So far, T2K has published first results for neutrino and antineutrino operation [Abe18] while NOνA has published only data from the neutrino mode [Ada17a; Ace18]. The results disfavour CP conservation and hint towards a CP-violating phase of $\delta = \frac{3}{2}\pi$. However, a global fit of neutrino oscillation parameters currently leads only to a disfavour of CP conservation at a confidence level of 70 % [Est17]. Larger datasets are needed to finally settle the question of CP-violation in the neutrino sector.

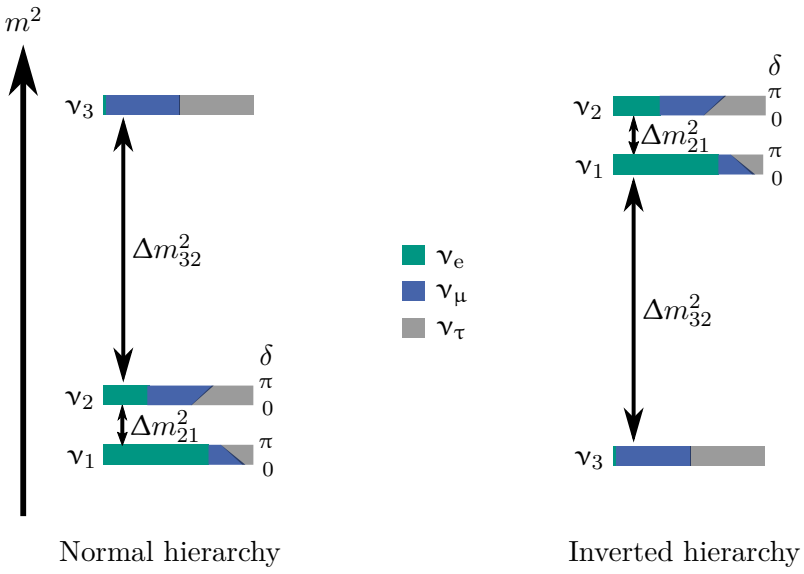

Figure 2.3.: Mass hierarchy of neutrinos. The chart shows the two possible orderings of neutrino mass eigenstates ν_i, the normal and the inverted hierarchy. The ordering of ν_1 and ν_2 is known due to the MSW effect. For every mass eigenstate, the flavour composition is given. The flavour compositions for ν_1 and ν_2 are dependent on the value of the CP-violating phase δ. For the values of Δm^2_{ij}, the reader is referred to table 2.2. Illustration according to [Qia15].

Mass Hierarchy

In principle, for the three mass eigenstates of the neutrinos, all conceivable orderings are possible. However, the observation of the MSW resonance in the sun fixes the mass ordering of the mass eigenvalues m_1 and m_2 [Zub11]: m_1 has to be smaller than m_2, because otherwise the MSW resonance of solar neutrinos would not be possible (see section 2.2.1). Since the sign of the mass difference Δm^2_{23} is not known yet, two possibilities for the mass hierarchy remain: in the normal hierarchy (NH), the mass eigenvalue m_3 is larger than m_2. In the inverted hierarchy (IH), m_3 is smaller than m_1. Both hierarchies are illustrated in figure 2.3. Solving this open question is one of the fundamental quests in neutrino physics.

Experimentally, the determination of the mass hierarchy needs either precision measurements of the disappearance channel or precision measurements of matter effects. In order to achieve the required precision, high-statistics experiments are necessary, and many collaborations are planning ambitious upgrades or new experiments in the 2020s. An overview of the planned efforts and the underlying theory of mass hierarchy detection is given in [Qia15]. Here, only two of the planned experiments shall be discussed briefly.

The Jiangmen Underground Neutrino Observatory (JUNO) based in China aims for a precision measurement of the electron-antineutrino disappearance of reactor neutrinos at a medium baseline of 53 km [An16b]. The detector will consist of 20 kt liquid scintillator. The planned energy resolution of $3\,\%/\sqrt{E(\mathrm{MeV})}$ sets high requirements on the used PMTs. JUNO will start data taking in 2020 for six years and will determine the mass hierarchy with a precision of 3-4 standard deviations (σ).

The Deep Underground Neutrino Experiment (DUNE) will be a long-baseline experiment with $L = 1300$ km [Acc16a; Acc16b]. The muon (anti-)neutrino beam will be produced at an accelerator at Fermilab near Chicago (Illinois, USA). The selected baseline enables

the detection of both the mass hierarchy and the CP-phase with 5σ. For determining the mass hierarchy, 3.5 years of data taking for each mode (neutrino and antineutrino) are necessary. DUNE will be operable in the mid of the 2020s. The far detector, a 40 kt liquid argon detector made of four time projection chamber modules, will be also able to study other kinds of neutrino sources, like for instance supernova neutrinos.

Fourth Neutrino Generation (Sterile Neutrinos)

If the PMNS-matrix (see equation 2.6) turns out to be non-unitary, the 3×3-matrix can be interpreted as a subset of a unitary $n \times n$-matrix with $n > 3$ [Par16]. Since the number of active neutrinos being lighter than half of the mass of the Z boson is limited to three, as already mentioned in section 2.1, such a fourth neutrino generation is assumed to be sterile [Sig17]. In general, there is no principle known so far which should constrain the mass of the sterile neutrino to a certain scale [Par16].

Neutrino oscillation experiments can contribute to this aspect of neutrino physics in two ways: firstly, by measuring the 3×3 neutrino oscillation parameters very precisely with future experiments like described in the paragraph on neutrino mass hierarchy before to check for unitary of the PMNS matrix, and secondly by direct searches for oscillations from an active into a sterile state. Precision measurements of the Standard Model oscillations will constrain the parameter space for sterile neutrinos. However, for the analysis of 3×3 oscillations the unitarity of the mixing matrix is normally used as a pre-assumption [Par16]. Therefore, a direct observation of oscillations of an active into a sterile flavour is preferable. Due to the relation of oscillation length and mass differences in equation 2.15, this approach is limited to sterile neutrinos on the eV/c^2 scale to achieve oscillation lengths on the order of metres.

Anomalies in the count rates of reactor neutrino experiments [Den17], gallium experiments [Giu11] and accelerator experiments [Agu10] hint towards such eV/c^2-scale sterile neutrinos, but can also be interpreted as uncertainties in the theoretical description of the reactor neutrino spectrum or in the cross-section calculations. Thus, several experiments are currently planned or under construction to look for oscillation patterns on very short baselines [Gar16]. One of them is the Baksan Experiment on Sterile Transitions (BEST) located in the Baksan Underground Laboratory in Russia [Gav15]. BEST will use a ^{51}Cr source with 110 PBq (3 MCi) being placed in a 50 t target of liquid gallium metal. The target is divided into two concentric zones, each of them with the same path lengths for the neutrinos of about 55 cm. According to equation 2.19, the electron neutrinos emitted by the source produce ^{71}Ge atoms in interactions with the gallium. After nine days, these are extracted and counted in proportional counters like in the aforementioned SAGE experiment. After 10 cycles, about 870 counts are expected for each of the two zones if no sterile neutrino is involved. A sterile neutrino would manifest in a reduced count rate in the outer zone. Assuming an uncertainty of 5 % on the measured count rate, BEST alone will constrain the parameter space for sterile neutrino oscillations to $\sin^2 2\theta = 0.1$ for $\Delta m^2 = 1\,\mathrm{eV}^2/c^4$ with 1σ sensitivity [Bar16a]. The result of BEST can also be combined with results from GALLEX and SAGE for an even better sensitivity.

2.3. Neutrino Mass

As discussed in the previous section, neutrino oscillation experiments are not sensitive to the absolute neutrino mass scale, but only to the differences of the squared mass eigenvalues. However, neutrino oscillations have demonstrated that neutrinos must have mass. This section focusses on this absolute mass scale and its measurement. In subsection 2.3.1, the importance of a non-zero neutrino mass for different research topics of astrophysics and

cosmology is reviewed. The theory of mass generation of neutrinos is discussed in the following subsection 2.3.2. The section ends with an overview of experimental efforts for neutrino mass determination in subsection 2.3.3.

2.3.1. The Relevance of a Non-Vanishing Neutrino Mass for Astrophysics and Cosmology

Besides the implications of a non-zero neutrino mass in particle physics, which are discussed in the next section 2.3.2, the absolute neutrino mass is also an important parameter for many problems in astrophysics and cosmology. Some of these problems are reviewed briefly in the following:

Dark Matter: The precise measurement of the cosmic microwave background with the Planck satellite led to a Dark Matter content of the Universe of $\Omega_{DM} = (25.89 \pm 0.57)\,\%$ [Ada16]. Since neutrinos decoupled at $T \approx 1\,\mathrm{MeV}$, while being relativistic, they have to be hot Dark Matter. However, common theories rule out hot Dark Matter as main component of the Dark Matter sector, because a bottom-up scenario of structure formation is assumed which would not be viable for relativistic Dark Matter washing out gravitational centres on small scales [Sig17]. Furthermore, the number density of relic neutrinos from the Big Bang in today's Universe of $336\,\mathrm{cm}^{-3}$ [Bil10] together with the current neutrino mass limits on the (sub-)eV scale (see section 2.3.3) lead to a contribution to overall energy density of around or less than 1 % according to [Sig17]

$$\Omega_\nu h^2 = \frac{\sum m_\nu}{92.5\,\mathrm{eV}} \ . \tag{2.33}$$

This is much less than expected for the Dark Matter in total. So the masses of active neutrinos are important parameters to understand the structure formation, but cannot solve the Dark Matter puzzle. However, sterile neutrinos in the keV-range are good Dark Matter candidates, and an overview of this topic can be found in [Adh17].

Big Bang baryogenesis and leptogenesis: One of the most astonishing facts of the Universe is that more matter than antimatter exists after the Big Bang [Sak67]. This might be fundamentally related to neutrino properties, especially to their mass generation [Sig17]. In order to explain the light neutrino masses, in the so-called seesaw mechanism very heavy righthanded neutrinos are introduced (see also section 2.3.2). They may decay in lepton number violating processes. This lepton number violation may translate into baryon number violation. The baryon density in the early Universe and the closely related Big Bang nucleosynthesis set limits on the decay chain and the mass of the sterile neutrino. As soon as the mass of the light neutrinos will be measured, new constraints on these theories will be set.

Supernovae: In core-collapse supernovae, about 99 % of the released energy are carried by neutrinos [Sig17]. One supernova neutrino has a typical energy in the MeV-range (see figure 2.2), so that the neutrino mass on the order of (sub)-eV/c^2 is often neglected in calculations and simulations [Jan17]. From the last core collapse supernova in the Milky Way, the supernova SN1987A, an upper mass limit for the neutrinos of approximately $5\,\mathrm{eV}/c^2$ was derived from about 20 neutrinos being detected [Lor02]. Since neutrinos arrive at Earth before the photons of a supernova, they are a good early-warning indicator for a galactic supernova. Today's neutrino observatories are able to detect several thousands of supernova neutrinos and have set up a warning system for optical observatories [Abe16a]. The determination of the neutrino mass in independent measurements would not only help to determine the distance of travel more precisely, but should also allow deeper insights in the dynamics of a supernova [Zub11].

2.3.2. Theory of Neutrino Mass Generation

The following brief overview of the theory of neutrino mass generation is based on the textbooks [Zub11; Sig17; Bil10], if not stated otherwise.

As already mentioned in section 2.1, neutrinos are massless in the Standard Model of Elementary Physics. The reason is that, in the Standard Model, Dirac particles obtain their masses through the mass term of the Lagrangian

$$\mathcal{L} = m_{\mathrm{D}} \overline{\psi} \psi \tag{2.34}$$

with m_{D} being the Dirac mass and ψ being the Dirac spinor. Rewritten in two-component Weyl spinors with R and L indicating right- and left-handed particles, respectively, the Dirac mass term becomes

$$\mathcal{L} = m_{\mathrm{D}} \left(\overline{\psi}_{\mathrm{L}} \psi_{\mathrm{R}} + \overline{\psi}_{\mathrm{R}} \psi_{\mathrm{L}} \right) \ . \tag{2.35}$$

As already discussed in section 2.1, the observation of parity non-conservation in weak interactions led to the formulation of the quantum electrodynamic part of the Standard Model as a $\mathrm{SU(2)_L} \otimes \mathrm{U(1)_Y}$ symmetry. This includes the left- and right-handed electron, but only a left-handed neutrino. Thus, the Dirac mass of the neutrino in the Standard Model has to be zero according to equation 2.35. However, it was discussed in detail in section 2.2 that there is clear evidence of a non-vanishing neutrino mass. Therefore, extensions of the Standard Model are necessary to incorporate neutrino masses into the existing theoretical framework.

The first possibility is to just add the right-handed neutrino singlet to the Standard Model. Then, the Dirac mass m_{D} of the neutrino is interpreted like for all the other Dirac particles, too, as Yukawa coupling to the Higgs field [Hig64a; Eng64; Hig64b; Kib67]

$$\Phi_0 = \frac{1}{\sqrt{2}} \begin{pmatrix} 0 & v \end{pmatrix}^{\mathrm{T}} \tag{2.36}$$

in the electroweak unification [Gla61; Wei67; Sal68]:

$$\begin{aligned} \mathcal{L}_{\mathrm{Yuk}} &= -c_{\nu} \overline{\nu}_{\mathrm{R}} (\overline{\Phi}_0^C)^{\dagger} \begin{pmatrix} \nu_{\mathrm{e,L}} \\ \mathrm{e_L} \end{pmatrix} + \mathrm{h.\,c.} \\ &= -c_{\nu} \frac{v}{\sqrt{2}} \overline{\nu} \nu \qquad (2.37) \\ \Rightarrow m_{D,\nu} &= c_{\nu} \frac{v}{\sqrt{2}} \ . \qquad (2.38) \end{aligned}$$

v is the Higgs vacuum expectation value, c_{ν} the coupling constant and $\overline{\Phi}_0^C = -\mathrm{i}\sigma_2/2 \cdot \Phi^*$, σ_2 being the second Pauli matrix, so that

$$\overline{\Phi}_0^C = \frac{1}{\sqrt{2}} \begin{pmatrix} v & 0 \end{pmatrix}^{\mathrm{T}} \ . \tag{2.39}$$

The coupling constant is not predicted by theory, but has to be measured empirically and has to be a factor of at least one million smaller for neutrinos than for any other elementary particle.

The second possibility to include neutrino masses in the Standard Model assumes that neutrinos are Majorana particles. Then, neutrinos and antineutrinos are the same particles,

but the discrimination in left- and right-handed still remains. This would explain why no right-handed neutrinos or left-handed antineutrinos are observed. The Lagrangian becomes

$$\mathcal{L} = \frac{1}{2}\left(m_{\mathrm{M}}\overline{\psi}\psi^{\mathrm{C}} + m_{\mathrm{M}}^{*}\overline{\psi}^{\mathrm{C}}\psi\right) \ . \tag{2.40}$$

ψ^{C} denotes the charge-conjugated spinor and m_{M} the complex Majorana mass. The complex Majorana mass is translated into two real masses $m_{\mathrm{L,R}}$, if left- and right-handed states are used:

$$\mathcal{L}_{\mathrm{L}} = \frac{1}{2}m_{\mathrm{L}}\left(\overline{\psi}_{\mathrm{L}}\psi_{\mathrm{R}}^{\mathrm{C}} + \overline{\psi}_{\mathrm{R}}^{\mathrm{C}}\psi_{\mathrm{L}}\right) \ , \tag{2.41}$$

$$\mathcal{L}_{\mathrm{R}} = \frac{1}{2}m_{\mathrm{R}}\left(\overline{\psi}_{\mathrm{L}}^{\mathrm{C}}\psi_{\mathrm{R}} + \overline{\psi}_{\mathrm{R}}\psi_{\mathrm{L}}^{\mathrm{C}}\right) \ . \tag{2.42}$$

Majorana neutrinos render the neutrinoless double beta decay possible, which is an important probe of both the neutrino's nature and its mass (see section 2.3.3).

The third possibility is to combine the Dirac and Majorana mass terms in the Lagrangian as the most general ansatz:

$$\mathcal{L} = \frac{1}{2}m_{\mathrm{D}}\left(\overline{\psi}_{\mathrm{L}}\psi_{\mathrm{R}} + \overline{\psi}_{\mathrm{L}}^{\mathrm{C}}\psi_{\mathrm{R}}^{\mathrm{C}}\right) + \frac{1}{2}m_{\mathrm{L}}\overline{\psi}_{\mathrm{L}}\psi_{\mathrm{R}}^{\mathrm{C}} + \frac{1}{2}m_{\mathrm{R}}\overline{\psi}_{\mathrm{L}}^{\mathrm{C}}\psi_{\mathrm{R}} + \mathrm{h.\,c.} \tag{2.43}$$

$$= \begin{pmatrix}\overline{\psi}_{\mathrm{L}} & \overline{\psi}_{\mathrm{L}}^{\mathrm{C}}\end{pmatrix}\begin{pmatrix}m_{\mathrm{L}} & m_{\mathrm{D}} \\ m_{\mathrm{D}} & m_{\mathrm{R}}\end{pmatrix}\begin{pmatrix}\psi_{\mathrm{R}}^{\mathrm{C}} \\ \psi_{\mathrm{R}}\end{pmatrix} + \mathrm{h.\,c.} \tag{2.44}$$

The most interesting case for the mass matrix in the last equation is the so-called seesaw mechanism with $m_{\mathrm{L}} \approx 0$ and $m_{\mathrm{R}} \gg m_{\mathrm{D}}$. Then, the eigenvalues of the matrix become

$$m_1 = \frac{m_{\mathrm{D}}^2}{m_{\mathrm{R}}} \ , \tag{2.45}$$

$$m_2 = m_{\mathrm{R}}\left(1 + \frac{m_{\mathrm{D}}^2}{m_{\mathrm{R}}^2}\right) \approx m_{\mathrm{R}} \ . \tag{2.46}$$

m_1 is interpreted as the light neutrino mass and values at (sub-)eV/c^2 level are possible for reasonable values of m_{D} in the MeV/c^2-GeV/c^2 range comparable to the masses of other Dirac particles [Zub11]. Furthermore, m_2 is interpreted as the mass of a right-handed and sterile neutrino, so that in total three heavy mass eigenstates are introduced. Since observations provide various hints towards sterile neutrinos at the eV/c^2- and/or keV/c^2-scale (see sections 2.2.2 and 2.3.1), further mechanisms are required to break down the very heavy m_2 eigenstate to those ranges [Adh17].

It should be noted here that there are a lot of other theories for the mass generation of neutrinos like, for example, an extended Higgs sector with more Higgs particles than just one, or supersymmetric approaches, for which the reader is referred to the literature (e. g. [Zub11]). For the progress of this field, the experimental determination of the light neutrino mass is very important to reduce the number of parameters. The efforts on the experimental side are discussed in the next section.

2.3.3. Neutrino Mass Experiments

There are three complementary possibilities to measure the neutrino mass: The first one is the indirect determination by cosmological observations, the second one is the search for the, so far hypothetical, neutrinoless double beta decay, and the last one is the direct measurement with precision spectroscopy of the decay electrons from beta decay and the

Table 2.3.: Approaches for neutrino mass determination and their current sensitivites. The table gives an overview of the three approaches of neutrino mass determination based on cosmology, neutrinoless double beta decay ($0\nu\beta\beta$) and single beta decay (β^-) and electron capture (EC). In the second column, the different observables are presented with $i = 1, 2, 3$ denominating the mass eigenvalues. In the third column, the currently best limit of each method is shown. It should be noted that the values in the third column should only be compared with some general caution. For related literature, the reader is referred to the corresponding paragraph of the main text.

Approach	Observable	Current limit (in eV/c^2)
Cosmology	$m_{\mathrm{cos}} = \sum_i m_{\mathrm{i}}$	$\lesssim 0.1 \ldots 1.0$
$0\nu\beta\beta$	$m_{\beta\beta} = \left\lvert \sum_i U_{\mathrm{ei}}^2 m_i \right\rvert$	$\lesssim 0.06 \ldots 0.52$
β^- and EC	$m_\beta = \sqrt{\sum_i \lvert U_{\mathrm{ei}} \rvert^2 m_i^2}$	< 2.0

X-ray and electron spectrum of electron capture. Each of the three methods measures a different kind of mass observable and has different model dependences. The achieved levels of sensitivity also differ from method to method. For an overview of the methods and their sensitivities, table 2.3 lists the observables and their current limits. They are also discussed in more detail in the following paragraphs.

Cosmology

On the large scales investigated by cosmology gravity is the dominant force. As already mentioned in section 2.3.1, there are 336 neutrinos per cubic centimetre in the sum of all flavours in today's Universe [Bil10]. Under the assumption that all mass states contribute with the same number density, cosmological observations are, to first order, only sensitive to the total gravitational influence of neutrinos, i. e. to the sum of their masses ($\mathrm{i} = 1, 2, 3$) [Les12]

$$m_{\mathrm{cos}} = \sum_i m_i \ . \tag{2.47}$$

Since neutrinos were highly relativistic in the early Universe and only interact weakly, they carried away mass from gravitational centres. This influence of the neutrinos can be probed today. The most relevant observables to constrain the sum of neutrino masses are the mass power spectrum, a probe of the large scale structures of the Universe, and the power spectrum of the temperature anisotropies in the cosmic microwave background radiation (CMB) [Les12]. The former mainly bases on the data of the Sloan Digital Sky Survey (SDSS, latest data release in 2018) [Abo18]. For the latter, the most recent data were acquired by the Planck satellite mission, and the results were published in 2016 [Ade16] with an update 2018 [Agh18]. The analysis of the data for the determination of the sum of the neutrino masses is complicated and strongly depends on the cosmological model and the selected data sets. To reach sensitivities of $\sum_i m_i \approx 0.1\,\mathrm{eV}/c^2$, combinations of independent data samples are necessary, e. g. a combination of CMB and SDSS observations, but also data from Lyman alpha forest measurements or dark energy surveys (see e. g. [Di 16; Yec17; Cue16]). Due to this strong model and data-set dependence, only a range of the upper limits on the neutrino mass sum can be given, based on [Yec17]

$$m_{\mathrm{cos}} \lesssim 0.1 \ldots 1.0\,\mathrm{eV}/c^2 \ . \tag{2.48}$$

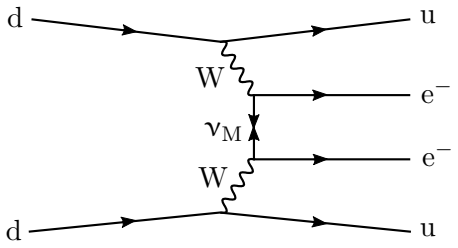

Figure 2.4.: Feynman graph of neutrinoless double beta decay. The graph shows the simultaneous decay of two d quarks as part of two neutrons into two u quarks as part of two protons. The Majorana transition is here depicted for a Majorana neutrino ν_M, but there are also other possibilities (see the main text).

Neutrinoless Double Beta Decay

Maria Goeppert-Mayer was the first who described the rare process of double beta decay [Goe35], in which a nucleus $X(Z, A)$ decays via two simultaneous beta decays into the daughter isotope $Y(Z + 2, A)$ with $m(Z, A) < m(Z + 1, A)$ and $m(Z, A) > m(Z + 2, A)$:

$$X(Z, A) \rightarrow Y(Z + 2, A) + 2e^- + 2\overline{\nu}_e \ . \tag{2.49}$$

This decay is only possible for nuclei with an even number of both neutrons and protons empirically described by the pairing energy in the Bethe-Weizsäcker mass formula [Wei35]. The decay in equation 2.49 can also occur with two β^+ decays or two electron captures or with one β^+ and one electron capture. Today, 36 isotopes undergoing double beta decay are known, with half-lives on the order of 10^{20} yr [Zub11].

Of great interest in neutrino and particle physics is the hypothetical process of neutrinoless double beta decay, first calculated and described in [Fur39]. In this case, the neutrinos are missing in the final state of equation 2.49, so that the decay is lepton-number violating with $\Delta L = 2$. It is only possible for massive neutrinos to account for the helicity in this process [Zub11]. The observation of this kind of decay would guarantee a Majorana contribution to the neutrino mass [Due11] (see also figure 2.4).

The effective Majorana mass is calculated in the coherent sum via the vertices of the Majorana neutrino in the decay to be [Zub11; Sig17]

$$m_{\beta\beta} = \left| \sum_i U_{ei}^2 m_i \right| \ . \tag{2.50}$$

It has to be noted that here the matrix elements U_{ei} contain two Majorana phases, which have to be taken into account. The phases can lead to a suppression or even cancellation of the sum. m_i denotes the Majorana mass of the mass eigenstate i.

Experimentally, the electrons from the neutrinoless double beta decay would occur in a tiny sharp peak above the continuous spectrum of the double beta decay electrons separated by twice the neutrino mass from the endpoint. From the observed count rate, a half-life $T_{1/2}^{0\nu}$ is obtained, which is related to $m_{\beta\beta}$ via [Zub11]

$$\frac{1}{T_{1/2}^{0\nu}} = G^{0\nu} \left| M^{0\nu} \right|^2 \left(\frac{m_{\beta\beta}}{m_e} \right)^2 \ . \tag{2.51}$$

$G^{0\nu}$ is the phase space integral, m_e the electron mass and $M^{0\nu}$ the transition matrix element including all effects of the quarks being bound in the nuclei.

For each neutrinoless double beta experiment, the reduction of the background by setting up the experiment in an underground lab, the use of only low-radioactivity materials and a very good shielding against radioactivity from the surrounding rocks are mandatory [Zub11]. Furthermore, to get a larger count rate per target mass, an isotope which can be enriched artificially is favoured. The measurement technique should be scalable to increase the exposure step by step.

There are several experiments currently running or under construction. Here, only three of them shall be mentioned as examples: The Germanium Detector Array (GERDA) is an experiment with bare germanium detectors enriched with ^{76}Ge. Located in the Gran Sasso Laboratory and shielded by liquid argon, GERDA achieved a nearly background-free measurement with a current limit of $m_{\beta\beta} < 0.12 - 0.26\,\mathrm{eV}/c^2$ (90 % C. L.) for a $46.7\,\mathrm{kg}\cdot\mathrm{yr}$ exposure [Ago18]. KamLAND-Zen is a ^{136}Xe-based scintillator experiment. ^{136}Xe is enriched to 90 % and an exposure of $504\,\mathrm{kg}\cdot\mathrm{yr}$ has been achieved. KamLAND-Zen sets the currently best limit on the neutrino Majorana mass of $m_{\beta\beta} < 0.061 - 0.165\,\mathrm{eV}/c^2$ (90 % C. L.) [Gan16]. The Cryogenic Underground Observatory for Rare Events (CUORE) investigates the double beta decay of ^{130}Te in 988 TeO_2 crystal bolometers and is also located in the Gran Sasso Laboratory. So far, it has collected an exposure of $86.3\,\mathrm{kg}\cdot\mathrm{yr}$, from which an upper limit on the Majorana neutrino mass of $m_{\beta\beta} < 0.11 - 0.52\,\mathrm{eV}/c^2$ (90 % C. L.) was derived [Ald18]. Based on these world-leading experiments, the current sensitivity of neutrinoless double beta decay search on the Majorana mass of the neutrino is estimated to be

$$m_{\beta\beta} \lesssim 0.06 \ldots 0.52\,\mathrm{eV}/c^2 \ . \tag{2.52}$$

Many efforts are done to push this level further down within the next years. For the interpretation of this upper limit, the following considerations have to be taken into account:

- As already mentioned above, the Majorana phases are unknown, so that the value of $m_{\beta\beta}$ can be much smaller than the value m_β obtained in single beta decay experiments.
- The calculation of the transition matrix elements in equation 2.51 is not trivial. The results differ by a factor of up to three depending on the method and pre-assumptions made [Eng17]. Hence, there are large theoretical uncertainties involved in this calculation, which can be hopefully reduced in the future to be sensitive to Majorana neutrino masses $< 0.1\,\mathrm{eV}/c^2$.
- In principle, the neutrinoless double beta decay is also possible with other lepton-number violating processes and exchange particles like e. g. supersymmetric particles [Päs15]. Due to loop corrections a certain Majorana contribution to the neutrino mass is always guaranteed, if the neutrinoless double beta decay is observed [Due11]. However, the observation alone cannot determine how large this contribution is and how the remaining contributions to the decay rate arise.

These three considerations make the interpretation of the results of neutrinoless double beta decay experiments very difficult and strongly model-dependent. These results can only be compared to those from the other approaches with great care and consideration, but a positive result would at least open the door to understanding the fundamental nature of neutrinos.

Beta Decay and Electron Capture

In contrast to the already introduced methods of neutrino mass determination, the measurement based on the kinematics of the endpoint region of the beta decay electron spectrum

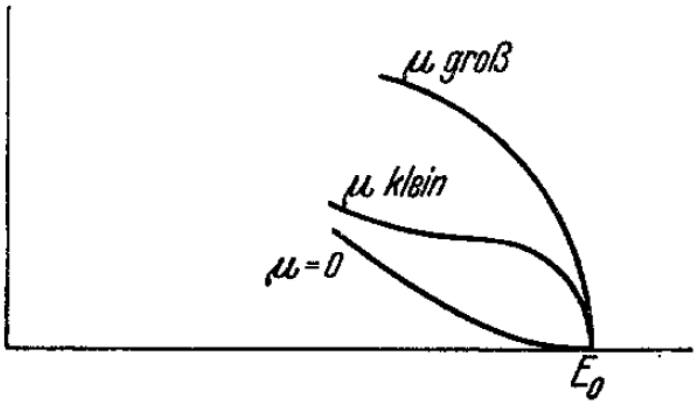

Figure 2.5.: Influence of the neutrino mass on the kinematic endpoint region of the β spectrum. With the development of his theory of β decay in 1934, Fermi investigated the influence of the neutrino mass on the kinematic endpoint of the β electrons. A non-vanishing neutrino mass (denoted as μ in the picture), changes the shape of the spectrum in the endpoint region. Resolving this shape is the measurement principle of direct neutrino mass experiments today. See the main text for more details. Reprinted by permission from Springer Nature [Fer34].

is not model-dependent. It basically depends only on the well-established Fermi theory of beta decay [Fer34] (see figure 2.5). Therefore, experimental progress on this field is of great importance for the correct interpretation of the results from cosmology and neutrinoless double beta decay.

The transition probability per unit time $\Gamma_{i\to f}$ for an atom undergoing a beta decay like in equation 2.1 is calculated with Fermi's golden rule, see e. g. [Zub11; Ott08]:

$$\Gamma_{i\to f} = \frac{2\pi}{\hbar} \left|\langle f \left|H_{if}\right| i\rangle\right|^2 \rho(E) \ . \tag{2.53}$$

Here, $\langle f \left|H_{if}\right| i\rangle$ is the transition matrix element from the initial state i to the final state f with the Hamilton operator H_{if}. $\rho(E)$ denotes the phase space density. The matrix element and the phase space density are calculated separately. For details of this calculation, the reader is referred to the literature [Ott08]. The final result for the differential energy spectrum is (for tritium):

$$\begin{aligned}\frac{\mathrm{d}\Gamma_{i\to f}}{\mathrm{d}E} =& \frac{G_\mathrm{F}\cos^2\theta_\mathrm{C}}{2\pi^3} \left|M_\mathrm{nuc}\right|^2 F\cdot(E_0+m_\mathrm{e}-\epsilon)\cdot\sqrt{(E_0+m_\mathrm{e}-\epsilon)^2-m_\mathrm{e}^2} \\ &\cdot\sum_{i,j}\left|U_{ei}\right|^2 P_j\cdot(\epsilon-V_j)\cdot\sqrt{(\epsilon-V_j)^2-m_i^2}\cdot\Theta(\epsilon-V_j-m_i) \ ,\end{aligned} \tag{2.54}$$

with the Fermi constant G_F, the Cabibbo angle θ_C, the nuclear matrix element M_nuc, the PMNS mixing matrix elements U_{ei}, the electron mass m_e, the neutrino mass eigenvalues m_i and $\epsilon = E_0 - E$, E_0 being the energy of the kinematic endpoint. $F(E, Z+1)$ is the Fermi function, which takes the electromagnetic interaction of the decay electron with the daughter nucleus into account. P_j and V_j are the probabilities of the electronic final states of the daughter system and their energies, respectively. The Heaviside function Θ guarantees that there is no negative energy with $\epsilon - V_j - m_i > 0$.

Often, the beta decay spectrum is linearised in the form of the so-called Kurie plot with [Kur36; Zub11]

$$\sqrt{\frac{\Gamma(E)}{p_\mathrm{e}^2 F(Z+1,E)}} = \frac{G_\mathrm{F}\cos^2\theta_\mathrm{C}}{2\pi^3}\,|M_\mathrm{nuc}|^2 \cdot (E_0 - E_\mathrm{e}) \cdot \left[1 - \left(\frac{m_\nu}{E_0 - E_\mathrm{e}}\right)^2\right]^{\frac{1}{4}} . \tag{2.55}$$

The spectrum is then plotted as a straight line and the x-intercept indicates the endpoint energy of the spectrum. A non-zero neutrino mass manifests as a shift of this endpoint energy by m_{ν_e} and as a change of the shape at the endpoint region, since the spectrum ends now perpendicular to the x-axis [Zub11].

From equation 2.54 it follows that the neutrino mass observable in beta decays is the incoherent sum of mass eigenstates weighted by the PMNS matrix elements, which is defined as the effective mass of the electron antineutrino $m_{\overline{\nu}_\mathrm{e}}$ [Ott08]

$$m_\beta = m_{\overline{\nu}_\mathrm{e}} = \sqrt{\sum_i |U_{ei}|^2\, m_i^2} . \tag{2.56}$$

Experimentally, there is a long tradition to use tritium as the beta emitter for the determination of the neutrino mass, with the reaction

$$\mathrm{T}_2 \rightarrow \mathrm{HeT}^+ + \mathrm{e}^- + \overline{\nu}_\mathrm{e} . \tag{2.57}$$

This is based on several advantages of this specific nuclide:

- The half-life of tritium is only 12.3 yr [Luc00]. This offers the possibility of a high-luminosity source with a comparably small amount of source material [Ott08].
- The decay of tritium is super-allowed, so that the matrix element in equation 2.54 becomes independent of energy [Ott08].
- Tritium normally exists as molecule. Since it is one of the simplest molecules, its electronic final states are calculable [Bod15].
- The kinematic endpoint of the tritium beta-spectrum is about 18.6 keV [Ott08], which is calculated from measurements of the mass difference of ^{3}T and ^{3}He [Mye15]. The tritium endpoint is one of the smallest known among all β emitters, so that the effect of the neutrino mass on the spectrum is comparatively large.

The history of tritium experiments starts already in 1947 [Kon47]. In the following decades, further experiments were performed, improving the sensitivity step by step. One important milestone was the first gaseous tritium source to reduce the systematic effects drastically, set up at the Los Alamos National Laboratory [Wil87]. In the 1990s, the experiments in Troitsk [Ase11] and Mainz [Kra05] became world-leading. In Troitsk, a gaseous source was used, in Mainz a quenched-condensed one. The other parts of the set-up were in both cases very similar to the next-generation experiment KATRIN, which is described in detail in chapter 3. The limits set by the Mainz ($m_{\overline{\nu}_\mathrm{e}} < 2.3\,\mathrm{eV}/c^2$, 95 % C. L.) and Troitsk ($m_{\overline{\nu}_\mathrm{e}} < 2.05\,\mathrm{eV}/c^2$, 95 % C. L.) experiments are still the best today and combined they are stated as [Tan18]

$$m_\beta = m_{\overline{\nu}_\mathrm{e}} < 2.0\,\mathrm{eV}/c^2 . \tag{2.58}$$

In 2009, a new technique to measure the electron antineutrino mass based on the detection of the cyclotron radiation of tritium decay electrons in strong magnetic fields was proposed [Mon09]. The Project 8 collaboration formed to apply this technique, and they have demonstrated the method of cyclotron emission radiation spectroscopy with the detection

of single conversion electrons from ^{83m}Kr [Asn15]. This was the major milestone of the phase I. In the recently started phase II, Project 8 will apply the method with tritium, using a setup similar in size and complexity as in phase I. For phase III, the source volume will be enlarged to $> 200\,\mathrm{cm}^3$ in order to reach a sensitivity on the electron antineutrino mass of about $2\,\mathrm{eV}/c^2$. To achieve a sensitivity on the order of 50 meV, Project 8 aims to develop an atomic tritium source for its phase IV. The data-taking of this final phase is foreseen to start in the late 2020s [Ash17].

For measurements of the mass of the electron neutrino, ^{163}Ho turned out to be a very suitable isotope, undergoing electron capture with the smallest Q-value of about 2.5 keV [De 82]. An independent measurement of the mass of the electron neutrino is an important test of the CPT invariance [Zub11]. The best limit so far is from 1987 with $m_{\nu_e} < 225\,\mathrm{eV}/c^2$ [Spr87]. Currently, there are several ongoing experimental efforts to push this limit below $1\,\mathrm{eV}/c^2$ with calorimetric measurements of the ^{163}Dy de-excitation spectrum of X-rays and electrons. The excited ^{163}Dy is produced in the electron capture process of ^{163}Ho.

The HOLMES experiment will use microcalorimeters read out with transition edge sensors to reach a sensitivity of $< 2.0\,\mathrm{eV}/c^2$ [Gia17]. An array of 1024 detectors is necessary for this sensitivity, starting data taking in 2019. Before, a test run with 64 pixels is planned to prove the principle. In the future, an upgrade to a mega-pixel experiment is planned to reach a sub-eV sensitivity.

A different detector design is used by the ECHo collaboration. They have developed metallic magnetic calorimeters with metallic paramagnetic temperature sensors. The temperature change of the calorimeter due to a particle interaction leads to a change of the magnetisation of the sensor which is recorded by a pick-up coil. The energy resolution of these calorimeters is $< 2\,\mathrm{eV}$ [Gas17]. Recently, ECHo demonstrated the performance of their calorimeters in a high-precision measurement of the ^{163}Dy spectrum [Ran17]. In the first phase of the experiment, for which data-taking has commenced in 2018, about 100 pixels are used to reach a sensitivity on the neutrino mass of $10\,\mathrm{eV}/c^2$. In the second phase, ECHo will apply a total activity of 1 MBq of ^{163}Ho to achieve a sub-eV sensitivity [Gas17].

3. The KATRIN Experiment

This chapter presents the Karlsruhe Tritium Neutrino (KATRIN) experiment in detail. Following an introduction with some remarks on the history of the experiment in section 3.1, the setup of the experiment together with the underlying measurement principle is discussed in section 3.2. The analysis and simulation software developed by the KATRIN collaboration is introduced in section 3.3. In section 3.4, it is explained how, exactly, the neutrino mass is derived with KATRIN. Furthermore, the corresponding sensitivity on the electron antineutrino mass and phenomena beyond the Standard Model are discussed. The chapter ends with a description of the objectives of the thesis at hand in section 3.5.

3.1. Introduction

Based on the results achieved and experience made in the neutrino mass experiments in Troitsk [Ase11], Mainz [Kra05] and Los Alamos [Rob91] (see section 2.3.3), it was decided to bundle the knowledge and to form a large collaboration to realize a next-generation tritium neutrino mass experiment. The aim to improve the currently best sensitivity of $2.0\,\mathrm{eV}/c^2$ (see equation 2.58) by a factor of 10 actually requires an improvement in sensitivity by a factor of 100 since the neutrino mass square is the quantity which enters the beta spectrum (see equation 2.54). Therefore, a highly luminous tritium source to obtain the required statistics is a pre-condition for the success of the experiment.

The Tritium Laboratory Karlsruhe (TLK) offers ideal conditions for such a source with a permission to handle up to 40 g of tritium [Bor11]. Therefore, a letter of intent for the Karlsruhe Tritium Neutrino (KATRIN) experiment was published in 2001 [Osi01], followed by the KATRIN Design Report in 2005 [Ang05]. The pre spectrometer was the first main component of the KATRIN beam line to arrive in Karlsruhe in 2003, followed by the main spectrometer in 2006. The beam line was completed in 2015 with the delivery of the Cryogenic Pumping Section (CPS) and the Windowless Gaseous Tritum Source (WGTS). The apparatus passed two important commissioning milestones with the First Light campaign in 2016 and a ^{83m}Kr measurement programme in 2017 [Are18b]. The excellent performance of the experiment in these pre-measurements enabled the first tritium commissioning in 2018.

KATRIN is an experiment of high complexity and sets new physical and technical limits. Some of the key features and challenges met by KATRIN are listed in the following:

- The envisaged source activity of 10^{11} Bq, stabilized to the 0.1 % level [Ang05] and maintained by a closed tritium cycle with a throughput of 40 g per day [Bor11], sets strong requirements on the tritium supply and processing in the TLK facilities.
- Excellent ultra-high vacuum conditions are crucial for the success of the experiment. The main spectrometer vessel with a volume of $1240\,\mathrm{m}^3$ is operated on the 10^{-11} mbar level [Are16] and is one of the largest UHV recipients ever built.

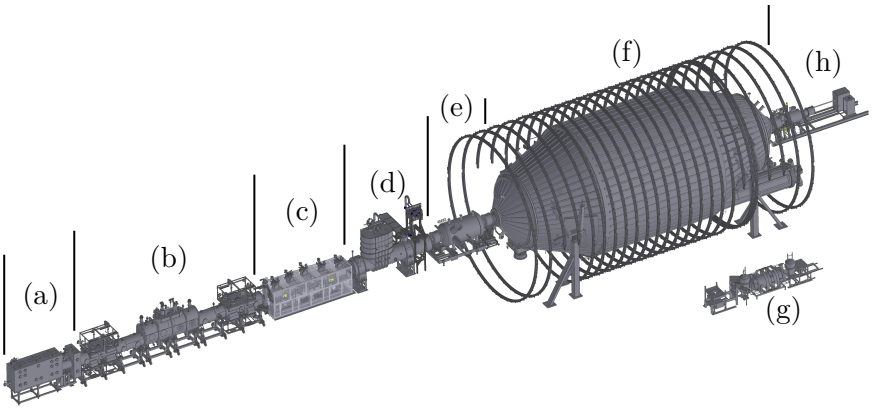

Figure 3.1.: The KATRIN beamline. The figure shows the entire 70-m long KATRIN beam line. The main components are: *(a)* the rear section (see section 3.2.2), *(b)* the windowless gaseous tritium source (WGTS) (see section 3.2.1), *(c)* the differential pumping section (DPS) (see section 3.2.3), *(d)* the cryogenic pumping section (CPS) (see section 3.2.4), *(e)* the pre spectrometer (see section 3.2.5), *(f)* the main spectrometer (see section 3.2.5), *(g)* the monitor spectrometer (see section 3.2.6), *(h)* the detector (see section 3.2.7). For a detailed discussion the reader is referred to the corresponding sections of the main text.

- In total 24 superconducting magnets along the entire KATRIN beam line are required in order to guarantee adiabatic transport of the beta electrons from the source to the detector. The magnets are designed for magnetic field strengths from 3.6- to 6.0 T [Are18c] in order to maintain a magnetic flux tube of 191 T cm^2 along the entire beam line for the guidance of the electrons.

3.2. Setup

This section gives a detailed overview of the main components of the KATRIN experiment. The 70 m beam line is depicted in figure 3.1. It can be divided into two sections: the Source and Transport Section (STS) and the Spectrometer and Detector Section (SDS). The STS comprises the windowless gaseous tritium source (WGTS, see section 3.2.1), the rear section for monitoring and calibration purposes (see section 3.2.2), the differential pumping section (DPS, see section 3.2.3) and the cryogenic pumping section (CPS, see section 3.2.4). The STS supplies the experiment with electrons from the highly luminous tritium source and retains all tritium within the closed pumping loop. At the end of the STS, the tritium flow towards the spectrometers is reduced by 14 orders of magnitude [Are16]. Since all STS components are exposed to tritium, the STS is located inside TLK. The SDS analyses the energy of the electrons with the spectrometers and measures the endpoint region of the beta-decay spectrum integrally with a count rate of about 1 count/min at an energy of 1 eV below the endpoint [Ang05]. A tritium contamination of this section has to be prevented to meet the strict requirements on the background rate.

In the following, the technical details of the main components of the apparatus are introduced, beginning with the WGTS and ending with the detector. For the discussion of the physics and the systematic uncertainties linked to the apparatus, the reader is referred to chapter 4.

3.2.1. The Windowless Gaseous Tritium Source

The WGTS cryostat has a length of 16 m, a width of 1.5 m and a height of 4 m. The total weight is 26 t [Gro08]. The cryostat is depicted in figure 3.2. The most crucial part of the

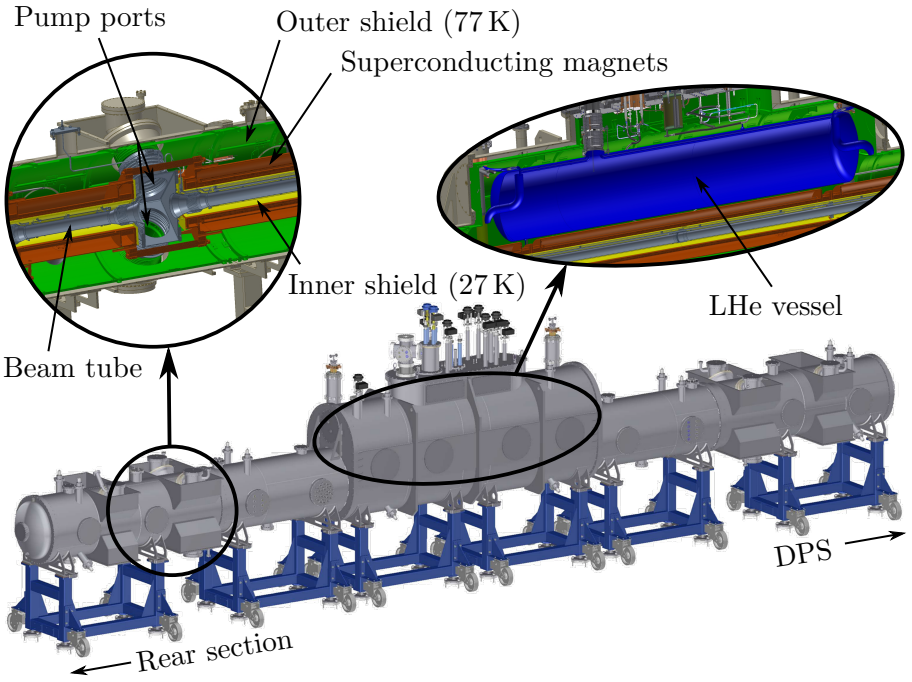

Figure 3.2.: The windowless gaseous tritium source. The windowless gaseous tritium source (WGTS) is a 16 m long cryostat set up in a multi-layer principle: The 30 K cold beam tube elements (grey) containing the tritium are surrounded by the inner shield (yellow), which is cooled by gaseous helium to 27 K. The inner shield reduces the influence of the 4 K cold superconducting magnets on the beam tube temperature stability. The seven magnets (red) with field strengths up to 5.6 T are surrounded by the outer shield (green), which is cooled with liquid nitrogen and reduces the heat transfer by radiation from the outer hull. The magnets are supplied with liquid helium from a large reservoir (blue) with $10^6\,\ell$ volume. The tritium is injected in the middle and pumped off by a total of six turbo molecular pumps at both sides of the machine, see also figure 3.3.

WGTS for the neutrino mass measurements is the 10 m-long central beam tube with a diameter of 90 mm. Here, the molecular tritium is injected in the middle. At the rear and the front side the central beam tube is followed by two differential pumping sections, the so-called DPS-1-R/F-1 and DPS-1-R/F-2. In both the DPS-1-R and the DPS-1-F, the tritium is pumped off by six turbo-molecular pumps, four of them being attached to the inner pump ports 1 and two of them to the outer pump ports 2. Two additional turbo-molecular pumps are installed in the pump port between WGTS and DPS. The pumps lead to a quasi-linear decrease of the tritium density with increasing distance to the tritium inlet as shown in figure 3.3. The total column density is 5×10^{17} molecules/cm^2 [Ang05]. The DPS-1-F reduces the tritium flow towards the spectrometers by two orders of magnitude till the end of the WGTS cryostat. The beam tube is surrounded by seven superconducting magnets designed to be operated at 3.6 T and 5.6 T (only the two magnets of DPS-1-F) [Are18c]. The magnetic fields enable an adiabatic transport of the electrons created in tritium beta decay towards the spectrometer section.

As discussed in a dedicated section 4.2, most of the systematic uncertainties of the KATRIN experiment are linked to the tritium source. One of them is the relative stability of the column density which has to be better than 2×10^{-3}. This directly translates to the temperature and injection pressure stability [Ang05]. The temperature of the central beam tube of 30 K was chosen as a compromise to reduce both the influence of the Doppler effect on the one hand and the clustering of tritium molecules at very low temperatures at the other hand [Ang05]. The temperature setting is realised through a novel two-phase

neon cooling system: two 16 mm tubes are brazed to both sides of the central beam tube and are half-filled with liquid neon. Neon was selected due to a suitable vapour pressure of about 2 bar at 30 K [Stu47]. Heat transfer from the beam tube lets the neon evaporate without a temperature increase, since latent heat only increases the entropy [Bod11; Mar17a]. The neon vapour diffuses towards the condenser at one end of two cooling tubes where it is condensed in a heat exchange with gaseous helium at about 25 K. The liquefied neon then flows back towards the cooling tubes. This thermosiphon works without any mechanical pumping. The evaporation of the neon can be controlled by four heating wires with 2 W each, installed in each of the cooling pipes [Gro08; Gro09; Gro11; Gro13].

The cooling of the four beam tube elements DPS-1-R/F-1 and -2 is done in separate cycles. The DPS-1-R/F-1 make also use of a two-phase neon cooling, while the DPS-1-R/F-2 are cooled with gaseous neon at about 80 K [Gro09]. Since the tritium density is much smaller at these outer sections of the WGTS beam tube, also the requirements on the stability are not as strict as in the central beam tube. The pump ports are heat-shielded and cooled with liquid nitrogen and neon to reduce the heat transfer from the pumps to the beam tube volume [Gro09].

The superconducting magnets surround the beam tube and are placed in a liquid helium bath with a temperature of 4.2 K (see figure 3.2). For this reason, the inner cooling system has to be shielded from the magnets to keep the temperature stable. This is done with the inner shield, which is cooled by the same gaseous helium circuit which condenses the neon of the two-phase cooling described before. An outer shield, operated at 77 K with liquid nitrogen and surrounding the superconducting magnets, reduces the heat load from the outer hull of the cryostat, which is at room temperature. The hull, the shields, the magnets and the beam tube are furthermore separated by an insulation vacuum of $< 10^{-5}$ mbar to reduce convection to a minimum. In a second operational mode of the WGTS, ^{83m}Kr is mixed to the tritium (see section 5.2). In this mode, the WGTS is operated at 100 K. For this purpose, the neon is exchanged by argon and the temperature of the shields is adjusted. In total, the cryostat comprises 13 fluid circuits and about 500 sensors. Especially the 24 PT500 sensors along the inner beam tube play an important part for KATRIN's neutrino mass analysis. They monitor the temperature stability and homogeneity. The temperature stabilisation and measurement are discussed in detail in section 6.2.

In order to achieve a stable tritium injection pressure of 1.8 mbar $\ell\,\mathrm{s}^{-1}$ at the 0.1 % level, the so-called inner loop is set up [Kaz08; Stu10a; Pri15] (see figure 3.3): Tritium gas pumped off in the DPS-1-R/F is guided to a permeator, where impurities like helium as daughter isotope of the tritium decay and methanes coming from wall interactions are separated. The contaminants are re-processed in the outer tritium loop, where in the last stage the hydrogen isotopologues are separated and tritium is highly enriched. This nearly pure tritium is re-injected to the inner loop via a buffer vessel. To collect enough statistics, the KATRIN requirement is that the isotopic tritium purity ϵ_T has to be always above 95 % at a stability level of 0.1 % [Ang05]. This is monitored by a laser Raman (LARA) system being part of the inner loop after the aforementioned buffer vessel [Sch13a; Sch13b; Sch13c; Fis14]. After passing the LARA system, the gas stream enters a temperature- and pressure-controlled buffer vessel from which the gas is guided to the transfer tube to WGTS via a controlled regulating valve [Pri15]. The transfer tube with a diameter of 2.1 mm is thermally coupled to the WGTS beam tube inside the cryostat to cool down the tritium gas before entering the injection chamber, consisting of 415 small orifices through which the tritium diffuses into the beam tube [Stu10a]. The complete inner loop is set up in glove boxes which act as a second containment for the safe handling of tritium.

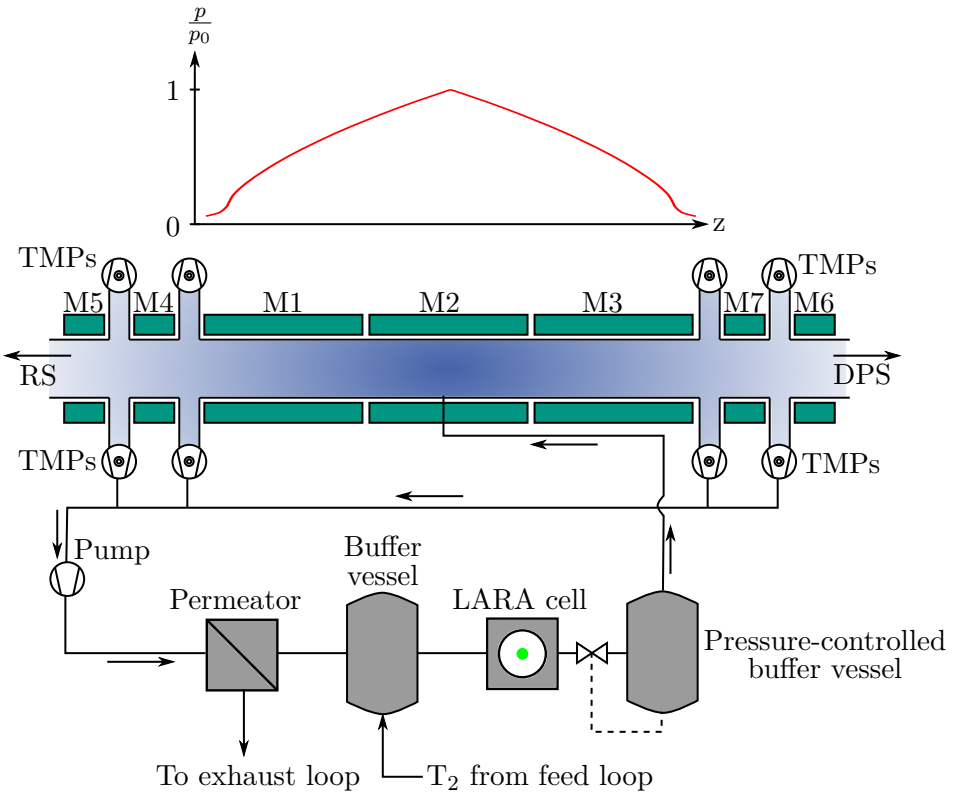

Figure 3.3.: Gas flow in WGTS and inner loop. The lower part of the figure shows the WGTS and the gas flow in the inner loop. The tritium is extracted at both sides of the WGTS with turbo molecular pumps (TMPs) and then pumped to a permeator, where about 1 % of the gas stream is separated and guided to the exhaust loop. In the buffer vessel, highly enriched tritium is injected again from the feed loop. Afterwards, the gas composition is analysed in a laser Raman (LARA) system. From a pressure- and temperature-controlled buffer vessel the gas is injected into the WGTS. The WGTS is surrounded by seven superconducting magnets (green, M1 to M7). The upper plot of the figure shows the triangular shape of the gas distribution inside the WGTS beam tube normalized to the injection pressure p_0 (based on the model of [Kuc16]).

3.2.2. The Rear Section

The rear section completes the KATRIN beam line in the upstream direction of the WGTS and is depicted in figure 3.4. It houses monitoring and calibration devices for the WGTS column density and activity and terminates the KATRIN beam line with the rear wall.

The rear wall is a gold-coated stainless-steel disk with a diameter of 6 inches [Sch16]. To guarantee that the full magnetic flux tube of 191 T cm^2 coming from the WGTS hits the rear wall, a superconducting magnet designed for magnetic field strengths up to 4.7 T is mounted behind the rear wall chamber [Are18c]. With the full magnetic flux tube hitting the rear wall, it is assumed that the rear wall potential will mainly determine the potential of the low-density plasma in the WGTS which forms due to tritium beta decay [Kuc16]. Therefore, the work function of the rear wall surface has to be very homogeneous with temporal and spatial fluctuations being smaller than 20 meV. The total potential of the rear wall can be controlled by a voltage supply in the range of ±10 V [Sch16]. Low energetic electrons can be created by the photoelectric effect with a UV light illumination of the rear wall. These will then compensate the space charge of the plasma and reduce the influence of the plasma on the tritium endpoint energy [Sch16].

Of the 10^{11} electrons being produced in tritium beta decay every second in the WGTS, more

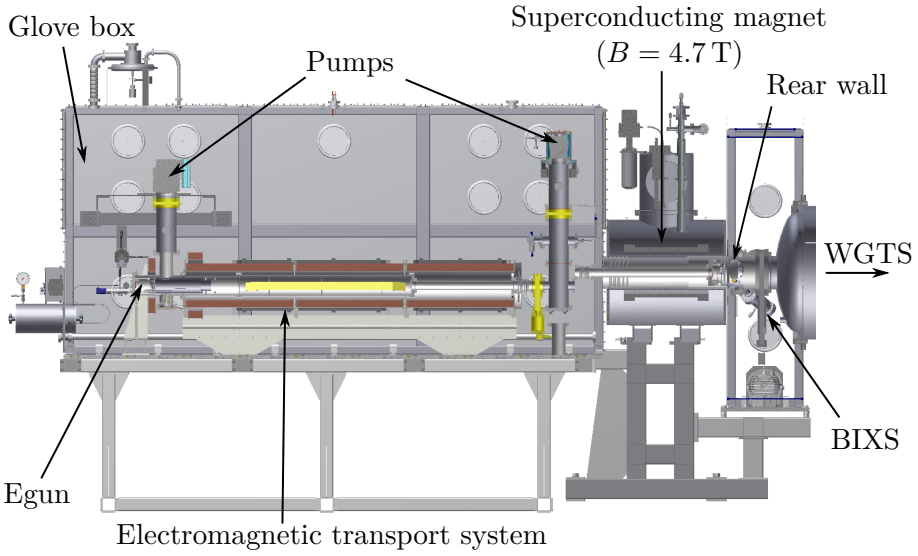

Figure 3.4.: The rear section. The rear section consists of three parts: the egun and the corresponding electromagnetic transport section to guide the electrons with electrodes and normal conducting magnets towards the rear wall, the superconducting magnet to guarantee the magnetic flux from the WGTS hitting the rear wall and finally the rear wall chamber with the rear wall inside and the BIXS systems to monitor the activity in the WGTS. The possibly tritiated components are surrounded by glove boxes as a second containment.

than 99.99 % hit the rear wall; a part of them directly, a part of them after being reflected by magnetic fields or the retarding voltage of the pre- and main spectrometer [Röl15]. This is used in two beta-induced X-ray spectroscopy (BIXS) systems which monitor the X-rays being induced by bremsstrahlung of the electrons hitting the rear wall. The X-rays are detected with two silicon drift detectors which are each protected from tritium contamination by gold-coated beryllium windows, which are transparent for X-rays. It was demonstrated that the two BIXS systems are suitable to monitor the WGTS activity on the 0.1 % level in 70 s of measurement time [Röl15].

Finally, with the electron gun (egun) the rear section houses a powerful calibration tool for the KATRIN apparatus. It offers electrons of well-defined polar angle and energy. The illumination of a cathode by a UV light source produces on the order of 10^4 electrons per second [Bab14; Sch16]. The electrons are accelerated by electrodes and then adiabatically guided by magnetic fields towards the rear wall. Here, they enter the beam tube through a 5 mm hole in the middle [Bab14]. The energy width of the beam is approximately 0.2 eV and different angles towards the magnetic field lines can be adjusted with a sharpness $< 4°$ in a magnetic field of 3.6 T [Bab14]. Dipole magnets mounted in the WGTS enable the scanning of the electron beam over the whole beam tube cross section [Bab14]. Thus, the egun is essential for many calibration and monitoring purposes of KATRIN, e. g. the monitoring of column density stability (see section 4.2.15) [Ang05; Bab14], the measurement of the energy loss function of electrons in the source due to inelastic scattering (see section 4.2.16) [Han17] and pixel-wise transmission function measurements of the main spectrometer (see equation 3.6) [Beh17a].

3.2.3. The Differential Pumping Section

The DPS fulfils three different tasks: the reduction of tritium flow towards the spectrometer section by five orders of magnitude, the adiabatic guiding of beta-decay electrons from the WGTS towards the spectrometers and the analysis and blocking of ions travelling

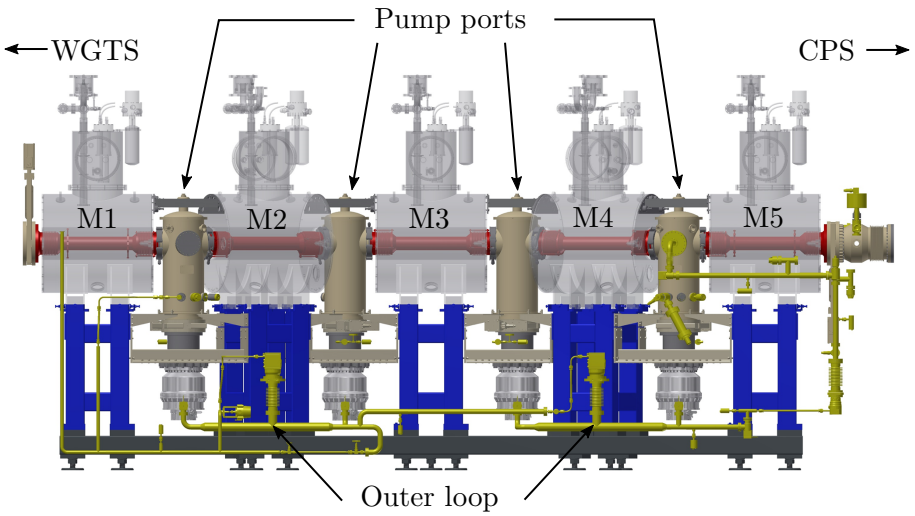

Figure 3.5.: The differential pumping section. The differential pumping section (DPS) consists of five beam tube elements (red) each of them surrounded by a superconducting magnet (grey, M1 to M5) designed for magnetic field strengths of up to 5.5 T. The beam tube elements are assembled in an Ω-shaped chicane with a tilting of 20°. Between the beam tube elements, four turbo molecular pumps plugged to the pump ports (brown) pump off the tritium. The gas is guided back to the TLK infrastructure for tritium enrichment by the outer loop (yellow).

towards the spectrometers [Ang05]. First, the DPS was planned as one large cryostat, but since problems with the superconducting magnets occurred during the commissioning in 2011 [Kos12], a re-design was necessary [Kos12; Jan15]. The new system was successfully commissioned in 2015 [Hac15]. The new design shown in figure 3.5 consists of five 1 m-long beam tube elements, each of them surrounded by a standalone superconducting magnet designed for up to 5.5 T [Are18c]. The five beam tube elements are separated by four pump ports equipped with one turbo molecular pump each. The entire DPS has a length of 6.5 m. The beam line elements are tilted by 20° to each other in an "Ω shape". While the charged electrons are guided adiabatically around this chicane, neutral tritium molecules scatter off the walls. This reduces the molecular beaming effect (see e. g. [Zha12]) and enhances the pumping probability. First measurements with the old DPS design lead to an estimated tritium flow reduction factor of 2.5×10^4 [Kos12; Luk12], but simulations of the gas flow with the new DPS design indicate that the designed tritium flow reduction factor of 10^5 is achievable [Jan15].

Since in the final state of molecular tritium beta decay a charged ion HeT^+ remains (see equation 2.57), different other ions like $T_2{}^+$, $T_3{}^+$, $T_5{}^+$ and more can form in ionisation or chemical processes [Ubi09]. These ions are guided by the magnetic fields in the same way as the electrons and can reach the spectrometers where their decay would cause an unacceptable background rate [Ang05]. Therefore, the ion flux has to be blocked and analysed (see also section 4.2.9). For both tasks additional equipment is mounted into the DPS beam line elements: one ring electrode in beam tube element 5 of DPS and another one in the pump port 5 between DPS and CPS block positive ions with an applied positive potential of +100 V [Jan15; Kle18b]. Inside the beam tube elements 1 to 4 of DPS, dipole electrodes remove the reflected ions from the flux tube due to an $\vec{E} \times \vec{B}$ drift, so that the ions hit the stainless steel walls where they are neutralised. Downstream of the ring electrode in beam tube element 5, a Fourier transform ion cyclotron resonance (FT-ICR) device is mounted to analyse the remaining amount of the different ion species flowing towards the spectrometer section [Ubi09]. The ion blocking devices have been successfully

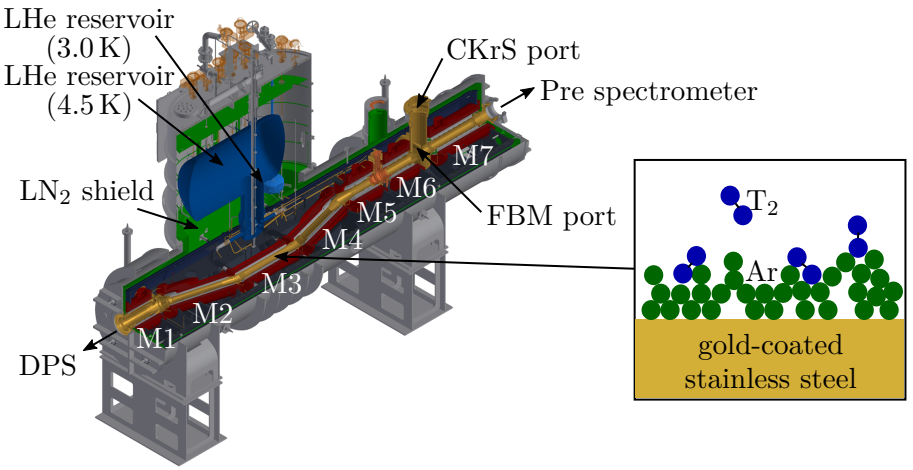

Figure 3.6.: The cryogenic pumping section. The cryogenic pumping section (CPS) contains seven superconducting magnets (red, M1 to M7) surrounding the beam tube elements (gold). The beam tube of the sections 2 to 5 is covered by an argon frost layer at 3 K which is renewed after every 60 days. The argon frost layer offers a large surface where tritium molecules freeze out (see sketch). The magnet cooling is guaranteed by a 1300 ℓ reservoir of liquid helium (LHe) at 4.5 K and the beam tube cooling by a small reservoir of 10.6 ℓ of LHe at 3.0 K (both in blue) [Jan15]. A 77 K shield of liquid nitrogen (green) protects the helium-cooled parts against heat radiation from the outer hull at room temperature. To increase the pumping efficiency, the elements 2 to 4 are assembled in a Ω-shaped chicane. In the pump port between the beam tube elements 6 and 7 the condensed Krypton source (CKrS) or the forward beam monitor (FBM) can be inserted.

tested during the KATRIN First Light campaign in 2016 and the first tritium campaign in 2018 [Hac17; Kle18b; Are18b].

3.2.4. The Cryogenic Pumping Section

The CPS, a 7 m-long cryostat, arrived at KIT in 2015. It forms the last pumping section before the spectrometers. The cryostat design is depicted in figure 3.6. The CPS has to reduce the partial pressure of tritium down below 10^{-16} mbar at the exit which represents a tritium flow reduction by a factor of 10^7 [Gil10]. Like the beam tube elements of DPS, the seven beam tube elements of CPS are also set up in an "Ω" shape with a tilting angle of 15° of the beam tube elements 2 and 4. The electrons are guided adiabatically through the chicane due to the magnetic fields created by seven superconducting magnets designed for magnetic field strengths up to 5.6 T [Are18c]. The neutral tritium gas molecules do not follow the magnetic field lines and hit the walls of the CPS. The walls of the sections 2-5 are cooled down to 3 K and covered with an argon frost layer, so that the tritium molecules are cold-trapped [Gil10; Jan15]. This principle has been tested successfully in a pre-measurement [Eic08] and indicated together with simulations [Jan15] a reduction factor smaller than 10^{10}. This is much better than the design value. Every 60 days, when approximately 1 Ci of tritium is accumulated in the argon frost layer in nominal KATRIN operation, the argon frost layer has to be renewed. Then, the beam tube temperature is increased and the argon together with the tritium is pumped off, before a new layer of argon is prepared. Details of this process can be found in [Jan15; Röt19].

The CPS houses also two calibration and monitoring devices which can be introduced into the beam tube between the beam tube elements 6 and 7. These are a condensed ^{83m}Kr source (CKrS) and a forward beam monitor (FBM). The CKrS can be introduced vertically to the CPS beamline. A sub mono-layer of ^{83m}Kr is condensed on a highly oriented pyrolytic graphite (HOPG) substrate with a diameter of 2 cm which can be moved

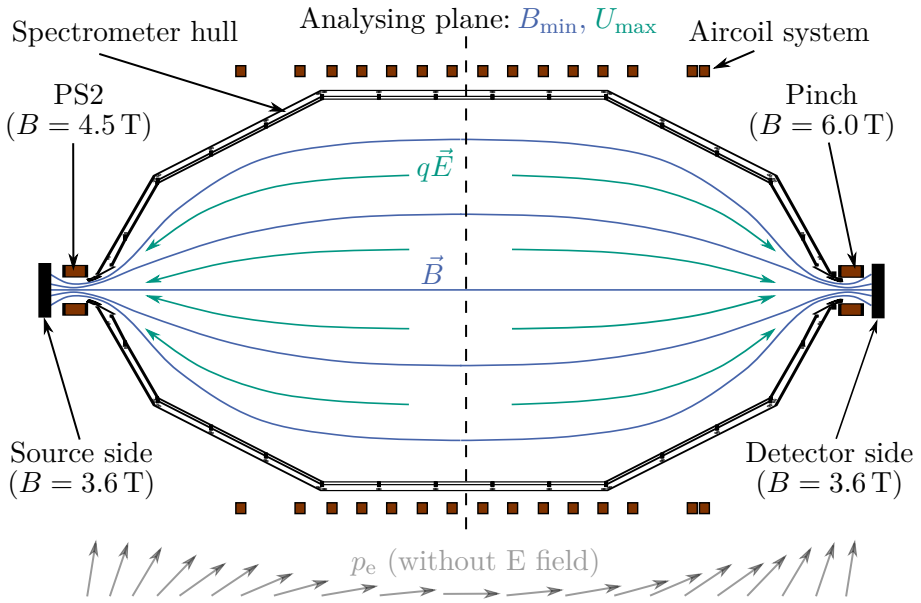

Figure 3.7.: The principle of KATRIN's main MAC-E filter. Electrons are created in the source and guided towards the spectrometer. After passing the PS2 magnet of the pre spectrometer, they enter the main spectrometer and experience a drop of the magnetic field strength down to $3 \times 10^{-4}\,\mathrm{T}$ in the analysing plane. This drastic drop of the magnetic field strength converts transverse into longitudinal momentum as depicted below the spectrometer vessel in the figure. At the same time, an electric potential of around $-18.6\,\mathrm{kV}$ applied to the vessel and an inner electrode system creates an electric field $\vec{E}$ decelerating the electrons and analysing their energy in an integral way. Electrons with energies smaller than qU are reflected. The electrons passing the analysing plane are accelerated again, go through the pinch magnet and reach the detector. The acceptance angle of the electron momentum to the magnetic field lines is determined by the ratio of source to pinch magnetic fields, while the energy resolution is determined by the minimum magnetic field in the analysing plane and the pinch magnetic field. For details see the main text. According to [Ang05].

in x and y direction inside the beam tube. This enables the pixel-wise scanning of the transmission properties of the spectrometers with the quasi-monoenergetic conversion electron lines from ^{83m}Kr (see table 5.2). The technical details of the CKrS are described in [Bau13a] and first promising commissioning results are presented in [Are18b].

The FBM is an additional monitoring tool for the stability of the column density (see section 3.2.1 and [Bab12]). Its detector board can be moved into the magnetic flux tube horizontally to scan the flux tube in x and y direction with a positioning precision of 0.1 mm [Ell17; Sch08]. Two *p-i-n* diodes, one hall sensor and a temperature gauge are mounted on the detector board. During standard KATRIN operation, the detector board is positioned to the outer region of the magnetic flux tube without shadowing the detector, so that the two *p-i-n* diodes determine the source activity to a precision of 0.1 % within one minute [Ell17]. In scanning mode, normal neutrino mass measurements are not possible, since the FBM is then moved through the beam tube to measure the radial and azimuthal dependence of the magnetic field and the source activity. For commissioning measurements, another detector board with a Faraday cup on it can be installed as a further possibility to investigate the flux of ions towards the spectrometers [Kle18b].

3.2.5. The Pre- and Main Spectrometer

Both the pre- and main spectrometer of KATRIN are operated as MAC-E (magnetic adiabatic collimation with electrostatic filtering) filters in a tandem configuration [Ang05]. The MAC-E filter principle is depicted in figure 3.7 with the main spectrometer of KATRIN as an example. The first MAC-E filter was built in 1980 [Bea80], and due to the high energy resolution of this measurement principle, also the previous direct neutrino mass measurements applied MAC-E filters [Kra05; Ase11]. A MAC-E filter needs a vacuum vessel accompanied by two strong magnets at the entrance and exit. Electrons coming from the source perform cyclotron motions around the magnetic field lines. Their kinetic energy is then shared between a longitudinal component $E_{\parallel}$ and a transverse component $E_{\perp}$ relative to the magnetic field lines, so that

$$E_{\mathrm{tot}} = E_{\parallel} + E_{\perp} \ . \tag{3.1}$$

The transverse energy of a cyclotron motion of an electron being guided adiabatically and being non-relativistic is expressed as [Zub11; Ang05]

$$E_{\perp} = -\vec{\mu}\vec{B} \tag{3.2}$$

with $\vec{\mu}$ being the magnetic moment and $\vec{B}$ being the magnetic field strength. As the magnetic field strength drops from the entrance with the strong magnet to the middle of the spectrometer by several orders of magnitude, transverse energy is converted into longitudinal energy accordingly. Since the magnetic moment [Zub11]

$$\vec{\mu} = \frac{e}{2m_{\mathrm{e}}}\vec{L} \tag{3.3}$$

with e being the electric charge and m_{e} the mass of the electron is proportional to the angular momentum $\vec{L}$, it is conserved, because $\vec{L}$ is also conserved. Therefore, in an ideal case where the magnetic field strength in the middle of the spectrometer drops to zero, the full transverse energy is translated into longitudinal energy. This point is located on the so-called analysing plane of the MAC-E filter. If a negative retarding voltage is applied to the electrodes of the vacuum vessel, the energy of the adiabatically guided electrons can be analysed with high precision. As the magnetic field strength in the middle of the spectrometer B_{A} is in reality not zero, but very small, also the transverse energy is not zero. Thus, the relative energy resolution of a MAC-E filter is, applying the conversation of the magnetic moment in equation 3.2,

$$\frac{\Delta E}{E} = \frac{B_{\mathrm{A}}}{B_{\mathrm{max}}} \ . \tag{3.4}$$

For KATRIN's main spectrometer, the energy resolution is 0.93 eV at 18.6 keV for the design magnetic field values of $B_{\mathrm{A}} = 3 \times 10^{-4}\,\mathrm{T}$ and $B_{\mathrm{max}} = 6\,\mathrm{T}$.

If the electron source is placed in a magnetic field of the same strength than the one created by the strong magnets at both ends of the MAC-E filter, electrons with an angle between their momentum and the direction of the magnetic field lines of up to 90° are accepted. If the source is in a lower magnetic field, electrons with large angle are reflected due to the magnetic bottle effect [Ang05]. As mentioned in section 3.2.1, the source magnetic field B_{S} of KATRIN is designed to be 3.6 T, but the two superconducting magnets at the entrance and exit of the pre spectrometer have a design value of 4.5 T and the pinch magnet at the exit of the main spectrometer even of 6.0 T which is the maximum magnetic field B_{max} in the KATRIN beam line [Are18c]. This reduces the maximum KATRIN acceptance angle θ_{max} to [Ang05]

$$\sin\theta_{\mathrm{max}} = \sqrt{\frac{B_{\mathrm{S}}}{B_{\mathrm{max}}}} \quad \Rightarrow \quad \theta_{\mathrm{max}} = 51^{\circ} \ . \tag{3.5}$$

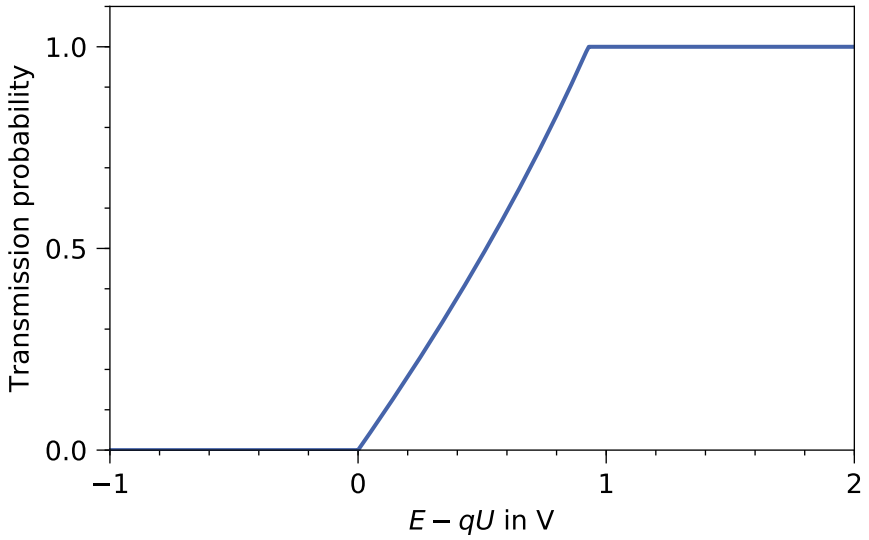

Figure 3.8.: Main spectrometer transmission function. The plot shows the transmission function of KATRIN's main spectrometer. The width of the step function is 0.93 eV, the energy resolution of the MAC-E filter. It is obvious that the main spectrometer acts as a high-pass filter. Only electrons with energies E larger than the applied retarding voltage qU are able to reach the detector. The transmission function data was generated with SSC (see section 3.3).

The reason to cut electrons with large angles is that they have a longer way through the source and they have therefore also a higher probability to scatter with residual gas. In such processes, they lose energy (see section 4.2.16). Also the amount of energy losses due to synchrotron radiation is higher for such electrons (see section 4.2.3). Based on the previous considerations, the analytical transmission function of the MAC-E filter for non-relativistic electrons is [Ang05]

$$T(E,qU) = \begin{cases} 0 & E - qU < 0 \\ \dfrac{1-\sqrt{1-\frac{E-qU}{E}\frac{B_\mathrm{S}}{B_\mathrm{A}}}}{1-\sqrt{1-\frac{\Delta E}{E}\frac{B_\mathrm{S}}{B_\mathrm{A}}}} & 0 \leq E - qU \leq \Delta E \\ 1 & E - qU > \Delta E \ . \end{cases} \tag{3.6}$$

E is the electron energy, q the electron charge, U the retarding potential and ΔE the energy resolution (see equation 3.4). A detailed derivation and discussion of the transmission function can be found in [Beh17a]. The transmission function is depicted in figure 3.8.

The size of the KATRIN spectrometer is determined by the measurement principle of the MAC-E filter: the diameter has to be large enough that the full magnetic flux tube coming from the source fits into it and no electrons are lost due to wall collisions, and the length has to be large enough that an adiabatic transport of the electrons is guaranteed. Thus, the pre spectrometer has a length of 3.4 m and a diameter of 1.7 m [Pra12], while the main spectrometer has a 10 m diameter and is 23 m long [Val09].

As one can see from the figures 3.1 and 3.7, the main spectrometer is surrounded by a large cage of air coils, which contains two separate systems for the fine-tuning of the magnetic field in the analysing plane [Glü13; Erh18]: The earth magnetic field compensation system (EMCS) consists of 26 current loops which create horizontally and vertically orientated planes parallel to the spectrometer axis. It follows the so-called $\cos\theta$ approach,

in which the current on the surface of a cylinder follows a $\cos\theta$ distribution to create a quasi-homogeneous field inside the volume, with θ being the azimuthal angle. With this system, the components of the earth magnetic field perpendicular to the main spectrometer axis are compensated with a precision of 3 µT. The low field correction system (LFCS) enables the generation of a well-defined magnetic field of low strength, which is typical by 3×10^{-4} T in standard KATRIN operation including the stray fields of the superconducting coils. The LFCS consists of 14 air coils with a diameter of 12.3 m each. Both the EMCS and the LFCS are supplied with individual currents up to 175 A. Since the magnetic field in the analysing plane has a large influence on the transmission characteristics and hence the neutrino mass measurements according to equation 3.6, a careful monitoring of the field is mandatory. This is done with two mobile units which move around the main spectrometer on the inner side of two air coil holding structures. Additionally, there are 38 stationary units distributed over the outer surface of the vacuum vessel [Osi12; Rei13; Erh16]. In order to account for stray fields from the steel of the building walls, two mobile units are mounted which can perform a fine-meshed magnetic field measurement in a plane parallel to the walls [Let18].

The high voltage system of the spectrometers is complex and has to fulfil strict requirements for the neutrino mass measurements: the high voltage has to be known and stabilised to the ppm level, which translates for Gaussian fluctuations into a limit of $\sigma < 60$ mV for standard KATRIN operation [Ang05]. Since the main spectrometer is a huge antenna for electromagnetic stray fields of any source, an active post-regulation system has been developed to achieve the stability [Kra16]. There are two options to monitor the absolute high voltage scale. One is the monitor spectrometer, a third MAC-E filter being not part of the KATRIN main beam line, but coupled to the high voltage of the main spectrometer and described in further detail in the next section 3.2.6. The other is a high-precision voltage divider developed at the University of Münster [Thü07; Thü09; Bau13b; Are18a; Res19].

The tandem spectrometers are operable up to −35 kV for ^{83m}Kr measurements, but at standard KATRIN operation voltages around −18.6 kV are typical (see section 3.4.1) [Kra16]. The pre spectrometer is always operated at a few hundred volts more positive than the main spectrometer to reduce the number of electrons in the main spectrometer and to keep the KATRIN requirements on the background rate [Pra12; Ang05]. For background reduction, the inner surfaces of the two spectrometers are further covered with an inner wire electrode system [Val09; Pra11; Zac15]. These wire electrodes are a few hundred of volts more negative than the vessel to reflect electrons coming from the walls, e. g. due to cosmic ray interactions, back to the surface [Lei14]. The tandem setup of the spectrometers and the electromagnetic design can lead to Penning traps filling up with stored electrons which again increase the background due to secondary processes [Val09]. Various countermeasures have been investigated and developed in the past years (see e. g. [Val09; Frä10; Frä14; Wie16; Hil17]), but an important pre-condition is the continuous maintenance of an ultra-high vacuum [Gör14; Are16]. The spectrometers are designed to reach vacuum conditions with pressures on the order of $10^{-11} - 10^{-12}$ mbar with a combination of turbo molecular and getter pumps. For these pressure ranges, also a bake-out of the spectrometers is mandatory. This is done with an integrated oil heating baking out the spectrometers at up to 350 °C. Three ring electrodes to block ions (see section 3.2.3) are mounted in the spectrometer section, one between CPS and pre spectrometer, one between the spectrometers and one between main spectrometer and detector.

The two spectrometers were the first KATRIN components on site with the pre spectrometer being delivered in 2003 and the main spectrometer being delivered in 2006. After assembling the inner electrode system [Hil11], several test measurements were performed

with the pre spectrometer [Frä10; Frä11; Mer12; Pra12; Wan13; Frä14] and the main spectrometer [Gör14; Lei14; Sch14; Gro15; Har15; Erh16; Kra16; Beh17a; Beh17b; Frä17; Hil17; Tro18] to investigate the background (see also section 4.2.18) and transmission properties (see also section 4.2.6).

3.2.6. The Monitor Spectrometer

Like the pre- and the main spectrometer, the monitor spectrometer works with the MAC-E filter principle. It has the task to monitor the voltage of the main spectrometer on the ppm level [Erh14]. The spectrometer used in the Mainz neutrino mass experiment is now integrated in KATRIN as the monitor spectrometer. With a length of about 4 m and a diameter of 1 m and equipped with four air coils and two superconducting magnets with field strengths of 6 T [Erh14] it is part of a second beam line in a separate building right next to the KATRIN spectrometer hall. The other parts of this separate beam line are an implanted ^{83}Rb/^{83m}Kr source [Are17; Sle15] and a 1.5 cm^2 *p-i-n* silicon detector accompanied by four small *p-i-n* diodes [Erh14]. ^{83m}Kr emits conversion electrons with well-defined energy (see table 5.2). The K-32 line is of special interest for KATRIN since its energy of 17.83 keV is close to the energy of the tritium endpoint of 18.6 keV. The gap can be closed by a bias voltage of up to −770 V which can directly be applied to the implanted sources [Erh14]. In KATRIN operation, the monitor spectrometer follows the voltage of the main spectrometer but scans the position of the K-32 line of ^{83m}Kr instead of the tritium endpoint. In several pre-measurements the conversion lines of the implanted ^{83}Rb/^{83m}Kr have been investigated, the sources have been characterised and the required stability on the ppm level has been demonstrated [Zbo11; Sle13; Zbo13; Erh14; Sle15; Are17].

3.2.7. The Detector

A drawing of the detector section is depicted in figure 3.9. The KATRIN focal plane detector is operated in a magnetic field of 3.6 T [Are18c]. It is a *p-i-n* silicon detector whose active area has a diameter of 90 mm [Ams15]. The active area is divided into 148 pixels of the same size, which are arranged in 12 rings of 12 pixels each and a bullseye of 4 pixels. The energy resolution of the detector is (1.52 ± 0.01) keV and the detection efficiency is $(95 \pm 1.8 \pm 2.2)$ % [Ams15]. The detector can handle up to 100 kcps, but then pile-up effects have to be considered. Such high rates are only relevant in calibration runs, in normal tritium operation the count rate will be around 1 cps [Ams15]. The detector can be calibrated with an ^{241}Am or a photoelectron source [Sch14; Ams15]. With the Precision Ultra-Low Current Integrating Normalization Electrometer for Low-Level Analysis (PULCINELLA), the photoelectron current can be measured and the detector efficiency can be determined. PULCINELLA also shields the detector from the spectrometer section, if necessary. Since the requirements on the background are very strict with 10 mcps for the total background rate [Ang05] (see also section 4.2.18), a post-acceleration electrode with 10 keV shifts the energies of the electrons coming from the main spectrometer to a region with less detector background. Further background reduction methods are the shielding of sensitive parts against cosmic rays, active vetoing and applying several selection criteria at the analysis level like the rejection of correlated events [Sch14]. Detector events can be observed in real-time due to the fast read-out and an appropriate software (see section 3.3) [Ams15]. The detector has been installed with the start of the spectrometer commissioning measurements in 2013 (see section 3.2.5). Since then, the detector has been characterised and commissioned and is now ready for standard operation [Ren11; Wal13; Sch14; Ams15; Mar17b].

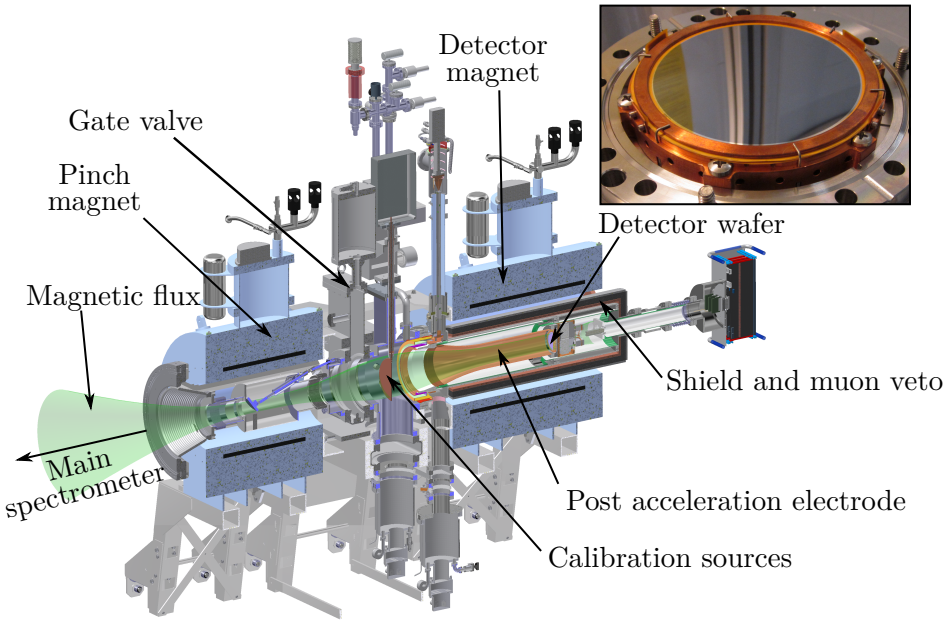

Figure 3.9.: The focal plane detector system. The sketch shows the focal plane detector system of KATRIN. The detector wafer itself is placed in a strong magnetic field of 3.6 T. The electrons coming from the main spectrometer are first bundled by the pinch magnet (6 T) and then accelerated by 10 kV by the post-acceleration electrode. The gate valve enables the separation of the detector chamber from the main spectrometer. Several calibration sources can be inserted (see main text), e. g. the PULCINELLA disk. Figure based on [Ams15].

3.3. Software for Data Acquisition, Analysis and Simulation

The KATRIN experiment comprises more than 15,000 slow control channels[1] of different kinds, e. g. temperature, pressure and magnetic field sensors, but also valves and electrical heaters. Not all of them are used for physics analysis, but they are also necessary to ensure and monitor the safe operation of the machine. No commercial software is available which can be used at the same time for simulation, data acquisition, analysis and book-keeping of thousands of sensors, and which can be extended easily if new processes or sensors have to be added. Thus, it was decided to develop most of the required software solutions in-house or make use of available open source software from other experiments, whenever possible. The KATRIN standard software is listed in table 3.1 together with a short description of its application. A more comprehensive overview is given in the following, for details the reader is referred to the literature ([Kle14] and the citations in the following descriptions).

ORCA The object-oriented real-time control and acquisition (ORCA) software[2] was originally developed for the SNO experiment [How04]. ORCA provides a graphical interface on MAC OS operating systems. At KATRIN, it is used for the run control and data acquisition of the focal plane detector and the monitor spectrometer detector. Also the parameters of the pre- and main spectrometer like the air coil currents and the high voltage can be set with ORCA. Via drag and drop it is possible to initialise the hardware, to start and perform a measurement e. g. with a dedicated runlist, to observe the detector events in real-time, to acquire the data and to distribute it to connected data-bases. The ORCA data output can be analysed with C++-based programs.

[1] Personal communication F. Heizmann, Mar 05, 2018.

[2] Documentation and download available at `http://orca.physics.unc.edu/~markhowe/Orca_Help/Home.html` (accessed on Dec 22, 2018).

Table 3.1.: Overview of the KATRIN standard software. The table gives an overview of the existing KATRIN software for data acquisition, analysis, simulation and book-keeping of the sensors and its application. For more explanations, the reader is referred to the main text.

Software	Application
ORCA	Focal plane detector and monitor spectrometer detector data acquisition
Siemens SIMATIC PCS 7	Monitoring and controlling of slow control channels for safe and automated KATRIN operation
ADEI	Slow control database and web-based time series plotter
KATRIN database	sensor mapping and calibration database
KASPER	Simulation and neutrino mass analysis framework based on C++ with several subpackages.

Siemens SIMATIC PCS 7 The Siemens SIMATIC PCS 7 software[3] (in the following only "PCS 7"), was developed for the operation and control of large industrial facilities like e. g. production facilities or power plants. With its implemented alarm management system, it is possible to allocate individual alarm levels to each sensor. Since the KATRIN PCS 7 comprises most of the slow control channels, it guarantees therefore the automated but safe operation of the apparatus and some of its subsystems. The software offers the possibility to observe time series of the implemented sensors in real-time and to adjust electrical heaters and engines or to open valves etc. With a strict user management it is guaranteed that some of the options are only possible for experienced and trained operators. The sensor data displayed in PCS 7 is stored in the database ADEI.

ADEI The Advanced Data Extraction Infrastructure[4] (ADEI) is a web-based tool to handle large amounts of time series data from numerous slow-control sensors. The data can be observed via the web-based application in real-time, but it is also possible to plot data from user-defined time ranges or to extract data in different formats for further processing. Caching techniques enable a quick data access within 500 ms. ADEI can extract further information from relational databases like the KATRIN database, which is of special interest for KATRIN if sensors have to be calibrated regularly and ADEI has to apply different calibration factors for different time ranges. At the front end, ADEI is compatible to LabView, which allows the implementation of ADEI time series into LabView programmes for the controlling of certain sensors. Further details can be found in [Chi10].

KATRIN database The KATRIN database is another database besides the ORCA run file storage and the ADEI slow-control database [Kle14]. In contrast to the other databases, the input is generated by the administrators manually. The KATRIN database works with SQL and contains several tables. In these tables, sensor-related data is stored, e. g. the KATRIN number, which is based on a KATRIN-internal numbering scheme to identify every single sensor, or calibration information to enable the analysis of old data with a newly generated and improved calibration and to

[3] For details see `http://w3.siemens.com/mcms/process-control-systems/en/distributed-control-system-simatic-pcs-7/Pages/distributed-control-system-simatic-pcs-7.aspx` (accessed on Dec 22, 2018).

[4] Documentation and download available at `http://adei.info/adei/` (accessed on Dec 22, 2018).

make the reproduction of previous analyses with former calibration factors possible. KATRIN numbers are further mapped to an ADEI path with the KATRIN database. If the analysis software KASPER calls for the data of a certain KATRIN number, this link is done by the KATRIN database.

KASPER KASPER is a C++-based framework for simulation and neutrino mass analysis tools developed by the KATRIN collaboration [Kle14; Beh17a]. It comprises several packages which can be installed individually depending on the user's preferences. The implementation of ROOT code is possible in KASPER, so that e. g. the graphical output of simulation results is enabled. One of the central design criteria is to keep the packages as flexible as feasible. Users can set the simulation and analysis parameters in .xml files. This allows studies on different levels of complexity with the same code depending on the required precision. In the following, the most important packages are shortly introduced.

Kommon The Kommon package includes physical constants, a random number generator, input and output tools and some basic mathematical functionalities. The other packages are linked to Kommon to make use of its elements [Kle14].

KGeoBag KGeoBag contains the geometries of KATRIN. For electromagnetic field calculations, the precise geometries and positions of magnets and electrodes are essential. Since several of the other simulation and analysis packages need these geometries, they were put into an own package for easier handling [Fur15; Gro15]. Recently, alignment measurements with the entire KATRIN beam line were performed in the KATRIN first light campaign [Hac17] and the geometries of all KATRIN main components are now available in KGeoBag [Def17].

KEMField KEMField calculates electromagnetic fields on the basis of geometries given by KGeoBag. Different field solving algorithms are available; details can be found in [Cor14; Bar16b]. The field calculations are very time-consuming, so that the parallelisation of the code execution on graphic processor units (GPU) was one of the design goals of KEMField. Recently, the precision of the KEMField calculations was improved to the 10^{-15} level [Hil17].

Kassiopeia Kassiopeia is a particle-tracking software package for charged particles in electromagnetic fields [Mer12; Käf12; Gro15; Fur15; Fur17; Tro18]. It accesses the geometries by KGeoBag and the field calculations by KEMField. The user can set the point of particle generation and termination in the given geometry. Energy losses like synchrotron radiation and scattering processes can be taken into account. By virtue of its modular architecture, Kassiopeia can also be used for other experiments (together with KEMField and KGeoBag) and is therefore available in the web[5]. Experimental results of KATRIN can be simulated in Kassiopeia to learn more about the apparatus, so that Kassiopeia is one of the most important and powerful software tools of KATRIN. Therefore, it was used extensively during the KATRIN commissioning measurements, e. g. for alignment studies [Hac17], for the determination of the transmission properties of the main spectrometer [Gro15; Erh16; Beh17a] and for background investigations [Har15].

KTrAP All transmission-related parts of the other KASPER packages are bundled in KTrAP [Gro15]. Based on the determination of analysing points of the main spectrometer MAC-E filter and flux tube simulations, KTrAP can be used to optimise the currents of the air coil system to achieve the best transmission properties for a given magnetic field in the analysing plane. For this minimisation problem KTrAP offers several minimisers for the user to choose from.

[5] see `http://katrin-experiment.github.io/Kassiopeia/index.html` (accessed on Dec 22, 2018)

SSC SSC enables the differential and integral spectrum calculation of the tritium beta decay [Höt12; Käf12; Kle14; Kle18a]. The spectrum is calculated analytically based on Fermi's theory, but takes several theoretical and experimental modifications into account like e. g. the gas dynamics inside the WGTS [Kuc16; Hei18], the final-state distribution of rotational and vibrational states of the molecule after the decay [Bod15] and further systematic effects, which will be discussed in section 4.2. Together with KaFit, SSC can be used to study the influence of systematic effects on KATRIN's neutrino mass sensitivity (see section 4.1.3), and later it will be used to determine the neutrino mass from the measured data. The generated spectrum can also serve as input for Kassiopeia simulations.

KaFit KaFit translates the beta spectrum calculated by SSC into expected count rates at the detector [Kle14]. It provides several statistics tools to evaluate the quality of observed data in comparison to the expected data from SSC, like e. g. chi-squared distribution analysis and Markov Chain Monte Carlo methods. With KaFit, the neutrino mass will be extracted from the measured spectrum. KaFit can be used to optimise the measurement time distribution on a given analysis interval in the endpoint region of the tritium beta decay and is therefore also very important for the planning of KATRIN measurements. To estimate the influence of a single systematic uncertainty on the neutrino mass sensitivity, KaFit can be used for so-called ensemble tests. Here, a large number of KATRIN experiments is simulated with the systematic uncertainty being "switched on" and the resulting neutrino mass distribution is compared to the case with the systematic uncertainty being "switched off". More on ensemble tests can be found in section 4.1.3.

KaLi KaLi is the interface between the simulation and analysis software and the data stored on the KDBServer [Kle14]. The user can ask for run-based data from the focal plane or monitor spectrometer detector but also for time series data from slow-control channels by including the required comments in the .xml files of the KASPER packages. The data downloaded by KaLi can be further processed and analysed by suitable software like ROOT or BEANS.

BEANS BEANS is an analysing software package written by S. Enomoto with a special emphasis on KATRIN-specific analysis [Kle14; Beh17a]. The design goal is to reduce the amount of code for common and regular KATRIN analysis tasks in order to make such tasks easier for beginners. BEANS downloads the data from KDBServer with KaLi and, subsequently, different methods can be applied, e. g. a detector calibration or different cuts (energy cuts, pixel cuts, ...). BEANS can also be used to create graphical outputs, e. g. pixel maps of the detector count rates, rate trend graphs over several runs, slow control time series graphs and much more. After applying the cuts, the data can be saved in a root file for further processing with ROOT or Python, if desired by the user. BEANS also offers the possibility for the user to extend the package with his/her own methods.

3.4. KATRIN's Sensitivity on the Neutrino Mass and Physics Beyond the Standard Model

In this section, KATRIN's sensitivity on the electron antineutrino mass and some phenomena beyond the Standard Model is discussed. In the first subsection 3.4.1 it is described, how KATRIN actually measures the neutrino mass. On this basis, in subsection 3.4.2, the KATRIN sensitivity on the electron antineutrino mass is derived. In subsection 3.4.3, the sensitivity of KATRIN on sterile neutrinos and right-handed currents is briefly discussed, both phenomena of physics beyond the Standard Model.

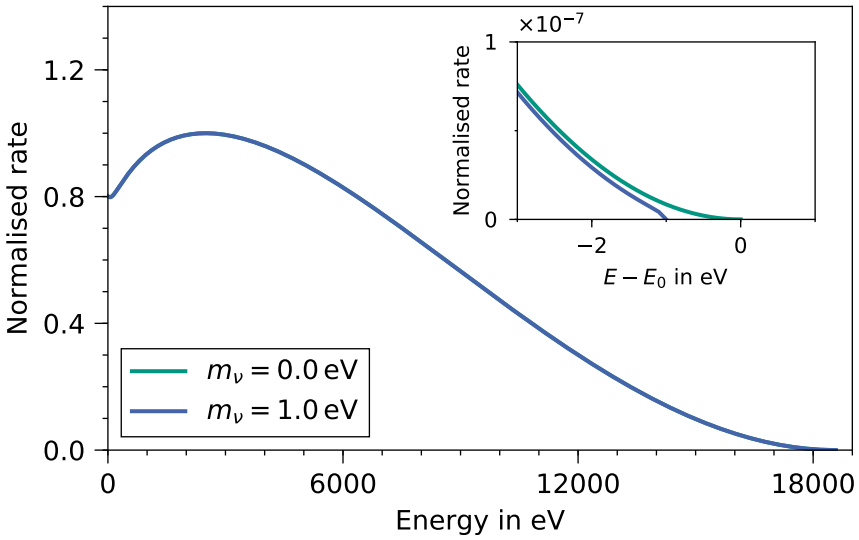

Figure 3.10.: Tritium beta-decay spectrum with and without neutrino mass. The plot shows the beta decay spectra of tritium without molecular corrections for a neutrino mass of $0\,\mathrm{eV}/c^2$(green) and $1\,\mathrm{eV}/c^2$ (blue). The inset zooms to the endpoint of the zero-mass spectrum E_0, where the effect of the neutrino mass is clearly visible as shift and shape distortion of the spectrum. The spectra are generated with SSC (see section 3.3).

3.4.1. A KATRIN Neutrino Mass Measurement Run

As one can see from figure 3.10, a non-vanishing neutrino mass will manifest in a shifted endpoint of the tritium beta-decay spectrum. This endpoint energy E_0 can be precisely calculated for a vanishing neutrino mass from the atomic Q value, molecular corrections E_D and the recoil energy E_rec of the daughter molecule, if a transition from the ground state to the ground state is assumed [Ott08; Bod15]:

$$E_0 = Q - E_\mathrm{D} - E_\mathrm{rec} \ . \tag{3.7}$$

The atomic Q value is the mass difference between the neutral mother and the neutral daughter atom in a radioactive decay. For ^{3}T and ^{3}He this mass difference was determined in Penning trap measurements to $Q = 18592.01(7)\,\mathrm{eV}/c^2$ [Mye15]. The maximum recoil of the daughter molecule is 1.7 eV and the corrections due to the binding energies in the mother and daughter molecules sum up to 16.3 eV [Bod15]. Therefore, the kinematic endpoint of the molecular tritium beta-decay spectrum for a vanishing neutrino mass is

$$E_0 = 18574\,\mathrm{eV} \ . \tag{3.8}$$

However, the endpoint of the spectrum alone is not a good measure of the neutrino mass, since KATRIN will not measure the physical, but rather a KATRIN-specific endpoint. Several effects, e. g. the work functions of the source and the main spectrometer, influence the KATRIN endpoint and will shift it to values other than the literature value stated above. In figure 3.11 it is visualised that a non-vanishing neutrino mass does not only influence the kinematic endpoint of the beta-decay spectrum, but also the shape of the spectrum in the endpoint region. The largest effect can be observed, when the signal of the spectrum is twice the background rate [Ott08], which is expected to occur at 4 eV below the endpoint for KATRIN's design parameters and a neutrino mass of $0.35\,\mathrm{eV}/c^2$ [Ang05] (see figure 3.11).

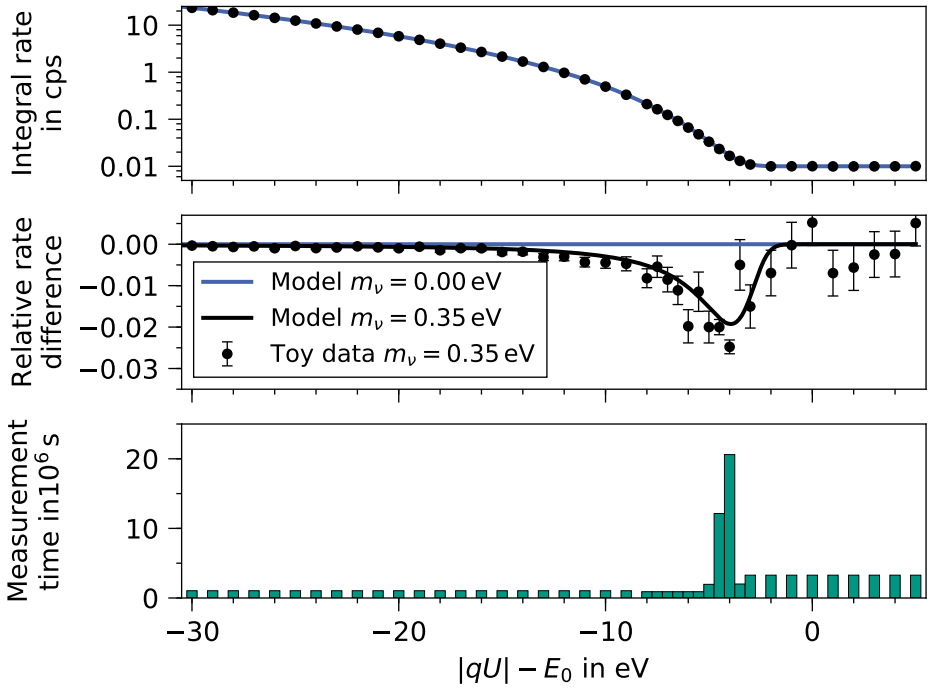

Figure 3.11.: Simulated KATRIN measurement of the neutrino mass. The plot at the top of the figure shows simulated toy data of an integral spectrum for $m_\nu = 0.35\,\mathrm{eV}/c^2$ generated with KaFit and SSC for KATRIN design conditions. The x axis is the retarding energy qU relative to the kinematic endpoint of the tritium beta spectrum E_0. The data are fitted with the corresponding model and the four fit parameters amplitude A_Sig, endpoint E_0, neutrino mass square m_ν^2 and background R_bg, again with KaFit/SSC. The plot in the middle shows the relative difference of the integrated spectrum (toy data and model) with $m_\nu = 0.35\,\mathrm{eV}/c^2$ to the integrated spectrum of $m_\nu = 0$. The largest deviation of $\approx 2\,\%$ is visible at about 4 eV below the endpoint. The plot at the bottom shows the design measurement time distribution of KATRIN, in which most of the measurement time is spent at the most sensitive point of the spectrum.

Based on this considerations, some principles of the KATRIN measurements can be discussed:

- Since the neutrino mass is imprinted on the shape of the beta spectrum, not only the endpoint E_0 but an interval around the endpoint has to be scanned with the main spectrometer. This interval was determined to be $[E_0 - 30\,\mathrm{eV}, E_0 + 5\,\mathrm{eV}]$ as a balance between increasing statistics and increasing systematic uncertainties if going deeper into the spectrum [Ang05]. The part above the endpoint is necessary to determine the background rate.
- Besides the squared neutrino mass m_ν^2 also the endpoint E_0 has to be a free fit parameter since it is not known a priori to the accuracy needed for being used as an external constraint. Further free fit parameters are the amplitude of the spectrum A_sig and the background rate R_bg (see figure 3.11).
- Every distortion in the shape of the beta spectrum which is not caused by the neutrino mass is a systematic effect and has to be taken into account in the fit function carefully. Furthermore, this sets strict stability requirements on many of the operational parameters of KATRIN, see section 4.2.

These principles are translated into a measurement procedure in practice: During one KATRIN run, the retarding voltage of the main spectrometer is varied in steps of e. g. 1 V

within the measurement interval. By design, the operational parameters are stable within the requirements on the order of 1 h, which defines the time length of one run [Ang05]. This time is distributed over the subruns, which is the data acquisition at one retarding voltage, in a sophisticated way to gain the maximum sensitivity on the four fit parameters [Kle14] (see figure 3.11). This can be done in two ways: either the measurement time for certain subruns which are especially sensitive to one of the fit parameters is increased or the step width in such regions of the spectrum is decreased while the measurement time is flatly distributed. Between two runs, a few minutes measurement time will be used for calibration measurements of the source column density with the rear section egun (see section 4.2.15), but besides these small interruptions the data taking will be performed 24/7 for 60 days. After 60 days, the argon frost layer of the CPS has to be exchanged (see section 3.2.4) and a longer break of several weeks is necessary. In total, this procedure will be repeated for 5 years, ending with a net measurement time of 3 years [Ang05].

The neutrino mass is determined in a fit to the measured data. The fit is done with the SSC and KaFit packages of KASPER in a maximum likelihood analysis (see section 3.3 and 4.1). The systematic uncertainties and slow control values have to be included in the fit function. Since the operational parameters will not be stable over the 3 years of net measurement time, each run will be fitted and later everything will be combined in a global analysis. The fit per run can also be performed in different ways: One can apply a fit to the total detector rate or one can do a ring-wise or even pixel-wise fit, depending on the homogeneity of the count rate and systematic effects over the detector area.

3.4.2. KATRIN's Sensitivity on the Electron Antineutrino Mass

KATRIN is designed to reach a sensitivity of $0.2\,\mathrm{eV}/c^2$ (90 % C. L.) which corresponds to a 5σ discovery potential of $0.35\,\mathrm{eV}/c^2$ [Ang05]. These numbers base on the following assumptions: The statistical uncertainty of KATRIN after three years of measuring time is calculated for a total background rate of $R_{\mathrm{bg}} = 10\,\mathrm{mcps}$ and a measurement interval of $[E_0 - 30\,\mathrm{eV}, E_0 + 5\,\mathrm{eV}]$ to

$$\sigma_{\mathrm{stat}} = 0.018\,\mathrm{eV}^2/c^4 \ . \tag{3.9}$$

Five major systematic uncertainties are assumed, each of them contributing at most $0.0075\,\mathrm{eV}^2/c^4$ to the total systematic uncertainty budget. They are added quadratically as independent systematic effects without correlations to

$$\sigma_{\mathrm{sys}} = 0.017\,\mathrm{eV}^2/c^4 \ , \tag{3.10}$$

balancing the statistical uncertainty. This leads to the total KATRIN uncertainty σ_{tot}

$$\sigma_{\mathrm{tot}} = \sqrt{\sigma_{\mathrm{stat}}^2 + \sigma_{\mathrm{sys}}^2} = 0.025\,\mathrm{eV}^2/c^4 \ . \tag{3.11}$$

The sensitivity can now be calculated via

$$L(90\,\%\ C.\,L.) = \sqrt{1.64 \cdot \sigma_{\mathrm{tot}}} \approx 200\,\mathrm{meV} \ , \tag{3.12}$$

$$L(5\sigma) = \sqrt{5 \cdot \sigma_{\mathrm{tot}}} \approx 350\,\mathrm{meV} \ . \tag{3.13}$$

Some estimations made in the KATRIN Design Report changed in the meanwhile due to the commissioning of the main spectrometer and ongoing research:

- It turned out that the background of the main spectrometer is 50 times higher than anticipated [Frä17]. An increased background can be counterbalanced to a certain extent by modifying the measurement time distribution in the measurement

interval [Kle14] (see also figure 3.11). Therefore, the sensitivity does decrease only slightly to 240 meV/c^2 (90 % C. L.) [Frä17] if countermeasures as the extension of the analysing interval and the increase of the magnetic field in the analysing plane are applied [Tro18]. A detailed discussion can be found in section 4.4.

- As the next chapter 4 shows, today several sources of systematic uncertainties are known in addition to the five major ones as assumed in the Design Report. These have to be evaluated in detail for a new careful estimation of the total uncertainty budget of KATRIN and the achievable sensitivity.

3.4.3. KATRIN's Sensitivity on Physics Beyond the Standard Model

Due to its highly luminous tritium source and the possibility of scanning wide ranges of the tritium beta decay spectrum, KATRIN also offers some opportunities to check the parameter space of rare processes beyond the standard model. The sensitivity of KATRIN to some of these beyond the standard model processes is discussed briefly in the following:

Sterile neutrinos on the eV scale: As mentioned already in section 2.2.2, there are some anomalies in neutrino oscillation experiments like e. g. the so-called reactor anomaly, which can be interpreted as a signature of a fourth neutrino generation. This neutrino generation is assumed to be sterile with a mass on the eV scale. According to equation 2.54, the tritium beta decay spectrum is a superposition of the spectra of the different mass eigenstates. Since KATRIN's energy resolution is not good enough, the three different mass eigenstates of the active neutrinos cannot be resolved. However, a sterile neutrino with a mass m_{ν_s} on the eV scale would manifest as a kink in the spectrum below the endpoint E_0 at $E_0 - m_{\nu_s}$ with ν_s being the sterile neutrino mass eigenstate [Zub11]. Since KATRIN measures the spectrum in the interval $[E_0 - 30\,\text{eV}, E_0 + 5\,\text{eV}]$, KATRIN tests this parameter range already in standard operation with a high sensitivity. Several publications show that KATRIN is able to reach mixing angles for an electron-to-sterile neutrino mixing on the order of $\sin^2 2\theta_s \approx 0.01$ [For11; Rii11; Esm12]. In a sensitivity calculation with the KASPER code (see section 3.3) and with the parameters from the reactor anomaly taken into account, KATRIN will be able to detect sterile neutrinos with a mass-square of $m^2_{\nu_s} = 0.753\,\text{eV}^2/c^4$ with 90 % C. L. for a mixing angle of $\sin^2 2\theta_s = 0.14$ [Kle14].

Sterile neutrinos on the keV scale: Sterile neutrinos with masses in the keV range are well-motivated candidates for Dark Matter [Adh17]. With a kinetic endpoint at 18.6 keV, the tritium beta spectrum offers, in principle, the possibility to search for sterile neutrinos with masses up to ≈ 18 keV. They would again be observable as kink in the spectrum below the endpoint at $E_0 - m_{\nu_s}$ [Alt18]. Two problems arise if one has to measure deeper in the spectrum to detect the kink: the rates, which have to be handled by the detector, are much larger and several of the systematic uncertainties become more prominent. The current KATRIN detector can only deal with about 100 kcps (see also section 3.2.7), so that a new design is necessary for a keV sterile neutrino search. This new detector system will be able to handle 10^9 cps in a differential measurement and is currently under development in the TRISTAN project [Alt18] to perform such a keV sterile run after the five years of standard KATRIN operation. Sensitivity studies taking into account also some systematic effects indicate that mixing angles on the order of $\sin^2\theta \approx 10^{-8}...10^{-6}$ can be probed with the upgraded KATRIN setup for masses of the sterile up to 18 keV [Mer15a; Mer15b].

Right-handed currents: Right-handed currents are part of the left-right symmetric model (LRSM), in which right-handed vector bosons with masses > 1 TeV are postulated (see e. g. [Moh75]). For neutrino physics this LRSM is of interest because it would

introduce a natural mass scale for sterile neutrinos in the seesaw range (see also section 2.3.2). The right-handed currents would influence the shape of the beta spectrum [Ste17]. The sensitivity of KATRIN on this shape distortion was studied in the presence of only active neutrinos [Bon11], in the presence of keV-scale sterile neutrinos [Bar14] and in the presence of eV-scale sterile neutrinos [Ste17]. In all three cases, KATRIN is not expected to set new limits, but will test some of the LHC bounds in a complementary method. Recently, also the sensitivity on light boson emission in the tritium beta decay has been investigated [Arc18].

3.5. Objectives of This Thesis

As outlined in the section before, several systematic effects were identified during the KATRIN setup and commissioning phase which were not accounted for in the KATRIN Design Report estimations. At the same time, some of the systematic uncertainties listed in the Design Report were measured in commissioning measurements or determined in simulations in the meanwhile. Thus, a new evaluation of the total systematics budget is necessary for an up-to-date KATRIN sensitivity calculation.

The thesis at hand contributes to this field of systematic uncertainties at the KATRIN experiment in two ways:

1. In chapter 4, the first complete list of all KATRIN systematic uncertainties is offered. In the time since the Design Report, many of new systematic uncertainties were discussed and treated in PhD theses and other student works. The thesis at hand summarises all systematic uncertainties to identify the most prominent ones, to identify open issues and to update the total systematic budget estimation in a coherent approach to determine individual systematics.

2. Many of the KATRIN systematic uncertainties are linked to the WGTS and processes inside the gas column density. Therefore, the basis for the success of KATRIN is the characterisation of the operation of the WGTS cryostat. In chapter 5, the results of the first test of the WGTS ^{83m}Kr mode are presented. This mode is necessary for the determination of the space charge in the source, one of KATRIN's systematic effects. It requires large changes in the operation of the WGTS to standard tritium mode. With the first tests, the general feasibility of the krypton mode is demonstrated and benchmarks for future ^{83m}Kr mode measurements are set. Chapter 6 bundles several test measurements of the WGTS to characterise its magnetic field and temperature stability performance. The uncertainties of the temperature measurement are precisely analysed which are important parameters for the determination of source-related systematics.

4. Systematic Uncertainties of KATRIN

The KATRIN Design Report in 2005 [Ang05] stated a systematic uncertainty budget of $\sigma_{\mathrm{sys}} = 0.017\,\mathrm{eV}^2/c^4$ (see also section 3.4.2). This value was obtained by assuming five independent major systematic uncertainty contributions of $\Delta m_\nu^2 = 7.5 \times 10^{-3}\,\mathrm{eV}^2/c^4$ each, added in quadrature. However, the Design Report also contains some detailed investigations of individual systematic effects, most of them known already from former neutrino mass experiments with tritium. The outcome of the investigations was, that there are actually more than five systematic uncertainties, but most of them are smaller than $\Delta m_\nu^2 = 7.5 \times 10^{-3}\,\mathrm{eV}^2/c^4$ if certain requirements on the experimental stability and accuracy are fulfilled.

In the years since the Design Report, it has been demonstrated by the KATRIN collaboration in many publications and theses that most of the Design Report requirements are fulfilled. Comprehensive simulation studies, commissioning measurements and countermeasures to many problems occurring during the set-up of the beam line have improved the understanding of the experiment drastically. The earlier assessment of the Design Report systematics has thus changed, some contributions now have a smaller impact on the neutrino mass than expected, but some also may have been underestimated to a certain degree. At the same time, new systematic effects have been found which were not considered in the Design Report.

In the past, one publication or one thesis often treated a single specific systematic effect only. However, with regular neutrino mass data-taking starting in early 2019, it is now necessary to investigate how all the changes to the Design Report systematic uncertainties together with newly discovered uncertainties contribute to a total systematic uncertainty budget. The thesis at hand offers the first comprehensive re-evaluation of systematic uncertainties since the Design Report. The relevant information has been collected from a large set of KATRIN publications and PhD theses enriched and complemented by own investigations and estimations. In some theses and publications it was for instance only proven that a certain requirement of the Design Report is fulfilled and that the performance is even better than expected. However, the impact on the neutrino-mass determination was not yet considered in all of these cases. These calculations have then been done in a consistent manner in the scope of the thesis at hand.

The chapter is structured as follows: the first section 4.1 starts with a description how the neutrino mass is derived from the KATRIN measurements. Then, three different methods are introduced how systematic uncertainties can be treated and implemented in the neutrino mass analysis. In the following section 4.2, all systematic effects are discussed in detail. Each effect is explained and experience from former neutrino mass experiments is reviewed. For each effect, the specific influence on the neutrino mass measurement in KATRIN is given and its relevance for the total uncertainty budget is assessed. In section 4.3, the

results from the previous section are summarised. Finally, in section 4.4 conclusions are drawn and an outlook on the next steps is given.

4.1. Treatment of Systematic Uncertainties in KATRIN

As described in section 3.4.1, KATRIN measures the beta-decay spectrum of tritium in an integral way at its kinematic endpoint. The main spectrometer is ramped through different retarding voltages in the interval of $[E_0 - 30\,\mathrm{eV}, E_0 + 5\,\mathrm{eV}]$ with E_0 being the endpoint energy [Ang05]. The observables are thus a set of electron count rates $N_{\mathrm{obs},\,i}$ for individual retarding voltages qU_i. The neutrino mass is imprinted on the shape of the spectrum and is derived in a fit of the $N_{\mathrm{obs},\,i}$. Fit parameters are the squared neutrino mass m_ν^2 together with three other parameters: the kinematic endpoint E_0, the signal amplitude A_{sig} and the background rate R_{bg} [Kle14]. For the fit, a likelihood function L is defined (notation according to [Kle14; Kle18a]):

$$L(m_\nu^2, E_0, A_{\mathrm{sig}}, R_{\mathrm{bg}}|N_{\mathrm{obs}}) = \prod_i p(N_{\mathrm{obs},\,i}|N_{\mathrm{theo},\,i}(qU_i, m_\nu^2, E_0, A_{\mathrm{sig}}, R_{\mathrm{bg}}))\ . \tag{4.1}$$

The theoretical count rates $N_{\mathrm{theo},\,i}$ are derived from an analytic model, which comprises the theoretical implementation of the beta-decay spectrum [Kle14; Kle18a], the experimental characteristics of the apparatus with a detailed source model based on sensor data [Kuc16; Hei18], the detector efficiency and the transmission properties of the spectrometers [Gro15; Erh16]. The fit is done in a maximum likelihood analysis: the four fit parameters are varied until L is maximised. The fit values are then the maximum likelihood estimators of the parameter values. However, since it is numerically more convenient to determine a minimum than a maximum, actually the function

$$-\log L(\theta|N_{\mathrm{obs},\,i}) = -\sum_i \log p(N_{\mathrm{obs},\,i}|N_{\mathrm{theo},\,i}(qU_i, \theta)) \tag{4.2}$$

is minimised, where θ denotes the vector of the four fit parameters. In order to minimise $-\log L$, an assumption has to be made for the underlying probability distribution $p(N_{\mathrm{obs}}|N_{\mathrm{theo}})$, that N_{obs} is measured when N_{theo} is expected. The count rate in the beta decay is Poisson-distributed, but for an expectation value $\mu > 25$, it can be approximated by a Gaussian [Kle14]:

$$p(N_{\mathrm{obs}}|N_{\mathrm{theo}}) = \frac{1}{\sigma\sqrt{2\pi}} \exp\left(-\frac{(N_{\mathrm{obs}} - N_{\mathrm{theo}})^2}{2\sigma^2}\right)\ . \tag{4.3}$$

The function $-2\log L(\theta|N_{\mathrm{obs},\,i})$ has the functional form of a χ^2 function

$$\chi^2(\theta|N_{\mathrm{obs}}) = \sum_i \left(\frac{N_{\mathrm{obs},\,i} - N_{\mathrm{theo},\,i}(\theta)}{\sigma_i}\right)^2\ . \tag{4.4}$$

The parameter σ_i denotes the statistical uncertainty of $N_{\mathrm{obs},\,i}$ and is dependent on the theoretical signal rate $N_{\mathrm{theo,\,sig},\,i}$ and the theoretical background rate $N_{\mathrm{theo,\,bg},\,i}$ [Kle14]:

$$\sigma_i = \sqrt{N_{\mathrm{theo},\,i}} = \sqrt{\sigma^2_{\mathrm{theo,\,sig}\,i} + \sigma^2_{\mathrm{theo,\,bg}\,i}} = \sqrt{N_{\mathrm{theo,\,sig}\,i} + N_{\mathrm{theo,\,bg}\,i}}\ . \tag{4.5}$$

So far, no systematic uncertainty is considered. However, the model for the calculation of $N_{\mathrm{theo},\,i}$ is fed with sensor data and theoretical calculations like the final-state distribution for instance, which bear uncertainties due to the sensors or due to methods or parameters used in the calculations. In order to derive confidence intervals on the final neutrino mass result (see [Kle14] for details), these systematic effects of the model have to be propagated to the neutrino mass fit result. There are several possibilities how to assess the influence of

the systematic uncertainties on the neutrino mass result. Three methods are used within the KATRIN collaboration for the assessment of systematic uncertainties, which are the pull method (see section 4.1.1), the covariance matrix method (see section 4.1.2) and the shift method (see section 4.1.3). Each of the three methods has some advantages and disadvantages, which are discussed in more detail in the following sections.

4.1.1. Pull Method

The pull method is a commonly used analysis method to include systematic uncertainties into a fit (see for instance [Fog02]). The idea is that parameters ψ with a systematic uncertainty σ_ψ are treated as additional fit parameters, but penalised in the χ^2 distribution with a so-called pull term. The KATRIN χ^2 is then written as [Kle14]

$$\chi^2(\theta, \psi | N_{\mathrm{obs}}) = \sum_i \left(\frac{N_{\mathrm{obs},\,i} - N_{\mathrm{theo},\,i}(\theta)}{\sigma_i} \right)^2 + \sum_k \left(\frac{\hat{\psi}_k - \psi_k}{\sigma_{\psi_k}} \right)^2 \ . \tag{4.6}$$

The best estimate of the systematic $\hat{\psi}_k$ and its uncertainty σ_{ψ_k} has to be determined, for instance, in calibration measurements.

The advantage of this method is that the influence of a single systematic uncertainty on the total result can be clearly seen. The goodness of fit is usually estimated with the reduced χ^2, χ^2/n, n being the number of degrees of freedom. For a good fit result, χ^2/n is expected to be close to 1. In case of $\chi^2/n > 1$, which is usually the case if the model is not sufficient to describe the data or if the systematic uncertainties are underestimated, systematic uncertainties with large contributions to the χ^2 result can be easily identified.

However, there are also some disadvantages. The pull method cannot take all systematic effects into account. Especially systematic effects which do not necessarily allow a description via an analytic form or a parametrisation like for instance the final-state distribution (see section 4.2.17) or the energy loss function measurement (see section 4.2.16), should be considered with a different method which accounts for binning and normalisation. Another disadvantage is related to the number of fit parameters. Since the operational parameters may change from one KATRIN run to another (see section 3.4.1 for a definition), the count rates obtained in different runs cannot be simply summed up. As the true value of m_ν^2 has to be the same for all KATRIN runs, a global χ^2 can be built comprising the χ^2 of all runs. Then, a global fit is performed with one global m_ν^2, but run-specific E_0, A_{sig}, R_{bg} and pull terms. This analysis was implemented in the Mainz experiment, but there the global fit had in total only 19 parameters [Kra05]. For KATRIN, one can assume several tens of thousands of addends to the χ^2, so that it is hard to achieve a minimisation of the χ^2 function and it is also much more complicated to identify single addends that cause an indefensible rise of the total χ^2.

4.1.2. Covariance Matrix Method

The covariance matrix method is another formulation of the χ^2 terms, but it can be shown that the result is exactly the same as with the pull method [Fog02]:

$$\chi^2_{\mathrm{cov}} = \chi^2_{\mathrm{pull}} \ . \tag{4.7}$$

In the covariance matrix method, the χ^2 is written as

$$\chi^2 = \sum_{i,j} (N_{\mathrm{obs},\,i} - N_{\mathrm{theo},\,i}(\theta)) V^{-1}_{i,j} (N_{\mathrm{obs},\,j} - N_{\mathrm{theo},\,j}(\theta)) \ . \tag{4.8}$$

The covariance matrix elements $V_{i,j}$ are defined as

$$V_{i,j} = \delta_{ij}\sigma_{\mathrm{stat},\,i}\sigma_{\mathrm{stat},\,j} + \sum_{k=1}^{K} \sigma^{k}_{\mathrm{sys},\,i}\sigma^{k}_{\mathrm{sys},\,j} \ . \tag{4.9}$$

Here, the σ_{stat} are the uncorrelated statistical uncertainties and the σ_{sys} the correlated systematic uncertainties of K systematic effects. Like in the pull method, the index i denotes retarding voltage steps qU_i applied at the main spectrometer. The correlation comes into play because usually all measured rates are influenced by all systematic effects at the same time. However, the systematics can have different impacts on the count rates at different voltage steps. For instance, one effect can lead to a rise of the measured rate at one retarding voltage and to a decrease at another measurement point at the same time. This different behaviour is considered in the covariance matrix. However, it has to be investigated in simulations and test measurements beforehand.

The advantage of the covariance matrix method is that all systematic contributions are considered at once. By virtue of simulations it is also easier to include effects like the energy loss function in the analysis, which is more difficult in the pull method, see section 4.1.1.

However, there are also two disadvantages: the covariance matrix has to be inverted, see equation 4.8. The more data points are involved, the more complicated the inversion gets. And here the same is true as for the pull method: the combination of different measurement runs with different conditions leads to a very large covariance matrix. The other disadvantage is that it is impossible to trace back the influence of one specific systematic uncertainty on the total χ^2. This makes it harder to investigate any deviations from $\chi^2/n \neq 1$.

Due to the equivalence of the covariance matrix method and the pull method, it is in principle possible to do a mixed analysis with considering some systematic uncertainties as pull terms and some in the covariance matrix. The KATRIN collaboration has implemented methods and developed software tools for both versions, but a decision on the procedure for the final neutrino mass analysis has not been made yet. For investigations of how to apply the covariance matrix approach for KATRIN, the reader is referred to [Sch19].

4.1.3. Shift Method

The shift method or ensemble test method calculates the influence of a single systematic uncertainty on the neutrino mass squared as shift of the fit result [Kle14]. A large number (typically 1000 to 10000) of KATRIN measurements is simulated. For the simulations, a set of standard operational parameters is used except for the parameter of interest, for which the standard value is reduced (or increased) by its uncertainty within pre-defined bounds. In the next step, each of the simulated measurements is fitted with the analysis model which comprises the four fit parameters neutrino mass squared m_ν^2, endpoint of the beta spectrum E_0, amplitude A_{sig} and background rate R_{bg}. The model is built again with the standard parameter values, also for the parameter of interest. If both the model for the simulation as well as the model for the analysis use exactly the same input parameters, the deviation of the simulated and fitted m_ν^2 should be exactly 0. However, if the parameter of interest has slightly different values in both steps, the fitted neutrino mass squared could differ from the simulated one. An example is shown in figure 4.1.

The advantage of the shift method is that the influence of one systematic effect on the final neutrino mass result of KATRIN is very well illustrated. This helps to classify the systematic contributions into minor and major ones and to identify those for which more

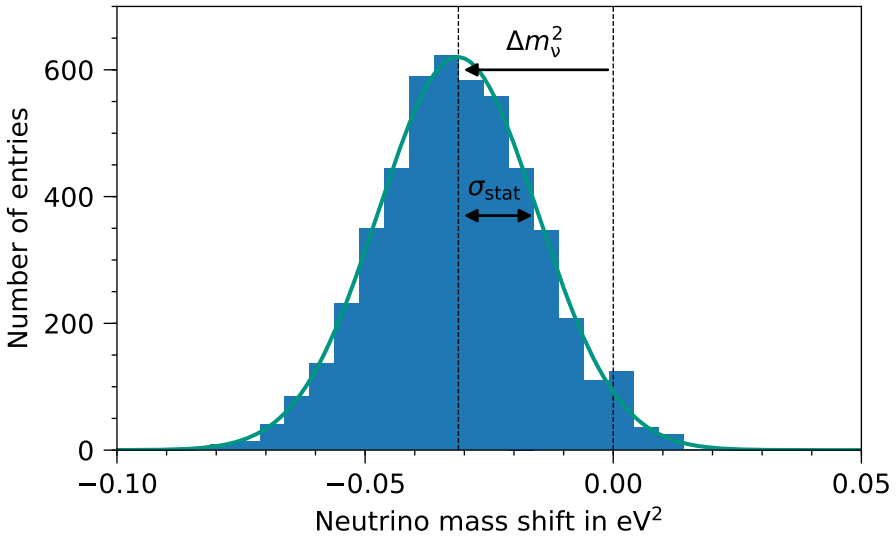

Figure 4.1.: Illustration of the shift method to estimate systematic uncertainties. The histogram shows the result of an ensemble test performed to estimate the neutrino mass shift if the synchrotron losses are neglected (see section 4.2.3). 5000 KATRIN experiments are simulated taking the synchrotron radiation into account and they are fitted without this effect. The systematic effect manifests as a clear shift of the mean of the distribution from zero. The width of the distribution is determined by the statistical uncertainty. Both parameters are calculated from the unbinned dataset.

work and other solutions are necessary to keep the overall systematic budget of $0.017\,\mathrm{eV}^2/c^4$. However, the shift method is not suited for the final KATRIN analysis. In order to account for correlations of two correlated parameters A and B, at least four simulation and analysis runs are necessary: one in which both values of A and B are increased by their uncertainty, one in which both are decreased, and two in which one of them is decreased and the other increased. Alternatively, the parameters have to be drawn randomly from their uncertainty intervals. Furthermore, the method is rather time-consuming. Depending on the level of detail included in the simulation and analysis model, the analysis of one systematic uncertainty takes more than one day. Since the analyses have to be repeated as soon as one operational parameter has changed, which can happen in between or during KATRIN runs, this method is of limited use for deriving the final neutrino mass result.

Nevertheless, in the scope of the thesis at hand, the systematic uncertainties of KATRIN are evaluated with the shift method. The main reasons are to ensure the compatibility with the KATRIN Design Report investigations [Ang05] and that it allows to investigate the influence of a single systematic uncertainty to identify the main contributions. In the next section 4.2, all systematic uncertainties from a series of previous publications are collected and critically reviewed. For a better comparability, all systematic uncertainties are investigated with the same setting for the ensemble test. The parameters of this setting can be found in table 4.1.

4.2. Classification and Evaluation of Systematic Uncertainties

In this section, all known systematic uncertainties of KATRIN are discussed in the same way: In each of the following subsections, the systematic effect is first described. Then, experience from former neutrino mass experiments (notably Los Alamos, Livermore, Troitsk and Mainz) is shortly reviewed. Afterwards, the KATRIN-specific implementation of the systematic effect is explained: how is the systematic uncertainty determined, which are

Table 4.1.: Basic settings for KATRIN ensemble tests. The table presents the basic parameter values for the ensemble tests performed in the scope of section 4.2. Each simulation run comprises the statistics of a full KATRIN measurement of 3 years net measurement time. With 5000 simulation runs, a statistical uncertainty of $0.2\times10^{-4}\,\mathrm{eV}^2/c^4$ on the neutrino mass shift is achieved. E_0 denotes the kinematic endpoint of the tritium beta-decay spectrum. With a number of 100 WGTS slices, inhomogeneities of the magnetic field (see figure 4.10), for instance, can be taken into account to satisfying accuracy in the ensemble-testing [Gro15].

Parameter	Design Report setting
Number of simulation runs	5000
Background level	10 mcps
Beam line magnets	100 %
Magnetic field in analysing plane	3×10^{-4} T
Spectral interval for analysis	$[E_0 - 30\,\mathrm{eV}, E_0 + 5\,\mathrm{eV}]$
Number of WGTS slices	100

the requirements and whether it has been demonstrated yet that they are met. The most important information regarding a systematic effect is its influence on the neutrino mass result. It should be noted that the term "neutrino mass shift" refers to Δm_ν^2 in the following. The shift is presented for every systematic uncertainty in the corresponding section, sometimes a value from literature could be taken and in many instances new ensemble tests (see section 4.1.3) were performed in this thesis. Finally, for every systematic effect the current status and its relevance for the overall systematic uncertainty budget of KATRIN are discussed briefly.

In total, there are 18 subsections following, some of them comprise actually more than one systematic uncertainty. For a first overview, table 4.2 lists all 18 effects and classifies them according to some properties, either being more theory-based or having to be determined experimentally in commissioning measurements or even through continuous monitoring. Table 4.2 helps also with the orientation, since it contains links to each of the subsections in which the specific systematic effect is discussed in detail.

4.2.1. Theoretical Corrections of the β Spectrum

Description. KATRIN will measure the shape of the tritium beta spectrum close to the kinematic endpoint with unprecedented precision. This makes it necessary to take corrections of the theoretical description of the beta-decay spectrum (see equation 2.54) into account. For a precise modelling of the beta-decay spectrum, the relevance of the following atomic and nuclear corrections have been investigated for KATRIN. For a detailed discussion, the reader is referred to [Kle18a] and the references therein:

- A small correction is introduced when the recoil energy of the daughter nucleus is calculated in a full relativistic three-body calculation.
- The Fermi function in equation 2.54 is often approximated in a (semi-)classical form. However, for KATRIN the full relativistic Fermi function is used.
- Radiative corrections $G(E, E_0)$ occur due to contributions from virtual and real photons.
- The Coulomb field of the daughter isotope ^{3}He is influenced by the charges of the $1s$ electrons. This screening effect $S(Z, E)$ is corrected in the precise modelling of the tritium beta spectrum.

Table 4.2.: Classification of systematic uncertainties of KATRIN. The table lists all systematic effects of KATRIN known so far. All systematic uncertainties mentioned in the KATRIN Design Report [Ang05] are marked in the second column. The effects are further classified according to several properties: the third column shows if the determination of a systematic uncertainty needs significant input from theory and simulations. A mark in the fourth column indicates that this systematic effect needs either a dedicated commissioning measurement or a continuous sensor-based monitoring during neutrino mass data-taking or both. The fifth column shows if a systematic uncertainty needs regular calibration measurements. This often means that neutrino mass data-taking has to be interrupted. Each systematic is discussed in detail in the section listed in the sixth column.

Systematic effect	Design Report	theory-based	experimental	regular calibration	section
Theoretical corrections of the β spectrum	(x)	x			4.2.1
Relativistic correction of transmission function		x			4.2.2
Synchrotron radiation	x	x			4.2.3
Doppler effect	x	x			4.2.4
Modified angular distribution of electrons		x			4.2.5
Analysing plane: potential and magnetic field		x	x	x	4.2.6
HV stability	x		x	x	4.2.7
Detector-related effects			x	x	4.2.8
Ions	(x)		x	x	4.2.9
Backscattering at rear wall	x	x			4.2.10
Source magnetic field	x		x	x	4.2.11
Trapped electrons in WGTS	x	x			4.2.12
Potential variations in WGTS	x	x	x	x	4.2.13
Gas dynamics in WGTS		x	x	x	4.2.14
Monitoring of column density	x	x	x	x	4.2.15
Energy loss function	x	x	x	x	4.2.16
Final-state distribution	x	x			4.2.17
Slope of the background rate	x		x		4.2.18

- The relativistic treatment of the beta decay leads to energy-dependent recoil effects, for instance weak magnetism, $V - A$ interference and modifications of the spectral shape. These effects are combined into one correction factor $R(E, E_0, M)$.
- The nucleus of the daughter isotope ^{3}He has a finite structure and is not point-like. Therefore, the shape of the Coulomb field deviates from the $1/r^2$ relation, and a correction factor $L(Z, E) + C(Z, E)$ has to be applied.
- When the beta electron leaves the Coulomb potential of the daughter isotope, the potential is not stationary but moving due to the recoil from the beta decay. The moving potential adds a correction factor $Q(Z, E, E_0, M)$ which can be taken into account.
- The beta electron leaving the molecule has a non-zero probability to interact with the electrons of the $1s$ orbital which is taken into account with the correction factor $I(Z, E)$.
- The factors G, R, Q depend on the endpoint energy and the phase space of an excited final state. The final states dependency can be neglected to accelerate the computations, but then an additional uncertainty is introduced.

Experience from former neutrino mass experiments. Former neutrino mass experiments did not consider details of the theoretical description of the beta spectrum on the level outlined above. The Mainz group took radiative corrections into account [Kra05].

Determination for KATRIN. All corrections described above can be applied in an analytical form to the spectrum [Kle18a]. They are implemented in SSC (see section 3.3) and the user can specify the level of detail of the spectrum model for various applications.

Impact on neutrino-mass determination. Most of the theoretical corrections induce only very tiny neutrino mass shifts of $\Delta m_\nu^2 < 10^{-5}\,\mathrm{eV}^2/c^4$, if they are neglected in the analysis [Kle18a]. The statistical uncertainty of the ensemble tests performed in this thesis is chosen to be $2 \times 10^{-4}\,\mathrm{eV}^2/c^4$, so that these effects are below the testable level. Therefore, only ensemble tests have been performed to quantify the influence of the radiative corrections on the neutrino mass estimate because their neglect adds a significant shift on the order of $\Delta m_\nu^2 = 2 \times 10^{-3}\,\mathrm{eV}^2/c^4$ [Kle18a]. The results are presented in table 4.3 and compared to the results from [Kle18a]. For the sake of completeness, the neutrino mass shifts calculated in [Kle18a] for the other effects are also given. The neutrino mass shift for radiative corrections was reproduced in the ensemble test, but with the opposite sign. This may be explained by a different initialisation of the ensemble tests. It should be kept in mind that the neutrino mass shifts of the theoretical corrections are zero when all effects are fully considered in the final neutrino mass analysis.

Relevance for KATRIN and current status. The theoretical corrections are not systematic effects in the usual meaning. They are just errors in the analysis if they are not taken into account. However, most of the theoretical corrections are negligible in the final neutrino mass analysis of KATRIN since they add only neutrino mass shifts on the order of $< 10^{-5}\,\mathrm{eV}^2/c^4$. Radiative corrections have to be applied because otherwise a significant neutrino mass shift of $-2 \times 10^{-3}\,\mathrm{eV}^2/c^4$ occurs. The correct implementation has to be guaranteed in the analysis chain.

4.2.2. Relativistic Correction of Transmission Function

Description. The analytical transmission function of the MAC-E filter stated in equation 3.6 does not take relativistic effects into account. However, electrons with energies

Table 4.3.: Neutrino mass shifts associated with theoretical corrections of the tritium beta spectrum. The table shows the neutrino mass shifts related to theoretical corrections as calculated in [Kle18a]. For radiative corrections, the neutrino mass shift was confirmed through ensemble tests (see table 4.1), but with opposite sign. The neutrino mass shifts given here always relate to fully neglecting the effect in question in the analysis. If the correction is fully implemented, no neutrino mass shift remains.

Effect	Δm_ν^2 [Kle18a] in $10^{-5}\,\mathrm{eV}^2/c^4$	Δm_ν^2 (this work) in $10^{-5}\,\mathrm{eV}^2/c^4$
Relativistic recoil calculation	0.03	-
Relativistic Fermi function	0.19	-
Radiative corrections	214.10	−206.6
Screening corrections	−2.82	-
Energy-dependent recoil effects	−0.12	-
Finite nuclear extension	< 0.01	-
Recoiling Coulomb field	−0.02	-
Orbital electron interactions	−0.02	-
Neglect final states dependency	13.50	-

of 18.6 keV move already with a velocity of $0.26c$. Thus, relativistic corrections to the transmission function can be relevant [Gro15].

Experience from former neutrino mass experiments. Former neutrino mass experiments did not use a relativistic transmission function [Kra05; Ase11].

Determination for KATRIN. The transmission function is modified by the Lorentz factors of the electrons in the source γ_S and the analysing plane γ_A to

$$T(E,qU) = \begin{cases} 0 & E - qU < 0 \\ \dfrac{1-\sqrt{1-\frac{E-qU}{E}\frac{B_\mathrm{S}}{B_\mathrm{A}}\frac{\gamma_\mathrm{S}+1}{\gamma_\mathrm{A}+1}}}{1-\sqrt{1-\frac{\Delta E}{E}\frac{B_\mathrm{S}}{B_\mathrm{A}}}} & 0 \leq E - qU \leq \Delta E \\ 1 & E - qU > \Delta E\ . \end{cases} \tag{4.10}$$

For electrons with 18.6 keV, the value of γ_S is 1.036. γ_A is ≈ 1 for electrons with $E \approx qU_\mathrm{ret}$ as they are decelerated by the retarding potential U_ret. The relativistic correction leads to a broadening of the transmission function of 1.8 % for the KATRIN nominal conditions of the Design Report (see figure 4.2) and is implemented in the SSC code for the analysis [Gro15].

Impact on neutrino-mass determination. Table 4.4 lists the neutrino mass shift that has to be taken into account if the relativistic correction of the transmission function is neglected in the analysis. The apparent difference in the calculated neutrino mass shifts (in both cases for the KATRIN Design Report settings) between a former work [Gro15] and this work may be explained by the use of slightly different configurations of ensemble tests.

Relevance for KATRIN and current status. The relativistic correction of the transmission function is not a systematic effect in its usual meaning, it is just an error in the analysis if it is not considered. The relativistic correction can be taken into account analytically, so that the associated shift of the neutrino mass is zero, if the relativistic correction is applied in the analysis.

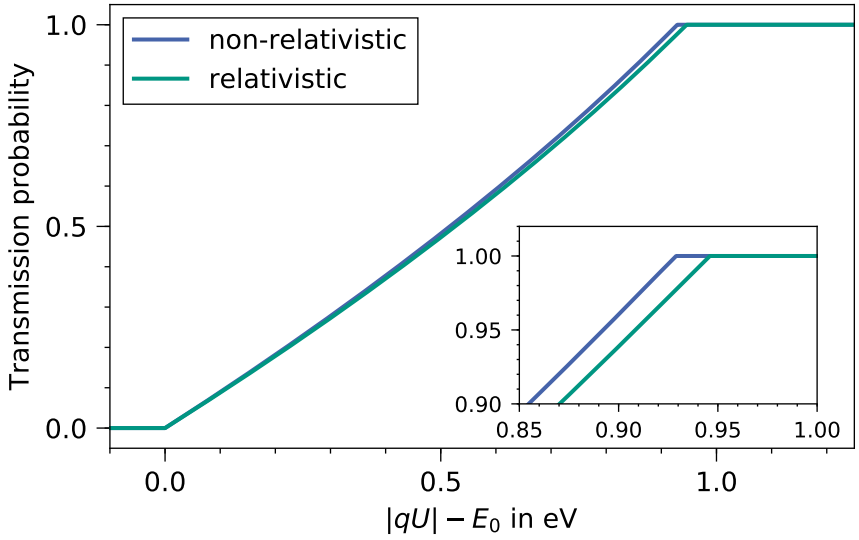

Figure 4.2.: Impact of the relativistic correction on the KATRIN transmission function. The plot shows the transmission function for electrons with an energy of $|qU| = 18575\,\mathrm{eV} \approx E_0$ and KATRIN nominal magnetic fields ($B_{\mathrm{WGTS}} = 3.6\,\mathrm{T}$, $B_{\mathrm{max}} = 6.0\,\mathrm{T}$, $B_{\mathrm{ana}} = 3.0 \times 10^{-4}\,\mathrm{T}$). The relativistic corrections broaden the transmission edge. The inset shows a close up of the non-negligible effect. The plotted data is generated with KaFit/SSC.

Table 4.4.: Neutrino mass shift associated with relativistic corrections of the transmission function in KATRIN. The table shows the neutrino mass shift determined in ensemble tests (see table 4.1). The result is compared to former investigations in [Gro15].

Δm_ν^2 in $10^{-3}\,\mathrm{eV}^2/c^4$ [Gro15]	Δm_ν^2 in $10^{-3}\,\mathrm{eV}^2/c^4$ (this work)
-7.6	-5.2

4.2.3. Synchrotron Radiation

Description. Charged particles performing a cyclotron motion around magnetic field lines emit synchrotron radiation. The associated energy loss can be expressed in a semi-classical way as [Gro15]

$$\Delta E_{\text{sync}} = \frac{-\mu_0}{3\pi c} \cdot \frac{q^4}{m^3} \cdot B^2 \cdot E_\perp \cdot \gamma \cdot t \ . \tag{4.11}$$

Here, μ_0 denotes the vacuum permeability, q the charge of the particle, which is $-e$ in the case of an electron, m is the mass of the particle, B is the magnetic field strength and γ is the Lorentz factor. $E_\perp = E \sin^2\theta$ denotes the kinetic energy of the electron associated with its perpendicular motion to the magnetic field lines. θ is the angle between the electron's momentum and the magnetic field lines, while t is the time the electron stays in the magnetic field strength B. A derivation of the equation can be found in [Fur15]. The dependence on the polar angle θ means that electrons created in the source with the same energy, but different polar angles, undergo energy losses of different magnitude due to synchrotron radiation. This influences the shape of the transmission function directly, so that the synchrotron radiation has to be taken into account in precise neutrino mass experiments with MAC-E filters.

Experience from former neutrino mass experiments. There are no hints in the literature that synchrotron radiation has been taken into account in former neutrino mass experiments. Presumably, it was not relevant for former experiments with sensitivity inferior to that of KATRIN. Interestingly, the Project 8 collaboration makes use of the synchrotron radiation "losses" as a signal feature to measure the tritium beta decay spectrum and to eventually extract a neutrino mass value [Mon09] (see also section 2.3.3).

Determination for KATRIN. The effect of synchrotron radiation losses on the transmission function of KATRIN can be calculated very precisely with the particle tracking software KASSIOPEIA [Fur17] and is incorporated into the code of SSC [Kle14; Kle18a]. The energy loss for electrons due to synchrotron radiation was determined in KASSIOPEIA simulations to be less than 100 meV [Gro15]. The effect on the transmission function is shown in figure 4.3.

In KaFit/SSC, the synchrotron energy loss is derived from a data file which contains the results from the Kassiopeia simulation runs for electrons started in the WGTS with different starting positions and polar angles. These simulations have been performed for electrons with an energy of 18575 eV and for nominal magnetic fields along the beam line. For other energies and magnetic fields, a correction factor has to be applied. With $t = s/(v \cdot \cos\theta)$, the time can be linked with the length s of the magnet coil. If v is replaced by $\sqrt{2E/m}$, the dependencies of equation 4.11 can be written as

$$\Delta E_{\text{sync}} \propto B^2 \cdot \gamma \cdot \sqrt{E} \ . \tag{4.12}$$

Since the Lorentz factor γ of electrons with an energy of 18.6 keV is ≈ 1.04, the non-relativistic approximation is feasible.

Impact on neutrino-mass determination. Different aspects of the synchrotron radiation losses have been investigated and the results are listed in table 4.5. The results demonstrate that the synchrotron radiation would result in a large uncertainty if neglected in the analysis. In the final neutrino mass analysis, the synchrotron radiation will be incorporated in the model. As described above, the value of the synchrotron energy losses relies on the simulations. The uncertainty of this simulated energy losses is estimated to be 1 %. This is reasonable, as the magnetic field simulation of the WGTS will be tested in a

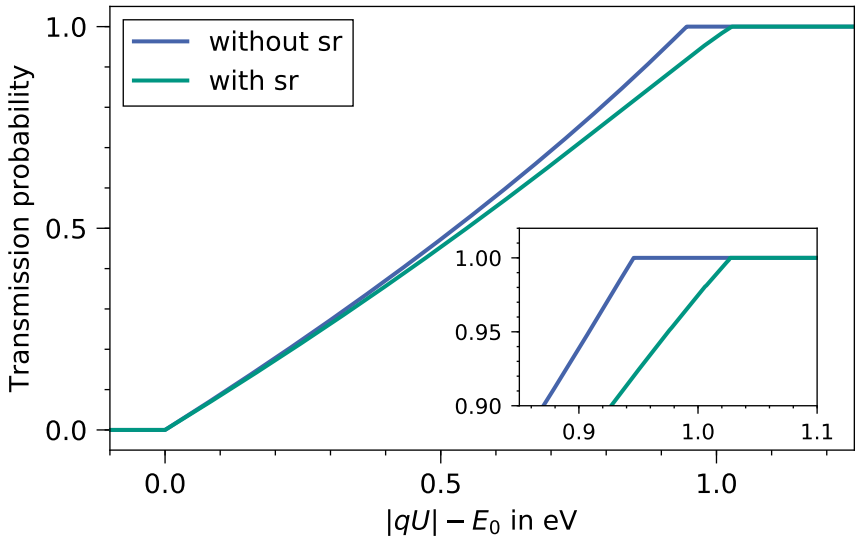

Figure 4.3.: Impact of the synchrotron energy losses on the KATRIN transmission function. The plot shows the non-relativistic transmission function for electrons with an energy of $|qU| = 18575\,\mathrm{eV} = E_0$ and KATRIN nominal magnetic fields ($B_{\mathrm{WGTS}} = 3.6\,\mathrm{T}$, $B_{\mathrm{max}} = 6.0\,\mathrm{T}$, $B_{\mathrm{ana}} = 3.0 \times 10^{-4}\,\mathrm{T}$). The synchrotron energy loss depends on the path length of the electrons and affects therefore electrons with a larger pitch angle more than electrons with a small pitch angle. Thus, the transmission function is significantly broadened. The inset shows a close-up. The plotted data is generated with SSC/KaFit.

Table 4.5.: Neutrino mass shifts associated with synchrotron radiation losses. The table presents the neutrino mass shifts related to synchrotron radiation losses obtained in ensemble tests (see table 4.1). The neutrino mass shift is listed for the cases when the synchrotron is totally neglected and when an uncertainty of 1 % is assumed for the synchrotron energy loss distribution. The second column gives the literature values from [Kle18a] as a reference.

Effect	Δm_ν^2 [Kle18a] in $10^{-3}\,\mathrm{eV}^2/c^4$	Δm_ν^2 (this work) in $10^{-3}\,\mathrm{eV}^2/c^4$
neglected	-29.4	-31.2
1 % uncertainty	-	-0.2

measurement with $\approx 0.5\,\%$ trueness[1] (see section 4.2.11). A further small uncertainty comes from the measurement interval. The synchrotron energy losses are assumed to be constant over the analysis interval, but in reality electrons with energies close to the endpoint of the tritium spectrum experience slightly larger synchrotron losses than electrons at the lower edge of the analysis interval. The difference is on the per mille level.

Relevance for KATRIN and current status. The influence of synchrotron radiation losses on KATRIN's spectrum measurement is well understood. With the particle tracking software Kassiopeia (see section 3.3), highly precise simulations are possible. As long as it is guaranteed that the synchrotron radiation effects are incorporated in the analysis,

[1]The term trueness describes the difference of the true value and the measurement value. In contrast, precision describes the reproducibility of a measurement. Accuracy comprises both trueness and precision. Although the terms are defined in the ISO 5725 as outlined in the sentences before, their use in this sense is not common in the scientific community. In the scope of this thesis, the ISO definitions are employed.

the associated systematic uncertainty is a minor one compared to the overall systematics budget.

4.2.4. Doppler Effect

Description. The thermal motion of the decaying tritium molecule increases the energy of the decay electron, if it is emitted into the same direction as the molecule moves. The energy of the electron is decreased in comparison to its original energy if it is emitted against the direction the molecules moves to. These shifts of the electron energy are described by the Doppler effect.

Experience from former neutrino mass experiments. For the Los Alamos neutrino mass experiment, the Doppler effect and its contribution to the systematic uncertainties of the final-state distribution was calculated, but it was negligible [Rob91]. From the other experiments, no investigations of the Doppler effect are known, probably because the effect is small for experiments with a sensitivity inferior to that of KATRIN.

Determination for KATRIN. In the WGTS, tritium molecules undergo two different kind of motions: on the one hand they follow a random thermal motion, on the other hand they exhibit a directed motion following the gas flow due to the pumping on both ends of the central beam tube. From both velocities, the component which is parallel to the emission direction of the electron is of interest. If it is parallel, the electron gains some energy, if it is anti-parallel, the electron loses some energy. This introduces an energy smearing σ_E which is found to be [Kle18a]

$$\sigma_\mathrm{E} = \sqrt{(E_\mathrm{CMS} + 2m_\mathrm{e}) \cdot E_\mathrm{CMS} \cdot \frac{k_\mathrm{B}T}{M}} \ . \tag{4.13}$$

E_CMS is the centre-of-mass energy of the electrons, T the beam tube temperature of the WGTS and M the mass of the tritium isotopologue involved in the decay. The thermal velocity at 30 K is $\approx 200\,\mathrm{m/s}$ and the mean bulk velocity $\approx 13\,\mathrm{m/s}$ [Kle18a], so that the thermal velocity has the largest influence on the Doppler-driven correction of the beta-decay spectrum of tritium. At the kinematic endpoint of 18.6 keV, the energy smearing is ($T = 30\,\mathrm{K}$) $\sigma_\mathrm{E} = 94\,\mathrm{meV}$.

As the bulk velocity depends on the z position in the WGTS, the Doppler effect has to be determined for a voxelised source. For every voxel, the bulk velocity has to be calculated from the gas dynamics model [Höt12; Kuc16; Kuc18], the temperature, which has a slight inhomogeneity along the beam tube (see section 6.2.2), and the gas density. The final spectrum fit is then a superposition of the spectra of the single voxels, from which up to 50 are used [Kle14]. Therefore, the computation of the Doppler shift is quite time-consuming, but since its corresponding energy shift is on the scale of KATRIN's neutrino mass sensitivity, it is necessary to incorporate the Doppler effect into the final analysis. This is illustrated in figure 4.4. In order to speed up the calculation, the Doppler effect can be applied to the final-state distribution, which gives the same result as the correction of the beta decay spectrum [Kle14].

Impact on neutrino-mass determination. Table 4.6 gives an overview on the neutrino mass shifts associated with the Doppler effect. If the Doppler effect is fully implemented in the analysing model, only the neutrino mass shift due to the temperature uncertainty remains. Since the computational time for the full consideration of the Doppler effect is very large, it may be more convenient in some cases to apply the Doppler effect to the final-state distribution to accelerate the calculation. However, then a neutrino mass shift of

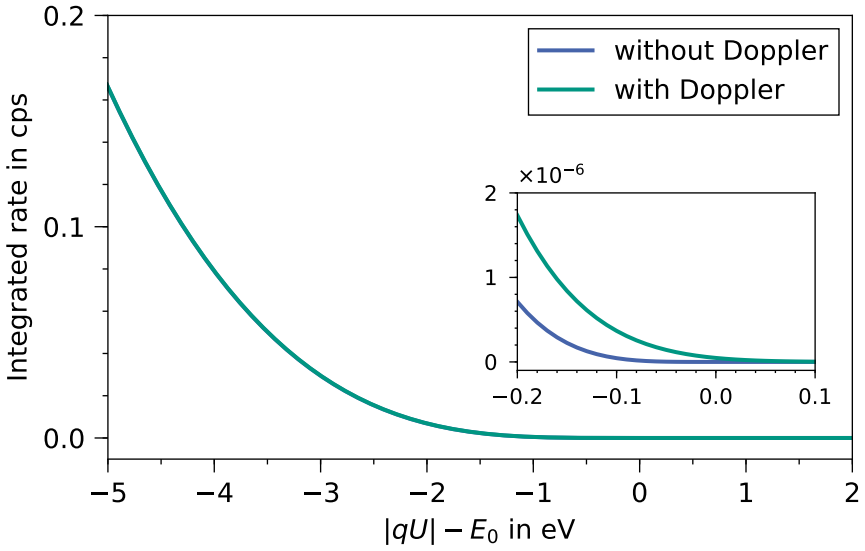

Figure 4.4.: Impact of the Doppler effect on the integrated spectrum. The plot shows the integrated spectrum simulated with KaFit/SSC for energies close to the kinematic endpoint E_0 of the tritium beta spectrum. The influence of the Doppler effect becomes clearly visible in the close up of the endpoint region in the inset. The Doppler effect broadens the spectrum and shifts the endpoint slightly towards larger energies. Furthermore, the shape of the spectrum at the endpoint region is changed, so that it is necessary to include the Doppler effect in the analysis model.

Table 4.6.: Neutrino mass shifts associated with the Doppler effect. The table presents the neutrino mass shifts for the ensemble tests performed with the KATRIN Design Report setting (see table 4.1). A neutrino mass shift occurs if the Doppler effect is neglected or applied to the final-state distribution in order to accelerate the computation. The temperature uncertainty calculated in appendix A.1 adds a small contribution. The results from [Kle18a] are given as reference.

Setting	Δm_ν^2 in $10^{-3}\,\mathrm{eV}^2/c^4$ ([Kle18a])	Δm_ν^2 in $10^{-3}\,\mathrm{eV}^2/c^4$
neglected	−15.5	−16.5
applied to FSD	1.0	1.9
$\Delta T = 0.16\,\mathrm{K}$	-	±0.2

$1.9 \times 10^{-3}\,\mathrm{eV}^2/c^4$ has to be taken into account. Former results by [Kle18a] were reproduced roughly; the differences are explained by different settings of the ensemble tests. The influence of the temperature trueness on the Doppler effect has not been considered before.

Relevance for KATRIN and current status. The Doppler effect modifying the energy of electrons due to the motion of tritium molecules is well understood and fully incorporated into the analysis code SSC. As long as it is taken into account for the analysis, only a minor contribution to the overall systematic uncertainty budget remains due to the trueness of the WGTS temperature. However, since the calculation of the Doppler effect is very time-consuming, an approximation may be used which introduces a small additional shift of the neutrino mass.

4.2.5. Modified Angular Distribution of Electrons

Description. The beta-decay electrons are emitted isotropically in the gaseous tritium source. However, for larger polar angles up to the maximum acceptance angle (see equa-

tion 3.5) the probability of inelastic scattering increases since the path length of the electrons through the source is longer. That means that the scattering probabilities are angular-dependent. As soon as the electrons leave the tritium source, the population of electrons undergoing a specific number of scattering processes is no longer isotropically distributed, so that the shape of the transmission function is changed. This effect is described and investigated in detail in [Zie13; Gro15; Kle18a].

Experience from former neutrino mass experiments. This systematic uncertainty has not been considered in former neutrino mass experiments.

Determination for KATRIN. Equation 3.6 states the isotropic and non-relativistic transmission function. For each population of i-fold scattered electrons an anisotropy has to be taken into account due to the angular-dependent scattering probabilities $P_i(\theta)$. Therefore, the isotropic distribution has to be weighted by the scattering probabilities for i-fold scattering $P_i(\theta)$:

$$\sin\theta \rightarrow \sin\theta \cdot P_i(\theta) \ . \tag{4.14}$$

Finally, this leads to the modified transmission functions per i-fold scattering, $T_i^*(E_\mathrm{S}, qU)$ (for details the reader is referred to [Gro15; Kle18a]):

$$T_i^*(E_\mathrm{S}, qU) = \begin{cases} 0 & E_\mathrm{S} - qU < 0 \\ \int\limits_{\theta=0}^{\theta_\mathrm{tr}(E_\mathrm{S}, qU)} \frac{\sin\theta \cdot P_i(\theta)}{(1-\cos\theta_\mathrm{max}) \cdot \overline{P}_i} & 0 \leq E_\mathrm{S} - qU \leq \Delta E \\ 1 & E_\mathrm{S} - qU > \Delta E \ . \end{cases} \tag{4.15}$$

Here, E_S denotes the starting energy of the electrons, $\overline{P}_i$ the mean scattering probabilities and $\theta_\mathrm{tr}(E_\mathrm{S}, qU)$ the transmission polar angle, which also includes the relativistic corrections (see equation 4.10), with

$$\theta_\mathrm{tr}(E_\mathrm{S}, qU) = \arcsin\left(\sqrt{\frac{E_\mathrm{S} - qU}{E_\mathrm{S}} \cdot \frac{B_\mathrm{S}}{B_\mathrm{A}} \cdot \frac{\gamma_\mathrm{A} + 1}{\gamma_\mathrm{S} + 1}}\right) \ . \tag{4.16}$$

It should be noted that every population of i-fold scattered electrons is non-isotropically distributed. Therefore, each population of i-fold scattered electrons has its own transmission function $T_i^*(E_\mathrm{S}, qU)$. As described in more detail in section 4.2.16, for KATRIN inelastic processes up to three-fold scattering are relevant, since the electrons then lose energy of around 30 eV, which falls into the KATRIN analysis interval assumed in the Design Report [Ang05]. Thus, T_0^* to T_3^* have to be considered in the model for a correct implementation of this correction to the transmission function. The impact on the transmission function is illustrated in figure 4.5 for T_0^*.

Impact on neutrino-mass determination. The result of the ensemble test performed for the KATRIN Design Report conditions is presented in table 4.7. The former results by [Gro15] are reproduced approximately. The difference is probably due to different settings in the ensemble tests. It is obvious that the modified angular distribution of the non-scattered electrons has the largest influence on the neutrino mass. However, since the effect can be calculated analytically, all corrections up to T_3^* can be included in the analysis model to reduce the neutrino mass shift to zero. In case that the time-consuming calculations are reduced to first-order effects only (T_0^*), the remaining uncertainty has to be taken into account for the neutrino mass analysis.

Relevance for KATRIN and current status. The non-isotropic angular distribution

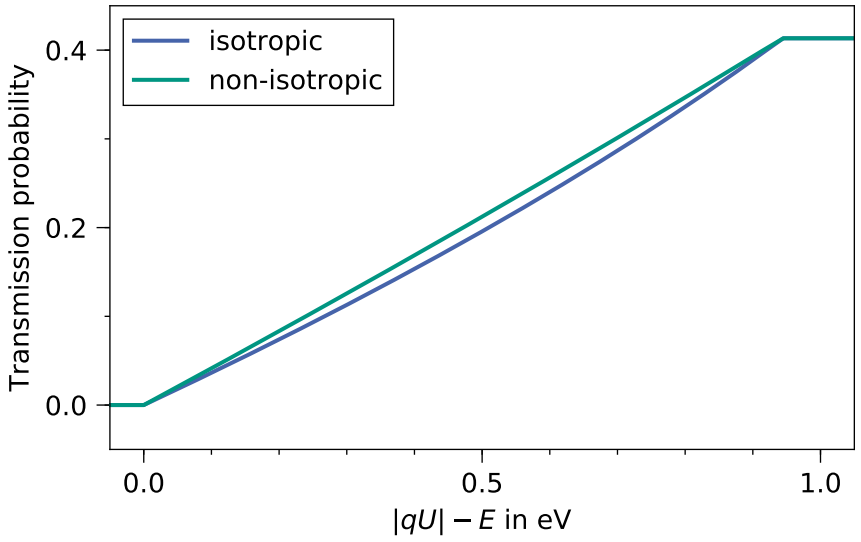

Figure 4.5.: Impact of the non-isotropic electron distribution on the KATRIN response function. The plot shows the response function for electrons with an energy of $|qU| = 18545\,\mathrm{eV} = E$ and KATRIN nominal magnetic fields ($B_{\mathrm{WGTS}} = 3.6\,\mathrm{T}$, $B_{\mathrm{max}} = 6.0\,\mathrm{T}$, $B_{\mathrm{ana}} = 3.0 \times 10^{-4}\,\mathrm{T}$) and a column density of $5 \times 10^{17}\,\mathrm{cm}^{-2}$. The response function takes the scattering processes in the source into account and is therefore a modification of the transmission function [Kle18a]. The transmission edge comprises only non-scattered electrons, so that the depicted correction of the response function is only based on T_0^*. The width of the transmission function stays the same. In standard conditions, 41 % of all electrons which are emitted towards the spectrometer leave the source without an inelastic scattering process. Therefore, T_0^* has the largest influence on the neutrino mass result, if the modified angular distribution is neglected in the analysis. The plotted data is generated with KaFit/SSC.

Table 4.7.: Neutrino mass shifts associated with the modified angular distribution of beta-decay electrons. The table lists the neutrino mass shifts due to the modified angular distribution for KATRIN Design Report conditions (see table 4.1) when the effect is totally neglected or when only the modified angular distribution for the non-scattered electrons T_0^* is considered. As a reference, the results of the investigations in [Gro15] are given.

Effect	Δm_ν^2 in $10^{-3}\,\mathrm{eV}^2/c^4$ ([Gro15])	Δm_ν^2 in $10^{-3}\,\mathrm{eV}^2/c^4$
neglected	11.9	9.8
only T_0^*	−2.3	−2.1

of electrons entering the main spectrometer is not a systematic uncertainty in its usual meaning. Instead, it is an error which can be made in the analysis if the associated correction of the isotropic transmission function is not considered. This correction to the transmission function can be calculated analytically and is well understood. It has a negligible effect on the squared neutrino mass measured in KATRIN, if it is fully implemented in the analysis model. When this is not the case, a significant error on m_ν^2 can be introduced. For the final neutrino mass analysis, it is therefore very important that the full implementation is guaranteed.

4.2.6. Analysing Plane: Potential and Magnetic Field

Description. The transmission function of a MAC-E filter as given in equation 3.6 is only an approximation. As discussed in this chapter, several corrections have to be applied, for instance the relativistic corrections (see section 4.2.2), a modified angular distribution of the electrons (see section 4.2.5), or the synchrotron radiation losses (see section 4.2.3). However, even after implementing all these corrections, there is not a single transmission function describing all electrons in the MAC-E filter at once. The reason is that the magnetic field and the electric potential are not homogeneous over the cross-section of the spectrometer, but they both show a radial dependence [Gro15; Erh16]. That means that there is no single analysing plane in the middle of the spectrometer at which the longitudinal energy of every traversing electron is minimised. In reality, there are analysing points, and electrons with different trajectories through the spectrometer volume have their analysing point at different z positions. Even electrons with the same trajectory have their analysing points at different z positions depending on their polar angle to the magnetic field lines. In order to account for the different transmission conditions for electrons at varying analysing points and with different polar angles, the inhomogeneities of the magnetic field and the electric potential in the spectrometer volume have to be known precisely and have to be included into the model for the neutrino mass analysis.

Experience from former neutrino mass experiments. The Mainz and Troitsk experiments, which used MAC-E filters, did not consider the effect of radial inhomogeneities of the magnetic field and the electric potential in their analysis. However, in Mainz a ring-segmented detector was in operation. The inner three rings of the detector were used for the analysis, but apparently without radial corrections [Kra05]. Neither the Livermore nor the Los Alamos group used a MAC-E filter. However, they both used a segmented detector [Rob91; Sto95]. The field configurations of the apparatuses were summarised in a so-called resolution function. The Los Alamos group mentions differences in the resolution functions for different detector segments explicitly as (small) uncertainty contribution to their systematic uncertainties budget [Rob91]. However, the instruments of the former neutrino mass experiments were much smaller than KATRIN so that radial effects could not become as relevant.

Determination for KATRIN. The KATRIN detector is divided into 148 pixels, which are assembled in 12 rings and a bullseye (see also section 3.2.7). Thus, it offers possibilities to correct radial dependencies, and to precisely measure them with an electron gun [Gro15; Erh16; Beh17a]. Based on simulations [Gro15], the total electric potential inhomogeneity is estimated to about 400 mV for KATRIN Design Report conditions (see figure 4.6). This means that, across any given pixel, a difference of 30 mV is mapped from its inner to its outer boundary, on average. This potential difference cannot be resolved further with the current KATRIN setup, so that this is the benchmark for the precision on the radial potential. The radial potential offset can be measured experimentally [Gro15; Erh16]: with an egun, different trajectories of electrons are tested, so that different pixels at the detector are hit. For every pixel hit and every egun position, a transmission function

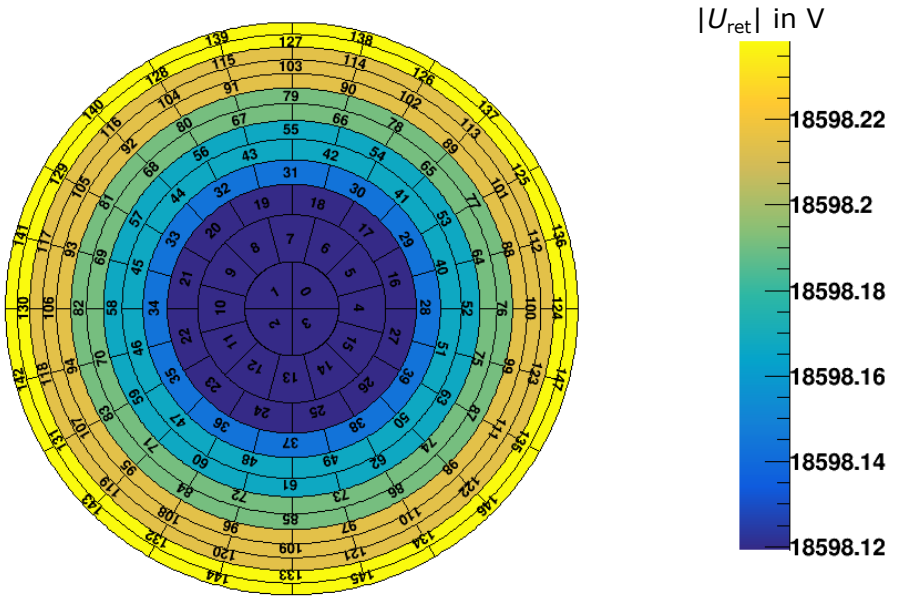

Figure 4.6.: Retarding potential in the analysing plane. The figure shows the simulated retarding potential in the analysing plane mapped on the focal plane detector. The simulation was performed for the KATRIN first tritium campaign in spring 2018 with a magnetic field of 6×10^{-4} T in the analysing plane. This explains why the inhomogeneity is less than the 400 mV mentioned in the main text, as the spectrometer volume mapped on the detector is smaller. The simulations have to be verified by pixel-wise transmission function measurements with the rear section egun or the condensed ^{83m}Kr source.

is measured. The analysing point is determined with the field simulation and tracking software Kassiopeia (see section 3.3). All egun parameters (energy spread, angular spread, etc.) are taken into account for the fit of the transmission function or are determined as fit parameters. The radial voltage value is determined as a free fitting parameter. This voltage value based on experimental measurements in the next step is compared to the result with a simulated voltage value for the same analysing point obtained in a full 3D electromagnetic field calculation. The standard deviation over the differences of all pairs of simulated and measured voltage values is taken as a measure of the precision of the radial voltage distribution obtained. The result for a magnetic field in the analysing plane of 3.8×10^{-4} T and a voltage set point of -18.6 kV is $\sigma_{\text{U}_\text{r}} = 14$ mV [2] [Erh16]. The stated values were derived in stand-alone measurements of the main spectrometer and detector section and need to be confirmed with the rear section egun and all KATRIN beam line magnets in operation. It should be noted here that a shift of the absolute potential value, adding the same voltage shift ΔU at every radial position, does not influence the neutrino mass result at all. It is absorbed in a shift of the effective endpoint of the beta decay spectrum E_0, as long as E_0 is also a free parameter in the neutrino mass fit [Gro15].

For the magnetic field in the analysing plane, first requirements were formulated in [Gro15]. In contrast to the electrostatic potential, the absolute value of the magnetic field in the analysing plane has a large influence on the neutrino mass fit result, since it influences the width of the transmission function directly. Thus, simulations demonstrated that it has to be determined very precisely with a relative trueness of $\Delta B_{\text{ana}}/B_{\text{ana}} = 5.5 \times 10^{-3}$ at 3.6×10^{-4} T. The same benchmark has to be applied for the determination of radial inhomogeneities. The magnetic field in the analysing plane is determined like the potential

[2] The uncertainty reduces to 6.2 mV, if the magnetic field is fixed. Since both the magnetic field and the potential inhomogeneities are determined in a combined fit, their correlations are taken into account, which increases the fit uncertainty.

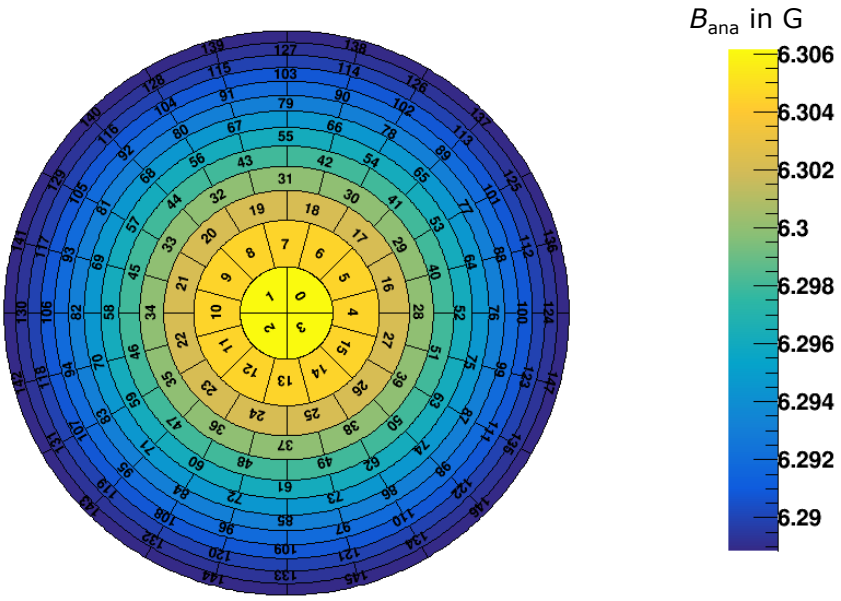

Figure 4.7.: Magnetic field in the analysing plane. The figure shows the magnetic field strength in the analysing plane mapped on the focal plane detector. The values were simulated for the first tritium measurement campaign in spring 2018 for a set value of 6×10^{-4} T in the analysing plane. The simulations have to be confirmed by pixel-wise transmission function measurements with the rear section egun or the condensed ^{83m}Kr source in the near future.

described above with egun measurements. Several transmission functions are recorded for different polar angles of the electrons to the magnetic field lines. The magnetic field is then an additional fit parameter in a global fit of the transmission functions. Compared to 3D simulations, the maximal deviation of 2 µT for a field of 3.8×10^{-4} T was proven for the magnetic field in the center [Erh16]. However, the measured radial inhomogeneity could not be reproduced by the simulations, because the alignment of the egun setup and the spectrometer section was not implemented correctly in the model. Figure 4.7 shows the radial magnetic field strength in the analysing plane as simulated for the operating conditions of the First Tritium campaign in 2018. The experimental verification of this model is still to be done for the full KATRIN beam line in operation as soon as the commissioning of the rear section egun is finished.

In contrast to the electrostatic potential, the magnetic field in the analysing plane experiences shifts, fluctuations and inhomogeneities from magnetic stray fields from inside and outside of the main spectrometer building. In measurements with the mobile sensor units (see section 3.2.5), it was found that the magnetised steel of the building walls has an influence on the field in the analysing plane [Erh16]. Such effects can only be measured and modelled to a certain extent, so that they add a systematic uncertainty to the magnetic field in the analysing plane.

Impact on neutrino-mass determination. In this work, three effects associated with the potential and magnetic field in the analysing plane are ensemble-tested which are the trueness of the absolute magnetic field and the uncertainties on the radial inhomogeneities of the magnetic field and the potential. The absolute values of the radial inhomogeneities are set according to [Gro15]. The uncertainties of the radial inhomogeneities were determined in [Erh16] to 21 mV for the electric potential and to 2 µT for the magnetic field strength. The results of the ensemble tests based on these boundary parameters are presented in table 4.8. The results from [Gro15] are reproduced roughly. Differences may be explained

Table 4.8.: Neutrino mass shifts associated with the electric and magnetic fields in the analysing plane. The table lists the neutrino mass shifts linked to the uncertainties for the determination of the electric potential (U_{ana}) and magnetic field strength (B_{ana}) in the analysing plane for KATRIN Design Report conditions (see table 4.1). The last row shows the result for an ensemble test when both the uncertainties of the magnetic field and electric potential are considered at the same time.

Effect	Δm_ν^2 in $10^{-3}\,\mathrm{eV}^2/c^4$ ([Gro15])	Δm_ν^2 in $10^{-3}\,\mathrm{eV}^2/c^4$ (this work)
Trueness B_{ana}	± 2.5	± 2.5
B_{ana} radial	-0.2	-0.8
U_{ana} radial	-0.6	-0.1
Radial combined	-	-0.3

by differing ensemble test parameters; in [Gro15] a slightly different magnetic field strength of $3.6 \times 10^{-4}\,\mathrm{T}$ was used, for instance.

There are further uncertainties linked to the magnetic field in the analysing plane as described in [Erh16]. For instance, the influence of stray fields in the analysing plane cause an additional shift of the neutrino mass. However, the magnetic field measurement system was upgraded in the meantime to be able to implement these stray fields coming from the building walls in the magnetic field model [Let18]. These effects should only add a correction of the neutrino mass on the order of $10^{-4}\,\mathrm{eV}^2/c^4$ [Erh16] and new results are expected in the nearer future.

Relevance for KATRIN and current status. Both the potential and the magnetic field in the analysing plane are very important input parameters for the analysis model of KATRIN. If the radial dependencies of the electromagnetic field are not considered, errors much larger than the total systematic budget of KATRIN of $0.017\,\mathrm{eV}^2/c^4$ are introduced [Kle18a]. Both effects have not been taken into account in the first systematic uncertainty estimation in the KATRIN Design Report [Ang05]. However, the investigations outlined above have demonstrated that the radial inhomogeneities of the electrostatic potential and the magnetic field in the analysing plane can be determined on a sufficient level to keep the associated systematic uncertainty reasonably small. Compared to the results in [Erh16], the possibilities of magnetic field monitoring have been improved in the meantime. Two additional mobile magnetic field monitoring devices have been mounted which perform scans along the spectrometer building walls to improve the implementation of their stray fields into the simulations [Erh18; Let18]. Another mobile sensor unit is currently being set up and will be operable in 2019. Thus, it is expected that the uncertainty contribution will be further reduced, so that it is well under control and only a minor contribution to the overall uncertainty budget.

Since the radial inhomogeneities used for the ensemble tests in this thesis are still based on the measurements in [Gro15; Erh16], a new experimental determination should be performed before the regular tritium operation of KATRIN starts. This will be done with the rear section egun and the condensed ^{83m}Kr source in order to provide important reference points for the detailed numerical models.

4.2.7. HV Stability

Description. As described in section 3.4.1, the neutrino mass squared is measured by varying the retarding voltage of the KATRIN main spectrometer at the kinematic endpoint of the tritium beta decay. The mass is imprinted on the shape of the spectrum. Thus, the

voltage itself is a source of systematic uncertainty due to the close connection of the high voltage with the energy scale. Any voltage imperfection can lead to a spectrum distortion with direct impact on the neutrino mass result if not considered in the analysis. Since the effective endpoint of the tritium spectrum is fitted as a free parameter (see section 3.4.1), it absorbs the absolute voltage value, which is therefore not required to be known precisely. However, the stability of the high voltage is critical: if there are unaccounted for fluctuations or drifts during a KATRIN measurement run, the shape of the beta-electron spectrum is affected [Ang05]. Thus, the high voltage has to be stabilised to reduce such effects to a minimum. A highly precise monitoring system is required to be able to measure the remaining voltage imperfections in order to take them into account for the final neutrino mass analysis.

Experience from former neutrino mass experiments. In the Troitsk experiment, the instability of the retarding voltage is one of the four major systematic effects [Ase11]. During the neutrino mass runs, voltage set points were only accepted if they were within $\pm 0.2\,\mathrm{V}$ around the nominal voltage value, which corresponds to a high voltage stability at 18.6 keV of $\approx 1 \times 10^{-5}$. The Mainz group selected even more strictly: only if the difference between the voltage set point and the nominal value was smaller than 0.1 V, the run was accepted [Kra05]. Therefore, the influence of the high voltage stability on the neutrino mass was reduced, so that its uncertainty contribution could be neglected in the final analysis.

Determination for KATRIN. The requirement for the high voltage stability is formulated in the KATRIN Design Report to be 3 ppm which equals fluctuations of 60 mV at a retarding voltage of $-18.6\,\mathrm{kV}$. This cannot be achieved without an active post-regulation system, which is described in detail in [Kra16]. The post-regulation system separates the AC component from the DC component of the high voltage via a capacitor, and both components are measured separately:

- The AC component is measured with a ripple probe. The high-voltage ripple is amplified and fed to a regulator, which controls the AC voltage that is applied to the main spectrometer to counterbalance the measured high-voltage fluctuations as part of the post-regulation system. Before it is amplified, the AC signal can be read out manually with an oscilloscope [Rod18]. With this system, the high-voltage ripple is reduced significantly, and mainly noise remains with $\sigma_{\mathrm{AC}} = 16\,\mathrm{mV}$ [Kra16]. Figure 4.8 shows a dataset from May 2018 recorded with an improved setup of the post-regulation system in comparison to [Kra16]. The noise is now even more reduced to $\sigma_{\mathrm{AC}} = 6\,\mathrm{mV}$ at a voltage of $-18.4\,\mathrm{kV}$.
- The DC component of the high voltage has a value of $\approx -18.6\,\mathrm{kV}$ and therefore cannot be measured directly with the required precision [Kra16]. Thus, a precision voltage divider is required to scale down the high voltage via precision resistors to $\approx 10\,\mathrm{V}$. Two custom-built precision dividers are available for KATRIN [Bau13b; Thü09]. The voltage is finally measured with a precision digital voltmeter [Bau13b]. As discussed below, the voltage divider has an excellent long-term stability [Are18a]. However, the measured DC value is not stable, but shows small fluctuations of $\sigma_{\mathrm{DC}} = 16\,\mathrm{mV}$ over a 5-minute interval which are caused by the post-regulation system and temperature fluctuations in the experiment hall [Kra16].

If both contributions are summed up quadratically, a total uncertainty on the high-voltage measurement of $\sigma_{\mathrm{tot}} = 23\,\mathrm{mV}$ is derived for the values obtained in [Kra16]. With the reduced noise of 6 mV in the AC component, the total uncertainty reduces to $\sigma_{\mathrm{tot}} = 17\,\mathrm{mV}$. Both results demonstrate that the post-regulation system works a factor of ≈ 3 better than the requirement.

To be able to measure these small fluctuations of the high voltage, the involved hardware

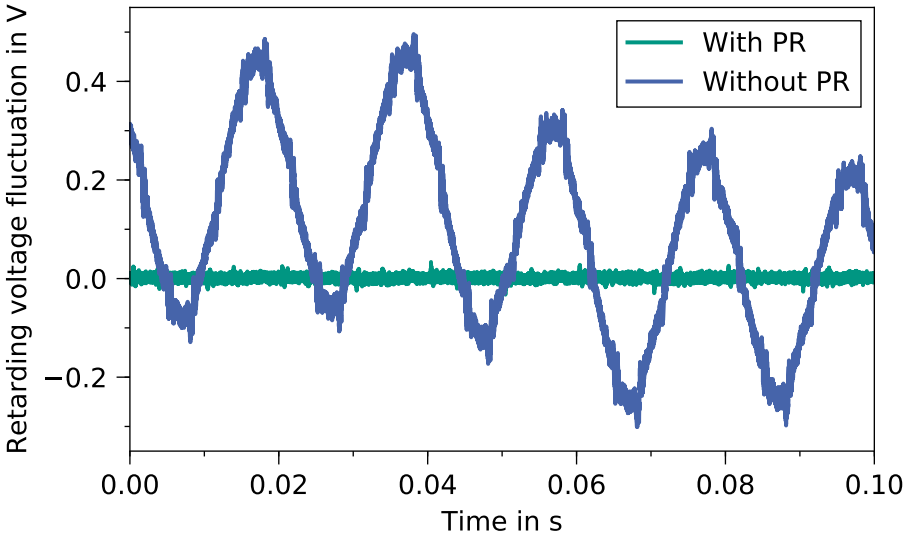

Figure 4.8.: Impact of the active post-regulation system on the high-voltage stability. The plot shows the high voltage fluctuation with and without active post-regulation (PR). Without post-regulation, the dominant contribution to the fluctuations is the 50 Hz AC voltage of the mains. This signal is completely removed and the voltage is smoothed with active post-regulation to a remaining noise value of $\sigma_{\mathrm{AC}} = 6\,\mathrm{mV}$. Data kindly provided by C. Rodenbeck.

has to be ultra-stable, too. The main challenge is that the scaling factor of the high voltage divider stays constant over time and that all the contacts and cabling of the precision resistors is done in a way that no further fluctuations are introduced [Bau13b; Thü09]. Additionally, the voltmeter has to be stable and should not show any drifts. This is guaranteed by regular calibrations, so that the influence of the voltmeter on the high voltage uncertainty is negligible [Rod18]. Also the scaling factor of the high voltage divider has to be calibrated in regular time intervals. Recently, during the ^{83m}Kr campaign described in chapter 5, a new calibration method was demonstrated successfully [Are18c]. It was shown that the scaling factor of the voltage divider has not changed significantly over four years. This means it can be assumed to be totally stable during KATRIN runs which are on the order of hours. With the new method, the scaling factor is determined with $< 5\,\mathrm{ppm}$ precision. It should be noted that this precision limits the determination of the absolute voltage value. For the stability determination, it is only of importance that the scaling factor stays constant over time. Hence, the requirements are fulfilled.

The DC component of the high voltage can also be measured with a second device, the monitor spectrometer (see section 3.2.6). The monitor spectrometer is coupled to the high voltage of the main spectrometer and determines the voltage value via the scanning of the position of the K-32 conversion electron line of ^{83m}Kr, which serves as nuclear standard [Erh14; Sle15]. Since the ^{83m}Kr atoms are implanted into a solid substrate [Are17], the work function difference between the monitor and the main spectrometer make it impossible to measure the absolute voltage value. However, the stability and time-dependent drifts can be measured precisely with $\Delta V = 15\,\mathrm{mV}$ in 15 minutes [Sle15]. This result fulfils the KATRIN requirement and is independent of the voltage-divider method.

Impact on neutrino-mass determination. The KATRIN Design Report states a systematic uncertainty budget of $m^2_{\nu,\,\mathrm{HV}} = 5 \times 10^{-3}\,\mathrm{eV}^2/c^4$ for HV variations of 3 ppm [Ang05].

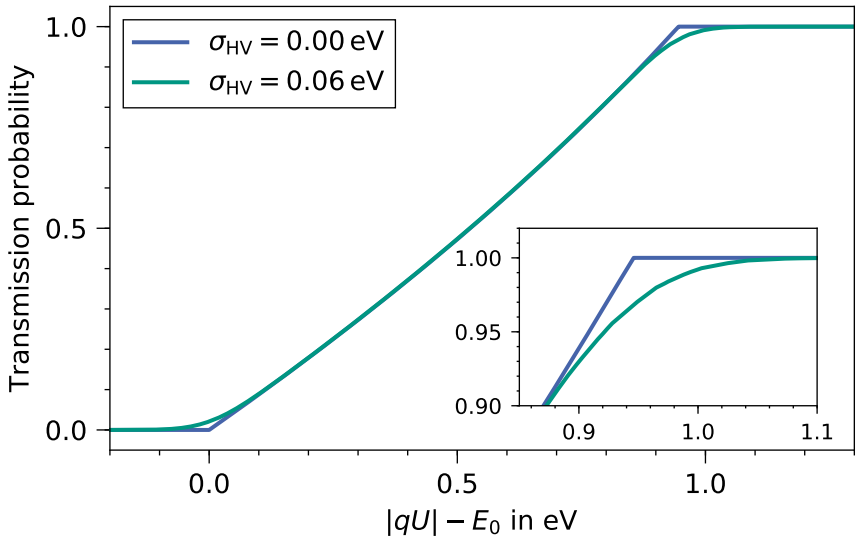

Figure 4.9.: Impact of the high-voltage fluctuation on the KATRIN transmission function. The plot shows the non-relativistic transmission function for electrons with an energy of $|qU| = 18575\,\mathrm{eV} = E_0$ and KATRIN nominal magnetic fields ($B_{\mathrm{WGTS}} = 3.6\,\mathrm{T}$, $B_{\mathrm{max}} = 6.0\,\mathrm{T}$, $B_{\mathrm{ana}} = 3.0 \times 10^{-4}\,\mathrm{T}$). The Gaussian high-voltage fluctuations of 60 meV as assumed in the KATRIN Design Report [Ang05] smooth the transmission edge at both sides and lead to a broadening. The inset shows a close up. The plotted data is generated with KaFit/SSC.

In an analytical estimation, the fluctuations σ_{HV} are translated into a neutrino mass shift via [Rob88]

$$\Delta m^2_{\nu,\,\mathrm{HV}} = -2\,\mathrm{e}^2/c^4 \cdot \sigma^2_{\mathrm{HV}}\ . \tag{4.17}$$

This reflects the smoothing and broadening of the transmission edge at both sides as illustrated in figure 4.9. Based on the data set shown in figure 4.8 with a total uncertainty of $\sigma_{\mathrm{tot}} = 17\,\mathrm{mV}$, the impact on the neutrino mass is

$$\Delta m^2_{\nu,\,\mathrm{HV}} = -0.6 \times 10^{-3}\,\mathrm{eV}^2/c^4 \tag{4.18}$$

which is nearly one order of magnitude better than estimated by the KATRIN Design Report.

Relevance for KATRIN and current status. The high voltage stability is well under control as a systematic effect of KATRIN. It only adds a minor contribution to the overall systematic uncertainty budget. However, the technical implementation of such a stable high voltage system is challenging, and continuous research of more than one decade was necessary to achieve the stable voltage supply with the post-regulation system, but also to develop monitoring devices which are precise and stable enough to measure the remaining tiny voltage fluctuations. As demonstrated in figure 4.8 and in [Kra16; Rod18], KATRIN cannot keep its systematic budget without the active post-regulation. Furthermore, the monitoring devices have to be calibrated periodically in order to avoid undetected drifts over time and to keep the neutrino mass shift stated in equation 4.18.

During the ^{83m}Kr measurements, which are described in more detail in chapter 5, it was possible to measure the high voltage ripple with the focal plane detector by analysing the rate over small time scales of ms. The fluctuations found are compatible with the fluctuations of the high voltage measured with the ripple probe. This means that the

high-voltage fluctuations are not only a phenomenon on the hull of the main spectrometer vessel where the ripple probe is attached, but that these fluctuations actually do affect the transmission of electrons and thus are a real systematic effect. With further measurements with ^{83m}Kr (gaseous or condensed source) it may be possible in the future to map the high-voltage ripple onto the detector and to measure if electrons traversing the inner volume of the main spectrometer are affected differently by the high-voltage fluctuation than electrons traversing closer to the vessel walls[3].

Finally, it should be emphasised again that the neutrino mass shift stated in equation 4.18 is only valid for measurements in which the voltage set point is kept stable for 5 minutes. For smaller time scales, the neutrino mass shift is also smaller and it is larger for larger time scales. As mentioned above, the reason is that the voltage measured with the voltage divider shows fluctuations which are correlated to the temperature of the experiment hall. The time scale of these oscillations is on the order of one hour. Therefore, the associated neutrino mass shift can change depending on the measurement strategy which is finally selected for KATRIN.

4.2.8. Detector-Related Effects

Description. The KATRIN detector is a *p-i-n* silicon detector with 148 pixels. Its design and the concept of the overall KATRIN detector system has been introduced already in section 3.2.7 and for details the reader is referred to [Ams15]. In this section, the focus is put on the actual detecting process and how the detector itself impacts the neutrino mass result via systematic effects. An electron hitting the detector creates electron-hole pairs, which are separated due to an electric field applied. The charge carriers are driven to the electrodes and induced charges on the electrodes make the signal which can be shaped. Energy entries in the region of interest (see equation 5.4) are counted as physical events. For the individual electron detection it is mandatory that the incident electron loses most of its energy in the so-called depletion zone. Near the surfaces at both sides of the detector, the depletion zone weakens and the p and n doping predominates, so that free charge carriers are available [Ren11]. Charge carriers created by the signal electron in these regions have a large probability to recombine. Therefore, dead layers are formed on the order of 100 nm in thickness, in which an event is not detected, or only with reduced energy.

The dead layer is responsible for several effects which make the detector efficiency dependent on properties of the incident electron. Thus, the spectral shape of the tritium beta decay can be changed, which causes systematic uncertainties. These effects and properties are the following [Ren11]:

- The larger the incident angle of the electrons on the detector, the longer their way through the dead layer becomes. Therefore, electrons with a larger incident angle have a larger probability to be detected with reduced energy. Thus, the detection efficiency depends on the angle of incidence and on the region-of-interest cut applied.
- Electrons with larger energies deposit most of their energy deeper in the detector material than electrons with smaller energy. Therefore, electrons with smaller energy lose a larger fraction of energy in the dead layer than electrons with more energy, so that the detection becomes dependent on the incident energy.
- In order to keep all the detrimental effects as small as possible, the dead layer should be narrow. During operation, its width can increase due to gas molecules sticking to the cold surface, so that a regular monitoring should be performed.

[3] S. Enomoto, C. Rodenbeck, internal talk, 35th KATRIN Collaboration Meeting, 2018.

Besides dead layer effects, also backscattering of electrons has to be considered carefully [Ren11; Kor16]. Electrons hitting the detector scatter off the silicon atoms. In the scattering processes they change direction, so that they have a non-zero probability to leave the detector and travel back towards the spectrometer. There, they are reflected by the magnetic fields and the retarding potential so that they reach the detector again. This process can be repeated several times, so that one electron can cause multiple events on the detector. These are counted separately if the electron hits different pixels or if the travel time is larger than the event separation time of the detector. Since the backscattering probability depends on the electron kinematics (incident angle and energy), this effect can cause a distortion to the spectrum and therefore has to be investigated as systematic uncertainty.

As the backscattered electrons increase the rate registered by the detector, there is a higher probability for further systematic effects: pile-up and charge sharing [Ams15]. There are two sorts of pile-up, the peak pile-up and the tail pile-up. The former means that two electrons hit one pixel within such a short time interval that they are not counted as separate events but as one with the combined energy. Tail pile-up means, that the tail of one event signal is overlaid by another signal, so that a wrong energy for the second signal is recorded. The probability for tail pile-up is small in standard KATRIN operation since the count rates are on the order of $\approx 1\,\mathrm{cps/pixel}$ and the signal tails are on the order of $1\,\mathrm{ms}$[4]. Since for the neutrino mass analysis only electrons in the region of interest are counted, the pile-up can influence the recorded rate by shifting events outside of this region of interest [Blo18]. Charge sharing describes multiple-pixel events, where the electron hits one pixel close to the pixel boundary, so that parts of the charges flow to neighbouring pixels. The total energy of the electron is then shared by the firing pixels, so that the event can be shifted outside the region of interest. Charge-sharing events are mimicked by backscattered electrons which are reflected to a neighbouring pixel by the magnetic fields and potential of the main spectrometer.

Experience from former neutrino mass experiments. The former direct neutrino mass experiments also used silicon detectors but with fewer pixels than the KATRIN detector. However, the treatment of the detector systematic uncertainties differs a lot. The Los Alamos experiment observed a small dependence of the efficiency of their apparatus with the acceleration voltage, but this is not explicitly related to the detector [Rob91]. For the Troitsk experiment, pile-up effects of their detector are reported for the tritium beta spectrum below 18.4 keV. However, since the analysis is done closer to the tritium endpoint, detector systematics are neglected for the neutrino mass result [Ase11]. The Livermore group has chosen a setup in which the electrons hit the detector always with the same energy, so that effects of an energy-dependent response are ruled out [Sto95]. Detailed studies to the systematic effects of the detector were done in the Mainz experiment [Kra05]. The energy-dependent efficiency was determined and included into the analysis as a small systematic uncertainty.

Determination for KATRIN. The KATRIN detector section equipment (see section 3.2.7) comprises calibration sources which allow for the determination of the detector efficiency. It was found to be $95.0\,\% \pm 1.8\,\%_{\mathrm{stat}} \pm 2.2\,\%_{\mathrm{sys}}$ for 18.6 keV electrons [Ams15]. Also the dead layer thickness of the detector was measured, and a value of $(155.4 \pm 0.5 \pm 0.2)\,\mathrm{nm}$, somewhat larger than specified by the manufacturer, was found [Wal13; Ams15]. Since the systematic effects related to the detector efficiency and dead layer outlined above exhibit a mutual influence, detailed simulations are crucial to understand and quantify them[5] [Ren11].

[4] Personal communication S. Enomoto, Dec 7, 2018.
[5] Personal communication S. Enomoto, Dec 4, 2018.

For an experimental characterisation, a stable and high-luminosity electron source is necessary as the effects described are expected to be small. KATRIN has several sources available and foreseen for this purpose, for instance the gaseous ^{83m}Kr source and the rear section egun.

Impact on neutrino-mass determination. Simulations have been performed to investigate the effect of backscattering, pile-up and space-charging at the focal plane detector[6]: the results indicate that the effects are small or even negligible. Furthermore, measurements during the gaseous ^{83m}Kr campaign (see chapter 5) were performed: the source magnetic field was decreased to 50 % of its nominal strength while the other magnets in the beam tube were kept at 70 %. This changes the pitch angle distribution of the electrons hitting the detector, and from simulations a small change of the transmission function of the main spectrometer was expected due to the detector-related systematics. The observed effect of the transmission function of L_3-32 conversion electrons (see table 5.2) was larger than simulated[7]. As long as the simulations and measurements do not agree, no neutrino mass shift value can be associated to the detector-related systematic uncertainties.

Relevance for KATRIN and current status. Detector-related systematics seem to have only a minor influence on the neutrino mass analysis in KATRIN. Although simulations show that the systematic effects like pile-up, charge-sharing and backscattering should only have a small or even negligible impact, the simulations still need a verification by a measurement. So far, the performed measurements and simulations do not agree. When the effects are fully understood, they can be implemented in the analysis model to reduce the impact on the neutrino mass even further. Further investigations are currently ongoing.

4.2.9. Ions

Description. In each beta decay of molecular tritium, an electron antineutrino, an electron and a positive HeT^+ ion is created. Via ionisation of the residual gas in the tritium source, further pairs of charged ions and electrons are formed. If the low energy electrons combine with a neutral molecule, also negative ions occur, and if now the ions scatter off each other or off neutral molecules, all kinds of ions can be produced: $T^+, T^-, T_3{}^+, T_3{}^-, T_5{}^+$, etc. [Kle18b] These ions cause problems in direct neutrino mass experiments with gaseous tritium: the final-state distribution of the ions is different from the one for the neutral hydrogen isotopologues T_2, DT, HT [Ang05]. Depending on the analysing window at the kinematic endpoint region of the beta decay, these additional final-state branches have to be taken into account. Another shift of the endpoint can occur, if the ions form space-charge regions. Beta electrons created in space-charge regions gain or lose energy when they leave the potential well. As charged particles, ions are guided along the magnetic field lines towards the spectrometers. If they decay inside the spectrometer volume, the decay electrons can ionise the residual gas and secondary electrons may lead to an increase of background. If the negative ions do not decay, they are reflected by the retarding potential, since they have too low energies to pass it. They travel back towards the tritium source, where they are decelerated by the gas flow and back-reflected towards the spectrometer. Thus, they get trapped. Plasma instabilities might occur, which come along with a time-dependent electric field which would change the energy of beta electrons travelling from the source towards the spectrometer [Ang05]. These effects are discussed in more detail in [Kle18b].

[6] Personal communication M. Korzeczek, Dec 6, 2018.
[7] F. Block, S. Enomoto, M. Korzeczek, internal talk, KATRIN analysis workshop, Aug 07, 2017.

Therefore, several countermeasures have to be applied [Kle18b]: monitoring tools are needed to identify the different ion species and to quantify them. Blocking devices are necessary which prevent ions from reaching the spectrometer section, and trapped ions have to be removed. The ions and the countermeasures introduce systematic effects and uncertainties which have to be taken into account in the neutrino mass analysis.

Experience from former neutrino mass experiments. The Los Alamos investigated whether tritium ions were trapped in the source, but did not find any evidence [Rob91]. The Livermore experiment had its source on a potential of +5 kV. This did not reduce the tritium contamination of the spectrometer, but electrons coming from beta decays inside the spectrometer volume could be cut due to their lower energy [Sto95]. Ion-related systematic uncertainties do not enter the final result of the Troitsk experiment [Ase11].

Determination for KATRIN. As simulations have shown, the flow of tritium ions towards the spectrometer is several orders of magnitude larger than the flux which could be tolerated in terms of background [Ang05]. Thus, several instruments have been mounted in the KATRIN beam tube to detect and block the different ion species: several short ring electrodes are inserted in the beam line to which a positive voltage is applied to block positive ions on their way to the spectrometer. Dipole electrodes in the DPS drift the ions to the walls, where they are neutralised. Thus, the ions cannot get trapped. Additionally, Fourier transform ion cyclotron resonance (FT-ICR) devices monitor and quantify the ion composition (for all the countermeasures mounted in the DPS, see also section 3.2.7). These measurements can be verified with a Faraday cup mounted to the forward beam monitor, see section 3.2.4.

However, these countermeasures do not only decrease the amount of ions in the beam line, so that space charge/plasma effects and the smearing of the endpoint region of the spectrum are reduced to a minimum. They also introduce systematic effects themselves [Kle18b]: the tritium density inside the DPS is not zero. Beta electrons which are created inside the volume of a dipole electrode get additional energy due to the negative potential applied. Their kinematic endpoint is therefore shifted towards higher energies. Added to the tritium spectrum from the WGTS, a smearing of the endpoint region occurs which has a direct influence on the neutrino mass result. Therefore, the voltage applied to the dipole electrodes has to be optimised in a way that on the one hand the influence on the neutrino mass result is minimised, but on the other hand the ions coming from the WGTS are still removed efficiently. The second systematic effect related to the dipole electrodes is the stability of the applied voltage. If the voltage is unstable, electrons passing through a dipole electrode gain or lose a small amount of energy. This is comparable to the influence of the ripple of the high voltage in the main spectrometer, see section 4.2.7. To minimise this effect, a voltage supply with a small voltage ripple of 2 mV peak-to-peak is installed. Finally, propagating electrons experience an $\vec{E} \times \vec{B}$ drift when they pass the dipole electrodes, being shifted by $< 43\,\mu\text{m}$ in radial direction [Kle18b]. Thus, the $\vec{E} \times \vec{B}$ drift influences the mapping of electrons from the WGTS onto the focal plane detector.

Impact on neutrino-mass determination. In the KATRIN Design Report, a neutrino mass shift of $0.1 \times 10^{-3}\,\text{eV}^2/c^4$ is assigned to the influence of T^- ions on the endpoint region of the molecular spectrum [Ang05]. Their relative amount is estimated to $n(T^-)/n(T_2) = 2 \times 10^{-8}$. For the other systematic effects described above, no estimations of the neutrino mass shifts are currently available. Therefore, the overall contribution of ion-related effects to the total systematic budget of KATRIN is unknown at the moment and cannot be quantified in the scope of this thesis.

Relevance for KATRIN and current status. A functioning ion detection and removal system is crucial for the success of KATRIN because otherwise the strict requirements on the systematic uncertainties cannot be kept. However, the combination of the different ion-related sensors and subsystems is not trivial and the correct implementation in the analysis is very complex. Therefore, the first tritium campaign in spring 2018 was a good opportunity to test the ion blocking and detecting devices [Kle18b]. However, the systematic effects outlined above still need a quantification. Comprehensive simulation studies as well as possible test measurements with the rear section egun or ^{83m}Kr have to be designed and performed to determine the influence of ion-related systematic uncertainties on the final neutrino mass analysis. Further investigations are currently ongoing [Rei19; Kel20].

4.2.10. Backscattering at the Rear Wall

Description. Electrons which are emitted towards the rear side of the WGTS can be reflected by the rear wall and afterwards cross the entire beam line to impinge onto the detector. This effect is especially relevant for electrons which are created with an angle of their momentum to the magnetic field lines larger than the acceptance angle (see equation 3.5). They may change their angle and their energy due to the scattering off the rear wall, so that afterwards they are able to reach the detector. These additional electrons influence the shape of the spectrum and therefore have to be considered in the analysis [Ang05].

Experience from former neutrino mass experiments. Since the backscattering is a function of the atomic number Z, in the Mainz experiment graphite with $Z = 6$ was selected as substrate for the quench-condensed tritium film to keep the influence of this effect as low as possible [Kra05]. A linear function with a correction factor of $3.1 \times 10^{-5}\,\mathrm{eV}^{-1}$ was applied to the spectrum to take the small correction by this effect into account.

There are no published results on backscattering from experiments with gaseous sources.

Determination for KATRIN. The rate of backscattering at the rear wall can only be estimated in simulations. In KATRIN, the rear wall is a gold-coated stainless steel plate, so that $Z = 79$ and a larger influence than in Mainz can be expected. However, after being scattered off the rear wall, the electrons have to traverse the full column density of the WGTS, so that they have a large probability to scatter inelastically at least once. Thus, it is assumed that backscattered electrons do not affect the tritium spectrum in the KATRIN analysis interval down to 30 eV below the endpoint [Ang05]. This is confirmed in simulations [För17].

Impact on neutrino-mass determination. Since the effect is considered to be negligible, no sizeable neutrino mass shift is associated with it.

Relevance for KATRIN and current status. Although the backscattering off the rear wall is not a relevant effect for standard KATRIN operation, it is of importance for the keV-sterile neutrino search, when the complete spectrum has to be understood in each and every detail. Therefore, several countermeasures have been investigated in simulation studies [För17].

4.2.11. Source Magnetic Field

Description. In order to guide the beta decay electrons from the source to the detector, the source has to be placed in a magnetic field. This source magnetic field strength determines some of the major characteristics of neutrino mass experiments with MAC-E filters: It

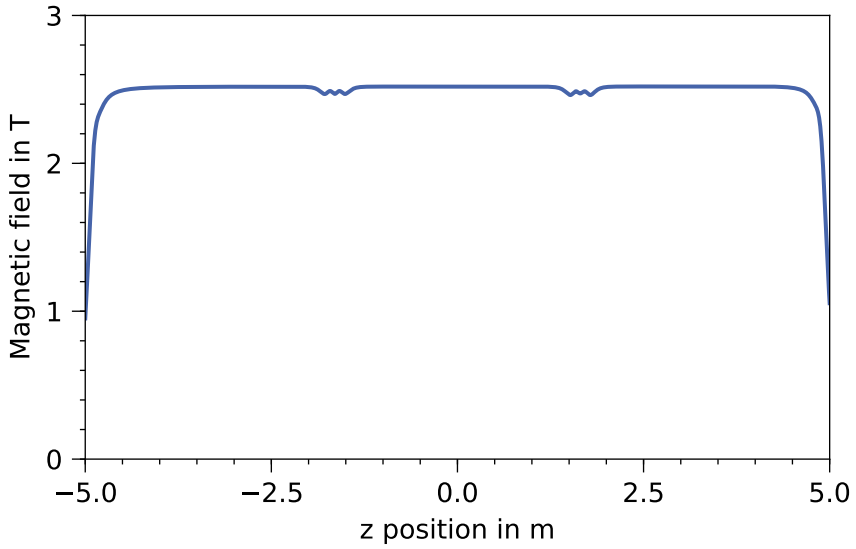

Figure 4.10.: Magnetic field of the WGTS. The plot shows the magnetic field strength inside the WGTS central beam tube for KATRIN standard operation (70 % of nominal magnetic field value) simulated with Kassiopeia. The z position is shown relative to the middle of the WGTS central beam tube. The small dips at $\approx \pm 1.5$ m are the gaps between the three superconducting coils of the central beam tube. In order to reduce the decrease of the magnetic field strength in these gaps to a minimum, correction coils are mounted there. Towards the pump ports the magnetic field strength drops drastically at both sides of the central beam tube.

directly enters the transmission function of the MAC-E filter (see equation 3.6) and the maximum acceptance angle due to the magnetic mirror effect (see equation 3.5). If the maximum acceptance angle $\theta_{\max}$ changes, also the scattering probabilities in the source change: if $\theta_{\max}$ gets smaller, only electrons with a smaller path length through the source are accepted, so that the probability to reach the detector unscattered is increased, while the probabilities for n-fold scattering are decreased (see equation 4.27). These modified scattering probabilities together with the different shape of the transmission function, influence the response function of the MAC-E filter (see figure 4.5) and the rate at different retarding potentials. Therefore, unaccounted for inhomogeneities, fluctuations and drifts of the source magnetic field influence the neutrino mass result and should be included in the analysis.

Experience from former neutrino mass experiments. In former neutrino mass experiments, the uncertainty and stability of the source magnetic field was neglected since they were dominated by other, much larger systematic effects.

Determination for KATRIN. For KATRIN, three aspects of the source magnetic field strength have to be investigated, which are the stability in time, the homogeneity along the WGTS beam tube and the trueness of the absolute value. The WGTS cryostat comprises seven superconducting solenoids [Are18c]. Three power supplies provide the current for the magnets, one for the magnets M1-3, one for M4 and M5 and one for M6 and M7 (see figure 3.3). For the determination of the magnetic field stability, the readout of the power supplies can be used. Furthermore, each power supply is monitored additionally by a current clamp. And finally, in every superconducting solenoid one Hall sensor is mounted. Thus, several measurement possibilities are provided to double-check the stability. More on the stability of the source magnetic field can be found in section 6.1.

Table 4.9.: Neutrino mass shifts associated with the source magnetic field. The table lists the results of the ensemble tests performed for the trueness of the source magnetic field of 0.5 % and its stability of 0.0015 % h^{-1} for the KATRIN Design Report setting (see table 4.2.11). For the trueness, one former ensemble test is known [Gro15] and the value is also stated in the table. The total uncertainty linked to the source magnetic field is derived by quadratic summation.

Effect	Δm_ν^2 in $10^{-3}\,\mathrm{eV}^2/c^4$ ([Gro15])	Δm_ν^2 in $10^{-3}\,\mathrm{eV}^2/c^4$ (this work)
stability	-	± 0.2
trueness	± 1.8	± 1.9
total	-	± 1.9

As depicted in figure 4.10, the magnetic field along the WGTS is not constant in z-direction. In the gaps between the three superconducting coils of the central beam tube, correction coils are mounted to minimise the field inhomogeneity to about 1-2 % for nominal magnet operation [Ang05]. According to equation 3.5, electrons which are created in these gap regions with the reduced magnetic field have a slightly smaller acceptance angle. This also affects the scattering probabilities as outlined above. Groh demonstrated the necessity to include these inhomogeneities in the analysis, since otherwise a significant error on the neutrino mass is incurred [Gro15], see also the following paragraph. To take these inhomogeneities into account, the WGTS has to be analysed in a voxelised way, as already mentioned in the Doppler effect section 4.2.4. Groh's investigation indicates that 100 slices are required and appropriate. Linked to the magnetic field inhomogeneities is also the third aspect, the trueness of the magnetic field values. In order to determine the correct maximum acceptance angle and to keep the corresponding neutrino mass shift on a small level, the true value of the magnetic field inside the WGTS beam tube has to be known with high precision of <1 % [Gro15]. Since there are no possibilities to measure the magnetic field inside the beam tube directly, it has to be propagated from outside. The positioning of the Hall sensors in the cryostat is not known exactly, so that they cannot be used for an absolute measurement. Also, the positioning of the magnets inside the cryostat is not known exactly and cannot be measured since the cryostat is closed. Therefore, a new magnetic field measurement system was conceived and set up outside of the cryostat [Hei18]. Based on measurements with this system, the magnetic field values inside the beam tube can be determined with a trueness of ≈ 0.5 %. First commissioning measurements have been performed already [Hei18].

Impact on neutrino-mass determination. The KATRIN Design Report estimates the associated neutrino mass shift of the source magnetic field to be [Ang05]

$$\Delta m_{\nu,\mathrm{B_{WGTS}}} = 2.0 \times 10^{-3}\,\mathrm{eV}^2/c^4\ . \tag{4.19}$$

From the three systematic effects linked to the source magnetic field as outlined above the inhomogeneity along the WGTS beam tube can be neglected as long as the source is sliced sufficiently [Gro15]. Therefore, the stability and the trueness of the magnetic field remain as systematic contributions. The stability was measured in the scope of the thesis at hand to be 0.0015 % h^{-1} (see section 6.1). Furthermore, a trueness for the magnetic field measurement of 0.5 % is assumed [Hei18]. Both values are used to determine the associated neutrino mass shift in ensemble tests with the KATRIN Design Report (see table 4.1). The results are presented in table 4.9. The neutrino mass shift associated with the magnetic field stability is probably overestimated due to the limited statistical sensitivity of the ensemble test and the uncertainty of the magnetic field calculation.

Relevance for KATRIN and current status. The magnetic field inside the WGTS is one of the major sources of systematic uncertainties at KATRIN. Since it influences the important maximum acceptance angle directly, one can introduce large errors on the analysis of the neutrino mass if it is not taken into account correctly. The newly designed source magnetic field measurement system was tested in 2018 with first estimations of the measurement uncertainty [Hei18]. Since also the number of slices used in the analysis has an effect on the uncertainty due to the inhomogeneities of the magnetic field in the pump ports, it has to be made sure that always a sufficient number of slices of the WGTS is used. As the investigation in section 6.1 has demonstrated, the stability of the magnetic field in the WGTS is on the 10^{-5} level and introduces only a negligible systematic uncertainty.

4.2.12. Trapped Electrons in the WGTS

Description. Beta electrons created in regions of low magnetic field B_{low} surrounded by higher magnetic fields B_{high} experience the magnetic mirror effect: according to equation 3.5 they are reflected by the higher magnetic field if the angle θ of their momentum to the magnetic field lines is larger than

$$\theta \geq \theta_{\text{trap}} = \arcsin \sqrt{\frac{B_{\text{low}}}{B_{\text{high}}}} \, . \tag{4.20}$$

As soon as the higher magnetic field strengths are on both sides of the low magnetic field strength, the electrons are reflected back and forth and trapped in a so-called magnetic bottle. Due to elastic and inelastic scattering off gas molecules, the trapped electrons lose energy but also change their angle θ. The angular changes in inelastic scattering are $< 1°$. In elastic scattering, the mean angular changes are $\approx 3°$ [Gro15]. After some scattering processes, their angle might be small enough to leave the trap and to reach the detector. Since they have a smaller energy than originally in their creation, they change the shape of the beta spectrum and lead to a shift of the neutrino mass if not accounted for in the analysis [Ang05]. Therefore, such electron traps have to be avoided or minimised in the design of a highly precise neutrino mass measurement.

Experience from former neutrino mass experiments. For the Troitsk experiment, the trapping of electrons in the WGTS is one of the major systematic effects [Ase11]. The Troitsk WGTS is set on a magnetic field of 0.8 T, surrounded by magnetic fields of 5.0 T in forward and rear direction. This configuration prevents electrons coming from tritium decays at the walls from being guided to the detector. Although only a fraction of 10^{-4} of all detectable electrons comes from the trap, the effect on the neutrino mass is quite large since the modelling of the energy loss of the trapped electrons has an uncertainty of 20 %.

The Los Alamos setup was improved after first measurements to avoid trapping of electrons in the source [Rob91], because in the original setup about 11 % of the electrons were trapped [Wil87]. In the new magnetic design, the trapping of the electrons is no longer a systematic effect to consider.

Determination for KATRIN. The KATRIN magnetic system is designed in a way that the probability for electrons being trapped is reduced to the largest extent possible [Ang05]. The WGTS superconducting coils are designed for 3.6 T for the central beam tube and 5.5 T for the two DPS elements towards the transport section. However, electrons which are reflected at that magnetic mirror, are absorbed by the rear wall and cannot reach the detector since the magnetic field in rearward direction is the same as in the central WGTS. Nevertheless, there are still some small regions with reduced magnetic field: between the three separated coils of the central beam tube there are two correction

coils to keep the magnetic field as homogeneous as possible (see figure 4.10). Nevertheless, the field strength in these regions is about one per cent smaller than overall. Furthermore, the field inside the pump ports drops to about 0.5 T if the magnets are operated as designed. For the correction coil part, only a very small contribution to the uncertainty budget is assumed because the small differences of the magnetic field lead to cut-off angles close to 90°. Since in the pump ports the gas density is a factor of 100 less than at the injection point, also only a small contribution of trapped electrons from the pump ports is expected. For the quantification of the effect, only simulations and no measurements can be done, in which the gas density of the regions of low magnetic field strengths is calculated and translated into a count rate contribution of the trapped electrons at the detector.

Impact on neutrino-mass determination. The KATRIN Design Report estimates the neutrino mass shift associated with trapped electrons in the WGTS to be $\Delta m^2_{\nu,\mathrm{trap}} < 1.0 \times 10^{-4}\,\mathrm{eV}^2/c^4$.

Relevance for KATRIN and current status. The trapped electrons in the WGTS are one of the minor contributions to KATRIN's systematic uncertainty budget. It is negligible and no further action is deemed to be required on this topic.

4.2.13. Potential Variations in WGTS

Description. While the decay electrons leave the source towards the detector, the much slower positive daughter molecules remain there. In scattering processes, they form other kinds of ions (see section 4.2.9) or recombine to neutral molecules which can leave the magnetic field and can be pumped. The decay electrons can produce further secondary electrons in scattering processes off gas molecules. In equilibrium, a net space charge region forms, which influences the beta electrons: if this space charge is positive, electrons created inside this positive potential lose energy when leaving the potential well. As long as the space charge is constant over time and homogeneous over the entire source, its influence on the spectrum is energy-independent and only shifts the whole spectrum and the kinematic endpoint towards lower energies (for a negative space charge a shift towards higher energies occurs) without changing the spectral shape. Since the endpoint is usually a free fit parameter (see section 3.4.1), this does not affect the estimate of the neutrino mass. However, as soon as the potential is not constant or homogeneous, regions with different net space charges directly affect the shape of the spectrum. Thus, also the estimate of the neutrino mass is influenced. The actual magnitude of the effect depends on several parameters of the tritium source, such as boundary conditions set by the geometry, the temperature, the magnetic field and the local gas density. The geometry, the temperature and the magnetic field define the duration of stay of the ions inside the source. Furthermore, the geometry, the magnetic field and the gas density influence the path length of the decay electrons through the source. The path length again has an impact on the number of secondary electrons produced due to ionisation. To reduce the effect of potential space-charging on the neutrino mass analysis, it has to be controlled, stabilised, measured and optionally actively removed.

Experience from former neutrino mass experiments. The Troitsk group reported a dedicated measurement campaign with ^{83m}Kr to measure space-charging in their windowless gaseous tritium source [Bel08]. ^{83m}Kr was selected because it has a half-life of about 1.8 h and deexcites via internal conversion. In this transition, electrons of well-defined energies are emitted. The lines have energies of up to 32 keV and line widths of around 2 eV (see also table 5.2). By comparing the line positions of measurements with ^{83m}Kr but without tritium to measurements together with tritium in the source, the Troitsk group determined the mean potential inside the source volume. By doing the same study for the width, the

potential variations were extracted [Bel08]. In order to prevent ^{83m}Kr from freezing out, the operational temperature of the Troitsk source had to be raised to 110 K instead of 30 K in standard operation. Therefore, the obtained result gives only an upper limit on the influence of space-charging on the neutrino mass at the tritium-operation temperature. While the Troitsk group did not find a significant line broadening, they demonstrated a shift of the line position due to a negative potential in the source, which was in opposite to the expectations. However, the neutrino mass estimate was not affected by these results [Ase11].

Although other experiments with gaseous sources did not take space-charge effects into account, it should be noted here that they also made use of ^{83m}Kr for energy calibration, high voltage monitoring and energy loss determination [Dec90b; Rob91; Sto95]. In the Mainz experiment, in which a quench-condensed tritium source was used, a positive charging of the tritium film was observed. This was likewise investigated with condensed ^{83m}Kr [Kra05].

Determination for KATRIN. Like the Troitsk experiment, KATRIN uses a gaseous ^{83m}Kr source to measure possible potential variations inside the tritium source tube. This requires several changes to the WGTS operation: based on the experience of the Troitsk experiment, a WGKrS operation temperature of 100-110 K is planned for KATRIN. This requires the exchange of neon in the WGTS cooling system by argon, which has feasible pressures in the range of 90-110 K [Stu47]. At these temperatures, ^{83m}Kr is still gaseous due to its low partial pressure $\ll 10^{-3}$ mbar [Lem70]. However, temperatures smaller than 100 K are not preferable since the ^{83m}Kr throughput decreases with temperature [Sen18]. For tritium, the temperatures much larger than in standard operation result in a larger throughput. In order to obtain a comparable column density to 30 K operation, the injection pressure has to be raised by a factor of ~ 4 due to the better conductivity at higher temperatures. Finally, the loop circulation has to be changed for Krypton operation, because ^{83m}Kr would be filtered out by the permeator of the inner loop (see figure 3.3). Thus, the permeator is bypassed and the tritium-krypton mixture is re-injected to the WGTS without passing the inner loop systems like LARA or the pressure-controlled buffer vessel.

Based on plasma simulations it is expected that the plasma potential in the WGTS tube is mainly dominated by the rear wall. Furthermore, electrons can be produced by a rear wall irradiation with UV light to counterbalance the positive space charge and to reduce the plasma inhomogeneities which influence the neutrino mass measurements (see section 3.2.2 and [Kuc16; Sch16] for details). The effectiveness of this countermeasure is investigated with the WGKrS. In the KATRIN Design Report it is assumed that the inhomogeneity of the space charge will not be larger than 10 meV [Ang05], so that the ^{83m}Kr measurements have to be sensitive to this level.

It turned out that the procedure for measuring the potential inhomogeneity applied in the Troitsk experiment is not suitable for KATRIN, since the sensitivity on the line width is not good enough. A new procedure for the potential inhomogeneity measurement was therefore developed in [Mac16]: when ^{83m}Kr is mixed to the tritium carrier gas at a standard column density of $5 \times 10^{17}\,\mathrm{cm}^{-2}$, about 20 % of the conversion electrons scatter once inelastically off the tritium in the source. In this inelastic scattering process, an electron lose about 13 eV of energy (see figure 4.15). Thus the scattered electrons appear as an additional line 13 eV below their original energy in the spectrum of ^{83m}Kr (see figure 4.11). The scattering probability depends on the path length of a conversion electron in the source. Electrons being created at the rear end thus have a much larger probability to scatter at least once than electrons being created at the front end of the WGTS tube close to the DPS. Therefore, the line of the single-scattered electrons is mainly

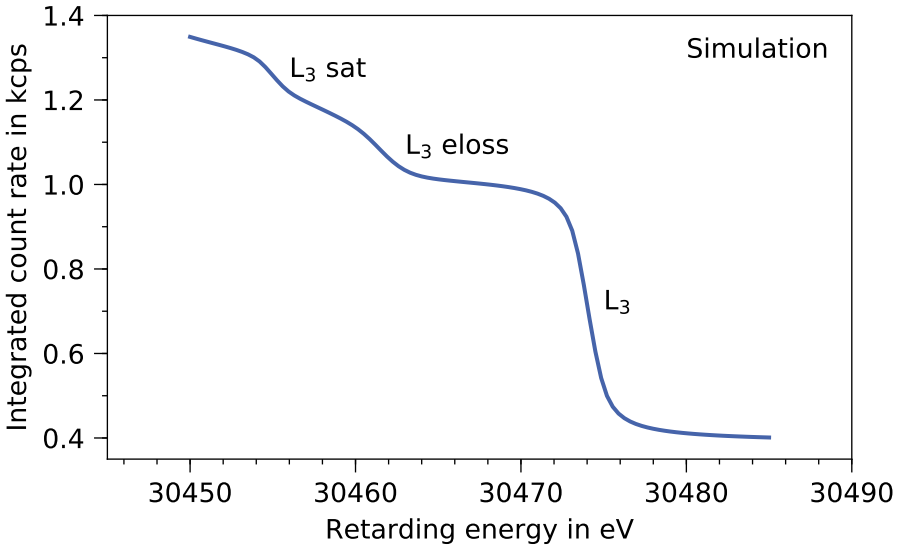

Figure 4.11.: Simulated ^{83m}Kr L$_3$-32 line and its first energy loss peak. The plot shows a simulation of the ^{83m}Kr L$_3$-32 line for the standard column density of $5 \times 10^{17}\,\mathrm{cm}^{-2}$. The single-scattered electrons are clearly visible as a step with an intensity of about 20 % of the main line (L$_3$ eloss). The shake-up satellite line of the L$_3$ line is clearly separated from the energy loss line. The energy difference between the L$_3$ line and the single-scattered electron line is the major parameter to determine the plasma potential inhomogeneity in the WGTS. Plotted data kindly provided by M. Machatschek [Mac16].

built by electrons from the rear half of the WGTS and the corresponding conversion line is mainly built by electrons from the front half as long as the column density is at its standard value of $5 \times 10^{17}\,\mathrm{cm}^{-2}$. The energy difference between the two lines is hence a measure of the potential difference of the front to the rear half of the WGTS (see figure 4.12). It is expected from simulations [Kuc16] that the potential of the rear half of the WGTS is more positive than in the front half so that the energy difference between the L$_3$32 line and its corresponding energy loss line should be larger than in measurements without tritium and thus without a plasma in the source (e. g., in deuterium measurements).

In measurements with deuterium and ^{83m}Kr, this measurement principle was tested in fall 2018. The first preliminary results indicate that it is possible to measure the difference between the L$_3$-32 line and the line of the one-fold scattered electrons to a precision around 10 meV within one day. Including the adjustment and optimisation of the rear wall voltage, a sequence of several measurements will have to be performed so that a total measurement time of one week is realistic[8].

Impact on neutrino-mass determination. The idea for estimating the influence of the plasma potential on the final neutrino mass result is to test the plasma simulations and the optimised rear wall voltage at 100 K with gaseous ^{83m}Kr measurements. If the simulations can be confirmed and an optimised voltage is found, the potential at 30 K is calculated. Due to the voltage optimisation the plasma potential at 30 K should only have a small influence on the neutrino mass, since the remaining plasma inhomogeneities should be small. In the scope of this thesis, only the last step of the procedure was quantified in ensemble tests. The results are shown in table 4.10. The potential used in the ensemble test is the same as used in [Mac16] which is based on [Kuc16]. It is calculated for 30 K. The ensemble test uses the potential for generation of toy data and a zero potential for

[8] Personal communication M. Machatschek, Dec 13, 2018.

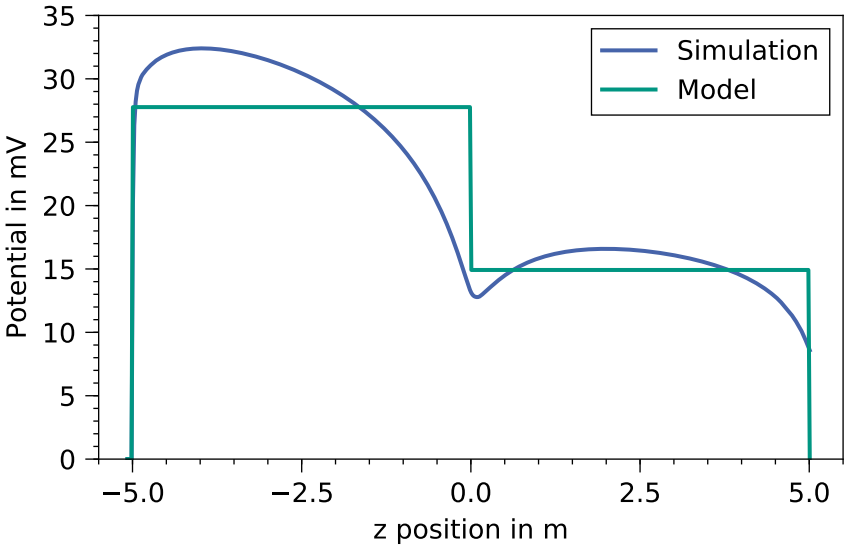

Figure 4.12.: The WGTS plasma potential and its measurement. The simulated plasma potential is asymmetric, which can be explained by the fact that towards the rear side (negative z) the beam tube is closed by the rear wall, while towards the DPS (positive z) the beam tube is open. It is not possible to extract the precise shape of the potential from ^{83m}Kr measurements, but in a simplified model and under the assumption that the simulated potential is correct, the different mean values of the potential in the rear half and front half of the WGTS can be measured. This is based on the precise measurement of the position of the L_3 main line and the corresponding shifted line of single-scattered electrons (see figure 4.11). Plotted data kindly provided by M. Machatschek [Mac16].

Table 4.10.: Neutrino mass shifts associated with a non-vanishing plasma potential in the WGTS. The table shows the neutrino mass shift determined in ensemble tests for KATRIN Design Report conditions (see table 4.1). As a reference the result from [Mac16] is given.

Δm_ν^2 in $10^{-3}\,\mathrm{eV}^2/c^4$ ([Mac16])	Δm_ν^2 in $10^{-3}\,\mathrm{eV}^2/c^4$ (this work)
−0.3	−0.7

the analysis model. However, currently it is still under investigation how to propagate uncertainties of the gaseous ^{83m}Kr measurement to conditions at 30 K. Furthermore, the voltage optimisation at the rear wall needs to be proven. Therefore, the neutrino mass shift stated in table 4.10 is a first estimate and might be slightly higher if all effects are considered. The result is a factor of two larger than the one from previous studies [Mac16]. The reason is probably a differing initialisation of the ensemble tests.

Relevance for KATRIN and current status. The associated neutrino mass shift of potential variations inside the WGTS is quite small compared to other systematic effects. However, its measurement is time-consuming and technically challenging. The WGTS has to be ramped to an operational temperature of 100 K. The tritium-data taking is interrupted for at least one week. Especially at the beginning of tritium operation it is assumed that the WGTS potential will be measured in regular intervals to learn more about its stability in time and to investigate the dependence of the potential inhomogeneity on the rear wall voltage and illumination. Later on, when the effect is fully understood and the best settings for the rear wall are found, the ^{83m}Kr mode measurements will not be required any more in every calibration break.

The WGKrS mode was tested in a dedicated measurement campaign in July 2017. As discussed in much more detail in chapter 5, this campaign was performed without carrier gas in the WGTS, so that the procedure to measure the potential inside WGTS could not be tested then. However, the outcome of the measurement campaign demonstrated that the WGKrS is a useful and powerful calibration tool not only for the determination of the WGTS potential inhomogeneity. The lessons learnt during the campaign were an important input for the next WGKrS campaign in fall 2018, where ^{83m}Kr was circulated in the bypassed inner loop for the first time, but with deuterium as carrier gas instead of tritium as in the upcoming measurements. This campaign offered the first possibility to observe the line of the single-scattered electrons of the conversion line. The basic principle of the measurement procedure was demonstrated successfully. A detailed analysis is currently ongoing [Mac19].

4.2.14. Gas Dynamics in WGTS

Description. The column density ρd is one of the most important input parameters of the analysis of a gaseous tritium source in direct neutrino mass experiments. Electrons which are created in the source always have to travel through a certain amount of gas, and their scattering probabilities are functions of the product of the inelastic cross-section σ_{inel} and ρd: $P = P(\sigma_{\text{inel}} \cdot \rho d)$ (see equation 4.27) [Ang05; Kuc18]. However, since the tritium is pumped in a closed loop system, the tritium density is not constant over the entire source tube, but it is decreasing from the point of injection over several orders of magnitude towards the pumps (see figure 3.3). The gas is thus in different flow regimes, ranging from viscous to free-molecular streaming with a transition regime in between [Kuc18]. For extended sources as in the WGTS, input data from several sensors are available for the gas dynamics model [Hei18]: temperature data along the beam tube, the injection and outlet pressure, for instance. Temperature inhomogeneities along the source tube have to be taken into account to make a position-dependent calculation possible. As experimental conditions can change over time, regular adjustments of the gas dynamics model are mandatory [Kuc18]. Besides the experimental uncertainties, the model itself includes parameters which are only known with limited accuracy, like the tritium viscosity, so that the model itself contributes to the total uncertainty budget of a direct neutrino mass experiment. This section focusses on the gas dynamics model, while monitoring of the stability of the column density is described in the following section 4.2.15.

Experience from former neutrino mass experiments. The Los Alamos group had an uncertainty of $\pm 5\,\%$ on their source density. However, this introduced only a minor contribution to their overall systematic uncertainty [Rob91]. In the Livermore experiment, the tritium partial pressure was kept stable to $0.5\,\%$ via a computer-controlled regulation valve [Sto95]. The associated uncertainty in the neutrino mass was neglected in the final analysis. In both the Livermore and the Los Alamos experiment the retarding voltage at the spectrometer was set in a randomised order to minimise the influence of any drift in the column density on the neutrino mass result. For the Troitsk experiment, the column density is one of the major systematic uncertainties [Ase11]. Its value was determined within $\pm 3\,\%$ and this uncertainty was propagated on the scattering probabilities and hence on the response function. In a previous work, the Troitsk group used the determination of the column density also for a measurement of the total inelastic cross-section of electrons scattering off tritium molecules [Ase00].

Determination for KATRIN. According to the KATRIN Design Report, the column density has to be stable on the $0.2\,\%$ level [Ang05]. However, for the scattering probabilities also the total value of the product $\sigma_{\text{inel}} \cdot \rho d$ has to be known with the same requirement [Kuc18]. The inelastic scattering cross-section σ_{inel} for $18.6\,\text{keV}$ electrons in

tritium gas has been measured in the Troitsk experiment with an uncertainty of 2 % [Ase00]. Since the calculation of the column density ρd based on sensor data with the gas dynamics model has an uncertainty of the same size [Kuc18], the model-based calculation of the product $\sigma_{\text{inel}} \cdot \rho d$ does not keep the KATRIN limits. Therefore, an improved measurement of the product is necessary: rates of the rear section egun without and with gas in the source are compared for the first plateau of the response function, which gives the amount of the non-scattered electrons (see figure 4.13). In this way, the zero-scattering probability can be calculated, and based on equation 4.27, the product of $\sigma_{\text{inel}} \cdot \rho d$ is derived. With this measurement, it is estimated that the product can be determined with an uncertainty of 0.15 % [Kuc18]. However, the result strongly depends on the performance of the rear section egun which is currently undergoing its final commissioning. A disadvantage of the measurement is that it always needs a reference egun rate determination without gas inside the source, which would interrupt the neutrino mass measurements. Thus, the strategy is to first determine the absolute value of $\sigma_{\text{inel}} \cdot \rho d$, and then to control its stability with the sensor data described in section 4.2.15. From time to time the model is updated to account for drifts in the measured parameters and thus in the column density. If larger changes in the sensor data occur, the absolute value has to be determined again.

Impact on neutrino-mass determination. There are three uncertainty contributions which determine the total neutrino mass shift associated with the gas dynamics model: the uncertainty on the product $\Delta(\rho d \cdot \sigma_{\text{inel}})$, the uncertainty on the single factors of the product, $\Delta\rho d$ and $\Delta\sigma_{\text{inel}}$, and the uncertainty on the model. As outlined above, the product uncertainty is assumed with 0.2 %. The two factors are known with an uncertainty of 2 % each. The two gas density profiles used for the ensemble test differ by up to 5 % [Kuc18]. For all three uncertainty contributions, ensemble tests were performed according to table 4.1 and the results are presented in table 4.11. The absolute neutrino mass shifts from literature for the Design Report setting are reproduced well. However, in [Kuc18] only one-sided neutrino mass shifts are considered. As demonstrated in the ensemble tests performed in this thesis, actually a two-sided shift has to be taken into account depending on whether the true values are under- or overestimated in the model. Small asymmetries obtained for the upper and lower neutrino mass shift on the order of $10^{-4}\,\text{eV}^2/c^4$ are neglected.

The three uncertainties are correlated and therefore have to be tested in a combined ensemble test. For a full picture, the model of the plasma potential inside the WGTS has to be included (see figure 4.12) which has a slight influence on the combined result. The plasma potential shifts the result of this work towards positive values, while in previous studies [Kuc18; Kuc16], the result is shifted to a more negative value. The discrepancy is explained by a different source potential being applied. In this work, the same 1D potential as for the WGTS space charge investigations in section 4.2.13 is used. For the total uncertainty of the gas model, the neutrino mass shift due to the monitoring of the column density has to be added, see section 4.2.15.

Relevance for KATRIN and current status. The code for the gas dynamics calculation is fully implemented into the KASPER framework. However, it has to be demonstrated in test measurements that an uncertainty of 0.2 % or better on the product $\rho d \cdot \sigma_{\text{inel}}$ can be achieved with the egun. Likewise, the calculations have to be verified: the code can be used to make predictions on the column density if e. g. one pump of the WGTS is switched off. This has been investigated in fall 2018 and the measurements are currently being evaluated [9]. Also the stability of the column density has to be observed over typical lengths of KATRIN neutrino mass data taking periods (approx. 60 days) to investigate how often

[9] F. Sharipov (2018), KATRIN internal report.

Table 4.11.: Neutrino mass shifts associated with the gas dynamics model. The table lists the neutrino mass shifts associated with the determination of the gas dynamics model for the KATRIN Design Report setting (see table 4.1). As a reference, the estimated neutrino mass shifts from [Kuc18] are given. The table entries are further explained in the main text.

Setting	Δm_ν^2 in $10^{-3}\,\mathrm{eV}^2/c^4$ ([Kuc18; Kuc16])	Δm_ν^2 in $10^{-3}\,\mathrm{eV}^2/c^4$
$\Delta(\rho d \cdot \sigma_{\mathrm{inel}})$	-2.6	± 2.3
$\Delta\rho d$ and $\Delta\sigma_{\mathrm{inel}}$	-0.3	± 0.3
Model	-0.8	± 0.5
Combined	-2.6	± 3.3
Combined with plasma model	-3.1	± 3.0

updates of the absolute value of the product are necessary.

The neutrino mass shift associated with the gas dynamics has not been considered in the KATRIN Design Report to its full extent, since only the uncertainty on the monitoring was mentioned [Ang05]. Thus, it is an additional effect which has to be taken into account in the total budget. As the investigation in this thesis has shown, it has a significant effect.

The model does not include the tritium purity and the gas composition explicitly. Only the viscosity of tritium is taken into account, but with an uncertainty of 2.5 % for the non-included hydrogen isotopologues [Kuc16]. It should be kept in mind that at the beginning of the KATRIN tritium operation it is expected that the tritium purity will not reach its nominal value due to wall effects and exchange reactions with other isotopologues being present in the system. Especially, the tritium content measured with the LARA system will probably not be the same value which will arrive in the WGTS beam tube (see also section 4.2.17). Thus, the uncertainty of the model for gas mixtures with tritium purities below 95 % might be underestimated and requires a re-evaluation. First results were obtained in the first tritium campaign 2018, where low amounts of tritium were employed [Hei18].

4.2.15. Monitoring of Column Density

Description. Besides the determination of the absolute value of the product of column density and inelastic scattering cross section $\rho d \cdot \sigma_{\mathrm{inel}}$ (see the previous section 4.2.14), the column density has to be stabilised to ensure a stable beta electron rate during the spectrum scans. An unstable tritium source would change the shape of the beta spectrum and could mimic a wrong neutrino mass if it is not accounted for in the analysis. For large-scale gaseous sources like the WGTS, this is a technical and analytical challenge: keeping the column density stable on the per mille level sets strong requirements on the temperature and the pressure stability, but also on the gas purity. At the same time, monitoring systems have to be designed which are able to track the column density and the gas composition on the required stability level. And finally, the sensor data has to be interpreted and incorporated into the spectrum model in the correct way.

Experience from former neutrino mass experiments. See the previous section 4.2.14.

Determination for KATRIN. The KATRIN WGTS is designed in a way that the column density is determined by four parameters, which are the inlet pressure p_{in}, the outlet pressure at both ends of the WGTS beam tube p_{ex}, the beam tube temperature T

and the isotopic tritium purity ϵ_T [Ang05]. Out of the four parameters only the first three influence the total column density. Instabilities of these parameters directly translate to instabilities of the rate but also of the scattering probabilities according to equation 4.27. Both can cause a significant neutrino mass shift if they are not taken into account. However, the tritium purity does not affect the total column density, but the tritium column density which is the part of the column density containing tritiated isotopologues. Therefore, it only influences the rate and not the scattering probabilities, but purity fluctuations can also cause a significant uncertainty on the final neutrino mass result if they are not included in the analysis. The source density has to be stabilised at two per mille [Ang05], and in a rough estimate the four parameters have to be stable on the same level. This means the monitoring precision of the four parameters has to be even better. Three different monitoring systems of the source column density can be distinguished:

- The monitoring of the beta electron rate is done by the BIXS systems (see section 3.2.1) and the FBM (see section 3.2.4) with a precision of 0.1 % within a few minutes of measurement time. A deviation from the required rate stability of one per mille points directly to instabilities of one of the four column density parameters, which are therefore also monitored separately.

- The source temperature is recorded with 24 Pt500 elements (see also section 6.2.1). The temperature stability and the homogeneity, which means the temperature profile along the beam tube, are critical parameters for the column density. Both are determined in the scope of the thesis at hand, see section 6.2.2. The inhomogeneity along the beam tube of (1.98 ± 0.75) % can be fully implemented in the spectrum model because it is constant over time with a temperature stability of $(0.005 \pm 0.001)\,\%\,\mathrm{h}^{-1}$. The inlet pressure is measured and stabilised in the pressure-controlled (and temperature-stabilised) buffer vessel as part of the inner loop (see figure 3.3). The pressure sensor is a capacitance manometer and a stability of 1×10^{-4} was demonstrated in a stand-alone measurement [Pri15]. The outlet pressure is not measured directly, it is mainly dependent on the rotational speed of the turbo molecular pumps. The Design Report gives a target precision of 0.06 %, but in reality it can be expected to be much more stable because of the steady rotation frequency of the turbo molecular pumps. Finally, the molecular gas composition is determined with a Laser Raman system in the inner loop (see figure 3.3). Here, a precision of 0.34×10^{-3} was achieved for the monitoring of a tritiated gas mixture under KATRIN conditions (comparable gas composition and pressure) in a measurement time of 29.5 s [Fis14].

- The column density stability can also be measured with the electron gun mounted in the rear section (see section 3.2.2). Based on measurements at three points of the response function (see figure 4.13), one at the plateau, one at roughly the first and one at roughly the second scattering edge, it is assumed to measure the product of inelastic cross section and column density, $\sigma_{\mathrm{inel}} \cdot \rho d$ with a precision better than 1×10^{-3} [Ang05]. Depending on the egun rate only a few minutes are necessary for this procedure, which will be scheduled in between two measurement runs not disturbing the neutrino mass data taking.

Impact on neutrino-mass determination. The Design Report estimates the neutrino mass shift associated with a monitoring precision of the column density of 2×10^{-3} to $\Delta m^2_{\nu,\rho d} = 1.5 \times 10^{-3}\,\mathrm{eV}^2/c^4$ [Ang05]. However, it turned out that besides the monitoring of the column density, also a detailed gas dynamics model is necessary, see section 4.2.14. The model-related uncertainties are presented in table 4.11. Here, the uncertainty of monitoring the column density via the temperature, the pressure and the Laser Raman system between two determinations with the electron gun is discussed. For the temperature,

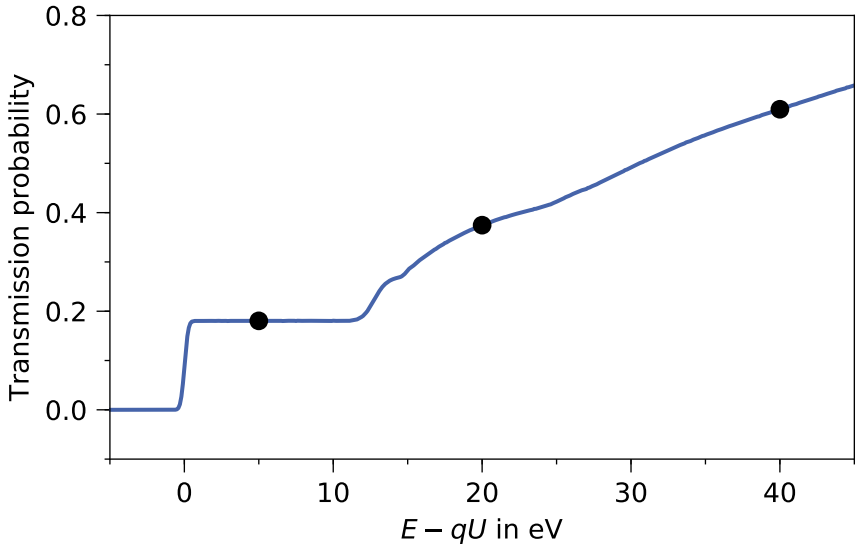

Figure 4.13.: Monitoring of the column density with the rear section egun. The plot shows the simulated response function for the nominal column density of $\rho d = 5 \times 10^{17}\,\mathrm{cm}^{-2}$ as transmission probability over the excess energy of electrons from the rear section egun to the retarding voltage. The black dots mark possible measurement points for the egun to determine the product of $\rho d \cdot \sigma_{\mathrm{inel}}$. For the absolute determination, only the first measurement point at the plateau of unscattered electrons is necessary. However, a reference measurement with evacuated source beam tube has to be done before to measure the egun intensity. For a relative measurement for monitoring purposes, three measurement points are necessary: one in the range of the unscattered electrons, one in the range of the single- and one in the range of the twofold-scattered electrons. Then, the absolute count rate can be eliminated from the equations and relative changes of $\rho d \cdot \sigma_{\mathrm{inel}}$ are measured. Principle according to [Ang05].

a relative stability of 5×10^{-5} according to the results of the thesis at hand is assumed. The relative stability of the inlet pressure and the outlet pressure was determined in the first tritium campaign in summer 2018 to 9.8×10^{-5} and 1.7×10^{-3}, respectively [Hei18]. Since the first tritium campaign was performed with traces of tritium mixed to deuterium, the relative stability of the deuterium molar fraction of 6.9×10^{-4} derived in those measurements [Hei18] is used here as an estimate of the tritium purity stability in the future. Leaving out correlations, each of these stability values (besides the tritium purity one) can be transformed conservatively into a corresponding fluctuation of the column density. The factors are 1.24 for the inlet pressure, 1.06 for the temperature and 0.029 for the outlet pressure [Kuc16; Kuc18]. Summing up the corresponding column density fluctuations quadratically, a fluctuation of $\Delta\rho d/\rho d = 1.4 \times 10^{-4}$ is obtained. Thus, two ensemble tests are performed, one testing the fluctuation of the total column density and one testing the fluctuation of the tritium column density. The combined value gives the uncertainty linked to the monitoring of the column density in between two egun measurements and the results are presented in table 4.12. The result has to be added to the one of the gas dynamics in section 4.2.14 in order to derive the total uncertainty linked to the column density.

Relevance for KATRIN and current status. The monitoring of the column density is one of the most important systematic effects for KATRIN. This is underlined by the huge effort put in the development of different monitoring systems for the column density and its determining parameters. Fortunately, the associated neutrino mass shift can be kept well under control, if the sensor values are used to update the gas dynamics model, since the performance of the inner loop and the WGTS is much better than specified. However,

Table 4.12.: Neutrino mass shifts associated with the column density monitoring. The table shows the results of the ensemble tests for the KATRIN Design Report settings (see table 4.1) for the monitoring of the column density. The details of the implemented test parameters are found in the main text.

Parameter	Δm_ν^2 in $10^{-3}\,\mathrm{eV}^2/c^4$ (this work)
Total column density	±0.2
Tritium column density	±0.1
Combined	±0.2

as the model uncertainties have not been taken into account in the Design Report, the overall uncertainty related to the column density is still about a factor of two larger than originally estimated.

It should be emphasised that the stability values of the pressures and the temperature can change during KATRIN operation. For the source tube temperature, such changes are reported in this thesis (see, for instance, figure 6.5). Several cooling circuits are involved in the complex WGTS cryostat and the interplay of the circuits is not trivial, so that changes in the operational temperature can occur. Therefore, the values used in the table only give an estimate and have to be re-evaluated for every KATRIN run again. As demonstrated in this thesis for the WGTS temperature behaviour in Krypton mode in section 6.2.4, especially the time synchronisation of the different monitoring devices is a point to consider in the interplay of the sensor data and the gas dynamics model. Therefore, further investigations are necessary and ongoing.

Finally, the total systematic uncertainty of the column density critically depends on the egun performance. It is the only system capable of determining the absolute value of the product $\rho d \cdot \sigma_{\mathrm{inel}}$, but it is also necessary for the determination of relative changes of the column density to be able to update the model.

4.2.16. Energy Loss Function

Description. The energy loss function describes the probability that electrons with an energy E lose the energy amount ΔE in scattering interactions with gas molecules in the tritium source. There are two different kinds of scattering processes: In elastic scattering, the molecule only gains a tiny amount of translational energy from the electron. The median energy loss of the electron is 4 meV [Kle18a]. In inelastic scattering, the electron dissociates or ionises the molecule or leads to internal excitations. The energy loss of the electron is at least $\approx 12\,\mathrm{eV}$ (see figure 4.15). The cross section of the inelastic process is $\sigma_{\mathrm{inel}} = (3.40 \pm 0.07) \times 10^{-18}\,\mathrm{cm}^2$ [Ase00], which is about one order of magnitude larger than the one of the elastic scattering [Liu87].

The energy loss function only depends on the energy of the electrons and the gas species present in the source. KATRIN is only interested in electrons near the kinematic endpoint of the tritium beta-decay for the determination of the electron antineutrino mass, where the cross-sections can be taken as constant with a negligible energy dependence. Furthermore, the gas composition in the tritium source should always be dominated by T_2. Therefore, it is sufficient to determine the energy loss function only once under neutrino mass measurement conditions. Two methods have been developed to measure the energy loss function as outlined in the corresponding paragraph below.

Experience from former neutrino mass experiments. The electron energy loss is

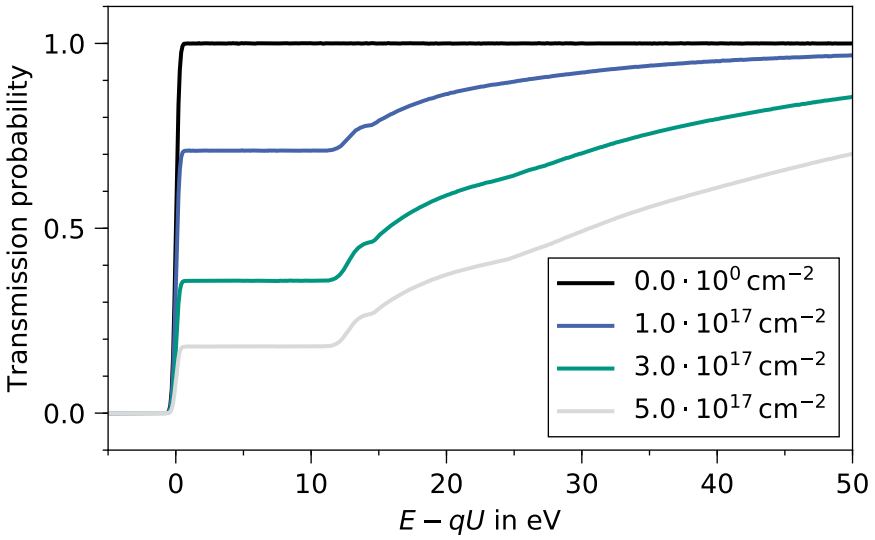

Figure 4.14.: Response functions for the energy loss function deconvolution. The figure shows four simulated response functions for four different column densities which are required to deconvolve the energy loss function. For each voltage step qU, 10^7 egun electrons with an energy $E = 18.6\,\mathrm{keV}$ are simulated. The x-axis shows the surplus energy of the egun electrons, the y-axis the transmission probability. It is clearly visible that the scattering probability rises with increasing column density. The first scattering is visible at around 12 eV, the second at around 24 eV. The simulation was performed using the code described in [Han17].

a well-known systematic effect. It played an even more important role in neutrino mass experiments with solid sources (see e. g. [Rob88]). The large energy loss in solids was one of the main reasons to switch to a gaseous tritium source in the Los Alamos experiment [Wil87; Rob91]. Here, the energy loss function was calculated based on measured scattering off H_2 and it was still one of the major systematic uncertainty contributions [Rob91]. At the Troitsk experiment, the energy loss function was measured experimentally with an electron gun [Ase00; Abd17]. However, for KATRIN a new and more precise measurement is required [Ang05].

Determination for KATRIN. The measurement and analysis procedure for the first method to determine the energy loss function is described in detail in [Han17] and is outlined briefly in the following: With the rear section egun (see section 3.2.2), the transmission function with an empty source ($\rho d = 0$) and three response functions at different column densities ($\rho d = \{1, 3, 5\} \times 10^{17}\,\mathrm{cm}^{-2}$) are measured. The energy of the egun electrons is set to a constant value of $E = 18.6\,\mathrm{keV}$ while the retarding voltage at the main spectrometer is varied in the interval $[qU - 50\,\mathrm{V}, qU + 5\,\mathrm{V}]$ with a voltage step size of $\Delta U = 0.1\,\mathrm{V}$. For each voltage step, 10^7 counts have to be collected. As the egun produces on the order of 10^4 electrons per second, the total measurement time for the four column densities is on the order of one month.

The transmission function T_{egun} measured with the egun for zero column density is a convolution of the spectrometer transmission function (see equation 3.6) and the expected performance parameters of the egun (energy smearing and angular uncertainty). The response functions $R(E - qU)$(see figure 4.14) are defined as

$$R(E - qU) = P_0 \cdot T_{\mathrm{egun}} + P_1 \cdot T_{\mathrm{egun}} \otimes f(\Delta E) + P_2 \cdot T_{\mathrm{egun}} \otimes f(\Delta E) \otimes f(\Delta E) + \dots \,. \tag{4.21}$$

Here, P_i are the scattering probabilities for i-fold scattering, which are strongly dependent on the column density, and $f(\Delta E)$ is the energy loss function. As can be seen from figure 4.15, the energy transfer in inelastic scattering processes is at least 12 eV, thus, only up to three-fold scattering has to be taken into account for an analysing interval up to 30 eV surplus energy of the egun electrons. Defining the scattering functions ϵ_i as

$$\epsilon_0 = T_{\text{egun}} \ , \tag{4.22}$$
$$\epsilon_1 = T_{\text{egun}} \otimes f(\Delta E) \ , \tag{4.23}$$
$$\epsilon_2 = T_{\text{egun}} \otimes f(\Delta E) \otimes f(\Delta E) \ , \tag{4.24}$$
$$\epsilon_3 = T_{\text{egun}} \otimes f(\Delta E) \otimes f(\Delta E) \otimes f(\Delta E) \ , \tag{4.25}$$

a system of linear equations can be formed based on equation 4.21 for three different column densities α, β, γ:

$$\begin{aligned} R^\alpha(E-qU) - P_0^\alpha \cdot T_{\text{egun}}(E-qU) &= P_1^\alpha \cdot \epsilon_1 + P_2^\alpha \cdot \epsilon_2 + P_3^\alpha \cdot \epsilon_3 \ , \\ R^\beta(E-qU) - P_0^\beta \cdot T_{\text{egun}}(E-qU) &= P_1^\beta \cdot \epsilon_1 + P_2^\beta \cdot \epsilon_2 + P_3^\beta \cdot \epsilon_3 \ , \\ R^\gamma(E-qU) - P_0^\gamma \cdot T_{\text{egun}}(E-qU) &= P_1^\gamma \cdot \epsilon_1 + P_2^\gamma \cdot \epsilon_2 + P_3^\gamma \cdot \epsilon_3 \ . \end{aligned} \tag{4.26}$$

The $P_i^{\alpha,\beta,\gamma}$ can be calculated independently for a Poisson distribution to

$$P_i(\mu(\theta)) = \frac{\mu^i(\theta)}{i!} \mathrm{e}^{-\mu(\theta)} \tag{4.27}$$

with

$$\mu(\theta) = \frac{\rho d \cdot \sigma_{\text{tot}}}{\cos\theta} \tag{4.28}$$

being the column density and σ_{tot} being the total scattering cross section. For the determination of the energy loss function, one has to solve the system of linear equations (see equations 4.26) to calculate the one-fold scattering function ϵ_1 (see equation 4.23), from which $f(\Delta E)$ can be deconvolved. Since discrete voltage values are used in the measurement, equation 4.23 can be rewritten as

$$\epsilon_1 = T_{\text{egun}} \otimes f(\Delta E) = \sum_{j=0}^{N-1} T_{\text{egun}}(E - qU_j - \Delta E_j) f(\Delta E_j) \ , \tag{4.29}$$

$$\vec{\epsilon_1} = \mathbf{T}_{\text{egun}} \vec{f} \ . \tag{4.30}$$

Here, $\mathbf{T}_{\text{egun}}$ is an $N \times N$ matrix with N being the number of voltage steps. The matrix contains the values of the transmission function (with $E_j = E - qU_j$):

$$\mathbf{T}_{\text{egun}} = \begin{pmatrix} T_{\text{egun}}(E_0) & 0 & & & \dots & 0 \\ T_{\text{egun}}(E_1) & T_{\text{egun}}(E_0) & 0 & & \dots & 0 \\ T_{\text{egun}}(E_2) & T_{\text{egun}}(E_1) & T_{\text{egun}}(E_0) & 0 & \dots & 0 \\ \vdots & \vdots & \vdots & \vdots & \vdots & \vdots \\ T_{\text{egun}}(E_{N-1}) & T_{\text{egun}}(E_{N-2}) & & & \dots & T_{\text{egun}}(E_0) \end{pmatrix} . \tag{4.31}$$

For the deconvolution of the energy loss function, the matrix $\mathbf{T}_{\text{egun}}$ has to be inverted. Since the matrix is nearly singular, equation 4.30 has to be solved differently. Several methods have been investigated and the singular value decomposition method turned out to be the most suitable [Han17]. Here, the matrix $\mathbf{T}_{\text{egun}}$ is written as a product of two orthogonal $N \times N$ matrices $\mathbf{U}$ and $\mathbf{V}$ and a diagonal matrix $\mathbf{W}$:

$$\begin{aligned} \vec{\epsilon_1} = \mathbf{T}_{\text{egun}} \vec{f} &= \mathbf{U} \cdot \mathbf{W} \cdot \mathbf{V}^{\mathbf{T}} \cdot \vec{f} \\ \Rightarrow \vec{f} &\approx \mathbf{V} \cdot \tilde{\mathbf{W}}^{-\mathbf{1}} \cdot \mathbf{U}^{\mathbf{T}} \cdot \vec{\epsilon_1} \ . \end{aligned} \tag{4.32}$$

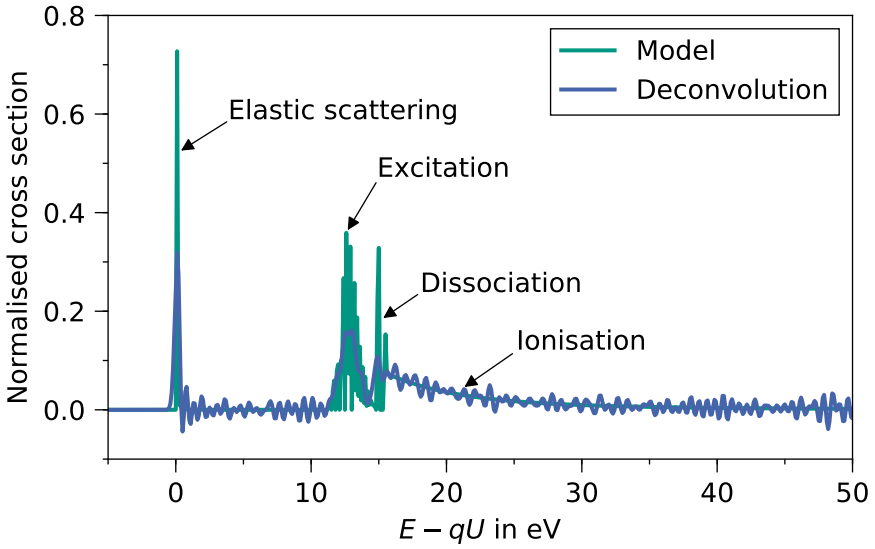

Figure 4.15.: Comparison of energy loss model and deconvoluted function. The model shows an elastic scattering peak, the molecule excitations, the dissociation peaks and the long ionisation tail. These structures can be reproduced by the deconvolution method outlined in the main text. The deconvoluted energy loss function shown here was produced based on the simulated response functions in figure 4.14 with the simulation code of [Han17].

The matrix $\mathbf{W}$ contains the so-called singular values w_i, and its inverse contains their reciprocals $1/w_i$. Since some of the w_i of $\mathbf{T}_{\text{egun}}$ are very small, their reciprocals are very large and could cause numerical problems in the calculation. Therefore, a threshold value has to be found, so that $w_i < w_{\text{thres}}$ are set to zero before the inversion. This enables the construction of an approximate inverse $\tilde{\mathbf{W}}^{-1}$. A suitable threshold value is found based on simulations and the impact on the neutrino mass determination is checked. The process is iterated until a satisfying result is achieved. The result of one deconvolution based on simulated transmission functions is presented in figure 4.15.

Since this first method is very demanding in terms of measurement time and prone to uncertainties due to small fluctuations of operational parameters during data-taking, a second method is currently under development and first test measurements in fall 2018 were very promising. This alternative exploits the MAC-E filter combined with a time-of-flight technique[10] [Bon99]. Then, the rear section egun is driven in pulsed mode, so that the time of flight of the electrons from the egun to the detector can be measured. This permits a differential measurement of the energy loss function without a complicated deconvolution analysis. The measurement time is on the order of hours to days instead of weeks [Sch20; Sac20; Rod21]. More comprehensive time of flight studies are expected for 2019. Since the energy loss function is assumed to be one of the major systematic uncertainties, this second method is an important independent test of the deconvolution outlined above. From the combined analysis of both methods, a precise experimental model of energy losses in the source will be derived.

Besides the experimental determination of the energy loss function, also theoretical models are investigated. A first model was developed by F. Glück (see figure 4.15 and [Han17]). This model was carefully revised in [Tro18] and extended by the possibility to incorporate

[10] C. Weinheimer (2018), *Direct determination of the energy loss spectrum by applying a single time-of-flight cut*, KATRIN internal report.

the broadening of the excitation states due to the source temperature and energy resolution. Furthermore, there are two parametrisations of the energy loss function available from the Troitsk experiment which were derived in egun measurements [Ase00; Abd17]. Currently, the application of the various models for KATRIN is being evaluated. Important parameters are for instance the model uncertainties which define the associated neutrino mass shift, but also differences between the models have to be understood.

Impact on neutrino mass determination. The KATRIN Design Report estimates the neutrino mass shift associated with the determination of the energy loss function to $\Delta m_\nu^2 < 6 \times 10^{-3}\,\mathrm{eV}^2/c^4$ [Ang05]. In this thesis, no update on the neutrino mass shift can be given. First, a high-statistics measurement of the energy loss function with KATRIN is required, and then the correct model has to be built to ensemble-test the measurement against it. Furthermore, the involved uncertainties of both the measurement and the model have to be fully evaluated. The necessary investigations are currently in progress and first results are expected for early 2019.

Relevance for KATRIN and current status. The energy loss function is one of the major systematic uncertainties and its correct and precise determination is mandatory for the success of the experiment. Large efforts were put in the development of measurement methods and theoretical models over the past years. In order to be able to quantify the influence of the energy loss function on the neutrino mass, the following next steps are necessary:

- Both measurement methods outlined above were tested in autumn 2018. In a next step, high-statistics measurements are necessary together with a full characterisation of the involved uncertainties, which are for instance the egun rate stability or the stability of the column density.
- So far, literature-based models alone (including the one developed recently in [Tro18]) do not fully satisfy the stringent uncertainty requirements of KATRIN, despite considerable progress made. Improvements from either the theoretical/numerical or the experimental side are necessary to determine the model parameters with the required accuracy. The parametrisations of the energy loss function from Troitsk [Ase00; Abd17] have to be evaluated whether they are directly applicable for KATRIN. Adjustments may be necessary to account for the different energy resolution of KATRIN, for instance.
- The integration of elastic scattering processes in the final neutrino mass analysis can be done in several ways. One possibility is to include the elastic scattering in the energy loss function and to derive it in the unfolding procedure as done in [Han17] or in the time of flight measurements. However, as the unfolding procedure applies retarding voltage steps of 0.1 V and the elastic energy loss is on the order of 0.004 eV on average [Kle18a], its contribution is easily overestimated by a factor of ≈ 25. The elastic energy losses can be calculated accurately and have such a small effect on the neutrino mass result that they are neglected in some works [Kle18a; Tro18]. At the same time, the elastic scattering leads to a small slope of the plateau of the response function (see figure 4.14) and therefore has an influence on the extracted energy loss function. A final decision on how to include the elastic scattering in the analysis model has not yet been made.

All open issues listed here are currently under investigation in the KATRIN collaboration and expected to be completed during the first neutrino mass run in 2019. It should be kept in mind that only one dedicated measurement of the energy loss is required. In principle, it is even sufficient to perform this at the end of the KATRIN tritium data-taking period.

Therefore, the KATRIN tritium operation can start in 2019 even if this crucial systematic uncertainty is not fully determined then.

4.2.17. Final-State Distribution

Description. So far only molecular tritium sources have been used for neutrino mass experiments. The problem of molecular sources is that they introduce additional degrees of freedom due to rotational and vibrational excitations on top of electronic ones of the daughter molecule. Some of the decay energy is transferred into the population of these final states, so that the shape of the beta-decay spectrum is modified (see equation 2.54). Precise theoretical calculations are required to account for this effect in a correct way and to keep the influence of the final-state distribution on the neutrino mass result as small as possible. These calculations predict the energy levels of the daughter molecule and the probability density distribution for populating them in the wake of the beta decay.

In the case of molecular tritium, a source consisting of 100 % pure T_2 is not feasible. Actually, a mixture of hydrogen isotopologues T_2, D_2, H_2, DT, HT, HD is present. The final-state distributions of different isotopologues exhibit small, distinct differences, so that final-state calculations for the tritiated molecules T_2, DT and HT are required with the corresponding daughter molecules $^3HeT^+$, $^3HeD^+$ and $^3HeH^+$. These bound states have only one electron and are therefore among the simplest molecules. Nevertheless, extensive calculations are necessary [Bod15].

The precision and trueness of the theoretical calculation introduces an uncertainty on the tritium beta-decay spectrum and thus a shift of the neutrino mass. Besides this uncertainty contribution from the theoretical description, there are additional contributions from experimental parameters which enter the final-state calculation as input variables. These experimental parameters are the tritium source temperature and the gas composition [Bod15]. Both are discussed in more detail in the following.

The *WGTS gas composition* is an important input parameter to the initial- and final-state distribution. As mentioned above, the final-state distributions for the tritiated molecules T_2, DT, HT differ slightly from each other. Also the beta spectra of the three isotopologues are different. In the final analysis, they are summed up according to their fraction of the total gas flow. Hence, the gas composition has to be measured and the trueness of the measurement is an uncertainty contribution for the total initial- and final-state distribution. The same is true for the stability of the gas composition, which introduces also an uncertainty on the molecular states. From the three tritiated molecules, T_2 as a homonuclear molecule has furthermore a sub-distribution of ortho (nuclear spin $I = 1$, triplet) and para ($I = 0$, singlet) states. Since the total wave function of T_2 has to be antisymmetric, the antisymmetric para state comes with a symmetric spatial wave function (even J), and the symmetric ortho state comes with an anti-symmetric spatial wave function (odd J). Transitions between ortho and para states are suppressed at cryogenic temperatures. As the ortho-para ratio influences the rotational excitation distribution of T_2, the main gas component of the source, it is an essential ingredient for the final-state distribution calculation. The T_2 molecules start at room temperature with an ortho-para ratio of $\lambda = 0.75$. How the ratio evolves towards the cryogenic temperatures inside the beam tube depends on the retention time of the molecules at cryogenic temperatures. Thus, the cryogenic ortho-para ratio has either to be measured or to be simulated. More details on the ortho-para ratio can be found in [Bod15; Kro14].

The *WGTS temperature* affects the final-state distribution calculation in several ways: through the trueness of the absolute temperature determination, through the stability of the

WGTS temperature over time and through the excitation of higher rotational states [Bod15]. On the one hand, the trueness of the temperature measurement introduces a smearing of the initial and final states, and on the other hand an uncertainty on the resulting Doppler broadening of the distribution. Both the initial- and final-state distribution and the Doppler contribution are also affected by the temperature stability of the source, since temperature fluctuations cause an additional smearing. Finally, the measured beam-tube temperature will not necessarily equal the temperature of the rotational states in the case of T_2. At temperatures of 30 K, the population of only the ground rotational state and the first rotationally excited state are expected. However, since the gas is accommodated at room temperatures before it is guided towards the WGTS central beam tube and as the selection rules due to ortho-para states prevent transitions with $\Delta J = 1$, it can be the case that higher rotational states survive in the WGTS. Their contributions have to be estimated and in the best case measured.

Experience from former neutrino mass experiments. The influence of the final-state distribution on the neutrino mass result is a well-known problem for many tritium-based experiments and was firstly discussed in [Ber71], see also the reviews [Rob88; Ott08]. Different experiments have utilised independent final-state calculations: Mainz [Kra05] implemented the Saenz calculation [Sae00], while Troitsk [Ase11] relied on the calculations by Jonsell [Jon96]. Because of the large effect of the assumed final-state distribution on the beta decay spectrum, results from two neutrino mass experiments with varying final-state calculations should be compared very carefully. This is illustrated by the experience of the Los Alamos neutrino mass experiment, which gave a final result of $m_\nu^2 = (-147 \pm 68 \pm 41)\,\mathrm{eV}^2/c^4$ [Rob91]. Reevaluating the old data sets with today's final-state distribution calculation eliminates the negative mass squares [Bod15]. This shows how important accurate and reliable final-state distributions are for the outcome of a neutrino mass experiment based on a molecular source.

Determination for KATRIN. Two different code sets are available for KATRIN, one calculation by Saenz et al. [Sae00] and one by Doss [Dos06; Dos07]. Both provide ASCII files for the initial rotational states $J_i = 0, 1, 2, 3$ of the tritiated molecules T_2 and DT (Doss) and T_2 and HT (Saenz) containing the energy states and the corresponding probability of the final states. The Doss data provides a binning of 0.01 eV and the Saenz data a binning of 0.1 eV for the ground state and a binning of 1 eV for the electronic excitations. An example for T_2 is plotted in figure 4.16. In SSC (see section 3.3), the files are weighted with the gas composition of the source and the Boltzmann distribution of the initial states calculated with the source temperature. Here, the ortho-para ratio of T_2 has to be taken into account. If now a complex source model is needed in which the source is divided into a large number of slices/voxels, the weighting of the final-state distributions for every voxel is very time-consuming. To reduce the computation time, a rebinning scheme is implemented, which adapts the binning size at the user's discretion, since the binning in the provided files by Doss is smaller than required [Kle14].

The two final-state distributions available for KATRIN agree well for excitation energies below 40 eV [Dos07]. For higher energies, deviations occur. Therefore, the Saenz group is currently working out a new calculation of the final-state distribution including an estimate of theoretical/numerical uncertainties. A user-friendly code will be provided to the KATRIN collaboration to allow for user-defined binnings. Especially the theoretical uncertainties are important information, since there are only very limited possibilities to access the final-state spectrum experimentally. One testable prediction of the theory is the branching ratio into the bound $^3HeT^+$ state. Former experiments reported deviations from theory. Hence, a new experiment, the Tritium Recoil-Ion Mass Spectrometer (TRIMS),

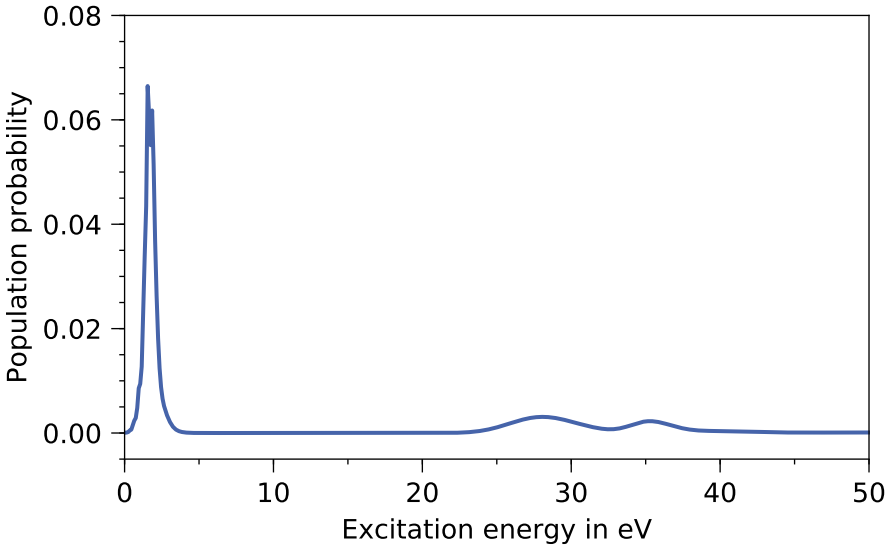

Figure 4.16.: Final-state distribution for T_2 decay in HeT^+. The plot shows the population probability for excited states in the bound $^3HeT^+$ after the decay of T_2 ($J = 0$). The peak at $\approx 2\,\text{eV}$ is the electronic ground state. Electronic excitations start at excitation energies of $> 25\,\text{eV}$. Plotted data from [Dos07] in a 0.1 eV binning.

will test more precisely the conditions to which theoretical calculations apply [Bod15].

Many efforts are also put in the precise determination of the experimental input parameters for the initial-state distribution. The WGTS temperature is measured with 24 PT500 sensors distributed along the central beam tube. In the scope of the thesis at hand it is demonstrated that the trueness of the calibrated temperature sensors at 30 K is 160 mK (83 mK if the settings are improved) with a relative stability of $(0.005 \pm 0.001)\,\%$ per hour, see section 6.2.2 and appendix A.1. These results are close to the temperature trueness requirement for the final states of 150 mK at 30 K and well below the stability requirement of 0.1 % [Bod15].

The gas composition is determined with a laser Raman (LARA) system developed for KATRIN purposes [Stu10b; Sch13a]. It is mounted in the inner loop (see figure 3.3). The Raman effect, a second-order inelastic scattering process of light off gas molecules, is used to determine the gas species present in the mixture as well as their relative amount. The parameters of interest are the isotopic purity ϵ_T, which represents the relative amount of tritium isotopes in the gas mixture, and the HT to DT ratio κ. The trueness requirements for both quantities are $\Delta\epsilon_T/\epsilon_T \leq 0.03$ and $\Delta\kappa/\kappa \leq 0.1$. It was demonstrated that the requirements are kept with $\Delta\epsilon_T/\epsilon_T = 0.001$ and $\Delta\kappa/\kappa = 0.05$ [Zel17].

The ortho-para ratio cannot be measured in the current KATRIN setup. Measurements at room temperature are in principle possible with the LARA system, but such measurements are not able to determine the actual ortho-para ratio λ inside the beam tube at cryogenic temperatures. Thus, simulations were performed. Due to a very short transit time of 1.5 s of the T_2 molecules at the 30 K region of the WGTS, it can be assumed that the ortho-para ratio of room temperature ($\lambda = 0.75$) is also maintained in the WGTS with an uncertainty of 3 % [Kro14].

The rotational temperature of the tritiated molecules can be assumed to be thermalised to

Table 4.13.: Uncertainties of the molecular final-state distribution. The table presents the target uncertainties related to the final states and the corresponding neutrino mass shifts as calculated in [Bod15]. The values have to be updated as soon as the new calculation of the final-state distribution (FSD) is approved by the KATRIN collaboration.

Systematic effect	Uncertainty	Δm_ν^2 in $10^{-3}\,\mathrm{eV}^2/c^4$
Theoretical calculation	$\lvert\Delta\sigma_{\mathrm{FSD}}/\sigma_{\mathrm{FSD}}\rvert \leq 1\,\%$	6
Temperature calibration	$\lvert\Delta T/T\rvert = 0.005$	
Translational		0.05
FSD		0.06
Temperature stability	$\lvert\Delta T/T\rvert = 0.001$	
Translational		0.009
FSD		0.01
Ortho-para ratio	$\lvert\Delta\lambda/\lambda\rvert = 0.03$	0.44
Isotopic impurities		
Tritium purity	$\lvert\Delta\epsilon_{\mathrm{T}}/\epsilon_{\mathrm{T}}\rvert \leq 0.03$	2.9
HT to DT ratio	$\lvert\Delta\kappa/\kappa\rvert \leq 0.1$	0.03
Higher rotational states	$\lvert\Delta T_{\mathrm{rot}}/T_{\mathrm{rot}}\rvert \leq 0.1$	1.00

the physical temperature of 30 K. This is the result of a calculation[11]. The requirement formulated in [Bod15] aims for a determination of the rotational temperature with 10 % trueness, which should be kept according to the calculations. However, further studies are necessary to check if all pre-conditions of the calculation, e. g. a Maxwell-Boltzmann distribution of velocities, are fulfilled. It should be noted that the rotational temperature does not influence the ortho-para ratio. The distribution of the ortho and the para states follow the rotational temperature independent of each other, so that the overall ortho-para ratio stays the same.

Impact on neutrino-mass determination. The KATRIN Design Report sets an upper limit on the neutrino mass shift associated with the final-state distribution of $\Delta m^2_{\nu,\mathrm{FSD}} < 6.0 \times 10^{-3}\,\mathrm{eV}^2/c^4$ [Ang05]. This equals an uncertainty of 1 % of the theoretical calculations, but does not take any uncertainties of the experimental input values into account. A more comprehensive picture is given in [Bod15] and the results from this publication are summarised in table 4.13. It should be noted that the given uncertainties are estimations based on KATRIN Design Report values and they have to be updated when the new calculations of the final-state distribution by the Saenz group are available. Especially the 1 % uncertainty of the theoretical calculations as the largest uncertainty contribution has to be confirmed or improved. Furthermore, the neutrino mass shifts of the experimental parameters are based on a semi-classical calculation of the width of the final-state distribution [Bod15]. The calculations should be repeated with the widths from the new calculations and with actual measurement values of the input parameters. As outlined above, in most of the cases the experimental uncertainties of the input parameters are much smaller than assumed in the table, so that the total uncertainty of the final-state distribution will be dominated by the theoretical calculation. However, an updated neutrino mass shift cannot be stated here for the time being.

Relevance for KATRIN and current status. The final-state distribution is one of the major uncertainties of KATRIN, even early on during the first data-taking. The correct implementation of the final-state distribution requires precise theoretical calculations,

[11] M. Schlösser and A. G. Ureña (2015), *Rotational temperature of tritium in the WGTS gas feed*, KATRIN internal report.

simulations and experimental input from several sensors from the WGTS. The interplay of these different parameters has to be considered carefully. The fact that with a new final-state calculation it was possible to eliminate the negative neutrino mass squares of the Los Alamos experiment as mentioned above should be, on the one hand, a warning, but on the other hand this can also be a hint that today's calculations should be able to achieve the required precision. Alas, the new code by the Saenz group is not finished yet. The uncertainties listed in table 4.13 have to be updated as soon as the new calculations are verified and implemented.

Besides the theory input, there are still some open questions regarding the experimental values. It is known from test measurements that the tritium purity can exhibit temporal and spatial variations due to exchange reactions with hydrogen isotopologues present in the walls of the tubes [Fis11]. Since the laser Raman cell is mounted several meters before the WGTS beam tube, an estimation is necessary how the gas composition can change on its way towards the source tube. Furthermore, an experimental determination of the rotational temperature and the ortho-para ratio would enhance the reliability of the simulation results and could reduce the uncertainties.

4.2.18. Slope of the Background Rate

Description. As shown in figure 3.11, the background rate of KATRIN is one of four free fit parameters, and to measure it, about one third of the measurement time is distributed uniformly in an interval comprising at least 5 eV above the endpoint of the spectrum. A flat background rate influences the statistical uncertainty at every retarding voltage step. Would the background rate depend on the retarding voltage, this slope would influence the shape of the beta spectrum, and, if not accounted for in the analysis, would cause an error on the neutrino mass analysis [Ang05].

Experience from former neutrino mass experiments. Also in previous experiments such as the ones at Mainz and Troitsk, the background rate was one of four fit parameters. While in Mainz no slope of the background rate was found and the background was taken as constant [Kra03], in Troitsk a slope of $< 0.5\,\mathrm{mcps/keV}$ was measured [Ang05]. Both experiments showed a total background rate on the order of 10 mcps.

Determination for KATRIN. The KATRIN setup comprises several measures to counteract background. For instance, the detector is shielded against external radioactivity (see section 3.2.7), and the main spectrometer has an inner layer of electrodes to reject electrons coming from the spectrometer walls (see section 3.2.5). Nevertheless, the background rate in the main spectrometer of the order of 0.5 cps [Are18b] is a factor of ≈ 50 larger than anticipated in the Design Report [Ang05]. In the last years, several background processes like muon-induced electrons, Penning traps or secondary electrons from the decay of ^{219}Rn/^{220}Rn were successfully suppressed and ruled out as major background contributions [Frä17]. Investigations have shown that the inner surface of the main spectrometer is contaminated with $\approx 1\,\mathrm{kBq}$ of ^{210}Pb [Frä17]. Neutral Rydberg atoms created in the decay of ^{210}Pb can reach the inner volume of the main spectrometer, where they are ionised by thermal radiation. This process is assumed to be the major remaining background contribution of KATRIN [Frä17; Tro18].

The slope of the background rate is also a systematic effect. The energy spectrum of background electrons coming from Rydberg states is expected to be independent of the main spectrometer retarding voltage [Blo18]. However, background electrons with energies $> 1.2\,\mathrm{eV}$ can be stored in the volume of the main spectrometer depending on their emission angle towards the magnetic field. As storage conditions depend on the retarding voltage,

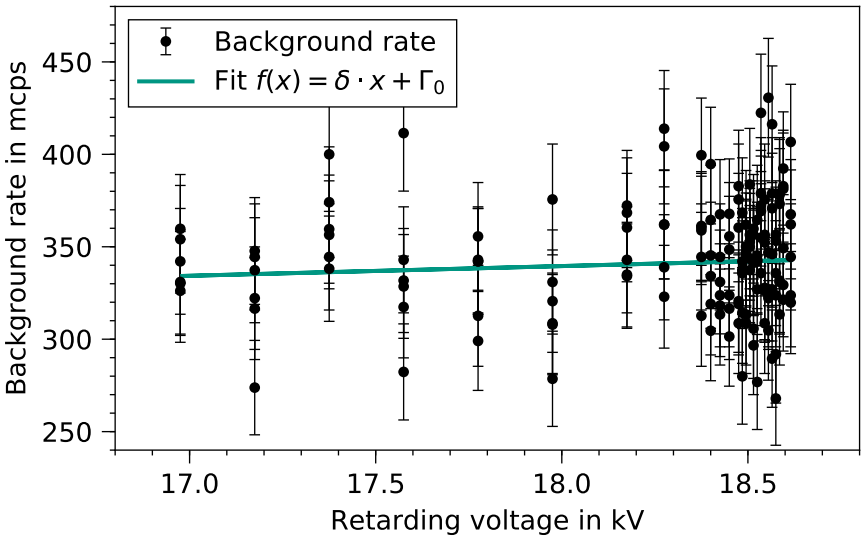

Figure 4.17.: Slope of the background rate. The plot shows background data taken with a magnetic field of 6×10^{-4} T in the analysing plane for ≈ 20 h during KATRIN's first tritium campaign in summer 2018. The valve to the transport section is closed, so that only background from the spectrometer section is recorded. The region of interest (see equation 5.4) is set to [14 keV, 32 keV]. The fit parameters are $\delta = (5.3 \pm 4.9)$ mcps/keV and $\Gamma_0 = (244.9 \pm 89.3)$ mcps. The reduced χ^2 value is 1.1. An upper limit of $\delta < 7.8$ mcps/keV (68 % C. L.) is derived. A linear model is selected according to [Ang05]. Data kindly provided by F. Block.

this effect could lead to a slope of the background rate. Since the energies of the background electrons range up to the eV scale[12], a dependence of the background rate on the retarding voltage cannot be excluded [Blo18].

In the region below the endpoint energy of tritium (< 18.6 keV), the background slope can only be measured with the full KATRIN beam line before tritium is injected to the source. Above the endpoint, the full beam line can be used when tritium is in the source. The determination of the background slope is quite time-consuming due to the low count rate. At the end of 2017 and beginning of 2018, three campaigns to measure the background slope were conducted with measurement times of up to one week for five data points distributed between 18.0 and 19.0 keV [Blo18]. The result of a new measurement[13] with more data points but less measurement time performed in summer 2018 is presented in figure 4.17.

Impact on neutrino-mass determination. In the KATRIN Design Report, a neutrino mass shift of $1.2 \times 10^{-3}\,\mathrm{eV}^2/c^4$ is assigned for a slope of the background rate of < 0.5 mcps/keV [Ang05]. Based on the upper limit of the background slope of $\delta < 7.8$ mcps/keV (68 % C. L.) derived from the data plotted in figure 4.17, a neutrino mass shift of $\Delta m_{\nu,\,\mathrm{slope}} < 14.2 \times 10^{-3}\,\mathrm{eV}^2/c^4$ is introduced if the slope is ignored in the final analysis. It should be noted that this measurement was performed with an increased magnetic field strength in the analysing plane of 6×10^{-4} T. Therefore, it cannot be compared to the neutrino mass shifts given for the other systematic uncertainties in this thesis directly. Furthermore, the low statistical significance of this result and the fact that the data plotted in figure 4.17 is also well described with a constant of (320 ± 2) mcps

[12] A. Pollithy, internal talk, 35th KATRIN collaboration meeting, 2018.

[13] For details of the measurement and the analysis, see the internal report by F. Block and A. Pollithy (2018), *KATRIN Analysis Report. Voltage dependence of the main spectrometer background near the endpoint of tritium.*

(reduced χ^2 value of 1.1) without any background slope makes it impossible to state a shift in the neutrino mass value here which is well motivated. The uncertainties are too large calling for more detailed investigations.

Relevance for KATRIN and current status. The slope of the background rate is currently one of KATRIN's major open questions. Taken face value, the upper limit stated above is close to the overall systematics budget of KATRIN of $0.017\,\mathrm{eV}^2/\mathrm{c}^4$. However, the statistical significance is too low to provide a reliable constraint. Due to the small count rate, very long measurement times are necessary to measure the background slope more precisely. As soon as the background slope is measured and it is verified that the slope is stable over time, it can be incorporated in the analysing model. Then, of course, the associated neutrino mass shift can be drastically reduced compared to the case when the background slope is neglected all together [Blo18]. Therefore, further investigations on this effect are crucial for the success of KATRIN.

Even if the investigations will show that the background slope is vanishing, the increased background level in comparison to the KATRIN design goal of 10 mcps make several countermeasures in KATRIN operation necessary to compensate for the corresponding decrease of statistical sensitivity. Possible measures currently being studied are the increase of the magnetic field strength in the analysing plane in order to reduce the volume of the main spectrometer being mapped on the focal plane detector, the extension of the analysing interval and an optimised measurement time distribution for the retarding voltage steps [Kle14; Tro18]. Simulations have shown that such measures would be efficient in recovering the statistical sensitivity [Tro18]. However, these changes of operational parameters can also affect some of the systematic effects discussed in the previous sections, so that the background has an indirect influence on the systematic budget of KATRIN which goes beyond the background slope determination. The consequences for the other systematic effects of these countermeasures are further discussed in section 4.4.

4.3. Summary of Systematic Uncertainties

The results of the previous section are summarised in table 4.14. The full evaluation of all systematic effects at Design Report conditions has shown that there are still five systematic effects which have not been finally quantified yet. With the final-state distribution, the energy loss function and the slope of the background rate, three large contributions are currently pending a concluding evaluation, while the systematic effects related to detector effects or to ions in the transport section are expected to be small in comparison.

The table allows the specification of systematic effects of KATRIN: there are theoretical corrections, which do not influence the final neutrino mass result as long as they are fully incorporated in the model, the relativistic correction of the transmission function, for instance. A second class of uncertainties leads to constant shifts towards negative or positive values of m_ν^2. These are constant distortions of the integral spectrum which can only be accounted for to a certain level of uncertainty in the model. The third class of uncertainties are fluctuating parameters which directly translate into a two-sided uncertainty of m_ν^2. It should be mentioned here that these two-sided uncertainties lead often to slightly asymmetric Δm_ν^2, which is neglected in the scope of this thesis.

4.4. Conclusion

In this chapter, the systematic effects of KATRIN have been evaluated and quantified whenever it was possible. Based on this evaluation for KATRIN Design Report conditions, the

Table 4.14.: Systematic uncertainties of KATRIN. The table summarises the results of section 4.2. The neutrino mass shift is given for the KATRIN Design Report setting (see table 4.1). The results are discussed in the main text.

Systematic effect	$\Delta m^2_{\nu,\mathrm{KDR}}$ in $10^{-3}\,\mathrm{eV}^2/c^4$	section
Theoretical corrections of the β spectrum	0.0	4.2.1
Relativistic correction of transmission function	0.0	4.2.2
Synchrotron radiation	−0.2	4.2.3
Doppler effect	±0.2	4.2.4
Modified angular distribution of electrons	0.0	4.2.5
Analysing plane: potential and magnetic field		4.2.6
– absolute magnetic field	±2.5	
– radial inhomogeneities	−0.3	
HV stability	−0.6	4.2.7
Detector-related effects	in progress	4.2.8
Ions	in progress	4.2.9
Backscattering at rear wall	< 0.1	4.2.10
Source magnetic field	±1.9	4.2.11
Trapped electrons in WGTS	< 0.1	4.2.12
Potential variations in WGTS	−0.7	4.2.13
Gas dynamics in WGTS	±3.0	4.2.14
Monitoring of column density	±0.2	4.2.15
Energy loss function	in progress	4.2.16
Final-state distribution	in progress	4.2.17
Slope of the background rate	in progress	4.2.18

following conclusions can be drawn: this thesis offers the first complete list of systematics. Five out of eighteen systematic uncertainties cannot be conclusively quantified yet. With the investigations for their quantification ongoing, results are expected for 2019, so that the full systematic budget will be known when regular tritium operation starts. Most of the systematic uncertainties which were quantified in this thesis, add only small contributions on the order of $10^{-4}\,\mathrm{eV}^2/c^4$ to the total uncertainty budget. The largest known contributions come from the uncertainty of the magnetic field strength in the analysing plane, the source magnetic field and the gas dynamics in the source.

In this thesis, a consistent setting was used for all ensemble tests performed. This helped to identify discrepancies to former investigations: for the radiative corrections of the beta spectrum (see section 4.2.1), the opposite sign was found for the associated neutrino mass shift than stated in the corresponding paper. For the gas dynamics, in the literature only a one-sided neutrino mass shift was given, but it was demonstrated in the ensemble tests that actually a two-sided neutrino mass shift has to be taken into account (see section 4.2.14). The independent check of all systematic uncertainties performed in this thesis is therefore a helpful contribution towards the correct implementation of the systematic effects in the analysis of the KATRIN neutrino mass data-taking starting in 2019.

It should be emphasised again that the presented neutrino mass shifts are derived for KATRIN Design Report conditions (see table 4.1). As already shortly discussed in sec-

tion 4.2.18, the actual background rate in the main spectrometer is a factor of ≈ 30-50 larger than expected. The increased background leads to a reduced statistical uncertainty of KATRIN and hence to a deteriorated neutrino mass sensitivity. However, several countermeasures have already been discussed [Kle14; Tro18]: first, increasing the magnetic field in the analysing plane reduces the volume of the main spectrometer being mapped on the focal plane detector. This reduces also the background rate. Second, the analysing interval can be extended deeper into the tritium beta spectrum, for instance until 50 eV below the endpoint. This reduces the statistical uncertainty further. Third, the measurement time distribution of the voltage set points can be optimised. As depicted in figure 3.11, the standard KATRIN measurement time distribution is flat besides one prominent peak at a signal to noise ratio of 2. It was demonstrated that the measurement time can be placed more efficiently to reduce the statistical uncertainty [Kle14].

These countermeasures also affect the determination and quantification of systematic effects. An increased magnetic field in the analysing plane will broaden the edge of the transmission function, for instance. This could presumably influence the neutrino mass shift associated with effects like synchrotron radiation which manifest as a change of the shape of the transmission edge. An increase of the analysing interval will require the incorporation of scattering processes of higher orders (more than three-fold scattering). This will have a direct impact on the systematic uncertainties of the gas dynamics and the energy loss function.

Therefore, there are detailed studies ongoing at the moment in the KATRIN collaboration to find optimised operational parameters which reduce the impact of the increased background rate on the statistical uncertainty and the systematic uncertainties at the same time. The neutrino mass shifts for KATRIN Design Report conditions obtained in this thesis are therefore important benchmarks. As soon as the optimised setting is found, a re-evaluation is necessary.

Towards the determination of the total systematic uncertainty budget, the following recommendations are made:

- In this thesis, the individual contributions to the systematic uncertainty budget of single effects have been derived in ensemble tests. The results obtained are sometimes not comparable to former investigations since the settings of the ensemble tests may differ. It is therefore recommended to define a standard set of ensemble-test parameters to make comparisons between different investigations more straightforward.
- The ensemble-test method is very time-consuming on the order of several weeks to months of computation time on a lab-grade compute cluster for determining the full systematic uncertainty budget. With 5000 KATRIN measurements being simulated per ensemble test, the statistical uncertainty on the neutrino mass shifts was $0.2\,\mathrm{eV}^2/c^4$. If it is decided to investigate and quantify systematic effects with ensemble tests in the future, too, methods have to be developed to decrease computational demands or to use resources more efficiently so as to be able to react quickly on changes of the experimental operation.
- While in this work only ensemble tests have been performed, there are also investigations ongoing to determine the total uncertainty budget of KATRIN with the covariance matrix approach [Sch19] (see section 4.1). Furthermore, the pull method can be applied. As demonstrated in this thesis, there are different types of systematic effects involved in KATRIN. Some are determined in stand-alone commissioning measurements, some are frequently monitored and some are based on theoretical calculations and simulations. It is expected that some of these effects are taken into account better with one of the three methods, and others are taken into account

better with another method. The computational time is for instance one parameter which may differ between the methods for a given systematic effect. This requires detailed comparisons of the three different approaches, which should be performed before the first neutrino-mass result can be derived.

5. Commissioning the KATRIN Beam Line with ^{83m}Kr

In July 2017, a measurement campaign with ^{83m}Kr was performed using the entire KATRIN beam line. The metastable ^{83m}Kr de-excites via internal conversion and offers a spectrum of several sharp conversion electron lines which can be used for different calibration purposes (see figure 5.1). In section 5.1, the motivation for this dedicated measurement campaign and its experimental conditions and measurement goals are presented. Section 5.2 discusses why ^{83m}Kr is an important calibration tool and how it is used in the gaseous ^{83m}Kr source of KATRIN. The analysis of ^{83m}Kr conversion electron lines with KATRIN software is explained in section 5.3. In the gaseous ^{83m}Kr measurement campaign in July 2017, all parts of the ^{83m}Kr conversion electron spectrum have been measured and analysed. The results are presented and discussed in section 5.4. Final concluding remarks are given in section 5.5.

5.1. The Gaseous ^{83m}Kr Measurement Campaign 2017

The gaseous ^{83m}Kr measurement campaign in July 2017 was conducted in a preliminary configuration, since the setup of the inner loop system (see figure 3.3) was not yet finished at that time. Leading up to the tritium commissioning, this configuration allowed to test the operational readiness of the ^{83m}Kr generator and almost the entire data-taking and analysis chain of KATRIN. The various aspects of the motivation to perform this campaign are explained in section 5.1.1. The unusual configuration of the gaseous ^{83m}Kr generator required some additional changes of operational parameters of the KATRIN beam line in contrast to the standard operation with gaseous ^{83m}Kr in the WGTS. The measurement conditions and measurement goals are discussed in section 5.1.2.

5.1.1. Motivation

^{83m}Kr is a versatile nuclear standard for calibration purposes in astroparticle physics. Its usage is also reported for former neutrino mass experiments [Dec90b; Rob91; Pic92; Bel08]. Based on this experience, the KATRIN beam line comprises three different ^{83m}Kr sources [Ang05]: a gaseous source for the WGTS (see section 3.2.1), a condensed source in the CPS (see section 3.2.4) and an implanted one in the monitor spectrometer (see section 3.2.6). Since 2016, a comprehensive measurement programme for the commissioning of the sources was planned. However, it turned out at the beginning of 2017, that the standard loop operation of KATRIN, where the source gas is pumped in a closed loop system with a stabilised flow rate (see figure 3.3), would not be possible before 2018.

Therefore, as a major part of the work presented in this thesis, a measurement campaign with an adapted programme was proposed in which the loop operation would not be necessary. Two weeks of measurement were assigned to this campaign: one for the

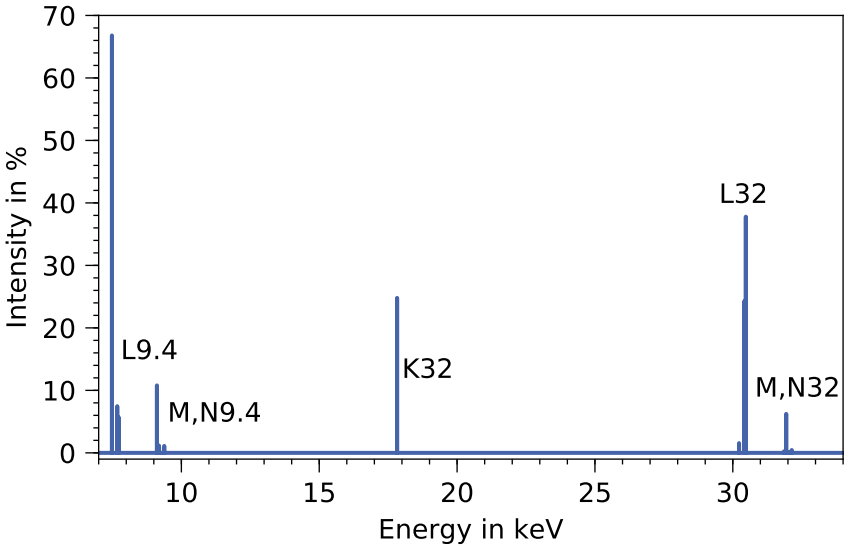

Figure 5.1.: Conversion electron spectrum of ^{83m}Kr. The plot shows the full conversion electron spectrum of ^{83m}Kr. The lines cover a wide energy interval from 7 keV to 32 keV. The intensities sum up to 100 % for the 9.4 keV and 32 keV transition individually (see figure 5.3). The properties of the conversion electron lines are listed in table 5.2.

gaseous source operation, one for the condensed source operation. Since the setup and the handling of both sources is not trivial, the main motivation was to get a first test of the final setups of the ^{83m}Kr sources with the entire KATRIN beam line and to test their performance. For the gaseous source, the main goal was to demonstrate its capability to measure the potential inside the WGTS as described in section 4.2.13. Since no tritium would be in the source during the proposed measurement campaign and therefore also no plasma potential created, it should be demonstrated that a conversion line position can be measured with meV precision, which is one important prerequisite for the potential determination. Moreover, during the preparation of the measurements, it became more and more obvious that the ^{83m}Kr campaign would have benefits for several more aspects of the KATRIN commissioning: the gaseous ^{83m}Kr in the WGTS would be the first possibility to test the KATRIN analysis chain from raw data to a high-level analysis with uniformly distributed electrons of isotropic angular emission, just as in the tritium case. Furthermore, it gave the first opportunity to train the control of the full KATRIN beam line including the operation of all superconducting magnets at once at standard field settings and the operation of the main spectrometer for voltages from 0 kV to −35 kV. Finally, there was the opportunity to characterise important properties of KATRIN, for instance the linearity of the overall energy scale, the system alignment and detector properties.

Thus, this two-weeks measurement campaign became one of the major milestones of the KATRIN experiment. As the next sections show, the findings of the ^{83m}Kr measurements in summer 2017 were the basis for the first tritium operation of KATRIN in 2018.

5.1.2. Setup and Measurement Goals

Running the source cryostat in ^{83m}Kr mode requires important changes to the WGTS operation, since the beam tube temperature has to be raised from 30 K to 100 K (see also sections 3.2.1 and 6.2.1). However, as the loops were not in operation during the gaseous ^{83m}Kr measurements presented here, also other KATRIN components were not operated under the standard conditions described in chapter 3. The following list gives a short

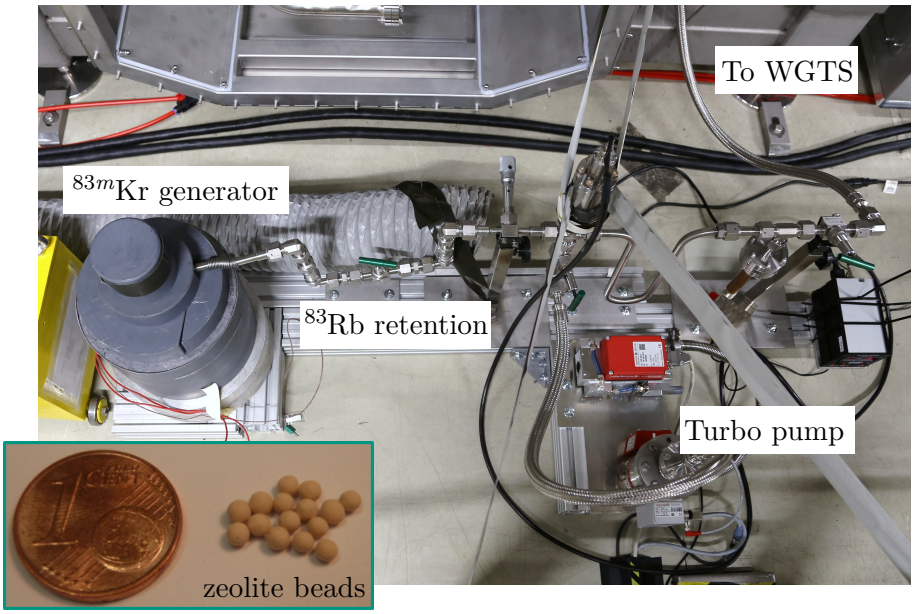

Figure 5.2.: The gaseous ^{83m}Kr generator. The picture shows the setup of the ^{83m}Kr generator next to the WGTS. Zeolite beads loaded with 1 GBq of ^{83}Rb are placed inside a shield of lead. The ^{83m}Kr emanates and diffuses towards the WGTS. On its way, several filters prevent the ^{83}Rb with a comparably long half life of 86.2 d [Vén18] from entering the WGTS to avoid long-term contaminations. The system can be evacuated by a turbo molecular pump. A detailed technical description can be found in [Sen18].

overview of the status of the KATRIN beam line during the gaseous ^{83m}Kr campaign in summer 2017:

- The magnetic fields along the entire KATRIN beam line were in standard operation, that means the field strength of all superconducting coils was 70 % of the nominal values stated in [Are18c]. The rear section magnet was always switched off.
- For the air coils of the main spectrometer, four different settings were determined in the course of this work to achieve four distinct magnetic field values in the analysing plane: 1.0×10^{-4} T, 2.7×10^{-4} T, 9.7×10^{-4} T, 13.5×10^{-4} T. They allowed to test different energy resolutions of the MAC-E filter according to equation 3.4.
- The high voltage of the main spectrometer was operated up to -35 kV. Since the resolution of the MAC-E filter depends on the magnetic field strength of the pinch magnet and the analysing plane, as well as on the energy of the electrons, see equation 3.4, the resolution is not constant over the voltage range. Table 5.1 lists the resolution for three different energy- and for each of the four magnetic field values in the analysing plane. The post-regulation system, which smoothes the high-voltage fluctuations, was not operable during the measurement campaign.
- The operational temperature of the WGTS was 100 K. As mentioned already in section 5.1.1, the loops were not connected. No pumps were running. The gaseous ^{83m}Kr generator (see figure 5.2) was directly connected to pump port 2F, which is the WGTS pump port adjacent to the DPS. The ^{83m}Kr was fed to the system, where it could distribute freely in the beam tubes of WGTS and DPS.
- The pumps at the DPS were not running either since the loops were not connected. Therefore, ^{83m}Kr atoms were present in the DPS and conversion electrons created there could reach the focal plane detector. Since the DPS was at room temperature, a larger thermal Doppler broadening of the ^{83m}Kr lines for electrons created in this

Table 5.1.: KATRIN main spectrometer resolution during ^{83m}Kr campaign. The table shows the resolution ΔE of the KATRIN main spectrometer calculated with equation 3.4 for a maximum magnetic field of 4.2 T in the pinch magnet, the four different magnetic field settings in the analysing plane (B_{ana}) and for three different energies: 9.0 keV is for the energy of conversion electrons of the 9.4 keV transition of ^{83m}Kr, 18.6 keV equals the tritium endpoint and is close to the K-32 line of ^{83m}Kr, 30.5 keV is close to the position of the frequently-measured L_3-32 line. For most of the measurements, the 2.7×10^{-4} T setting is used.

B_{ana} in 10^{-4} T	ΔE(9.0 keV) in eV	ΔE(18.6 keV) in eV	ΔE(30.5 keV) in eV
1.0	0.21	0.44	0.73
2.7	0.58	1.20	1.96
9.7	2.08	4.30	7.04
13.5	2.89	5.98	9.80

section was expected. To separate the electrons being created in the DPS from those from the WGTS, the dipole electrodes inside the DPS beam tube elements (see section 3.2.3) were operated as monopoles. For most of the measurements, a voltage of +350 V was applied, so that the electrons coming from the DPS had a lower starting energy and thus were filtered out by the main spectrometer retarding voltage.

- The CPS was the only pump running in the source and transport section during the measurement. Its beam tube temperature of the beam tube elements 2-5 was adjusted to ≈ 4.5 K. The beam tube elements were not covered by the argon frost layer as in standard KATRIN operation (see section 3.2.4), but ^{83m}Kr was adsorbed directly to the metal surface so that it could not reach the main spectrometer [Are18b]. In advance the CPS capacity was estimated to be large enough for the amount of krypton planned to be used.
- The monitor spectrometer ran in parallel to the other two ^{83m}Kr sources. The gaseous one and the condensed one cannot be operated at the same time, since the condensed source downstream of the CPS blocks the electrons coming from upstream.

Although the measurement conditions were somewhat different from the standard KATRIN operation, the benefits for KATRIN were expected to be large. For the detailed planning of the ^{83m}Kr measurement campaign, several measurement goals were defined in advance as a part of this thesis work. The measurement goals are discussed briefly in the following:

Measurement of K-32 and L_3-32 line The most important goal of the gaseous ^{83m}Kr campaign is to demonstrate the ability of KATRIN to measure the K-32 and L_3-32 line (see table 5.2). Both lines are of special interest for KATRIN: the K-32 line, with an energy of 17.8 keV, is situated close to the tritium endpoint of 18.6 keV. The L_3-32 line has a natural width of only 1.2 eV at an energy of 30.5 keV and is therefore a good candidate for precision measurements. Furthermore, both lines are the two most intense lines in the spectrum of the 32 keV transition. The demonstration of the capability to measure these lines means to identify their positions on the KATRIN energy scale with a precision on the order of meV [Mac16] and to gain a reasonable count rate of several thousands of counts per second. This would guarantee sufficient statistics for the standard ^{83m}Kr mode of the WGTS later on (see also section 4.2.13).

Linearity of energy scale ^{83m}Kr offers lines of conversion electrons up to 32.1 keV [Vén18] and is therefore a unique tool to test the linearity of KATRIN's energy scale over a wide energy range. For doing so, the line positions of all conversion lines have to be

measured precisely and compared to literature values. A measurement before tritium contamination enables also the investigation of the low-energy lines of the 9.4 keV transition, which will not be possible later on since these lines will be hidden in the background formed by the continuous tritium beta spectrum.

Stability of energy scale As described in section 4.2.7, the measurement of the retarding high voltage of the main spectrometer is not trivial. There are fluctuations in the high voltage because the main spectrometer acts as an antenna. These are normally smoothed by a post-regulation system, which was not yet in operation during the gaseous ^{83m}Kr campaign. In addition, also long-term drifts can occur if the high-voltage divider or the high-precision voltmeter do not work stably over time. Since the energies of the ^{83m}Kr electrons are constant, any observed drift of the measured position of the conversion electron lines during the measurement campaign directly points towards instabilities of the high-voltage system. This is the same principle also underlying the concept of using a monitor spectrometer (see section 3.2.6).

Work function benchmark before first tritium As explained in section 3.4.1, the energy of the tritium endpoint cannot be determined absolutely in KATRIN with high accuracy. Its value is influenced by several effects like for instance the work functions of the tritium source and the main spectrometer, which shift the energy of the electrons. The work function of the source can change with time, since it depends on the gases covering the inner surface [Sch16]. A precise line position measurement before any tritium contamination is therefore a very important reference for the future measurements, as it will help to disentangle the effects influencing the endpoint energy later on.

Adiabaticity measurements For KATRIN standard tritium operation, the full adiabaticity of guided electrons is crucial, because it guarantees a transport from the source to the spectrometer without energy loss [Ang05]. The adiabaticity condition is formulated in equation 3.2. However, for the planned sterile neutrino search, KATRIN will have to scan much deeper into the tritium beta spectrum. There will be electrons with surplus energies of several keV at certain retarding potentials, and it is expected that for them the adiabaticity of energy conversion from transverse to longitudinal energy (and vice versa) is no longer fulfilled. Therefore, these electrons will not pass the filter potential and thus will not be counted on the detector. This non-adiabaticity has to be measured and understood, and ^{83m}Kr offers very good possibilities for such investigations, since between the K-32 and the L-32 lines there is a gap of 10 keV. This region is very well-suited to investigate the adiabaticity behaviour of the high-energetic lines.

The fulfilment of these measurement goals also requires to reach several milestones of KATRIN sub-components: the 100 K operation of the WGTS has not been tested before, but it is necessary for the ^{83m}Kr mode (see also section 6.2.1). The results are discussed in section 6.2.3. Furthermore, the superconducting magnets have not run all together with KATRIN standard fields (70 % of nominal fields, see [Are18c]) before. The planned duration of about one week is also a first test of the long-term stability of their operation. For the forward beam monitor and the BIXS system, a radioactive gas in the WGTS is a unique possibility to get their "first light" from a uniformly distributed source gas. Finally, the correct interpretation of the measured rates at the detector requires the implementation of different sensor data from several KATRIN subsystems in the analysis chain.

The list above underlines that the ^{83m}Kr measurements is the first measurement campaign of KATRIN in which really all institutions of the collaboration are involved, because nearly

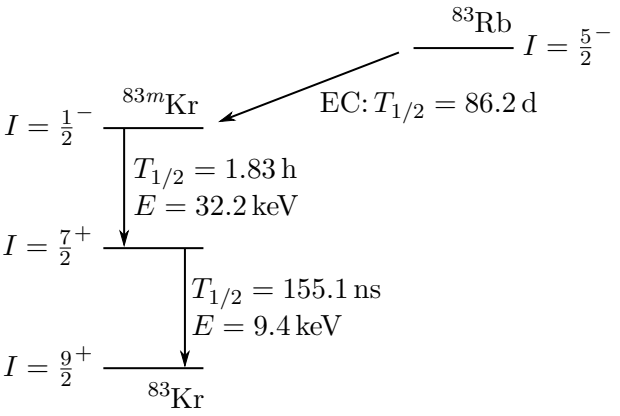

Figure 5.3.: Decay scheme of ^{83}Rb. ^{83}Rb decays in an electron capture process to metastable ^{83m}Kr with a half-life of 86.2 days. In 74 % of all ^{83}Rb decays the metastable state is produced. The ^{83m}Kr de-excites via two gamma-transitions: in the first transition with a half-life of 1.83 h, an energy of 32.2 keV is released. This transition is followed by a second transition with a half-life of 155.1 ns and an energy of 9.4 keV. The final configuration with a nuclear spin of $I = 9/2^+$ is stable ^{83}Kr. In the vast majority of the internal ^{83m}Kr transitions, the energy is not released in the form of γ rays, but as electrons, due to internal conversion (see table 5.2). The scheme is based on [Vén18].

all subsystems are in operation. This underlines the importance of these measurements on the way towards the first tritium of KATRIN.

5.2. ^{83m}Kr as a Tracer for the WGTS Potential

In KATRIN standard tritium operation with a column density of $\rho d = 5 \times 10^{17}\,\mathrm{cm}^{-2}$, about 10^{11} beta decays per second happen in the source. Most of the electrons leave the source very quickly, but the positively charged ions move much slower, so that a positive space charge is formed inside the WGTS beam tube. Together with the secondary electrons from scattering processes of the beta-decay electrons off gas molecules a low-density plasma forms. In case the local amount of negative and positive charges is not of the same size, the net energy of the beta electrons is changed. If for instance an electron is created in a positive space charge region, its energy measured with the MAC-E filter is underestimated since parts of its energy are lost for leaving the potential well. As long as this energy shift is homogeneous over the entire source, it does not affect the shape of the measured integrated spectrum and thus has no effect on the neutrino mass estimate, but only on the kinematic endpoint of the beta spectrum (see section 3.4.1). However, simulations have shown that the space charge may not be constant along the central beam tube of the WGTS [Kuc16] (see figure 4.12), so that it has to be treated as systematic effect (see section 4.2.13).

Besides spatial inhomogeneities of the plasma, also temporal instabilities could occur [Ang05; Kuc16]. Therefore, there is the option to irradiate the rear wall with UV light to compensate for the plasma and to reduce the probability of detrimental impact of plasma effects on the neutrino mass analysis [Sch16] (see also section 3.2.2). Furthermore, a voltage can be applied to the rear wall which is expected to dominate the plasma potential [Sch16]. However, to be able to adjust the rear wall voltage and irradiation in the best way for a minimum contribution of plasma effects to the overall systematics budget, the plasma has to be measured. This can be done with gaseous ^{83m}Kr as nuclear standard which is mixed to the tritium gas.

^{83m}Kr is a metastable isotope which is produced in the electron capture process of ^{83}Rb. As shown in figure 5.3, the combination of ^{83}Rb and ^{83m}Kr has several advantages for

Table 5.2.: Conversion electrons from ^{83m}Kr. The table shows the energy E_{ce}, the intensity per transition I_{ce} and the natural line width Γ_{ce} of conversion electrons from ^{83m}Kr for the two transitions of 9.4 keV and 32.2 keV. The lines are named after the shell (capital letter) and subshell (lowered number) which the electron is emitted from. The values are taken from [Vén18].

	9.4 keV transition			32.2 keV transition		
Line	E_{ce} in eV	I_{ce} in %	Γ_{ce} in eV	E_{ce} in eV	I_{ce} in %	Γ_{ce} in eV
K				17824.2(5)	24.8	2.71(20)
L_1	7481.1(10)	66.8(13)	3.75(93)	30226.8(9)	1.56(2)	3.75(93)
L_2	7673.7(6)	7.47(15)	1.25(25)	30419.5(5)	24.3(3)	1.25(25)
L_3	7726.4(6)	5.70(11)	1.19(24)	30472.2(5)	37.8(5)	1.19(24)
M_1	9112.9(7)	10.8(3)	3.5(4)	31858.7(6)	0.249(4)	3.5(4)
M_2	9183.5(6)	1.19(3)	1.6(2)	31929.3(5)	4.02(6)	1.6(2)
M_3	9191.1(6)	0.897(21)	1.1(1)	31936.9(5)	6.24(9)	1.1(1)
M_4	9310.6(6)	0.0175(4)	0.07(2)	32056.4(5)	0.0628(9)	0.07(2)
M_5	9311.9(6)	0.0156(4)	0.07(2)	32057.6(5)	0.0884(12)	0.07(2)
N_1	9378.1(6)	1.11(3)	0.40(4)	32123.9(5)	0.0255(4)	0.40(4)
N_2	9391.0(6)	0.0881(21)	-	32136.7(5)	0.300(4)	0.03
N_3	9391.6(6)	0.0655(16)	-	32137.4(5)	0.457(6)	0.03

the use as nuclear standard in KATRIN: the half-life of 86.2 days of ^{83}Rb guarantees a high ^{83m}Kr production rate with a comparably low amount of material required. Since the isotope ^{83}Rb is produced at NPI in Řež, Czech Republic, the short-duration transport to Karlsruhe does not reduce the activity, for any practical purpose [Vén14]. With a half-life of about three months, several sets of gaseous ^{83m}Kr measurements can be conducted before the ^{83}Rb source has to be refreshed. The ^{83m}Kr itself de-excites in two steps, one with an energy of 32.2 keV and one with 9.4 keV. In most of the cases, the energy is emitted as internal conversion electrons. In ^{83m}Kr, four atomic shells are populated with electrons, so that in total 12 different conversion electron lines can be distinguished for the 32.2 keV transition and 11 for the 9.4 keV transition. The lines and their energy, width and intensity are listed in table 5.2. Additional lines which are much smaller in intensity come from shake-up/off processes. Here, parts of the energy of the conversion electron are transmitted to a second electron, which is either excited to a higher state in the atomic shell (shake up) or totally removed from the atom (shake off) [Vén18]. The shake-up lines occur at least 15 eV below the parent line in the spectrum. In total, the conversion electron lines from ^{83m}Kr offer electrons with well-defined energy in a wide range from ≈ 7 keV to ≈ 32 keV. This makes ^{83m}Kr an ideal nuclear standard, considering also that its short half-life of 1.83 hours avoids any long-term contamination of the apparatus.

A big advantage of ^{83m}Kr is that it is used in gaseous form. Thus, it can be mixed to the tritium gas flow when the WGTS temperature is raised from 30 K to 100 K (see section 6.2.1). It is distributed in the source tube almost like the tritium gas and is therefore an excellent tracer for the source potential. The best conversion line for the monitoring of the WGTS potential would be the K-32 line, since it is only 750 eV below the tritium endpoint energy of 18.6 keV. However, at this energy the count rate of the integrated tritium spectrum is already larger than 10^6 cps, while the count rate of the K-32 line is expected to be on the order of $10^3 - 10^4$ cps for a ^{83}Rb source of 1 GBq [Are18b]. Therefore, the L_3-32 line is preferred because it has a comparably high intensity and small width, but has a much larger energy of 30472 eV (see table 5.2). While technical aspects of the gaseous ^{83m}Kr source have already been discussed in section 5.1.2, in the following it is described how the

potential of the WGTS influences the conversion lines of ^{83m}Kr.

A positive space charge in the source would on the one hand shift the line positions of the conversion electrons to smaller energies and on the other hand, a broadening of the lines would be observed if the space charge is not distributed homogeneously along the beam tube [Bel08]. However, a line shift can also be caused by the work function difference between the source and the MAC-E filter, and a broadening alone does not give a position-dependent distribution of the space charge. Another approach was developed in [Mac16]: besides the main line, also the line arising from conversion electrons which scattered once in the source volume is taken into account. Since electrons which are created in the rear half of the WGTS have a much larger probability of scattering in the source volume, but are also created at a different potential than the electrons from the front part (see figure 4.12), the line position of the energy loss line and the main line are affected differently by the WGTS potential. Therefore, the position difference between the energy loss line and the main line is a measure of the potential difference between the front and the rear half of the WGTS. This kind of measurement can only be performed when the column density is set to its standard value of $5 \times 10^{17}\,\mathrm{cm}^{-2}$. In the gaseous ^{83m}Kr measurements performed and analysed in the scope of this thesis, only ^{83m}Kr was used. Because of the very low pressure, scattering did not affect the measured spectrum. The investigations in this thesis are therefore important references for measurements in which scattering has a major impact. Furthermore, the sensitivity on the line position was studied that is achievable with the count rates provided by the gaseous ^{83m}Kr generator.

Although the focus of this chapter is put on the gaseous ^{83m}Kr source, the interplay with the other two ^{83m}Kr sources of KATRIN (the condensed ^{83m}Kr source in the CPS and the implanted ^{83m}Kr source in the monitor spectrometer) is discussed briefly in the following. The fact that there are three different types of sources enables direct comparisons of the line shapes and relative positions to identify typical systematic effects of the different source types. It is expected that the gaseous source should show the purest line shape, while especially the implanted source should also show some solid state effects which influence particularly the shape [Sle15]. While the gaseous source is isotropic and irradiates the full cross section of the detector (see figure 5.6), the condensed source is of such a small geometrical area that it only irradiates one single pixel [Dyb19]. Therefore, it is well-suited for a pixel-wise analysis of the transmission properties of the main spectrometer. This is also possible with the gaseous source, but then radial source effects have to be taken into account. Since the condensed source is also placed further downstream in the beam line than the gaseous source, its line positions are influenced by a different work function than the one in the WGTS. This can be helpful to disentangle the different work function contributions to the measurement and is required if the absolute endpoint energy of the tritium spectrum shall be determined. All in all, the three ^{83m}Kr sources complement one another and their interplay is crucial for the success of KATRIN.

5.3. Analysis of Krypton Lines

The analysis of ^{83m}Kr lines in the thesis at hand is done with the KaFit Krypton Fitter. This fitter is an extension of the KaFit and SSC software package (see section 3.3)[1]. The fitter works in principle like the neutrino mass analysis: a spectrum model is built and then

[1]The KaFit Krypton Fitter was mainly developed by M. Machatschek and W. Choi

fitted to the measured data points. The differential spectrum model is the Voigt profile V, which is a convolution of a Lorentzian distribution L

$$L(E, E_{\mathrm{ce}}, \Gamma_{\mathrm{ce}}) = \frac{1}{\pi} \cdot \frac{\frac{\Gamma_{\mathrm{ce}}}{2}}{\left(\frac{\Gamma_{\mathrm{ce}}}{2}\right)^2 + (E - E_{\mathrm{ce}})^2} \tag{5.1}$$

and a Gaussian distribution G

$$G(E, E_{\mathrm{ce}}, \sigma) = \frac{1}{\sqrt{2\pi} \cdot \sigma} \cdot \mathrm{e}^{-\frac{(E-E_{\mathrm{ce}})^2}{2\sigma^2}} \tag{5.2}$$

to

$$V(E, E_{\mathrm{ce}}, \Gamma_{\mathrm{ce}}, \sigma) = L * G = \int_{-\infty}^{+\infty} G(\epsilon, E_{\mathrm{ce}}, \sigma) \cdot L(E - \epsilon, E_{\mathrm{ce}}, \Gamma_{\mathrm{ce}}) \mathrm{d}\epsilon \ . \tag{5.3}$$

E_{ce} is the line position, Γ_{ce} is the Lorentzian width (FWHM) and σ is the standard deviation of the Gaussian. The Lorentzian part describes the natural line shape, while the Gaussian part describes influences of the measurement conditions, for instance the Doppler effect. The Voigt profile is convolved with the transmission function of the KATRIN main spectrometer (see figure 3.8) to derive the integral spectrum.

The measured data points of count rate and corresponding retarding voltage are not used directly for the fit. Several corrections have to be applied. Furthermore, the fit model has to take different systematic effects into account which influence both the shape of the transmission function and the shape of the conversion line. In detail, the following cuts and corrections are made:

Region of interest cut Electrons passing the main spectrometer gain momentum by the post-acceleration electrode before they hit the detector. This shifts the signal electrons to an energy region with smaller intrinsic background of the detector (see section 3.2.7). Therefore, a region of interest is defined in which electrons with energy E_e are counted as signals and used for the analysis [Are18b]:

$$E_i + q(U_{\mathrm{PAE}} + U_{\mathrm{BIAS}}) - 3\,\mathrm{keV} \leq E_e \leq E_i + q(U_{\mathrm{PAE}} + U_{\mathrm{BIAS}}) + 2\,\mathrm{keV} \ . \tag{5.4}$$

E_i is the expected conversion-electron energy from line being scanned, $U_{\mathrm{PAE}} = 10\,\mathrm{keV}$ is the applied post-acceleration voltage and U_{BIAS} the bias voltage of the focal plane detector.

Fields in the analysing plane As discussed in more detail in section 4.2.6, the magnetic field and the electric potential are not constant over the entire analysing plane in the middle of the main spectrometer. Electrons guided at different trajectories therefore experience slightly different transmission conditions of the MAC-E filter. Based on simulations, this effect can be corrected.

Doppler broadening The Doppler broadening and its influence on the neutrino mass measurement are discussed in section 4.2.4. For the measurements with ^{83m}Kr, the Doppler effect adds a Gaussian smearing to the line widths of the conversion electron lines (see equation 5.3). It is calculated according to equation 4.13 to $\sigma = 60\,\mathrm{meV}$ for an operational temperature of the WGTS beam tube of 100 K and an energy of 30472 eV (L_3-32 line). The analysis model takes this smearing into account.

Synchrotron radiation The synchrotron radiation is discussed in detail in section 4.2.3. With Kassiopeia (see section 3.3), the synchrotron loss for conversion electrons from ^{83m}Kr which is distributed in the WGTS according to figure 6.24 is calculated for

an energy of 30472 eV (L_3-32 line) and standard magnetic fields along the beam tube (70 % of nominal field strengths). The maximum energy loss is ≈ 120 meV and depends strongly on the starting position in the source and pitch angle (angle between momentum and magnetic field). The longer the path length, the larger the energy loss due to synchrotron radiation becomes. In total, more than 300,000 electron trajectories were simulated and their synchrotron energy loss distribution was stored in a data file for SSC/KaFit[2] to account for the corresponding broadening of the transmission function. For fits of lines other than L_3-32, a correction factor has to be applied in the SSC configuration file to adjust the synchrotron energy loss distribution accordingly. As the synchrotron energy loss is proportional to $B^2 \cdot \sqrt{E} \cdot \gamma$, the correction factor accounts for relative changes not only of the energy but also of the magnetic field setting in between measurements of individual lines, for instance K-32 and L_3-32.

High voltage fluctuation Fluctuations of the high voltage of the main spectrometer and their influence on the neutrino mass measurements are described in section 4.2.7. These fluctuations lead to a broadening of the transmission function edge and have to be incorporated in the fit model. The post-regulation system described in section 4.2.7 was not operable during the gaseous ^{83m}Kr measurements in July 2017. Therefore, high voltage fluctuations described by a sine wave of frequency 50 Hz and an amplitude of 0.21 V at −30 kV and 0.19 V at −18 kV were recorded [Are18a]. For retarding voltages of −11 kV (Auger lines, see section 5.4.5) and −8 kV (9.4 keV transition, see section 5.4.6) the amplitude is extrapolated to 0.18 V and 0.17 V, respectively. These values are used in the analysis model to account for this effect in the fit of the conversion lines.

The fit parameters are the line position E_{ce}, the squared line width Γ^2_{ce}, the line intensity I_{ce} and the background rate R_{bg}. The fitter offers several fitting options: it is possible to perform a uniform fit over the full detector, or to fit the spectrum ring-wise or even pixel-wise. The results discussed in section 5.4 have all been derived with a uniform fit of all irradiated pixels. In this thesis, the position values E_{ce} are given in "retarding energy" in order to underline that there are effects like the unknown work functions which are not quantified yet. Therefore, the fitted line positions should only be compared to literature values with care.

Due to the special setup of the ^{83m}Kr campaign 2017 (see section 5.1.2), also the fitting and analysis of the conversion lines is different than it will be in upcoming krypton runs:

- In normal gaseous ^{83m}Kr operation of the WGTS, not only ^{83m}Kr but also tritium will circulate in the source. Then the gas density will be much larger with a column density of $5 \times 10^{17}\,\mathrm{cm}^{-2}$. In the 2017 measurements, only ^{83m}Kr was present in the source with such a low density that scattering processes can be neglected.
- The ^{83m}Kr is spread out over the whole WGTS and the DPS in the 2017 campaign. The gas density profile is flat at least in the WGTS (see figure 6.24). For future ^{83m}Kr measurements, also a triangular-shaped profile can be expected (see figure 3.3).
- In the ^{83m}Kr measurements 2017, the automated input of sensor data to the model (see below) is limited to the high voltage reading. All other values and corrections like the magnetic field strengths and the WGTS temperature have to be added manually.

For the sensor data input, the concept designed for neutrino mass measurement runs was tested during the ^{83m}Kr campaign in 2017 the first time. The idea is that the fitter gets all

[2] Personal communication L. Schimpf, Nov 11, 2018.

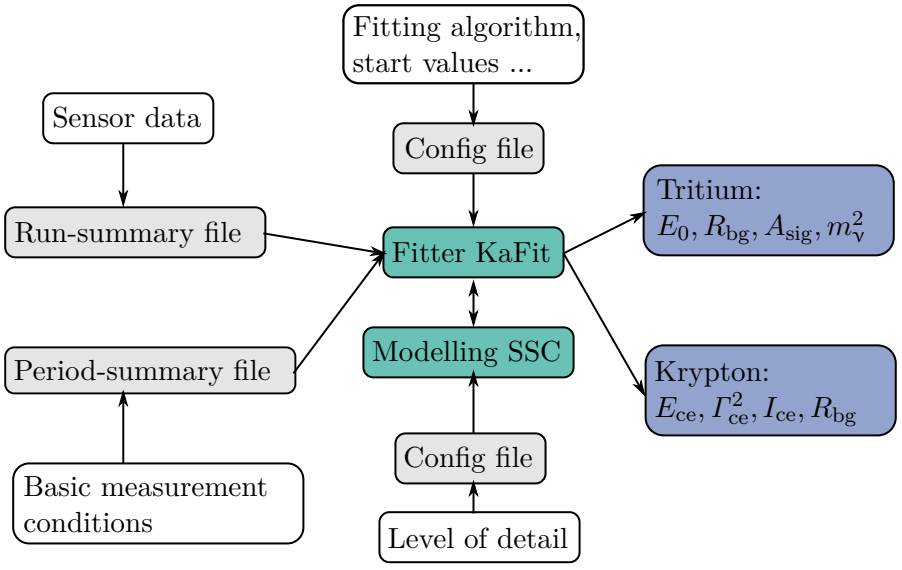

Figure 5.4.: Fitting procedure for tritium and krypton analyses. The figure shows the dependencies in the fitting procedure of a tritium or krypton spectrum. Main software tools are the fitter of KaFit and the model of SSC. The required parameters are loaded from a run-summary and a period-summary data file. The user can configure the fitter and the level of detail of the model via two config files. There are four fit parameters for tritium measurements (energy endpoint E_0, background rate R_{bg}, the signal amplitude A_{sig} and the neutrino mass squared m_ν^2) and four fit parameters for krypton measurements (line position E_{ce}, squared line width Γ_{ce}^2, line intensity I_{ce} and background rate R_{bg}).

relevant input parameters for the fit from two data files, which are the run-summary file and the period-summary file. The run-summary file contains measured values of parameters which could change from (sub-)run to (sub-)run. These are for instance the temperature values from the WGTS, the voltage steps of the main spectrometer, the count rates per detector pixel, the measurement time distribution and many more. The period-summary file offers parameters which are valid throughout a given KATRIN measurement period. These are mainly the magnetic field values along the entire beam tube and a 3D-field mapping of the electric potential and the magnetic field in the analysing plane of the main spectrometer. The fitter reads all parameters from these two data files and the user can decide about the level of detail of the analysis with two additional configuration files. The fitting procedure is illustrated in figure 5.4.

5.4. Results and Discussion

In this section, the results and findings of the gaseous ^{83m}Kr measurement campaign from July 2017 are presented and discussed. In subsection 5.4.1, the first signal of ^{83m}Kr conversion electrons on the focal plane detector is used to derive statements on the KATRIN beam line alignment and on the time until the ^{83m}Kr count rate reaches an equilibrium state. In subsection 5.4.2, the full integral spectrum of ^{83m}Kr recorded in July 2017 is presented and the included non-adiabatic effects are described. In the following subsections, key parts of the ^{83m}Kr conversion electron spectrum are discussed in more detail: in subsection 5.4.3, the focus is put on the conversion electron lines of the 32 keV transition. Their positions are determined which are important parameters for the determination of the WGTS potential in future KATRIN tritium operation. Here, they are used for a check of the linearity of KATRIN's energy scale in subsection 5.4.4. In between the 32 keV- and the 9.4 keV transition, an Auger cascade sets in. Several of these Auger electron lines are identified in subsection 5.4.5. Subsection 5.4.6 treats the spectrum of the 9.4 keV transition of ^{83m}Kr.

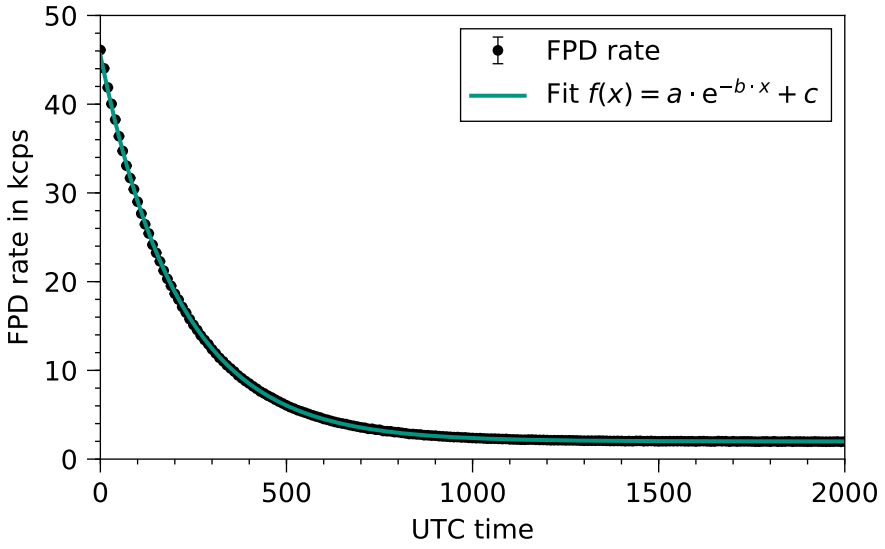

Figure 5.5.: Rate development of the first light of ^{83m}Kr. After opening the valve, the rate at the focal plane detector is about 50 kcps. The fit gives a time constant of $1/b = 210.5$ s. Thus, after about 30 min the rate is already stabilised at 2 kcps. It should be noted that the error bars of the rate are smaller than the markers.

The stability of the energy scale is investigated in subsection 5.4.7 with regular monitoring scans of the L_3-32 line. Besides the main conversion lines of ^{83m}Kr, also a few satellite lines due to shake-up processes were detected which are discussed in subsection 5.4.8. The section ends with a discussion of the measured line widths in subsection 5.4.9.

5.4.1. First Light and Alignment

Before the opening of the valve of the gaseous ^{83m}Kr generator to the WGTS, the generator needs 18 hours to reach an equilibrium between ^{83m}Kr and ^{83}Rb [Sen18]. As soon as the equilibrium is achieved, the amount of gaseous ^{83m}Kr follows the exponential decay of the ^{83}Rb. When the valve was opened for the first time at the beginning of the KATRIN krypton campaign in summer 2017, it was not known how long it would take for the ^{83m}Kr to be distributed in the KATRIN beam line and for the pumping by the CPS to achieve equilibrium with the krypton inlet. For the very beginning, a flush of ^{83m}Kr was expected. Since the focal plane detector was only capable to sustain count rates up to 100 kcps (see section 3.2.7), it was decided to ramp the main spectrometer voltage to -31.8 kV for safety reasons, so that only the M-32 and N-32 conversion electrons could reach the detector. These lines comprise about 11 % of all conversion electrons of the 32.2 keV transition (see table 5.2). The voltage was kept stable to investigate the time evolution of the detector rate after the valve was opened. The magnetic field in the analysing plane was 2.7×10^{-4} T. The rate over the measurement time is plotted in figure 5.5. Starting with a value of 48 kcps, the count rate stabilised at 2 kcps after ≈ 30 min. For the following measurements, this result was used as reference whenever the setting of the valve of the gaseous ^{83m}Kr generator was changed.

Another effect is already visible in this first run with gaseous ^{83m}Kr: the pixel map of the detector shows a clear misalignment of the system (see figure 5.6). Normally, the magnetic flux tube should be centred on the focal plane detector, but in this view it is shifted to the bottom left. The reasons for this misalignment are not conclusively determined yet. A slight effect may come from the fact that new alignment data obtained in [Hac17] was not fully implemented in the geometry of the KATRIN simulation tools for the krypton measurement

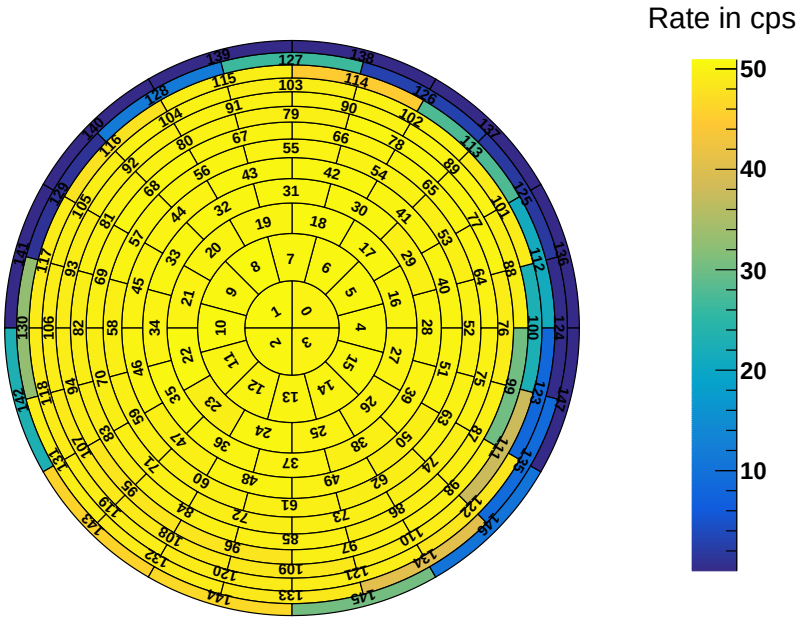

Figure 5.6.: Focal plane detector pixel map of gaseous ^{83m}Kr source. The figure shows the pixel map of the focal plane detector when the first electrons from the gaseous ^{83m}Kr source are detected. The main spectrometer is set to a voltage of −31.8 kV so that all electrons of the M and N lines are measured. A clear misalignment is visible, the flux tube is shifted a bit to the bottom of the detector. On the right-hand side, a few pixels (pixels 99, 100, 111) with less rate indicate the position of the forward beam monitor.

campaign [Def17]. Therefore, the optimisation of the air coil currents for the magnetic field in the analysing plane with KTrAP (see section 3.3) was done with the old geometry and alignment data. However, this can only explain a small part of the observed offset. Another explanation may be that there are further magnetic fields present in the spectrometer hall which are not accounted for in the models. Detailed investigations are ongoing and a new magnetic field measurement system has been set up for a better modelling of the impact of magnetised steel in the building walls [Let18]. In the measurements presented here, the misalignment is empirically corrected for in the period summary files (see figure 5.4), so that a uniform fit can be performed.

5.4.2. Full Integral ^{83m}Kr Spectrum and Adiabaticity

Figure 5.7 presents the full integral spectrum measured with KATRIN during the gaseous ^{83m}Kr campaign in July 2017. All line groups are covered (see table 5.2). The data plotted in the figure was recorded in two days of measurement time with the same measurement conditions as described in section 5.1.2: the conversion electrons coming from the DPS were blocked due to the applied potential of 350 V of the DPS dipole electrodes and the 2.7×10^{-4} T setting was selected for the magnetic field in the analysing plane. The only parameter that changed throughout the measurement besides the retarding voltage was the energy resolution of the main spectrometer. Its value depends linearly on the electron energy (see equation 3.4 and table 5.1) and becomes smaller for lower energies. The figure demonstrates the unique possibilities of KATRIN to measure electron energy spectra with high precision over large energy ranges and shows the system readiness for tritium operation.

In a closer look at figure 5.7, a basic characteristic of the MAC-E filter is visible: the non-adiabatic guiding of the electrons with large surplus energies. Since the MAC-E filter measures electron spectra in an integral way, normally the rate of high-energetic conversion

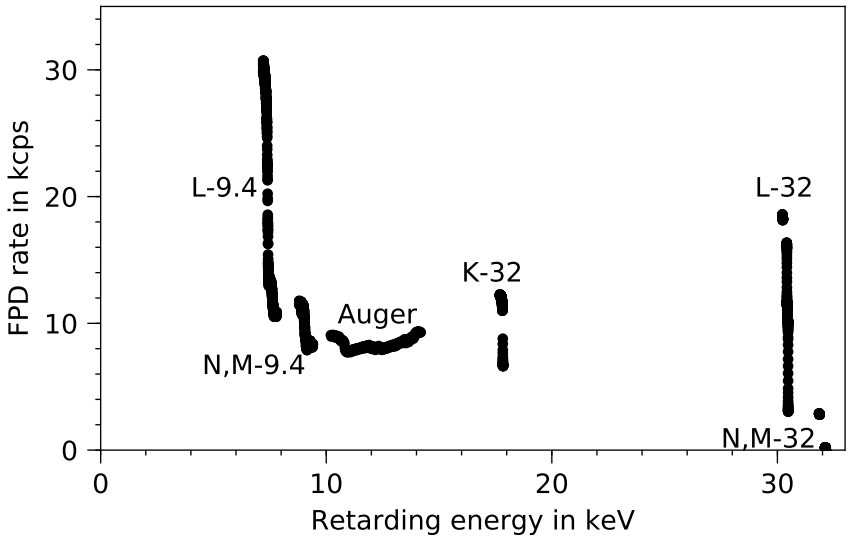

Figure 5.7.: Full integral spectrum of gaseous ^{83m}Kr recorded with KATRIN. The plot shows the measurement of all conversion electron line groups of ^{83m}Kr listed in table 5.2. Additionally, the Auger electron lines in the region of 10 to 14 keV have been scanned. Further Auger electron lines at energies around 1 keV and below could not be scanned due to time constraints, although investigations at these small voltages are also technically possible. See section 5.4.3 for details of the 32 keV transition, section 5.4.5 for details on the Auger electrons and section 5.4.6 for details on the 9.4 keV transition.

electron lines should be added to the rate of the lines with lower energy and hence result in a monotonous increase of the integrated rate when going from higher to lower energies. However, this is clearly not the case in the figure: the K-32 line, for instance, has a smaller total rate than the L-32 lines, although the latter can also pass the MAC-E filter when the retarding voltage is set to the K-32 line position. The reason for this discrepancy is that the number of electrons moving along non-adiabatic trajectories increases with their surplus energy compared to the retarding voltage. Non-adiabatically guided electrons do not pass the retarding voltage as the conversion from transversal to longitudinal energy is incomplete. Therefore they do not reach the detector. As demonstrated in figure 5.8, the non-adiabaticity is visible with a typical radial pattern on the focal plane detector.

Since in standard tritium scans KATRIN operates only within the last ≈ 30 eV below the kinematic endpoint of the tritium-beta decay, there are no non-adiabatic effects to be taken into account. However, for the sterile neutrino search (see section 3.4.3), measurements deeper in the spectrum have to be made and then the non-adiabatic effects have to be considered. Investigations are ongoing also with the data from the ^{83m}Kr campaign in July 2017 and details will be reported in [Hub19].

5.4.3. 32 keV Transition

One main objective of the gaseous ^{83m}Kr measurement campaign in July 2017 was to measure the positions of the conversion lines of the 32 keV transition with high precision. These lines are important for future calibration runs as discussed in section 5.2. Table 5.3 shows the determined mean positions and intensities of the 32 keV transition. All lines are recorded at a magnetic field setting of 2.7×10^{-4} T and except for the lines M_2 and M_3 also with the same setting of the gaseous ^{83m}Kr generator. The systematic uncertainties listed in section 5.3 are taken into account in the fits. The measurement time distributions are listed in table 5.4. Every conversion line was fitted in single fits, apart from $M_{4,5}$ and $N_{2,3}$

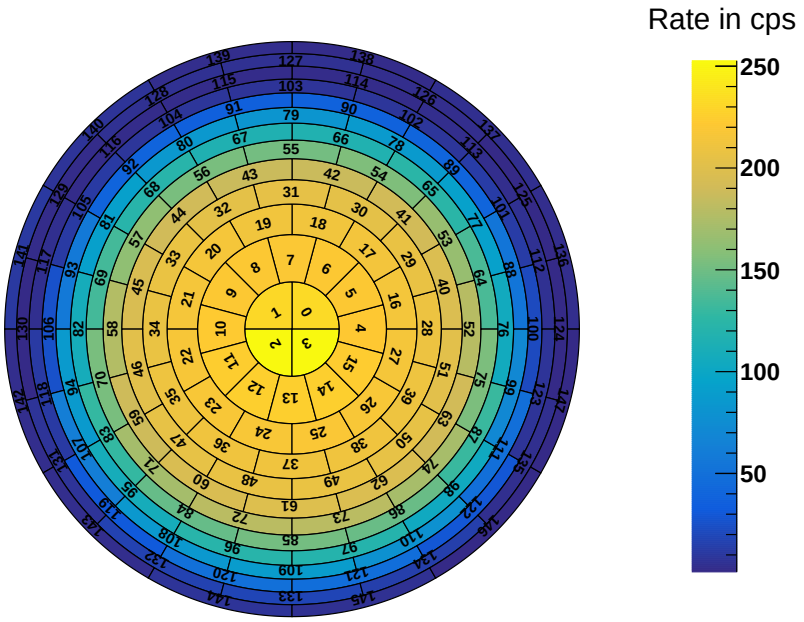

Figure 5.8.: Pixel map of the focal plane detector at $U_{\mathrm{ret}} = -18.1\,\mathrm{kV}$. The figure shows the rate at the focal plane detector for a spectrometer retarding voltage of −18.1 kV and a magnetic field setting of 2.7×10^{-4} T (no region of interest cut applied). The measurement time is 20 s. Compared to figure 5.6, the detector wafer is not illuminated uniformly. The rate reduction due to non-adiabatic effects is more pronounced for the outer radii since the corresponding magnetic field lines in the main spectrometer are more curved.

Table 5.3.: Fitted line positions and intensities of the 32 keV transition of ^{83m}Kr. The measured line positions $E_{\mathrm{ce,fit}}$ of the conversion electron lines of the 32 keV are listed in the second column. The values are given in terms of "retarding energy" (see section 5.3). The third column lists the binding energies E_{bind} [Vén18] for the test of the linearity of the energy scale in figure 5.11. The fourth column presents the fitted line intensities and the fifth column the relative line intensities when L_3 is normalised to 37.8 % which is the expectation from literature (see table 5.2). In the last column, the reduced χ^2 of the fits are listed. M_2 and M_3 (marked with an asterisk) have been measured at a different setting of the ^{83m}Kr generator and their intensity values are therefore not given here. The uncertainties are calculated as discussed in the main text.

Line	$E_{\mathrm{ce,fit}}$ in eV	E_{bind} in eV	$I_{\mathrm{ce,fit}}$ in cps	I_{rel} in %	χ^2/dof
K	17824.628(6)	14327.26(4)	3464.0 ± 5.5	23.37(4)	1.3
L_1	30226.311(501)	1924.60(8)	388.5 ± 64.4	2.62(43)	0.9
L_2	30419.935(6)	1731.91(6)	3700.6 ± 32.2	24.97(22)	1.5
L_3	30472.642(5)	1679.21(5)	5602.5 ± 20.8	37.8	1.2
M_1	31858.417(209)	292.74(29)	87.1 ± 5.1	0.59(3)	0.8
M_2^*	31929.424(36)	222.12(17)	-	-	0.9
M_3^*	31937.115(16)	214.54(11)	-	-	1.0
M_4	32057.007(159)	95.036(23)	14.3 ± 2.6	0.096(18)	1.1
M_5	32058.377(314)	93.79(2)	7.7 ± 2.7	0.052(18)	1.1
N_1	32123.891(373)	27.52(1)	4.0 ± 1.0	0.03(1)	1.1
N_2	32137.080(43)	14.67(1)	55.2 ± 4.2	0.37(3)	3.5
N_3	32137.758(15)	14.00(1)	83.0 ± 4.4	0.56(3)	3.5

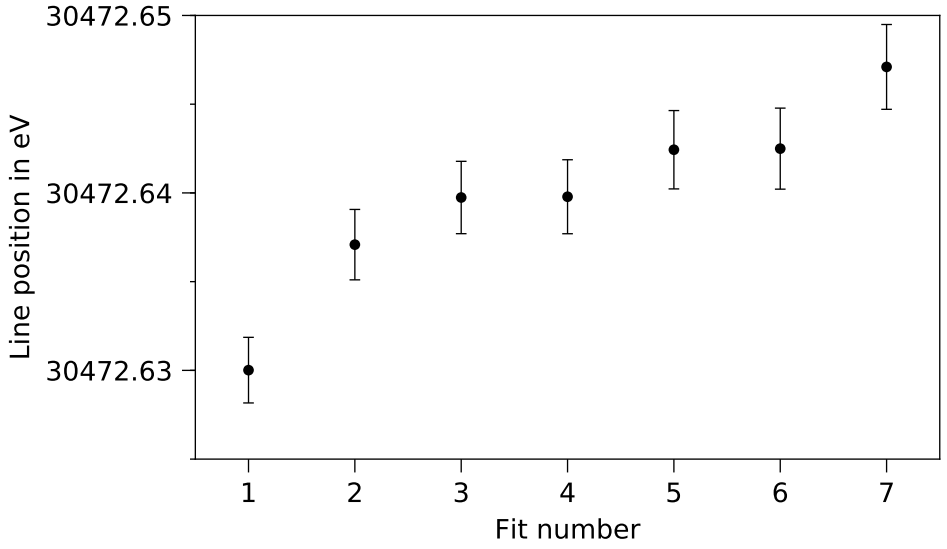

Figure 5.9.: Stability of the fitted line position of the L_3-32 line for different fit ranges. Fit 1 was performed for a fit range of [30460 eV, 30479 eV]. From fit 2 with a fit range of [30465 eV, 30479 eV] to fit 7 the fit range is decreased in 1 eV steps. The statistical uncertainty for a single fit is ≈ 2 meV, while the drift of the line position is nearly a factor of 10 larger.

which were fitted with line doublets because otherwise the fit did not converge. In view of limited statistics and resolution, these doublet fits only converged when the squared line widths were fixed as fit parameter (see figure 5.10).

For the uncertainty estimation of the fitted line positions and intensities, for every line or doublet up to 10 fits with different fit ranges are performed in order to select the best fit. However, it turned out that for several lines the fitted position values show a dependence on the fit range (see figure 5.9). A possible explanation for this behaviour are the measurement interval which may be too small for some lines so that the Lorentzian tail is not fully covered. Also the background from neighbouring lines may have an influence. A similar observation is made for the fitted line intensity. The fit value of the intensity depends strongly on the selected fit interval due to statistical fluctuations in the count rate. In order to take this fit range dependency into account and to reduce the bias in the analysis, the fit with the best reduced χ^2 value is selected and gives a first uncertainty contribution of the statistical fit uncertainty, σ_{fit}. Additionally, the influence of the fit range is considered as standard deviation of the line positions/intensities of the 10 fits, σ_{fitrange}. The total uncertainty of the position or intensity σ_{tot} is therefore

$$\sigma_{\text{tot}} = \sqrt{\sigma_{\text{fit}}^2 + \sigma_{\text{fitrange}}^2} \,. \tag{5.5}$$

The intensities of the conversion lines recorded at the same setting of the gaseous ^{83m}Kr can be compared to the literature values from [Vén18] which are listed in table 5.2. If the line intensities are normalised to the intensity of L_3, the relative intensities are close to the literature values. The only exception is the $M_{4,5}$ doublet, for which the results show a larger intensity for the M_5 than for the M_4 line. In literature, the values are ordered in the opposite way. The small deviations from the literature values can be explained by the fact that single line fits are performed without including the neighbouring lines in the model. Then, the model assumes a constant background. However, it has a slope due to the long Lorentzian tails of the other lines or due to non-adiabatic effects from electrons with high surplus energy.

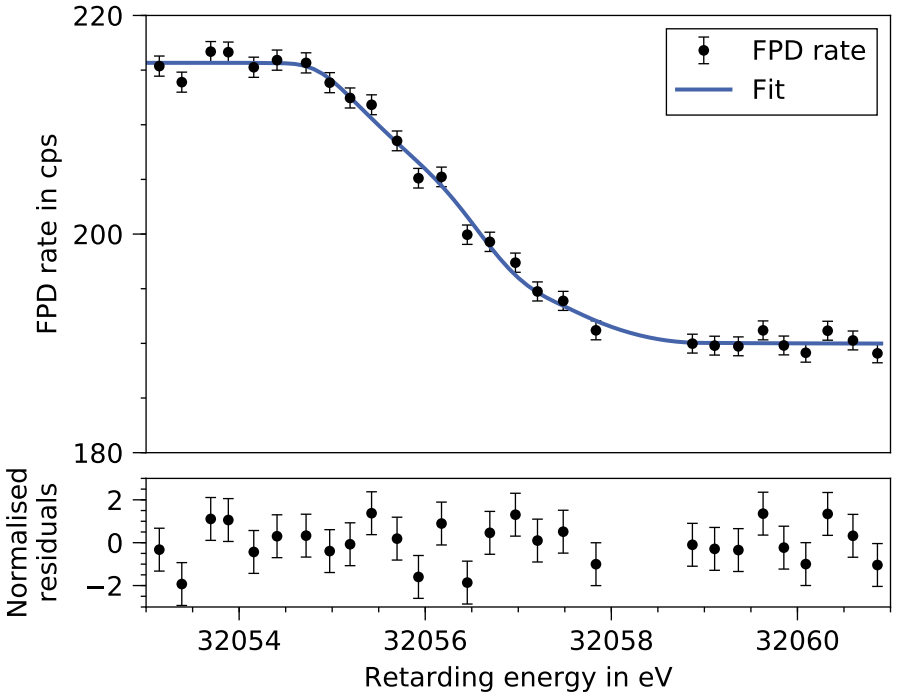

Figure 5.10.: Fit of the $M_{4,5}$-32 doublet. The plot shows the combined fit of the M_4 and M_5 line leading to the results given in table 5.3. The reduced χ^2 is 1.1. The fit only converges for a fixed value of the squared line width. The literature value of $\Gamma_{ce}^2 = 0.005\,\mathrm{eV}^2$ is selected (see table 5.2). The gap at 32058 eV is due to a missed data point. The residuals are normalised to the statistical uncertainties.

The results for the line positions of the intense lines K, L_2 and L_3 show that a sensitivity on the meV scale as required for the electric potential measurements in the WGTS is achieved on reasonable time scales of about 1 h for count rates of several kcps. For the potential determination also the position of the line of the electrons which scattered once in the source is required. The intensity of this line is simulated to be 20 % of its main line for the nominal column density of $5 \times 10^{17}\,\mathrm{cm}^{-2}$ [Mac16]. The results of the measurements show that conversion lines like the L_1-32 with a count rate comparable to that of the energy loss line exhibit a significantly larger uncertainty than the intense lines. However, a meV precision is also achievable if the measurement time or the source intensity is increased accordingly. Therefore, it can be concluded that a precise determination of the position of the ^{83m}Kr conversion and energy loss lines required for the measurement of the WGTS potential is experimentally possible. This is also illustrated by the fact that the two doublets $M_{4,5}$ and $N_{2,3}$ can be clearly separated in their positions. However, the reduced χ^2 value of the $N_{2,3}$ is 3.5 and indicates deviations of the data from the model. An improved measurement is possible with an optimised energy resolution of the spectrometer and more statistics. Based on the findings above, the proposed method from [Mac16] was tested in measurements in which ^{83m}Kr was mixed with deuterium to enable the scattering of the conversion electrons off gas in autumn 2018. The analysis of these measurements is currently ongoing[3].

Finally, the measured line positions of the 32 keV transition of ^{83m}Kr in table 5.3 can be compared to the literature values of the conversion electron energies in table 5.2. The measured line positions in "retarding energy" agree with the literature values within the uncertainties. However, it should be kept in mind that the position values measured with

[3]Personal communication M. Machatschek, Oct 29, 2018.

Table 5.4.: Measurement time distributions of the conversion electron lines of the 32 keV transition. The table lists the step width of the retarding voltage ΔU_{ret} and the measurement time t_{U} per step of the measurement of the conversion lines of the ^{83m}Kr 32 keV transition. The fourth column shows the applied measurement interval. The lines M_2 and M_3 (marked with an asterisk) have been recorded at a different setting of the gaseous ^{83m}Kr generator.

Line	ΔU_{ret} in V	t_{U} in s	Measurement interval
K	0.5	60	$[-17840\,\mathrm{V}, -17710\,\mathrm{V}]$
L_1	0.5	200	$[-30245\,\mathrm{V}, -30215\,\mathrm{V}]$
L_2, L_3	0.25	60	$[-30480\,\mathrm{V}, -30410\,\mathrm{V}]$
M_1	0.5	200	$[-31870\,\mathrm{V}, -31850\,\mathrm{V}]$
M_2^*, M_3^*	0.5	15	$[-31733\,\mathrm{V}, -31713\,\mathrm{V}]$
$M_{4,5}$	0.25	240	$[-32070\,\mathrm{V}, -32055\,\mathrm{V}]$
N_1, $N_{2,3}$	0.2	150	$[-32145\,\mathrm{V}, -32115\,\mathrm{V}]$

KATRIN depend on the work functions in the WGTS and main spectrometer. The work functions are unknown, so that the measured line positions may be shifted by an unknown value from the true values. A further uncertainty comes from the fitter and the simplified background modelling as outlined above. Especially for the weak lines the background model should take slopes due to neighbouring lines or non-adiabatic effects into account.

5.4.4. Linearity of Energy Scale

By comparing the measured line positions with the ones from literature, the linearity of the KATRIN energy scale can be tested. If the energy scale is linear, the position difference of two measured neighbouring lines should be the same as the position difference expected from the literature values. The line positions of the ^{83m}Kr conversion electron lines from literature listed in table 5.2 are calculated with the help of the relation [Vén18]

$$E_{\mathrm{ce}} = E_{\gamma} + E_{\gamma,\mathrm{rec}} - E_{\mathrm{bind}} - E_{\mathrm{rec}} \ . \tag{5.6}$$

E_{ce} is the energy of the emitted conversion electron, E_{γ} is the energy of the involved γ transition, $E_{\gamma,\mathrm{rec}}$ is a small correction of ≈ 0.1 eV due to the recoil of the ^{83m}Kr after the γ emission, E_{bind} is the binding energy of the electron emitted in the inner conversion process, which also has to be corrected by the corresponding recoil of the ^{83m}Kr atom E_{rec}. As long as only conversion electron lines belonging to the same gamma transition (see figure 5.3) are used for the analysis of the linearity of the energy scale, only the binding energies and the corresponding recoil correction due to the emission of the electron are required. This reduces the involved uncertainties.

The line positions of the K-32, L_1-32, L_2-32, L_3-32, M_1-32 and N_1-32 have been measured with the same settings of the gaseous ^{83m}Kr generator and the magnetic field settings during the krypton measurement campaign in summer 2017, so that they can be used for this kind of analysis. The line positions of the doublets $M_{4,5}$ and $N_{2,3}$ are not used as they are derived in a fit with fixed line width, for which the impact on the position determination is not well quantified. The conversion electron lines of the 9.4 keV transition have also been measured with the same settings, but these lines are split up into sub-lines due to ionisation effects (see section 5.4.6) and therefore cannot be used for the linearity check of the energy scale. The line positions of the six conversion electron lines of the 32 keV transition are plotted over their corresponding binding energy, taken from [Vén18], in figure 5.11. Since there are no a priori reasons to assume any non-linear energy scale for

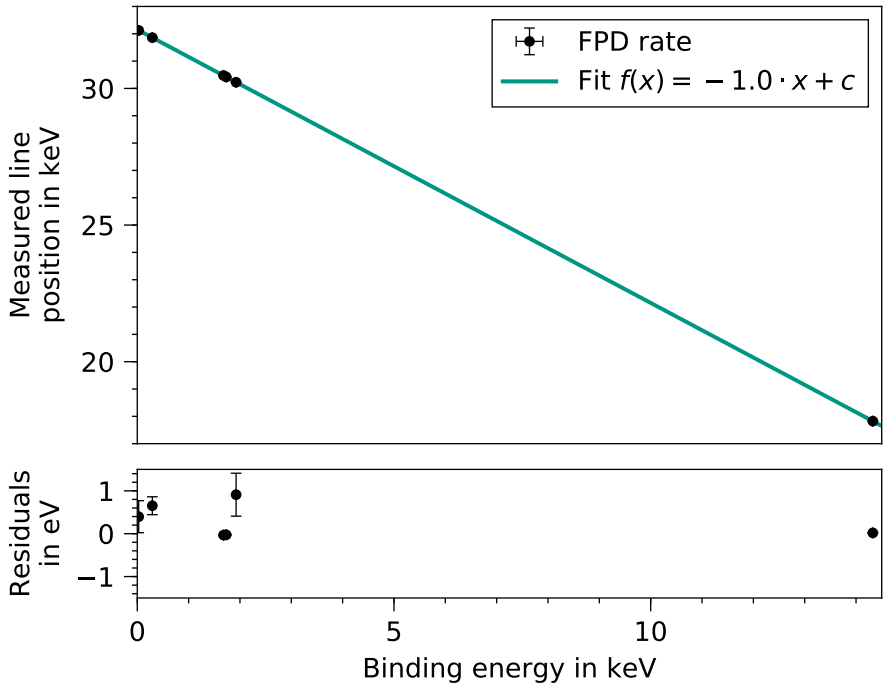

Figure 5.11.: Linearity of energy scale. The plot shows the fit of a linear function to the six data points of measured line position and binding energy. The values are listed in table 5.3. The error bars are often smaller than the marker size. The fit is discussed in detail in the main text.

a MAC-E filter, a linear model is fitted to the data points with $f(x) = -1.0 \cdot x + c$. The result for the fit parameter is

$$c = (32.15203 \pm 0.00003)\,\text{keV} \ . \tag{5.7}$$

The reduced χ^2 is 1.24. The residuals are not uniformly distributed around zero, so that a slight inhomogeneity cannot be fully excluded. Especially the line positions of the weak lines are shifted to higher energies in comparison to the expected linear dependence, whereas the intense lines are linear within a deviation of $< 0.03\,\text{eV}$. A residual non-linearity, if present, is small enough not to impact the neutrino mass measurement in the narrow energy regime close to the tritium endpoint. However, the results point towards a systematic effect of the fitter that shifts the line positions of lines of weak intensity. Similar effects are observed for the line widths (see section 5.4.9), where the line widths of weak lines are overestimated. A possible explanation may be again the background modelling for the weak lines as discussed above. The effect is further investigated with the ^{83m}Kr data from fall 2018 which are currently under analysis [Mac19].

5.4.5. Auger Electron Lines

As presented in figure 5.7, besides the conversion electron lines ^{83m}Kr also emits Auger electrons. The Auger electrons are produced in non-radiative transitions in the shell of the ^{83}Kr atom, when the hole left by the emitted conversion electron is filled by an electron from an outer shell [Kov92]. Therefore, also sharp electron lines with energies E_{Auger} form according to the binding energies $E_{\text{X,Y,Z}}$ of the three shells X, Y, Z being involved. X denotes the shell of the initial hole, Y the shell from which the electron fills up the hole and

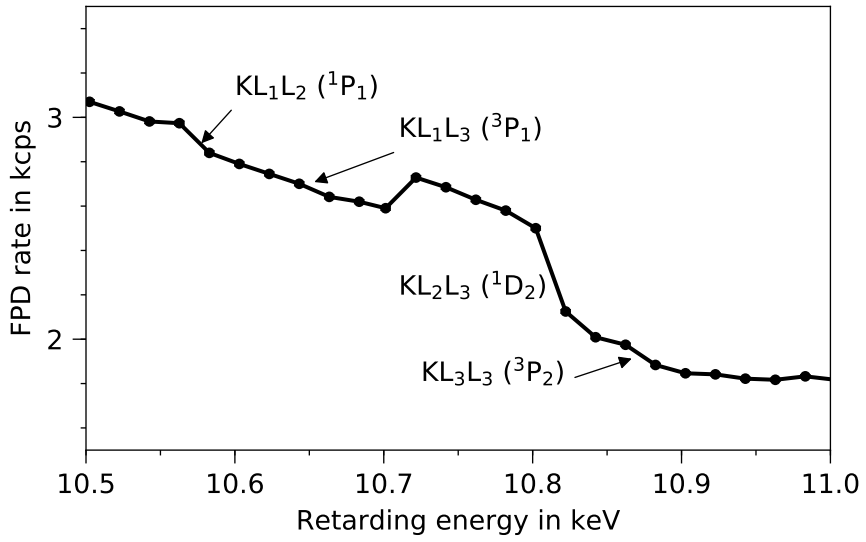

Figure 5.12.: Auger electron lines of ^{83m}Kr. The plot shows four of the nine Auger electron lines which can be identified in the July 2017 measurements with gaseous ^{83m}Kr. The term symbol in brackets denotes the electron configuration of the final state of the ion. The intensity of the lines is weak and some of them can only be identified as an Auger line because their positions are known from literature [Kov92]. For the position values see also table 5.5. The rate decrease when lowering the retarding potential below 10.7 keV (from right to left) is due to a failure in the data acquisition/processing system. The statistical uncertainty bars of the data points are smaller than the marker size.

Z the shell of the electron leaving the atom. Since Y and Z cannot be distinguished, the terms XYZ and XZY denote the same Auger electron line[4]. E_{Auger} can be approximated as

$$E_{\text{Auger}} = E_{\text{X}} - E_{\text{Y}} - E_{\text{Z}} \ . \tag{5.8}$$

This equation is an approximation. Upon a closer look, there are corrections which have to be taken into account for high-resolution spectra: as the atom is already ionised, the binding energies have to be corrected slightly [Cha71], see also section 5.4.6.

The ^{83m}Kr Auger spectrum can be divided into four parts: The LMX lines have energies between 900 eV and 1600 eV. The KLL spectrum can be found between 10.2 keV and 11.0 keV, followed by the KLX lines between 12.0 keV and 12.7 keV and finally the KMX spectrum between 13.6 keV and 14.2 keV. The full ^{83m}Kr spectrum was measured previously with a differential spectroscopy method at an energy resolution of $4 - 12$ eV [Kov92]. KATRIN's integral measurement achieves a much better resolution at these energies. However, due to time constraints only the parts of the Auger spectrum from 10.2 keV to 14.2 keV was measured in the 2017 campaign, with comparably large voltage steps of 20 V. This is enough to roughly determine the positions of the most intense Auger electron lines.

In total, nine lines were identified. Four of them are shown in figure 5.12. The lines are fitted with the KaFit krypton fitter. The line shape is also assumed to be a Voigt profile [Kov92]. Due to the large step size of 20 V, often only a few measurement points can be used for the fit so that the involved uncertainties are large. The uncertainties of the determined line positions are estimated to be 10 eV according to the voltage step size.

[4]To avoid these misunderstandings, Auger electron lines are denoted with the letters of the three atomic shells being involved in the transition ordered by their binding energies. Thus, only one possibility is used in reality.

Table 5.5.: Auger electron line positions from ^{83m}Kr. The table lists the positions of Auger electron lines from ^{83m}Kr measured with KATRIN during the gaseous ^{83m}Kr campaign in July 2017. The uncertainty on the position is estimated to be 10 eV for each of the lines due to a voltage step width of 20 V and the small number of data points involved in the fit. The Auger lines are identified according to the spectra published in [Kov92]. The term symbol in brackets denotes the electron configuration of the final state of the ion.

Line	$E_{\mathrm{Auger,fit}}$ in eV
KL_1L_1 ($^1S_0$)	10382
KL_1L_2 ($^1P_1$)	10582
KL_1L_3 ($^3P_1$)	10647
KL_2L_3 ($^1D_2$)	10814
KL_3L_3 ($^3P_2$)	10873
KL_1M_1	12080
KL_1M_2+KL_1M_3	12143
KL_2M_3	12363
KL_3M_2+KL_3M_3	12388

Nevertheless, the positions of the identified lines are still a useful benchmark for any future measurements in this energy range with KATRIN. The measured positions are listed in table 5.5.

5.4.6. 9.4 keV Transition

The low pressure of $< 1 \times 10^{-8}$ mbar inside the KATRIN beamline during the gaseous ^{83m}Kr campaign [Are18b] allowed the investigation of an effect at the 9.4 keV transition reported by Decman and Stoeffl [Dec90b]: after emitting the conversion electron of the 32 keV transition (see figure 5.3), the ^{83m}Kr atom remains in an ionised state with the charge $1e^+$ (in the following denoted as "1+"). The missing electron triggers a cascade of Auger transitions (see section 5.4.5), each of them increasing the positive charge of the ion by another 1+. Until the 9.4 keV conversion electron emission sets in after about 150 ns, the ^{83m}Kr atom is in a multiply ionised state, since the time for neutralisation is on the order of milliseconds at such pressures [Dec90b]. As every ionised state of the ^{83m}Kr atom leads to a shift of the binding energies of the remaining electrons, a splitting of the conversion electron lines of the 9.4 keV transition was observed by Decman and Stoeffl. Their observation triggered also some theoretical calculations of the binding energy shifts associated with different states of ionisation of the ^{83m}Kr atom [Dec90b; Man91; Ryš92]. To the best of knowledge, no other experimental values than the ones from Decman and Stoeffl on this effect have been published so far, and also no integral measurement of the split conversion electron lines are known.

Decman and Stoeffl used the setup of the Livermore neutrino mass experiment [Sto95] for their investigations. The gaseous ^{83m}Kr was injected at pressures comparable to the ones reported here [Dec90b]. Therefore, the gaseous ^{83m}Kr campaign offered the opportunity to measure this effect with KATRIN and to test the results reported in [Dec90b]. Although the 9.4 keV transition does not play a role for the standard KATRIN operation since its conversion electron lines are deep in the tritium spectrum, the determination of the line positions can still set important benchmarks for future comparisons of work function investigations, for instance. The 9.4 keV transition might also be important for the sterile neutrino search with KATRIN (see section 3.4.3), when the whole tritium spectrum is measured. Then, the 9.4 keV conversion electron lines are an important nuclear standard

to test the linearity of the energy scale between 7 keV and 9 keV (see table 5.2). However, the usage of the 9.4 keV transition depends strongly on the tritium background of the contaminated WGTS.

The main difference is that Decman and Stoeffl performed a differential measurement of the split conversion lines in contrast to the integral measurement of KATRIN. However, with the KATRIN setup a much better resolution than the 9.5 eV of the Livermore experiment is achieved. For energies of 9 keV and the magnetic field settings of the ^{83m}Kr campaign in July 2017 (2.7×10^{-4} T magnetic field in the analysing plane, 70 % of KATRIN nominal field along the entire beam line) a resolution of $\Delta E = 0.6$ eV is obtained (see table 5.1). In order to cover all lines at their expected position, the retarding voltage of the main spectrometer was ramped in the regions from -9400 V to -8800 V and from -7800 V to -7200 V in 1 V steps with 20 s of measurement time per step. The results are presented and discussed in the following.

According to table 5.2, the most intense conversion electron lines of the ^{83m}Kr 9.4 keV transition are the L lines (L_1, L_2 and L_3) and the M_1 line. These are also the lines visible in the gaseous ^{83m}Kr data recorded in July 2017, while the weaker lines are not detected. As expected due to the Decman and Stoeffl results, the four lines are split into several sub-lines. Figure 5.13 shows the measured sub-lines of the L_1-9.4 line, figure 5.14 the sub-lines of both the L_2-9.4 and the L_3-9.4 line and figure 5.15 the line-splitting of the M_1-9.4 line. In order to assign the correct ionisation state, the energy shifts of the sub-lines reported in the literature [Man91] are used (see also table 5.7) together with the information about the signal strength of the different sub-lines [Dec90b; Ryš92]. Since the measured line positions of the 32 keV transition coincide well with the literature values (see table 5.3), the same is assumed for the position of the conversion electron lines of the 9.4 keV transition for a neutral ^{83m}Kr atom.

Each of the sub-lines is fitted with the KaFit krypton fitter to determine the line position, the squared Lorentzian line width, the background and the signal strength (see figure 5.4). The systematic uncertainties listed in section 5.3 are taken into account. For every sub-line, up to 10 fits were performed, each of them with a different fit range around the sub-line. The uncertainties are derived as discussed in section 5.4.3 for the 32 keV transition. The reduced χ^2 values indicate that the model describe the conversion lines well. The deviations are explained by unaccounted for influences from neighbouring lines in the diffuse increase of the rate. For all sub-lines, an uncertainty of the position determination below 1 eV is achieved, and for the most intense sub-lines even an uncertainty better than 0.1 eV is obtained. This underlines the great capabilities of KATRIN for doing precision spectroscopy. Even more precise measurements are possible, if the step width of the retarding voltage is reduced and the count rate of the ^{83m}Kr is increased.

In the literature, the shift of the binding energies with increasing charge of the positive ^{83m}Kr ion is derived [Dec90b; Man91]. This shift is calculated as the difference of the line positions of two neighbouring sub-lines. The results are listed in table 5.7 in comparison to the experimental results by Decman and Stoeffl [Dec90b] and theoretical calculations [Man91]. However, both sources state only values for the L_1 and M_1 lines. For the L_2 and L_3 lines, calculations have been performed [Ryš92], but no measured line shifts have been published so far. Thus, the measured energy shifts for the L_2 and L_3 lines stated in the table can be considered the first published values for these lines to the best of knowledge.

Wherever a comparison to the former experimental values is possible, the energy shifts determined with KATRIN agree well. The only exception is the energy shift from the 6+

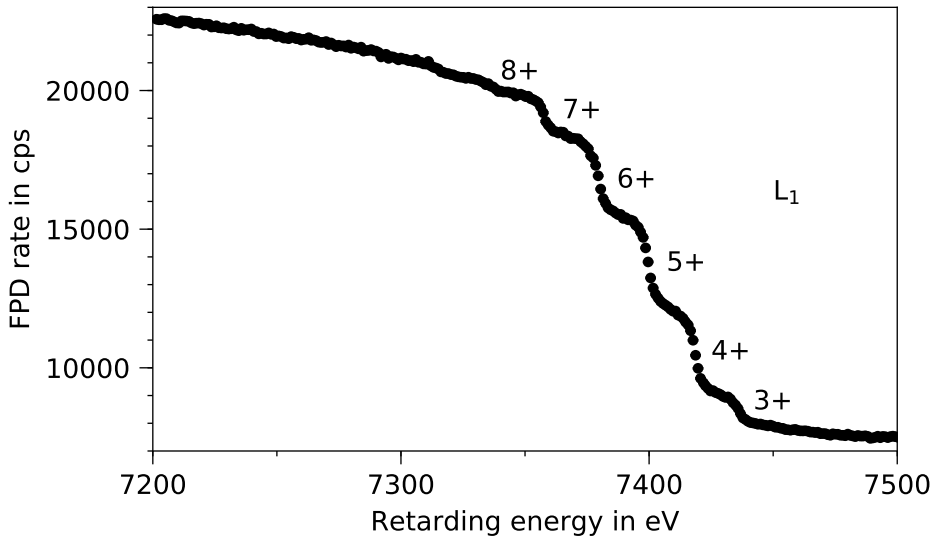

Figure 5.13.: Splitted L_1 line of the 9.4 keV transition of ^{83m}Kr. The L_1 line is the most intense line of the 9.4 keV transition (see table 5.2). Six separated lines are visible, which can be identified with their corresponding charge state according to the literature [Dec90b; Man91; Ryš92]. States which are less (1+, 2+) or more (>8+) ionised contribute to a diffuse increase of the count rate with decreasing retarding voltage without being visible as distinct line. The determined positions and signals of the lines are listed in table 5.6. The statistical uncertainties are smaller than the marker size.

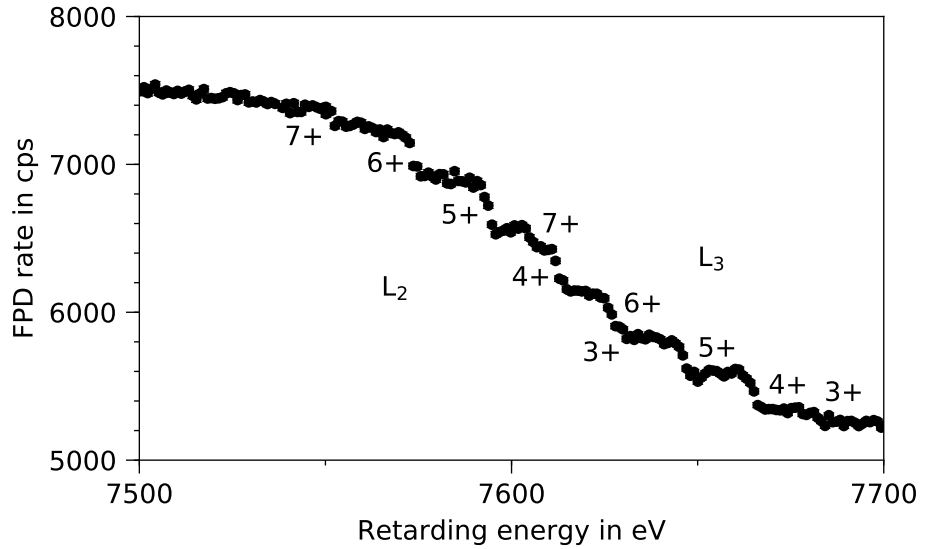

Figure 5.14.: Splitted L_2 and L_3 line of the 9.4 keV transition of ^{83m}Kr. The L_2 and the L_3 line of the ^{83m}Kr transition are separated by ≈ 50 eV (see table 5.2). Therefore, the sub-lines due to the ionisation of the ^{83m}Kr atom are found in the same energy range. However, the identification due to the line positions and intensities from literature is still possible [Ryš92]. The labels above the measurement points are belonging to the L_3 line, the labels below refer to the L_2 line. The fitted positions are listed in table 5.6. The statistical uncertainties are smaller than the marker size.

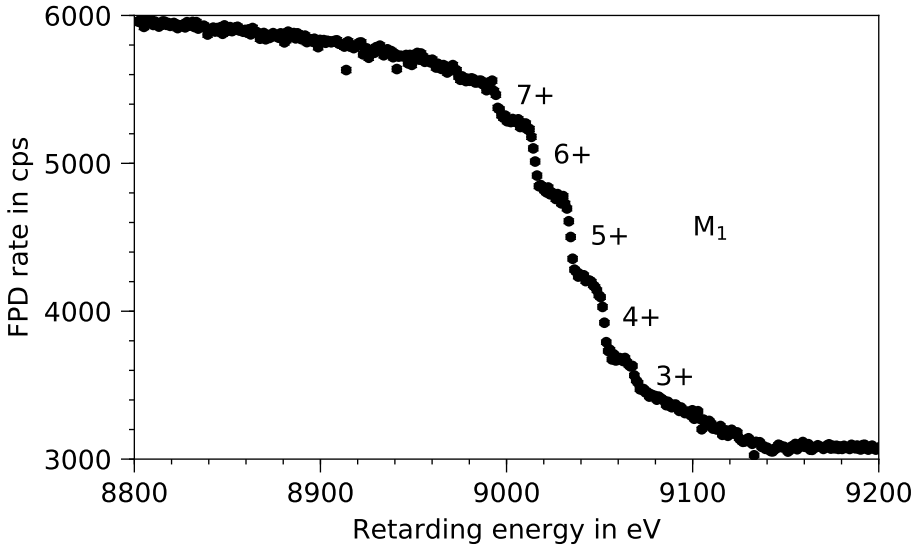

Figure 5.15.: Splitted M_1 line of the 9.4 keV transition of ^{83m}Kr. Among the M lines of the 9.4 keV transition of ^{83m}Kr, the M_1 line is the most intense one (see table 5.2). The sub-lines are clearly visible in the recorded data. Five ionised states of the ^{83m}Kr can be identified [Dec90b; Man91; Ryš92] and their fitted line positions are listed in table 5.6. Contributions from the M_2 and M_3 lines might be hidden in the diffuse rate increase around 9100 eV (see [Dec90b]). The statistical uncertainties are smaller than the marker size.

to the 7+ sub-line of the L_1 line, where the measured shift of the binding energy is 0.7 eV larger than reported by [Dec90b]. The precision of the Decman and Stoeffl measurements could not be achieved, but this should be possible with smaller retarding voltage steps and more measurement time per voltage step. In fall 2018, the lines of the 9.4 keV transition were again measured with KATRIN, but this time the ^{83m}Kr was circulated together with deuterium in the inner loop system. The line splitting was observed again, and higher count rates than reported here were obtained[5]. These measurements are currently under analysis and will probably improve the precision of the line positions to confirm or refute the deviation of the energy difference of the 6+ and 7+ ionisation state.

A comparison of measured line shifts to theory in table 5.7 shows that the calculations of [Ryš92] seem to underestimate the shifts for ionisation states of ^{83m}Kr up to 6+, while the calculated values of [Man91] fit well to measured data. This seems to change for the line shifts of higher-ionised states: for the line shift of the 7+ state, the values of [Ryš92] fit better to the measured data, while [Man91] seem to overestimate the shift. For even higher ionised states, this overestimation became even clearer for the measurements of [Dec90b]. Unfortunately, these higher ionised states could not be observed in the measurements reported here. However, the data show clear differences between the line shifts of the L sub-shells of up to 1 eV, much larger than the predictions by the theory calculations [Ryš92].

In table 5.7, also the line shifts of the 1+ and 2+ states of the L_1, L_2, L_3 and M_1 line are given from [Dec90b; Man91; Ryš92]. They can be used together with the absolute values determined for the 3+ states in table 5.6 to calculate the position of the corresponding conversion electron line for a neutral ^{83m}Kr atom. As the calculations of [Man91] seem to describe the line shifts for lower ionised states better than [Ryš92], only the values of [Man91] are used, so that this analysis can only be done for the L_1 and M_1 line. By

[5] Personal communication M. Machatschek, Oct 29, 2018.

Table 5.6.: Line positions and signal strengths of the ionised states of the ^{83m}Kr 9.4 keV transition. In the first column, the main line of the 9.4 keV transition is given, which is split up into sub-lines according to the ionisation state (column 2). The line positions in "retarding energy" (column 3) and signal strengths (column 4) are determined with the KaFit krypton fitter. Details on the uncertainty determination can be found in the main text. In the fifth column, the signal strengths are normalised to the ones of the 5+ states, which are the most intense ones in three of the four cases. The reduced χ^2 values of the fits are listed in the last column.

Line	Ionisation state	Line position in eV	Signal in cps	Normalised signal in %	χ^2/dof
L_1	3+	7436.20±0.13	1067±33	33.7	1.0
	4+	7418.86±0.05	2774±57	86.5	1.0
	5+	7399.91±0.04	3206±54	100.0	1.1
	6+	7379.88±0.08	2637±77	82.2	2.0
	7+	7357.81±0.11	1279±29	39.9	0.9
	8+	7335.89±0.60	660±84	20.6	0.7
L_2	3+	7630.34±0.18	68±15	16.6	0.6
	4+	7612.60±0.17	279±15	68.2	0.8
	5+	7594.01±0.22	410±36	100.0	1.9
	6+	7573.38±0.16	251±21	61.4	1.0
	7+	7552.12±0.24	101±13	24.6	1.0
L_3	3+	7682.10±0.69	66±23	29.9	1.5
	4+	7665.29±0.19	238±25	107.4	1.0
	5+	7646.53±0.19	222±29	100.0	1.4
	6+	7626.89±0.37	254±24	114.6	1.1
	7+	7605.41±0.37	136±16	61.4	0.9
M_1	3+	9069.48±0.42	204±23	39.3	1.2
	4+	9052.82±0.11	467±25	89.8	1.2
	5+	9034.67±0.10	520±22	100.0	1.4
	6+	9015.37±0.17	443±19	85.1	0.9
	7+	8995.31±0.25	228±13	43.9	1.7

adding the calculated shifts from [Man91] to the measured positions of the 3+ states in table 5.6, a position of 7479.5 eV for the L_1-9.4 line and 9112.2 eV for the M_1 line is obtained. Compared to the line positions of the neutral ^{83m}Kr atom in table 5.2 (7481.1(10) eV for the L_1 line and 9112.9(7) eV for the M_1 line), a slight shift on the order of 1 eV towards smaller energies is visible. Since for the theory values no uncertainties are given, several interpretations are conceivable. For instance, the shifts calculated from theory might be underestimated. This seems to be the case at least for the M_1 line, for which Decman and Stoeffl reported slightly larger shifts than predicted by theory (see table 5.7), while they confirmed the predictions for the L_1 line. The second possibility is that the measured lines are shifted towards smaller energies due to the work function difference of the source and the main spectrometer. However, such a shift should be the same for every line and should also be visible in the line positions of the 32 keV transition. Since this is not the case (see table 5.3), the work functions can be ruled out as a cause of the observed deviation. Finally, as a third explanation the energy scale of KATRIN could be non-linear. This can be investigated very well for the energy ranges of the 32 keV transition (see section 5.4.4), and the results are interpreted as a linear response. However, this does not necessarily mean

Table 5.7.: Relative line positions of the ionised states of the ^{83m}Kr 9.4 keV transition. The table lists the energy difference between two sub-lines of the 9.4 keV transition. $\Delta E_{\mathrm{theo},1}$ are calculated values from [Man91], $\Delta E_{\mathrm{theo},2}$ are the calculated values from [Ryš92] (data kindly provided by M. Ryšavý). The measured values by Decman and Stoeffl [Dec90b] are given in column 5 (ΔE_{meas}). The values determined in the scope of the thesis at hand are presented in the last column (ΔE_{new}).

Line	Ionisation states	$\Delta E_{\mathrm{theo},1}$ in eV	$\Delta E_{\mathrm{theo},2}$ in eV	ΔE_{meas} in eV	ΔE_{new} in eV
L_1	0→1	12.9	12.0		
	1→2	14.6	13.5	14.4(3)	
	2→3	15.8	15.1	15.9(2)	
	3→4	17.3	16.7	17.3(1)	17.34(14)
	4→5	18.2	17.8	18.7(1)	18.95(6)
	5→6	19.4	18.9	20.2(1)	20.03(9)
	6→7	21.5	21.0	21.4(1)	22.07(14)
	7→8	22.7	22.0	22.2(2)	21.92(61)
L_2	0→1		12.0		
	1→2		13.6		
	2→3		15.1		
	3→4		16.8		17.74(25)
	4→5		17.7		18.59(28)
	5→6		18.8		20.63(27)
	6→7		21.3		21.26(29)
L_3	0→1		12.0		
	1→2		13.6		
	2→3		15.0		
	3→4		16.6		16.81(72)
	4→5		17.9		18.76(27)
	5→6		19.0		19.64(42)
	6→7		21.2		21.48(52)
M_1	0→1	12.8	11.9		
	1→2	14.3	13.5	14.8(8)	
	2→3	15.6	14.9	16.4(4)	
	3→4	16.8	16.2	16.9(1)	16.66(43)
	4→5	17.9	17.3	17.9(1)	18.15(14)
	5→6	18.8	18.4	19.2(1)	19.30(20)
	6→7	20.8	20.1	20.1(1)	20.06(30)

that the energy scale is also linear for retarding voltages of −7 kV to −9 kV. A non-linear energy scale at these energies would not influence the standard KATRIN tritium data taking, since then the measurement interval is restricted to a region close to the kinematic endpoint of the tritium beta spectrum around 18.6 keV, but it could have an effect for the search for keV sterile neutrinos (see section 3.4.3), when the full tritium spectrum is measured. Therefore, the deviation found between the measured line positions and the line positions from literature of the 9.4 keV transition should be addressed again in future measurements.

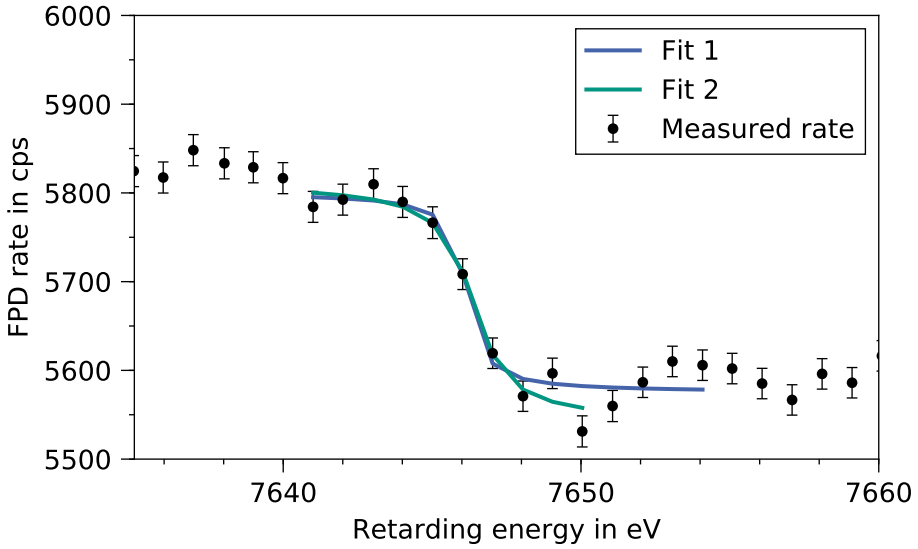

Figure 5.16.: Dependence of the fitted conversion electron line signal on the fit range. Shown are two fits of the L_3 5+ line. For a narrow fit range (fit 2), a larger signal strength is found than for a wider fit range (fit 1) due to the fluctuation of the rate right next to the line. Thus, a precise signal determination is not possible, which is also true for the other sub-lines of the L_3 transition.

The intensity of the sub-lines gives a direct measure of the charge distribution of the ^{83m}Kr ions before the 9.4 keV transition. Studies presented in [Dec90b; Ryš92] predict that most of the ^{83m}Kr ions are fivefold positively charged, so that the corresponding sub-lines should be the most intense ones in the spectra. This could be confirmed during the gaseous ^{83m}Kr campaign in July 2017 (see table 5.6). There is one exception, which is the L_3 line, for which the 4+ and 6+ states are more intense than the 5+ state. However, this can be partly explained by looking closer to the 5+ line in figure 5.16: the signal is only about 250 cps strong, but close to the line fluctuations of the order of 50 cps are visible. The fitted signal therefore strongly depends on the selected fit range for the line. The uncertainty is determined in the same way as for the position estimate of the lines and consists of the uncertainty of the selected fit and an uncertainty component associated with the fit range. Hence, although the best fit in terms of the reduced χ^2 value favours a signal strength of the 5+ state being smaller than the one of the 6+ state, the opposite cannot be ruled out here.

The intensity distribution along the charged states should be the same for every line. As illustrated in figure 5.17, this can be confirmed for the L_1 and M_1 states. Clear deviations are visible for the L_2 and L_3 states. Since the sub-lines of the L_2 and L_3 line are close to each other in the same energy range (see figure 5.14), a mutual influence on the intensities is probable, which may explain the observed deviations. The problems in determining the correct intensity for the 5+ state of the L_3 line outlined above and depicted in figure 5.16 are also present for the other sub-lines of L_2 and L_3. From the values listed in table 5.6 it can be concluded that the intensity of the 7+ state is always larger than the intensity of the 3+ state for all four lines. The 4+ and the 6+ state show comparable intensities with the 6+ state being more intense than the 4+ state in three of the cases and vice versa in the remaining case.

To conclude this section, it can be stated that KATRIN has the capability to perform high-precision spectroscopy around as well as far off the kinematic endpoint of tritium.

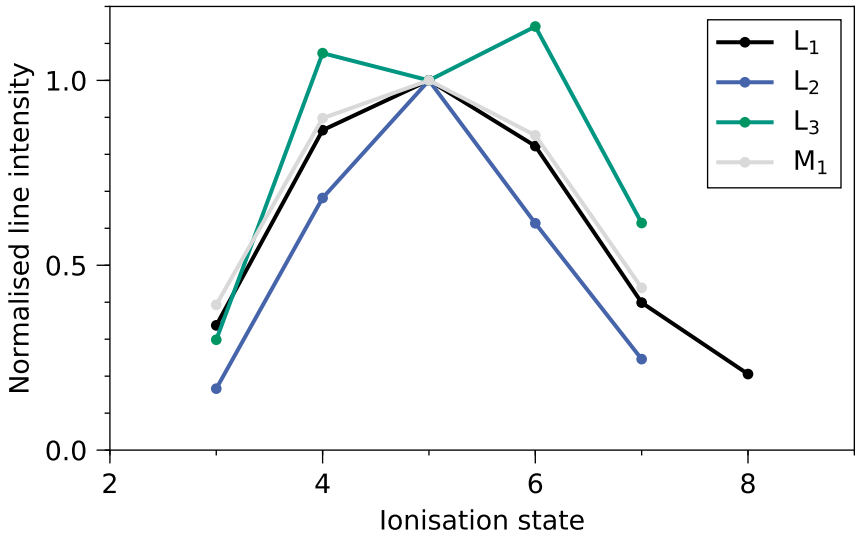

Figure 5.17.: Signal strengths of different ionised states of ^{83m}Kr in the 9.4 keV transition. The plot shows the signal strengths normalised to the intensity of the 5+ sub-line over the state of ionisation of the ^{83m}Kr for all measured lines of the 9.4 keV transition. It can be concluded that after the 32 keV transition and the following Auger electron cascade most of the ^{83m}Kr atoms are in a fivefold positive-charged state. The shape of the distribution should be the same for all four lines, but clear deviations are visible for the L_2 and L_3 line.

The line-splitting of the conversion electron lines of the 9.4 keV transition due to different ionisation states of ^{83m}Kr after the 32 keV transition and the following Auger cascade presents a phenomenon at the connection of nuclear and atomic physics: the nuclear effect of internal conversion helps to measure the change of the binding energy of electrons of different shells with the change of the ionisation. The results obtained in the scope of this thesis are mostly in agreement with former theoretical and experimental investigations of the effect. For the L_2 and the L_3 line, so far no experimental data has been published before to the best of knowledge. The measured line positions of the sub-lines may become important benchmarks for future measurements with KATRIN, if work function effects are investigated. There are hints that the measured line positions of the 9.4 keV transition differ from the values listed in table 5.2, which is not observed for the conversion electron lines from the 32 keV transition. This might either point towards a non-linear energy scale of KATRIN at lower energies, or to uncertainties in the theoretical energy shift calculation due to the ^{83m}Kr ionisation. This question should be re-investigated in view of a keV sterile neutrino search with KATRIN.

5.4.7. Line Position Stability

The gaseous ^{83m}Kr campaign offered the first opportunity to measure the energy-scale stability of the entire KATRIN beamline in operation. A well-suited test parameter for the energy-scale stability is the line position of the ^{83m}Kr conversion electrons. It is sensitive to many KATRIN parameters at different sections of the experiment: a shift of the line positions can occur due to drifts of the high voltage during the one week of measurement time, changes in the work function difference between the main spectrometer and the WGTS and unaccounted for drifts of the magnetic field in the source or the analysing plane.

A reference scan procedure of the L_3-32 was developed for the week of gaseous ^{83m}Kr measurements to determine the position of this line reproducibly under the same conditions.

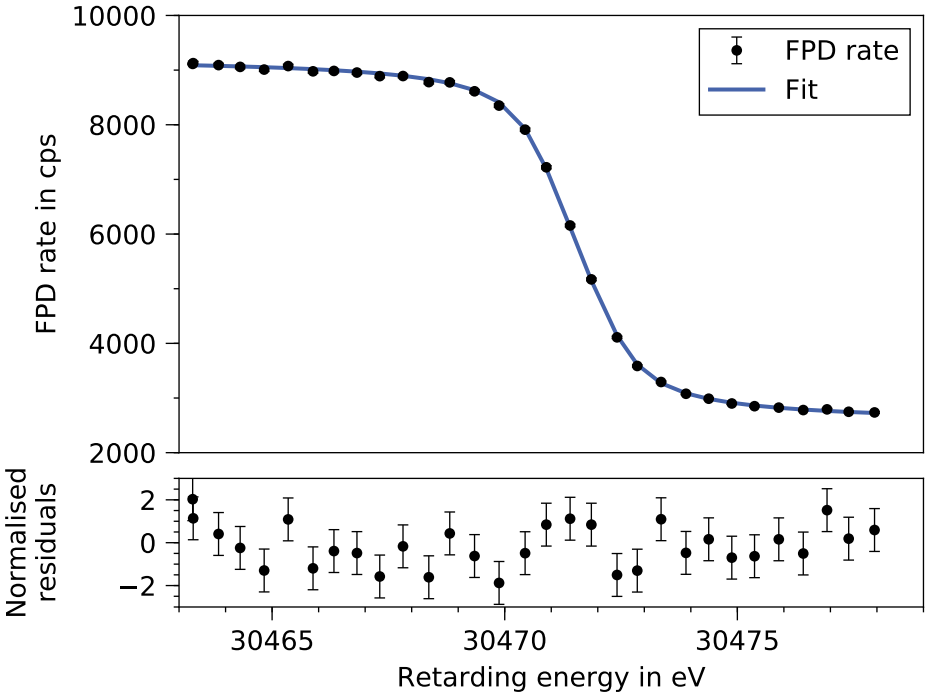

Figure 5.18.: Fit of a L_3-32 reference run. The plot shows a reference scan of the L_3-32 line. As all fits performed in this thesis, it is fitted with KaFit/SSC in a uniform fit (all detector pixels at once). The reduced χ^2 is 1.2. The values of the fit parameters are the line position in "retarding energy" $E_{\mathrm{ce}} = (30472.62 \pm 0.01)\,\mathrm{eV}$, the squared line width $\Gamma_{\mathrm{ce}}^2 = (1.39 \pm 0.05)\,\mathrm{eV}^2$, the line intensity $I_{\mathrm{ce}} = (5666 \pm 14)$ cps and the background rate $R_{\mathrm{bg}} = (2529 \pm 10)$ cps. The residuals are normalised to their statistical uncertainty. The statistical uncertainty bars of the data points in the upper plot are smaller than the marker size.

For these standard scans, the main spectrometer voltage was varied in 0.5 V steps in the range of −30480 V to −30465 V, where the L_3-32 line is expected (see table 5.2). The measurement time per retarding voltage set point was 10 s. The magnetic field in the analysing plane was always 2.7×10^{-4} T, all other magnetic fields were at their standard values (70 % of the nominal values, see [Are18c]). In total, 11 of these reference scans were performed, and one is shown in figure 5.18 together with the fit performed with KaFit/SSC. The fit model takes the systematic effects described in section 5.3 into account.

Figure 5.19 shows the fit results for the line position E_{ce} of the 11 reference scans. The stability of the energy scale is determined as the standard deviation of the 11 line position results and a value of 0.1 ppm is obtained. This exceeds the KATRIN requirement, which is formulated for the high-voltage stability at −18.6 kV to be 3 ppm [Ang05], by more than one order of magnitude. If the requirement is scaled to −30.4 kV, which corresponds to the position of the L_3-32 line, the stability should not exceed 1.8 ppm which is clearly the case. It should be kept in mind that the ^{83m}Kr line stability tests not only the high-voltage stability but further relevant effects for the energy scale, as outlined above. The measurement time of a reference scan is > 15 min if the time for the ramping of the retarding voltage is included. Short-term fluctuations like the high-voltage ripple (see section 4.2.7 and 5.3) are therefore not covered by this kind of analysis but have to be investigated separately. In KATRIN tritium operation, the system will be operated for 60 days until the CPS argon frost layer has to be refreshed (see section 3.2.4). The excellent stability of the energy scale

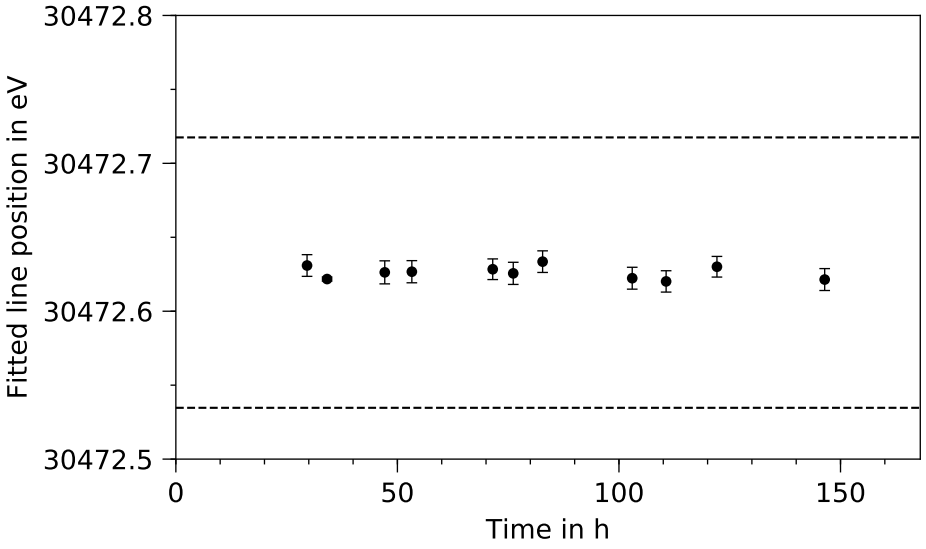

Figure 5.19.: Stability of the L_3-32 conversion line position over one week. The plot shows the fit estimates for the line position in "retarding energy" of all standard scans of the L_3-32 conversion line performed during the gaseous ^{83m}Kr campaign. The time axis is relative to the first opening of the gaseous ^{83m}Kr generator at the beginning of the measurement week. The dashed lines mark the KATRIN requirement of the high voltage stability of $\sigma_{\mathrm{HV}} = \pm 3\,\mathrm{ppm}$ (see section 4.2.7). All runs were performed with the same conditions as described in the main text.

demonstrated here for about one week is a strong hint that the requirements will also be kept for 60 days.

5.4.8. Satellite Lines

As mentioned in section 5.2, the main conversion lines of ^{83m}Kr are accompanied by weaker satellite lines due to shake-up effects which occur at energies $\gtrsim 20\,\mathrm{eV}$ below the main conversion lines. The mean line shifts and the relative intensities of the shake-up lines have been calculated [Car73] and several publications report the experimental determination of the positions of these satellite lines by photoionisation with high precision for the M [Spe74; Eri87] and N shells [Sve88; Kik96; Ali01; Cal06]. However, for the inner shells (K and L), only two measurements are reported, both performed with the setups of former experiments to determine the neutrino mass in tritium beta decay: the Los Alamos group investigated the satellite spectrum of the ^{83m}Kr K line [War91]; the Mainz group investigated the full ^{83m}Kr conversion electron spectrum and also identified several shake-up lines [Pic92].

Although the main focus of the ^{83m}Kr measurements with KATRIN in July 2017 was put on the investigation of the main conversion lines, also some satellite lines were recorded: one of the K line, one of the L_3-32 line and one of the L_1-9.4 line. The energy resolution of KATRIN is much better than the one of the Los Alamos setup. As the Mainz group used a condensed ^{83m}Kr source, the July 2017 measurements of the L_1-9.4 and L_3-32 satellite can be considered as the first measurements with a gaseous ^{83m}Kr source. The results are discussed in the following.

Figure 5.20 shows a satellite line of the K-32 line, another one of the 32 keV transition was recorded for the L_3-32 line. The satellite line of the K-32 line has a very long tail and does not possess the typical shape of the main lines. The line shape of the satellite lines is not described in literature, so that the Voigt profile applied here may not be the correct

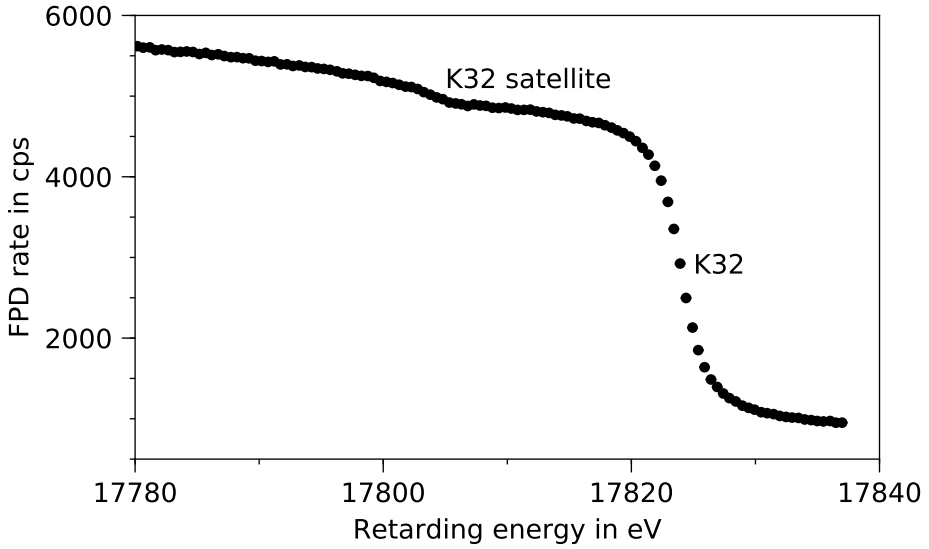

Figure 5.20.: K-32 conversion line of ^{83m}Kr with its first satellite line. The plot shows the measurement of the K-32 line and its first satellite. The retarding voltage step width and the measurement time per step are listed in table 5.4.

choice. However, the L_3-32 satellite line shows a shape that can be fitted with the Voigt profile (see figure 5.21). The fit results are presented in table 5.8. The satellite line of the L_3-32 main line occurs 21.006(134) eV below the main line. This is 2 eV less than reported by the Mainz group [Pic92] which used a condensed krypton source. By comparing the intensity of the satellite line with the intensity of the main line in table 5.3, a shake-up/off probability of (12.5 ± 0.7) % is derived. This is less than the total shake-up/off probability of 17.7 % [Vén18], but there are actually more satellite lines of L_3 which have not been recorded here [Car73].

Since the main conversion lines of the 9.4 keV transition are split into sub-lines according to the state of ionisation (see section 5.4.6), every sub-line labelled in the figures 5.13, 5.14 and 5.15 is in principle accompanied by shake-up lines which occur at least 15 eV below it. These satellite lines are much weaker than the main lines, so that in the recorded data of the gaseous ^{83m}Kr campaign of summer 2017 only one of these satellite lines is identified. Its parameters are listed in table 5.8. The satellite is 33.47(48) eV below its main line, which is the L_1 5+ line. This result coincides qualitatively with a former measurement of the L_1-9.4 line and its satellite [Pic92]. The shake-up/off probability is calculated to (8.8 ± 1.9) % based on the intensities of the main and satellite line.

For the fall 2018 measurements, ^{83m}Kr was circulated with deuterium in the inner loop and a larger count rate than in the measurements of summer 2017 was achieved. Due to the larger count rate, more satellite lines should be visible in the spectrum, especially in the 9.4 keV transition. These measurements are currently under analysis and results are expected soon [Mac19].

5.4.9. Conversion Electron Line Widths

Although the focus of the gaseous ^{83m}Kr campaign from July 2017 was put on the determination of the positions of the conversion lines and their intensities, the squared line width was also determined as one of the fitting parameters (see figure 5.4). These results shall be discussed briefly in the following.

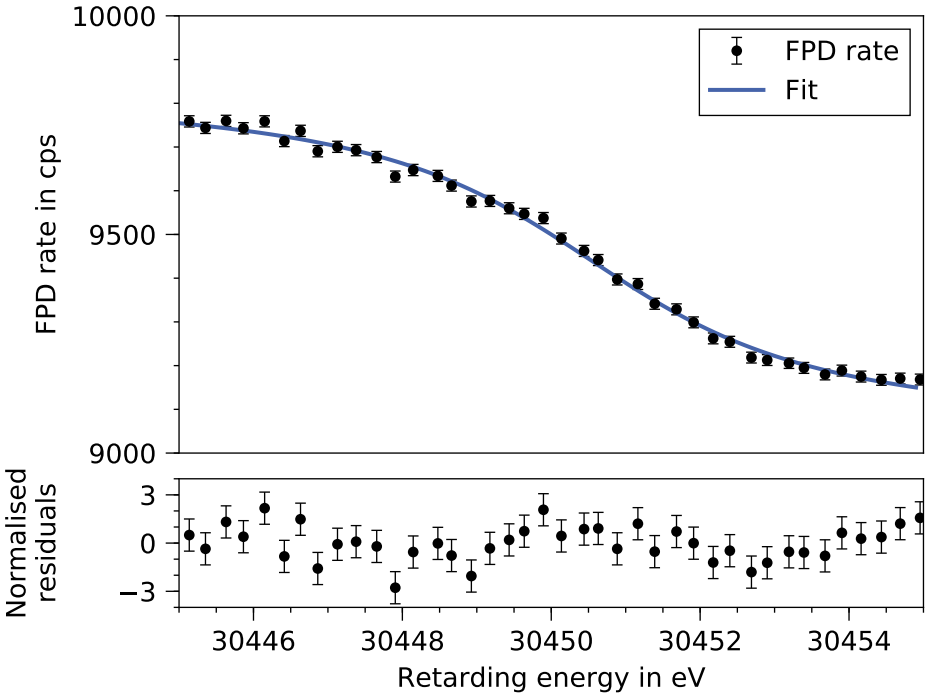

Figure 5.21.: Fit of the L_3-32 satellite line. The plot shows a reference scan of the L_3-32 line. A uniform fit (all detector pixels at once) is performed with KaFit/SSC. The reduced χ^2 is 1.3. The fit results are listed in table 5.8. The residuals are normalised to their statistical uncertainty.

Table 5.8.: Measured satellite lines during the gaseous ^{83m}Kr campaign in July 2017. The table presents the line position, line width and signal strength of the shake-up satellite lines of the L_3-32 and L_1-9.4 line which were measured during the gaseous ^{83m}Kr campaign in July 2017. The uncertainties are determined as described for the main lines in section 5.4.3. The relative values refer to the parameters of the main lines in table 5.3 and 5.6. In the last line, the reduced χ^2 values of the fits are presented.

Parameter	L_3^{sat}-32	L_1^{sat}-9.4 (5+)
Line position in eV	30451.636 ± 0.134	7366.44 ± 0.48
Relative line position in eV	21.006 ± 0.134	33.47 ± 0.48
Signal strength in cps	701 ± 37	281 ± 60
Relative intensity in %	12.5 ± 0.7	8.8 ± 1.9
Line width in eV	$4.39^{+0.39}_{-0.43}$	$2.12^{+0.93}_{-2.12}$
χ^2/dof	1.3	1.1

Table 5.9.: Conversion line widths of the 32 keV transition of ^{83m}Kr. The table presents the fitted Lorentzian line widths Γ_{ce} of the investigated lines of the 32 keV transition of ^{83m}Kr. The very narrow doublets $M_{4,5}$ and $N_{2,3}$ could only be fitted with fixed line widths (see section 5.4.3), so that no values are given here. The uncertainties are asymmetric as the symmetric fitting uncertainty on the squared line width is translated to the uncertainty on the line width. The lines M_2 and M_3 (marked with an asterisk) have been measured at a different setting of the gaseous ^{83m}Kr generator than the other lines listed here. For reference, the values from [Vén18] are listed in the second column.

Line	Γ_{ce} in eV [Vén18]	Γ_{ce} in eV (this work)
K	2.71(20)	$2.752^{+0.006}_{-0.006}$
L_1	3.75(93)	$9.600^{+2.012}_{-2.566}$
L_2	1.25(25)	$1.270^{+0.048}_{-0.049}$
L_3	1.19(24)	$1.163^{+0.015}_{-0.016}$
M_1	3.5(4)	$6.244^{+0.725}_{-0.822}$
M_2^*	1.6(2)	$1.910^{+0.269}_{-0.314}$
M_3^*	1.1(1)	$1.560^{+0.044}_{-0.045}$
N_1	0.0255(4)	$0.509^{+1.010}_{-1.010}$

Table 5.10.: Conversion line widths of the 9.4 keV transition of ^{83m}Kr. The table presents the fitted Lorentzian line widths Γ_{ce} of the investigated lines of the 9.4 keV transition of ^{83m}Kr. The lines are split due to the ionisation of the ^{83m}Kr. The Lorentzian widths of the ionised states for the L_1, L_2, L_3 and M_1 were measured. The uncertainties are asymmetric as the symmetric fitting uncertainty on the squared line width is translated to the uncertainty on the line width.

Ionisation state	$\Gamma_{ce}(L_1)$ in eV	$\Gamma_{ce}(L_2)$ in eV	$\Gamma_{ce}(L_3)$ in eV	$\Gamma_{ce}(M_1)$ in eV
+3	$4.69^{+0.22}_{-0.24}$	$0.00^{+0.05}_{-0.05}$	$1.23^{+3.67}_{-1.23}$	$3.46^{+0.55}_{-0.66}$
+4	$3.83^{+0.15}_{-0.16}$	$1.67^{+0.10}_{-0.11}$	$1.80^{+0.57}_{-0.87}$	$2.54^{+0.21}_{-0.23}$
+5	$4.38^{+0.15}_{-0.16}$	$2.61^{+0.24}_{-0.27}$	$1.94^{+0.57}_{-1.24}$	$2.45^{+0.21}_{-0.23}$
+6	$4.55^{+0.27}_{-0.28}$	$1.00^{+0.39}_{-0.73}$	$2.57^{+0.12}_{-0.12}$	$2.89^{+0.14}_{-0.15}$
+7	$3.48^{+0.12}_{-0.12}$	$0.64^{+0.15}_{-0.20}$	$1.52^{+0.29}_{-0.36}$	$2.42^{+0.19}_{-0.21}$
+8	$8.94^{+1.77}_{-2.23}$			

The fit results for the conversion lines of the 32 keV transition are presented in table 5.9. The uncertainties on the fit parameter, the squared line width, are calculated as for the line intensity and line position (see section 5.4.3). The comparison to the literature values given in table 5.2 shows that the measured widths of the intense lines (K, L_2, L_3) are in good agreement within the uncertainties with the natural line widths. These line width can also be determined to a good precision on the order of 10 meV. In contrast, the measured line widths of the weaker conversion lines L_1 and M_1 show a significant deviation from the literature values of 170-250 %, but also the precision is much worse. It is assumed that also for the weak conversion lines better results can be achieved when the step width of the retarding voltage is decreased and the measurement time per step is increased (see table 5.4). Furthermore, the selected measurement interval for both lines was maybe too small and better results may be possible with more data points at both sides of the lines.

The fitted Lorentzian line widths of the 9.4 keV transition conversion lines, which are split up due to the ionisation of the ^{83m}Kr, show an inconsistent picture: comparing the

obtained values with the literature values in table 5.2 for the non-ionised ^{83m}Kr, qualitative consistencies are found: L_2 and L_3 have smaller widths than L_1 and M_1. However, the actual deviations are large. Within the group of one main line there is no clear ordering recognisable. Often the lines with the smallest intensity within one group show the worst fit estimate compared to the literature value. It is assumed that the large deviations are caused by the fact that the sub-lines are quite close to each other and placed in a diffuse increase of the rate (see figures 5.13, 5.14 and 5.15). This could lead to an overestimation of the line width as it is observed here.

5.5. Conclusions

The gaseous ^{83m}Kr measurement campaign in July 2017 was an important step for KATRIN on its way towards the first tritium measurements in 2018. The most important findings are summarised briefly in the following:

- The main goal of the gaseous ^{83m}Kr measurement campaign in July 2017 was to demonstrate the operational readiness of the gaseous ^{83m}Kr generator for the determination of the WGTS potential as an important systematic effect of KATRIN standard tritium operation (see section 4.2.13). The gaseous ^{83m}Kr generator ran smoothly for the full week of allocated measurements and provided practicable count rates for several spectroscopic investigations of the ^{83m}Kr inner conversion electrons. It is ready for the operation in the closed inner loops together with tritium.

- The gaseous ^{83m}Kr measurement campaign in July 2017 was the first time that signal electrons from a uniformly distributed and isotropic source were measured with the full KATRIN beam line. High-precision spectroscopic measurements in the retarding voltage range from -7 kV to -33 kV demonstrate the excellent capabilities of KATRIN. All systems from the WGTS temperature to the magnetic fields and the high voltage ran smoothly for one week with an excellent stability (see chapter 6). Therefore, the ^{83m}Kr measurements were an important proof of KATRIN's operational readiness with a short-lived isotope before the first tritium campaign in summer 2018.

- Although the analysis of ^{83m}Kr conversion electron lines is different in the physical modelling from the analysis of the tritium beta spectrum, the two fitting tools developed by the KATRIN collaboration for krypton and tritium analysis as part of the KASPER software package (see section 3.3) share the same principle: the count rate measured with the focal plane detector has to be modelled under the implementation of several hundreds of slow control values like the magnetic fields, temperatures and pressures in the WGTS etc. During the gaseous ^{83m}Kr campaign in July 2017, it was the first time that the influence of some slow control values on the measured count rate could be taken into account automatically in the analysis. Based on this experience, the analysis software and underlying technical infrastructure was developed further for the first tritium measurements.

- For the determination of the potential inside the WGTS in later tritium operation of KATRIN, especially the precise position measurement of the L_3-32 line of ^{83m}Kr is important. It was demonstrated that a precision of a few meV is achievable for a measurement time of ≈ 1 h, which fulfils the requirement [Mac16].

- The line positions and line widths of conversion electron lines of the 32 keV transition were determined. These are important benchmarks for future ^{83m}Kr measurements with KATRIN, since in the measurements reported here the ^{83m}Kr was the only gas species in the source. In future operation, the ^{83m}Kr will be mixed either with deuterium or tritium to be pumped in the inner loop. The other gas species might have an influence on the line positions and widths as they can change the work

function in the WGTS or create a plasma potential (only in the case of tritium). The measurements of ^{83m}Kr without any additional gas species present will be crucial for understanding these effects.

- The linearity of the energy scale of the KATRIN experiment was measured by comparing the line positions of conversion electron lines of the ^{83m}Kr 32 keV transition with literature values of the corresponding binding energies. The energy scale was found to be linear. Deviations were found for the weak lines which have less precisely determined position values. However, a hint of a non-linearity towards smaller energies was found with the position of the conversion electron lines of the 9.4 keV transition. Since their interpretation is much more difficult due to ionisation effects of the ^{83m}Kr, it is recommended to repeat this investigation before the start of the KATRIN search for keV sterile neutrinos, when the whole tritium spectrum will be measured.

- Besides the linearity of the energy scale also the stability of the energy scale was monitored over one week with regular scans of the line position of the L_3-32 conversion electron line. The position stability was better than 0.1 ppm and thus more than one order of magnitude better than required.

- The conversion electron lines of the 9.4 keV transition split up into several sub-lines due to the ionisation of the atom after the 32 keV transition and the subsequent Auger cascade. This effect was measured during the gaseous ^{83m}Kr campaign in July 2017 for the first time in an integral way. Previous theoretically and experimentally determined position shifts of the sub-lines due to the change of binding energy were confirmed for the L_1-9.4 and M_1-9.4 line. For sub-lines of the L_2-9.4 and L_3-9.4, it was the first time that experimental values were derived. This demonstrates that KATRIN has also the capability to contribute to the fields of nuclear and atomic physics. With smaller retarding voltage steps and more measurement time, ultra-precise measurements of the line positions of the ionised ^{83m}Kr states are possible.

- The high intensity of the ^{83m}Kr source also enabled the measurement of three satellite lines which occur in the spectrum due to the shake-up effect. The satellite lines of the L_1-9.4 and L_3-32 have not been measured before with a gaseous ^{83m}Kr source.

There are some findings of the gaseous ^{83m}Kr measurement campaign of July 2017, which need re-investigation in future measurements. The first possibility to do so were the ^{83m}Kr measurements in fall 2018, for which data analysis is currently ongoing:

- It was found that conversion electron lines with a comparatively small intensity show much larger deviations in their fitted position and line widths from literature values than intense lines. The position of the weak lines is shifted slightly to larger energies and the line widths are overestimated. This hints to a systematic effect of the fitting tool which has not been accounted for so far. One possible explanation may be a small slope of the background while the model assumes a constant background rate. In the fall 2018 measurements, the obtained count rate was much larger, so that it is a good test if the same effect can be observed.

- Statements on the work functions at the WGTS and main spectrometer surfaces are not possible at the moment, so that the determined absolute values of the conversion line positions cannot be compared to the literature values directly. The position values presented here are benchmarks for future measurements. If deviations are found, this can be a hint of relative work function changes in the WGTS or main spectrometer, when the other measurement parameters are comparable. In order to interpret deviations correctly, the aforementioned count rate dependence of the fitting parameters has to be solved.

- The linearity of the energy scale of the KATRIN experiment at low energies ($< 10\,\mathrm{keV}$) should be investigated with dedicated data sets. The use of gaseous ^{83m}Kr is not suitable at such low pressures where the conversion lines of the 9.4 keV transition split into sub-lines according to the grade of ionisation. The results presented here hint towards a small non-linearity, but the uncertainties of this interpretation are large.

To conclude, the gaseous ^{83m}Kr measurement campaign of July 2017 was a great success for the KATRIN collaboration. The operational readiness of the beam line was proven. Important benchmarks were set for future investigations of systematic effects. The campaign demonstrated KATRIN's unprecedented stability performance and capability of high-precision spectroscopy over a wide energy range. It was one of the major milestones on the way towards the first tritium measurements in May 2018.

6. Characterisation of the WGTS Cryostat

In this chapter, the operational performance parameters of the WGTS cryostat are analysed with special focus on the question if the design specifications are met. The two most important operational parameters of the WGTS which have direct influence on the neutrino mass analysis are the source magnetic field and the temperature of the beam tube. The magnetic field stability is discussed in section 6.1. The discussion of the beam tube temperature in section 6.2 comprises analyses for the two operational modes, at 30 K and 100 K. All results of the chapter are summarised in section 6.3.

6.1. WGTS Magnetic Field Stability

As outlined in section 4.2.11, the source magnetic field has an important impact on the scattering probabilities of electrons in the source and the acceptance angle of electrons in the pinch magnet. Thus, changes of the magnetic field in the source directly lead to changes of the rate of beta electrons to be observed at the detector. To take these related effects into account in a detailed study of systematic effects, the magnetic field trueness, its stability over time and its homogeneity along the WGTS beam tube have to be measured. The KATRIN Design Report considered only the inhomogeneity contribution to the overall systematic uncertainty budget and set a requirement of $\Delta B_\mathrm{S}/B_\mathrm{S} < 0.2\,\%$. The associated neutrino mass shift was estimated to be $2 \times 10^{-3}\,\mathrm{eV}^2/c^4$, see equation 4.19. In order to not exceed this budget, the effects of all three parameters in total – trueness, stability and homogeneity – have to be within the required limit. For the trueness and homogeneity determination, a new measurement system was built. First results were obtained in autumn 2018 [Hei18], but the required positioning precision of the magnetic field sensor is not reached yet. In the scope of the thesis at hand, the stability of the magnetic field of the WGTS is investigated and discussed in the following.

There are three different ways to measure the magnetic field stability of the WGTS: the first method is to analyse the stability of the inducted current value from the readings of three power supplies for the seven superconducting magnets. The second method are current clamps, which are mounted to each of the three circuits for an independent current measurement. Finally, the third method are Hall sensors mounted in each of the seven superconducting coils. Since the exact orientation of the Hall sensors inside the WGTS cryostat is not determined accurately enough, they can only be used for stability measurements but not for absolute magnetic field measurements.

The ^{83m}Kr campaign in July 2017 (see chapter 5) offered the first possibility to investigate the magnetic field stability in standard conditions. It should be noted that standard conditions means that all magnets along the entire beam line are driven with 70 % of their nominal field strengths stated in the KATRIN Design Report [Are18c]. These new standard

Table 6.1.: Settings of the superconducting magnets of the WGTS. The table shows the nominal magnetic field strength B_{nom}, the standard magnetic field strength in the 70 % configuration B_{70} and the corresponding currents I_{nom} and I_{70}. The WGTS-R circuit comprises the magnets M1, M4 and M5. The magnets M2 and M3 are driven by the WGTS-C circuit, and M6 and M7 by the WGTS-F circuit. The reader is referred to figure 3.3 for the numbering scheme of the seven superconducting magnets of the WGTS. Details of the superconducting magnets of KATRIN can be found in [Are18c].

Section	B_{nom} in T	I_{nom} in A	B_{70} in T	I_{70} in A
WGTS-R	3.60	309.95	2.52	216.97
WGTS-C	3.60	308.84	2.52	216.19
WGTS-F	5.60	208.84	3.92	146.19

conditions were selected to decrease the quenching probability of the superconducting coils along the beam line. An overview of the field strengths and current set points is given in table 6.1. Figure 6.1 shows the magnetic field strength of the central beam tube during the one-week gaseous ^{83m}Kr measurement campaign in July 2017, as monitored by the three different kinds of sensors. The strong fluctuations of $\pm 1\,\%$ of the current clamp measurement are noticeable. Since they are not visible in the other two sensors, it is concluded that these fluctuations are not linked to the magnetic field, but are some kind of nuisance signal from other sources. Thus, the current clamps are not suited to measure the magnetic field stability. The difference in the absolute current values of power supply and current clamp has to be investigated further with the absolute magnetic field measurement to find out which one is the correct one and which current arrives finally at the coils. Both the power supply and the Hall sensor show a very stable signal. While the power supply sometimes seems to fluctuate between two digits due to its resolution, the Hall sensor shows a stable value without any fluctuations over hours. A similar behaviour is also observed for the other current circuits and Hall sensors not shown in the figure.

In order to assign an upper limit on the stability of the magnetic field in a conservative estimate, it was decided to analyse the fluctuations of the power supplies further. For all three power supplies, the week of measurement time is cut into one-hour intervals. For each such interval, the relative stability, defined as the standard deviation of the magnetic field strength divided by its mean, is calculated. The time during which the magnets are ramped down/up is excluded, and the remaining data are filled into one histogram, which is shown in figure 6.2. Most of the time also the power supplies do not have any sizeable fluctuations, leading to the prominent peak at bin zero. Based on the observed fluctuations, one can derive a very conservative upper limit on the magnetic field stability per hour of

$$\Delta B_{\mathrm{S}}/B_{\mathrm{S}} < 0.0011\,\frac{\%}{\mathrm{h}}\,. \tag{6.1}$$

The stated value gives the 90th percentile. That means that the vast majority of the systematic uncertainty budget linked to the source magnetic field is left for the homogeneity and trueness, which are investigated with a special sensor setup [Hei18]. Notably, the stability of the power supply and the magnetic field is much better than the resolution of the sensors most of the time, so that only a conservative limit can be stated here.

6.2. WGTS Temperature

In this section, the temperature behaviour of the WGTS cryostat is analysed in detail. The section is structured as follows: In section 6.2.1, the basics of the WGTS cooling system are summarised and its specifications are discussed. In section 6.2.2 and 6.2.3,

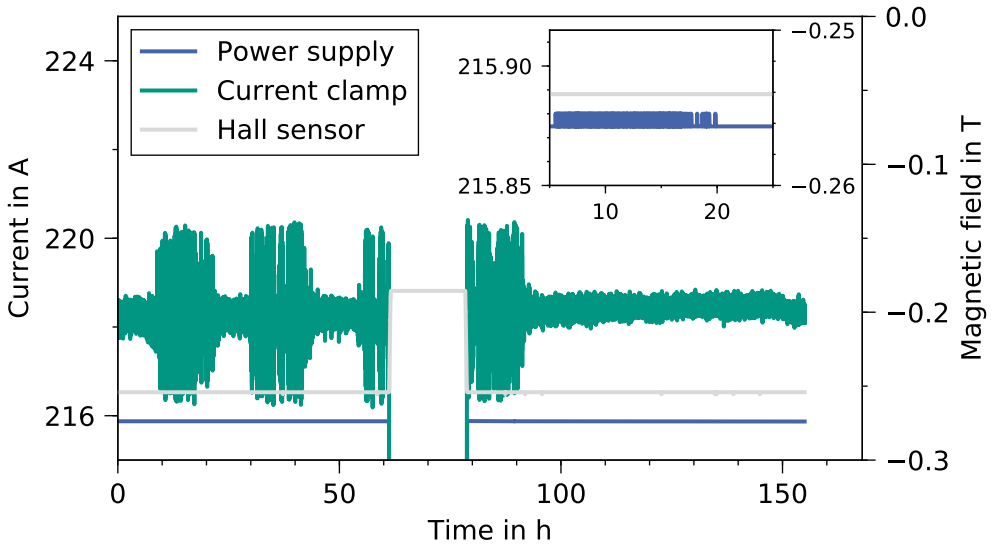

Figure 6.1.: Three different approaches to magnetic field monitoring during gaseous ^{83m}Kr campaign in July 2017. The plot shows the magnetic field monitoring during the gaseous ^{83m}Kr campaign starting on July 4th, 2017, at 00:00 UTC time. The power supply and the current clamp belong to the circuit of the central beam tube (magnets M2 and M3) and measure the current applied to the superconducting coils. The Hall sensor is mounted in magnet M2 and measures the magnetic field strength, but since its orientation is not known, the absolute value does not give any information. In the time between 60 and 80 hours, the magnetic field was ramped down to 50 % of its nominal value to test detector-related effects with reduced source magnetic field. The inset shows the trend of the power supply and the Hall sensor for the time between 5 and 25 hours in more detail, when the current clamp signal fluctuates the first time strongly by about ±1 %.

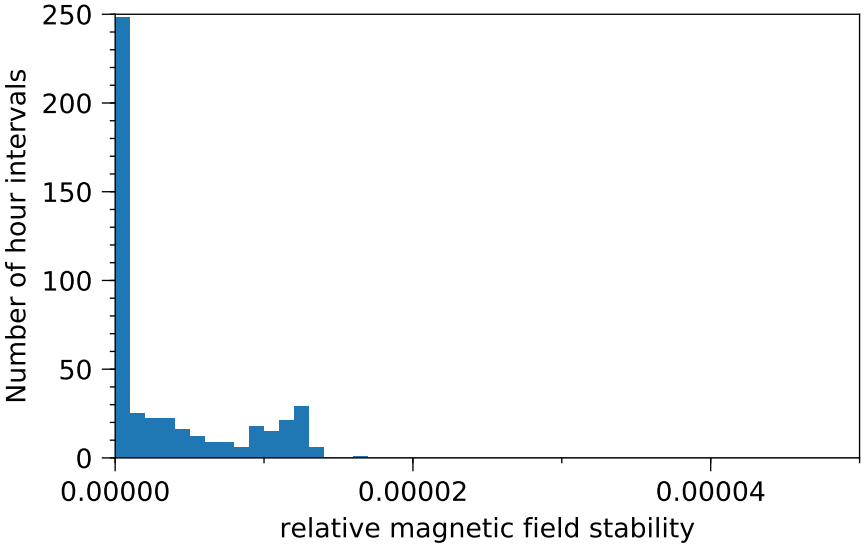

Figure 6.2.: Relative magnetic field stability of WGTS magnets at 70 % of nominal field strength. The histogram shows the stability per hour of the three power supplies of the seven superconducting magnets of the WGTS during the gaseous ^{83m}Kr campaign in July 2017. The bin size is 1×10^{-6}. The mean of the distribution demonstrates a relative stability of 3.3×10^{-6} with a standard deviation of 4.5×10^{-6}. The worst stability measured in a one-hour interval is 1.65×10^{-5}.

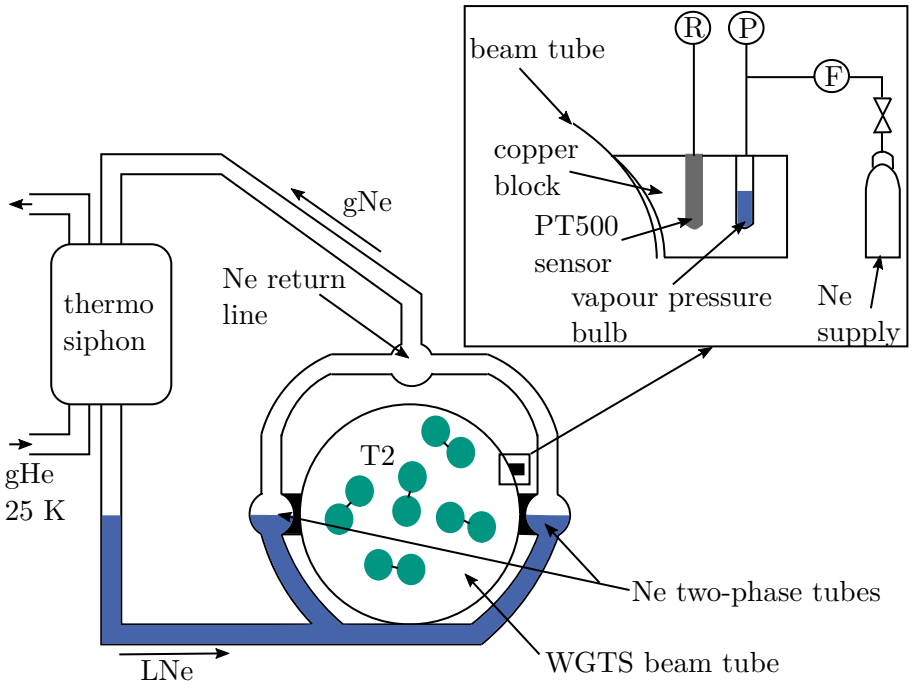

Figure 6.3.: The WGTS cooling principle. The liquid neon (or argon in the 100 K mode) evaporates due to heat introduction from the beam tube and is guided towards the thermosiphon. There, it is reliquefied in a heat exchange with the gaseous helium circuit (inner shield). The two-phase cooling system is extremely stable as additional heat does not change the temperature directly, since it is stored as latent heat in the system which is then removed at the thermosiphon. Since the absolute temperature value and its stability are important input parameters to the KATRIN analysis model, see also the main text, both have to be monitored carefully. At the central beam tube, 24 copper blocks are brazed to the beam tube, each of them containing one PT500 sensor and one vapour pressure bulb for calibration. For calibration at 30 K, again two-phase neon is used, while at 100 K no calibration is possible (see section 6.2.3). During the calibration process, neon is condensed into the bulbs. The amount is controlled via a flow meter (F) to guarantee that the bulbs are filled approximately by half. After the equilibrium has formed, a pressure gauge (P) measures the vapour pressure, from which the actual temperature can be deduced. Based on this temperature, the characteristic curve of the PT500 is corrected, since the resistance is well-known due to a four-contact measurement (R).

respectively, the fulfilment of these specifications at 30 K operation and 100 K operation is investigated. Finally, the analysis of a measurement of the gaseous ^{83m}Kr campaign is presented in section 6.2.4, in which the time difference between a temperature signal in the WGTS temperature sensors and a correlated response in the ^{83m}Kr rate was determined.

6.2.1. Introduction

The basic principle of the WGTS cooling system is explained in section 3.2.1 and visualised in figure 6.3. For the discussions in this section, the following aspects shall be emphasised again:

- The cooling works without mechanical pumping just by heat transfer from the two-phase neon circuit to the gaseous helium of the inner shield circuit of the cryostat. In the thermosiphon, the gaseous neon is reliquefied and flows back to the two-phase tube brazed to the beam tube sections of the WGTS.
- In total there are three cooling circuits like the one depicted in figure 6.3: One for the 10 m long central beam tube, one for the DPS1-R-1 and one for the DPS1-F-1.

There are two further cooling circuits for the DPS1-R/F-2, but they are operated with gaseous neon only (no two-phase cooling) and the neon circuit is coupled to the liquid nitrogen cooling circuit of the outer shield of the cryostat. The pump ports, finally, are directly cooled by the gaseous helium circuit without any condenser or two-phase cooling system.

- For the 100 K operation in the WGTS ^{83m}Kr mode, the neon is exchanged by argon and the temperature of the gaseous helium circuit is raised from $\approx 25\,\mathrm{K}$ to $\approx 95\,\mathrm{K}$.
- The temperature is monitored by several temperature sensors: 24 PT500 sensors are mounted along the central beam tube. In each of the pump ports PP1-R/F, there are also two PT500. In each of the pump ports PP2-R/F, two PT1000 sensors are placed. There are six PT1000 in each of the DPS1-R/F-1 and four in each of the DPS1-R/F-2. Thus, in total 52 temperature sensors are mounted along the WGTS beam tube sections and there are many more in the cooling circuits of the cryostat.

As discussed in detail in chapter 4, both the absolute temperature value and the temperature stability are important parameters for several systematic uncertainties of the KATRIN analysis model. Examples are, amongst others, the molecular final-state distribution (see section 4.2.17), the stability of the column density (see section 4.2.15) and the Doppler effect (see section 4.2.4). The most important temperature sensors are the 24 PT500 sensors along the central beam tube and the four sensors in the pump ports PP1-R/F, since most of the tritium decays will occur there in standard KATRIN operation. Therefore, these sensors are accompanied by a vapour pressure measuring system for calibration (see figure 6.3), since the stand-alone sensor uncertainty is too large for KATRIN requirements [Gro11]. Especially the individual uncertainty for the operation in magnetic fields and the sensor dispersion (different lengths of platinum wires) lead to large uncertainties which cannot be corrected globally but only through in situ calibrations of each PT500 sensor. The positions of the sensors along the beam tube are shown in figure 6.10.

The specifications and requirements of the temperature stability for the central beamtube (CB) for both modes (30 K and 100 K) are [Ang05][1]

$$\left|\frac{\Delta T}{T}\right|_{\mathrm{CB}} < 0.1\,\frac{\%}{\mathrm{h}}\ . \tag{6.2}$$

For the DPS1-R/F, this requirement is loosened for both modes due to the reduced gas density in these WGTS sections to

$$\left|\frac{\Delta T}{T}\right|_{\mathrm{DPS1-R/F}} < 1.0\,\frac{\%}{\mathrm{h}}\ . \tag{6.3}$$

The reduced gas density in the DPS sections is also the reason why the homogeneity requirement is only formulated for the central beam tube and specified to

$$\left|\frac{\Delta T}{T}\right|_{\mathrm{hom}} < 0.1\,\%\ . \tag{6.4}$$

Homogeneity means that the temperature along the inner 95 % of the beam tube should not differ by more than a given value (here: one per mille). To be able to verify this homogeneity, the trueness of the temperature measurement should not exceed[2]

$$|\Delta T|_{\mathrm{true}} < 10\,\mathrm{mK}\ . \tag{6.5}$$

[1] See also B. Bornschein and R. Gehring (2004), *Specification of the Superconducting Magnet System WGTS for the KATRIN Experiment*, KATRIN-internal document 10-DSP-2030-2.

[2] see for details R. Ramalingam and M. Süßer (2008), *Study of Platinum sensors (PT-500) for the temperature measurement of the KATRIN WGTS-Beam Tube*, FZKA Internal Report FE.5130.0013.0012/M.

In the scope of the thesis at hand, comprehensive studies of the WGTS temperature performance have been done. Data taken in both temperature operating modes have been analysed, and the results are presented in the following sections.

6.2.2. Stability and Homogeneity at 30 K

The first opportunity to measure the temperature stability and homogeneity at 30 K was in autumn 2016 after the WGTS cryostat was fully integrated and connected to the cooling infrastructure and ready for commissioning. The data of this first WGTS operation at cryogenic temperatures were analysed in [Mar17a]. However, the commissioning showed also some problems of the existing system: the 52 temperature sensors of the beam tube and further temperature sensors from the WGTS cooling circuits were all read out via the custom-made software TES ("Temperaturerfassungssystem"). To handle so many sensors at once, the sensor read-out channels are connected to multiplexers, which are again connected to digital multimeters which finally read out the voltages. The multiplexers turned out to be a weak link in the chain: after several duty cycles they broke and had to be exchanged, leading to a crash of the TES. Furthermore, the read-out of all the sensors took more than 20 s so that only about every 25 s a new value was available in ADEI (other KATRIN sensors: every ≈ 3 s; for ADEI see section 3.3). Therefore, it was decided to restructure the whole temperature monitoring and controlling equipment: only the 24 central beam tube sensors and the in total 4 sensors of the pump ports PP1-R/F were kept in the TES because they can be calibrated and the TES is here the best option for controlling the required valves. However, the multiplexers were removed and replaced by Gantner modules, which have a longer life-time and better reliability. All the other WGTS temperature sensors are also read out by Gantner modules[3] now, but they feed their values directly to the PCS-7/ADEI and no longer to the TES. The current supply remains a Keithley Model 6220 DC Current Source[4], set to 250 µA instead of 500 µA for the old system. With these changes, the read out time of the central beam tube sensors was shortened by a factor of 5 to ≈ 5 s.

The new setup was completed and fully implemented in the TES software in January 2018. In this thesis, the performances of both systems are compared referring to the WGTS specifications listed in the previous section. For this purpose, one week of measurement time performed with each system has been selected. The PT500 sensors have been calibrated and the WGTS was in a stable configuration at 30 K with zero magnetic field for each of the two weeks. The selected time periods are visualised by one sensor of the central beam tube in figure 6.4 for the old, multiplexer-based system and in figure 6.5 for the Gantner-module based system. In the following, the obtained results are discussed:

Temperature trueness: First studies indicated a temperature trueness of the calibrated PT500 sensors of about 4 mK at 30 K [Gro11] for the multiplexer-based system. However, in [Mar17a] more uncertainty parameters have been taken into account, leading to a trueness of 8.3 mK. A critical review of these results yields a strongly increased trueness of

$$|\Delta T|_{\text{true,old}} = 50.7\,\text{mK}\ . \tag{6.6}$$

The increase can be explained by a different uncertainty estimation of the PT500 instrumentation. All contributions to the value stated in equation 6.6 are listed in table A.1 and discussed in appendix A.1.1. Although the trueness requirement

[3] The central beam tube sensors are connected to Gantner Q.bloxx A107, the DPS1-R/F-1 to Gantner Q.bloxx A105. See `www.gantner-instruments.com` (accessed on Jul 13, 2018) for more information.

[4] see `https://de.tek.com/keithley-low-level-sensitive-and-specialty-instruments/keithley-ultra-sensitive-current-sources-seri` for the datasheet (accessed on August 17, 2018).

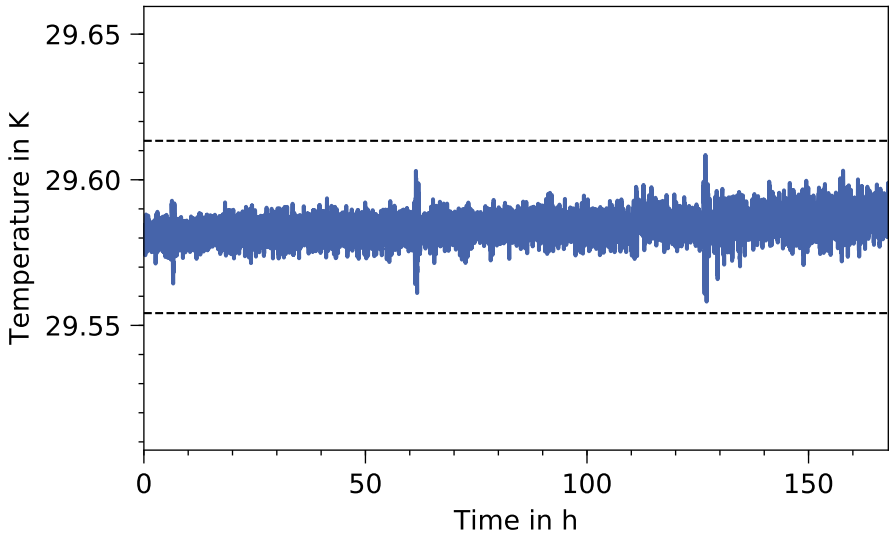

Figure 6.4.: Temperature stability of WGTS central beam tube at 30 K in one week of measurement time in autumn 2016. The plot presents the temperature trend of the sensor RTP-3-5101 for the time range of October 29, 00:00 UTC time, to November 04, 23:59 UTC time. The dashed lines show the ±0.1 % limits. The sensor is placed at the front end of the central beam tube and has a stability (standard deviation) of (4.3 ± 0.4) mK over the entire time range, which equals a relative stability of (0.015 ± 0.001) %. The uncertainty is calculated in appendix A.1.2. For the other temperature sensors of the central beam tube not plotted here, relative stabilities over the entire week of up to (0.092 ± 0.001) % are recorded, which are still within the limits.

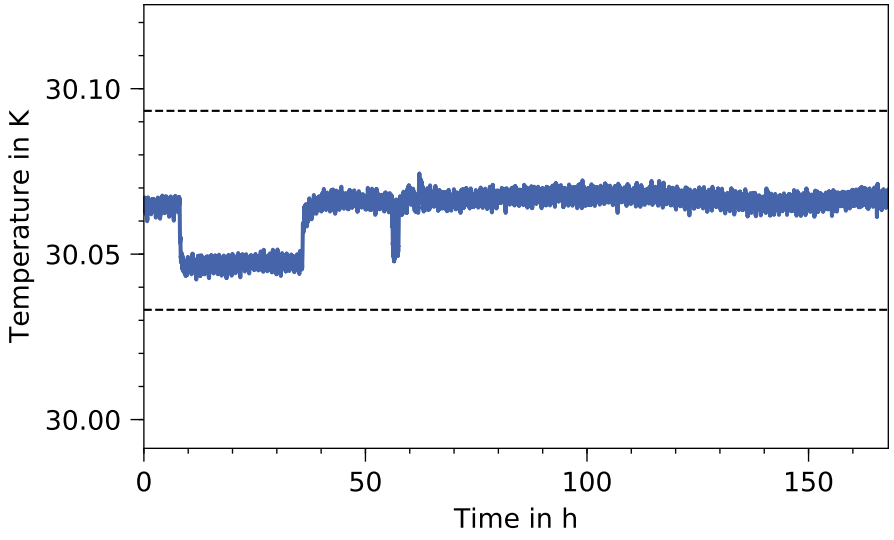

Figure 6.5.: Temperature stability of WGTS central beam tube at 30 K in one week of measurement time in spring 2018. The plot shows the temperature trend of the sensor RTP-3-5101 for the time range from March 27th, 00:00 UTC time, to April 2nd, 23:59 UTC time, 2018. The dashed lines mark the ±0.1 % requirement. Like in figure 6.4, sensor RTP-3-5101 at the front end of WGTS is presented here. Read-out failures are removed. The visible temperature dip on the first day can only be found in sensors on the front side of WGTS and in sensors of the DPS1-F sections. It is caused by a read-out failure/crash of the software. Nevertheless, the relative stability of the sensor is still 2.5×10^{-4} for the entire week, and also the other 21 working sensors of the central beam tube show an excellent temperature stability $< 3.5 \times 10^{-4}$.

stated in equation 6.5 is not fulfilled, this does not influence the WGTS performance negatively. The trueness requirement was formulated for a maximum inhomogeneity of 30 mK along the central beam tube. Since the inhomogeneity, as shown further below, is much larger, also the trueness requirement can be relaxed. Furthermore, the achieved trueness is still better than required by the final-state distribution (see section 4.2.17).

The Gantner modules change the instrumentation uncertainty on the voltage measurement of the PT500 sensors. The calculation can be found in appendix A.1.1, and all contributions to the following value are listed in table A.1. The total temperature trueness of

$$|\Delta T|_{\text{true,new}} = 160.0\,\text{mK} \tag{6.7}$$

is a factor of 16 worse than the requirement in equation 6.5. This is caused by the increased uncertainty of the PT500 instrumentation (see table A.1). The requirement was formulated to measure a temperature inhomogeneity of 30 mK. However, since the actual temperature inhomogeneity (see below) is much worse, also the requirement on the trueness can be loosened. Of more importance is that this trueness is not sufficient to keep the systematic uncertainty of the final-state distribution, see section 4.2.17. If the current supply of the PT500 is set again to 500 µA as for the old multiplexer-based system, a total trueness of 83 mK is possible as long as the other contributions listed in table A.1 stay the same. Then, the requirements for the final-state distribution can be kept.

Temperature stability central beam tube: In [Mar17a], one hour of WGTS operation was selected to determine the stability of all 24 central beam tube sensors. Here, the approach is more general: from the autumn 2016 data, the week from October 29th to November 4th was selected for an in-depth analysis. During that time range, the WGTS was in a stable configuration with calibrated central beam tube sensors and magnets switched off. As demonstrated in figure 6.4, the stability requirement of ±0.1 % is not only kept for one hour, but also for the whole week. Since the typical run length of one spectrum scan is estimated to be on the order of one hour [Ang05], the stability on this time scale is investigated in figure 6.6. This analysis shows, that for 90 % of the one-hour intervals the stability with the multiplexer-based system is better than

$$\left|\frac{\Delta T}{T}\right|_{\text{CB,old}} < (0.016 \pm 0.001)\,\frac{\%}{\text{h}}\,, \tag{6.8}$$

which is at least a factor of six better than specified (see equation 6.2). The uncertainty is based on the considerations in the appendix A.1.2; the relative value is calculated for a temperature of 30 K.

The stability value in equation 6.8 does not only contain temperature fluctuations, but also a contribution from fluctuations which occur in the electronic devices or in the cabling. To estimate this contribution, a precision resistor of 10 Ω was mounted as a replacement of one of the non-working PT500 sensors. Its resistance is treated by the temperature monitoring system like the signal of the PT500 sensors, thus showing a temperature of ≈ 30 K. Its stability is analysed for one week in November 2016, showing a relative standard deviation of 1.3×10^{-5} per hour in average. This indicates only a small influence of the electronics on the total stability value in equation 6.8. However, the real PT500 sensors are mounted inside the WGTS with several meters more cabling than the precision resistor, which is mounted in a distribution pillar

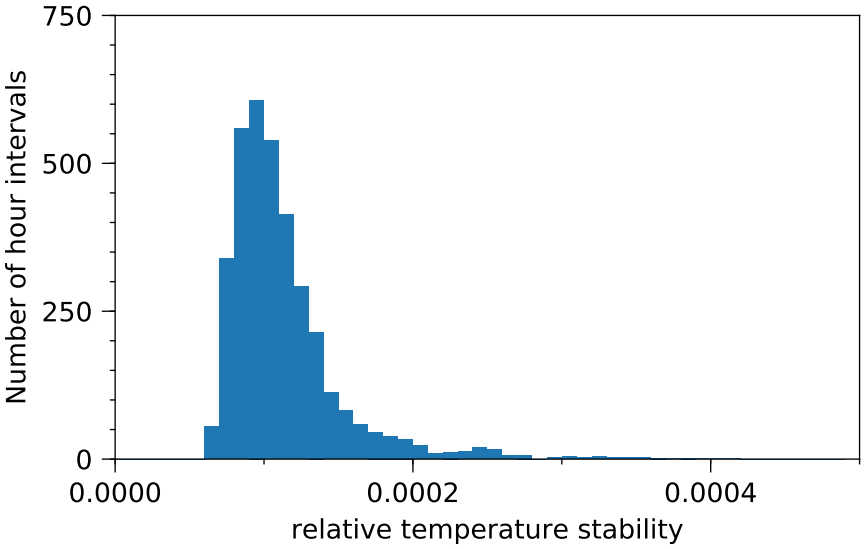

Figure 6.6.: Relative temperature stability of WGTS central beam tube at 30 K analysed in one-hour intervals (autumn 2016). For the histogram, all time series of the 21 working temperature sensors (not working: RTP-3-5106, -09, -14) like the one presented in figure 6.4 are split into 168 one-hour intervals. For each of the one-hour intervals, the relative temperature stability, which is defined as the ratio of the standard deviation and the mean, is calculated and filled into the histogram. The bin size is 1×10^{-5}. The mean of the distribution is 1.1×10^{-4}, the standard deviation is 0.4×10^{-4} and the worst stability entry is at 4.1×10^{-4}.

outside of the cryostat. Nevertheless, the stability value of the precision resistor determines the ultimate limit of the stability value of the PT500 sensors.

The same stability analysis is done for the Gantner module-based system: the selected time range displayed in figure 6.5 was divided into intervals of one hour and the stability of every hour and for every working sensor was calculated. The result is shown in figure 6.7. For 90 % of the intervals, the central beam tube sensors show a stability of

$$\left|\frac{\Delta T}{T}\right|_{\mathrm{CB,new}} < (0.005 \pm 0.001)\,\frac{\%}{\mathrm{h}}\,, \tag{6.9}$$

which is more than an order of magnitude better than the requirement (see equation 6.2). The uncertainty is calculated in appendix A.1.2. The stability is also better than the one derived for autumn 2016 (see equation 6.8). This might be directly related to the Gantner modules, since they have an internal possibility to apply a high- or low-pass filter to the data. Based on COMSOL simulations, it was decided to apply a low-pass filter of 2 Hz, since faster fluctuations are not able to propagate to the inner volume of the central beam tube[5]. Besides this filter, also the temperature regulation with the heaters inside the two-phase cooling tubes has improved based on the first experience in autumn 2016, which might also explain the improved stability.

Again, a precision resistor of 10 Ω was mounted to estimate the influence of the electronics on the stability value. It shows a relative standard deviation of 6.6×10^{-5} per hour in average over the one week of analysed measurement time. Compared to the result in equation 6.9, it is an indication that the measured stability is already at

[5]Personal communication A. Jansen, Jul 17, 2018.

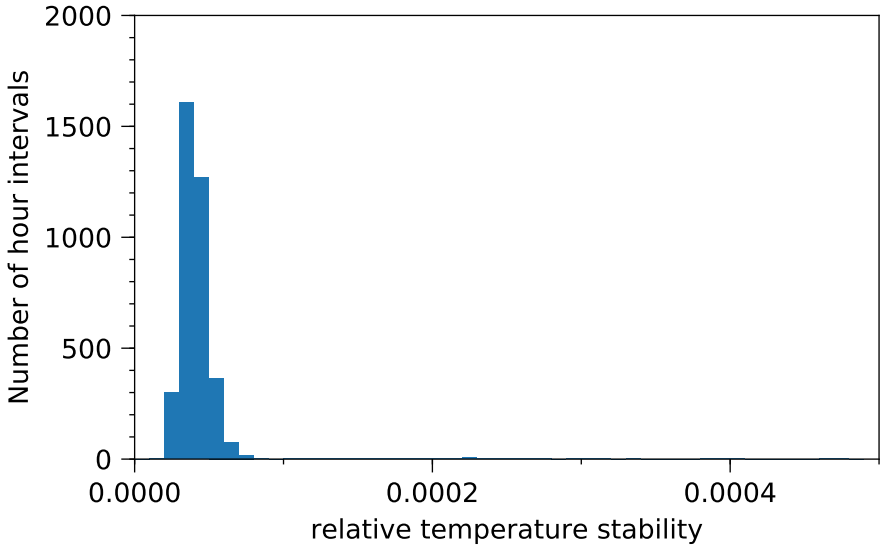

Figure 6.7.: Relative emperature stability of WGTS central beam tube at 30 K analysed in one-hour intervals (spring 2018). For the histogram, all time series of the 22 working temperature sensors (not working: RTP-3-5103 and -09) like the one presented in figure 6.5 are split into 168 one-hour intervals. For each of the one-hour intervals, the relative temperature stability, which is defined as the ratio of the standard deviation and the mean, is calculated and filled into the histogram. The bin size is 1×10^{-5}. The mean of the distribution is 4.4×10^{-5}, the standard deviation is 2.9×10^{-5} and the worst stability entry is at 4.7×10^{-4}.

its optimum value, which is defined by the stability of the electronics. Compared to the old setup (see above), the fluctuations of the electronic devices and the cabling have increased. This trend is also visible in the 100 K case, see section 6.2.3 and the appendix A.2.2.

Temperature stability DPS1: The analysis of the stability of the DPS1-R/F for the multiplexer-based system is presented in figure 6.8. The results show that 90 % of one-hour intervals have a stability of

$$\left|\frac{\Delta T}{T}\right|_{\mathrm{DPS1-R/F,old}} < 0.110 \pm 0.001 \, \frac{\%}{\mathrm{h}} \, , \tag{6.10}$$

which is a factor of nine better than specified. During the analysed data range of one week, the DPS1-R/F-1 sensors were calibrated (see caption of figure 6.8), and after the calibration also the heaters in the two-phase cooling tubes were switched on. Both could have a slight influence on the stability results. The uncertainty calculation is given in appendix A.3.

For the DPS1-R/F sensors of the Gantner module-based system, the same analysis has been performed. All sensors were working in the spring 2018 measurement. The histogram with the measured one-hour stability values is shown in figure 6.9. The stability is for 90 % of the intervals better than

$$\left|\frac{\Delta T}{T}\right|_{\mathrm{DPS1-R/F,new}} < (0.008 \pm 0.001) \, \frac{\%}{\mathrm{h}} \, , \tag{6.11}$$

which is more than two orders of magnitude better than required (see equation 6.3). For the uncertainty calculation the reader is referred to appendix A.3. The result is more than one order of magnitude better than the one from autumn 2016 (see

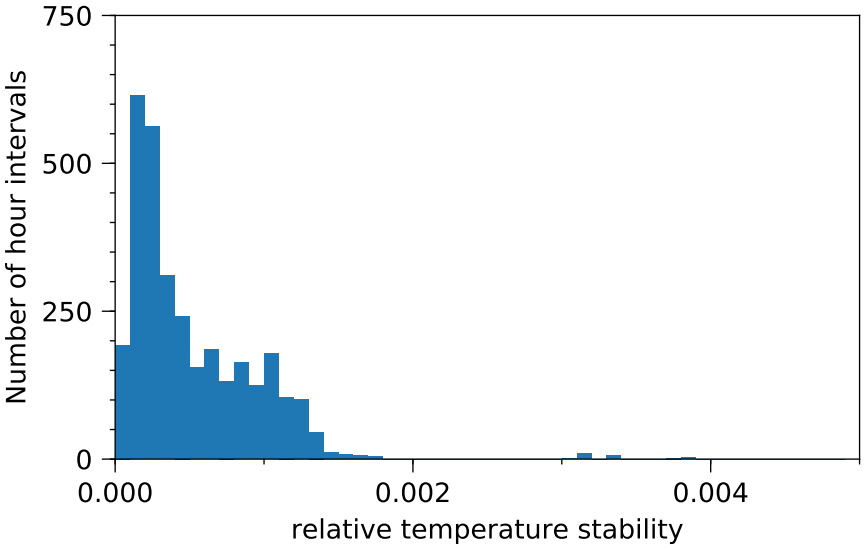

Figure 6.8.: Relative temperature stability of WGTS DPS1-R/F at 30 K analysed in one-hour intervals (autumn 2016). For the histogram, all time series of the working temperature sensors of the DPS1-R/F-1/2 (not working: RTP-3-7101) are split into one-hour intervals. In hour 129, the DPS1-R/F-1 sensors have been calibrated, so that this hour is excluded from the analysis. For each of the one-hour intervals, the relative temperature stability, which is defined as the ratio of the standard deviation and the mean, is calculated and filled into the histogram. The bin size is 1×10^{-4}. The mean of the distribution is 5×10^{-4}, the standard deviation is 6×10^{-4} and the worst stability entry is at 9.0×10^{-3}.

equation 6.10), although there are some outliers. The reason for this improvement is probably again not linked to the Gantner modules, but to a better WGTS temperature control due to improved understanding of the cooling circuits.

Temperature homogeneity: The temperature homogeneity is specified to be better than one per mille along the inner 95 % of the beam tube, see equation 6.4. In this region (± 4.75 m with respect to the middle of the beam tube), the 24 PT500 sensors of the central beam tube are mounted (see figure 6.10). After calibration, they can be used to measure the homogeneity. As figure 6.10 shows, the results show a clear inhomogeneity of (534.7 ± 71.9) mK towards the rear end of the central beam tube for the multiplexer-based system. For the uncertainty calculation, the trueness stated in equation 6.6 is propagated on the difference between the maximum and minimum value. This is a relative inhomogeneity of

$$\left|\frac{\Delta T}{T}\right|_{\text{hom,old}} = (1.80 \pm 0.24)\,\% \ . \tag{6.12}$$

It is a factor of ≈ 20 larger than specified. An even larger inhomogeneity of up to 0.8 K had been measured with the demonstrator experiment of the WGTS which was set up to prove the principle of the two-phase cooling system with original components of the WGTS [Gro13]. However, in the demonstrator the inhomogeneity occurred towards the front end of the WGTS. The capillaries which are needed to fill the vapour pressure bulbs with liquid neon for calibration of the PT500 sensors (see figure 6.3) were identified as the source of the increased heat load. Since electrons from the front end can reach the detector easily with only little scattering and are thus of particular relevance for the neutrino mass measurements, it was decided to turn around the central beam tube with the construction of the capillaries such as to

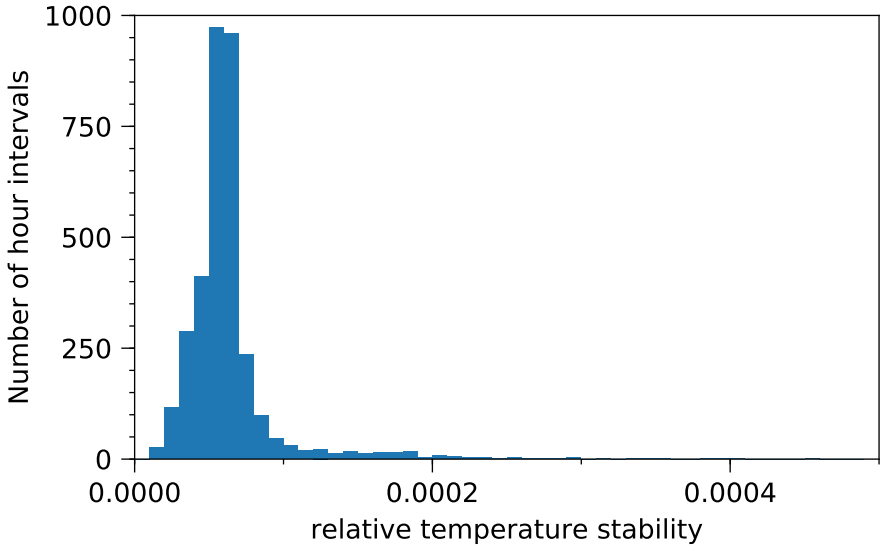

Figure 6.9.: Relative temperature stability of WGTS DPS1-R/F at 30 K analysed in one-hour intervals (spring 2018). For the histogram, all time series of the working temperature sensors of the DPS1-R/F-1/2 are split into one-hour intervals. For each of the one-hour intervals, the relative temperature stability, which is defined as the ratio of the standard deviation and the mean, is calculated and filled into the histogram. The bin size is 1×10^{-5}. The mean of the distribution is 6.4×10^{-5}, the standard deviation is 3.4×10^{-5} and the worst stability entry is at 6.0×10^{-4}.

have the increased temperature at the rear end. Electrons being created there have a much smaller probability to reach the detector unscattered as they have to pass the whole gas column density where they scatter and lose energy. Furthermore, the capillaries were coupled to the outer shield to reduce the heat transfer from outside. As the results show, this modification of the hardware was successful in reducing the inhomogeneity by $\approx 50\,\%$. As long as the inhomogeneity is stable over time, it can be included into the gas dynamic model without any influence on the neutrino mass fit result [Kuc16; Hei18]. Indeed, this stability has been demonstrated above.

For the temperature homogeneity of the Gantner module-based system, the mean values of all 22 working PT500 sensors along the central beam tube of the WGTS are calculated. In figure 6.11, a clear inhomogeneity towards the rear end of the WGTS is visible. An absolute inhomogeneity of $(597.4 \pm 226.3)\,\mathrm{mK}$ is measured, which represents a relative inhomogeneity of

$$\left|\frac{\Delta T}{T}\right|_{\mathrm{hom,new}} = (1.98 \pm 0.75)\,\% \ . \tag{6.13}$$

The uncertainty is calculated based on appendix A.1.1. The homogeneity requirement stated in equation 6.4 is missed by a factor of 20, but as discussed above, this does not harm the neutrino mass measurement. As long as the inhomogeneity is stable, and this was demonstrated above, it can be incorporated in the analysis model.

Besides the homogeneity and the trueness, all requirements and specifications for the WGTS cooling system at 30 K were successfully demonstrated in the WGTS stand-alone operation in autumn 2016. The results of the analysis of the WGTS temperature data of spring 2018 demonstrate that the exchange of the error-prone multiplexer-based voltage read-out by Gantner modules does not have a negative impact on the temperature performance of the WGTS cryostat. However, the increase of the absolute measurement uncertainties

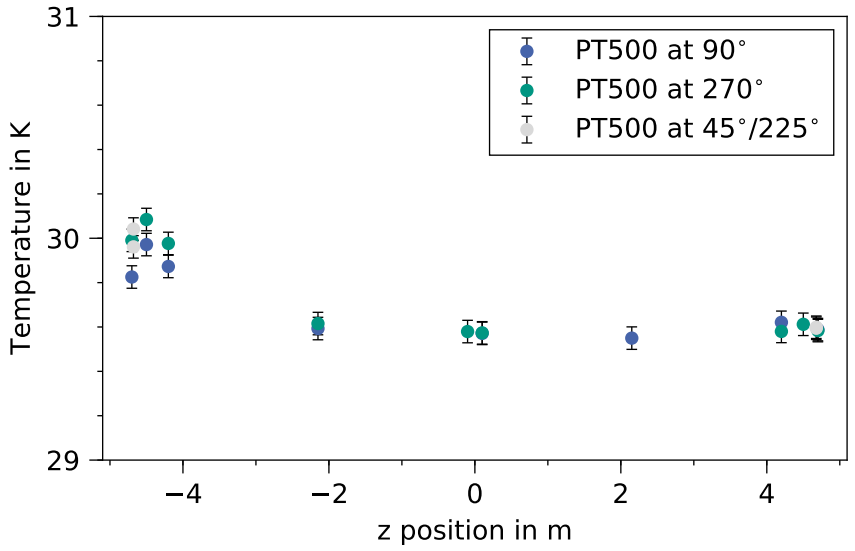

Figure 6.10.: Absolute temperature homogeneity of WGTS central beam tube at 30 K in one week of measurement time (autumn 2016). The plot shows the mean temperature during the one week of analysed measurement time of the 21 working PT500 sensors at their position along the central WGTS beam tube ($z = 0$ middle of beamtube, positive z towards DPS, negative z towards rear section). The sensors marked in blue are mounted on top of the beam tube (90°), the sensors marked in green are mounted on the bottom of the beam tube (270°) and the sensors marked in grey are mounted on positions in between (45°/225°). The error bars are based on table A.1. A clear inhomogeneity towards the rear end of the central beam tube is visible.

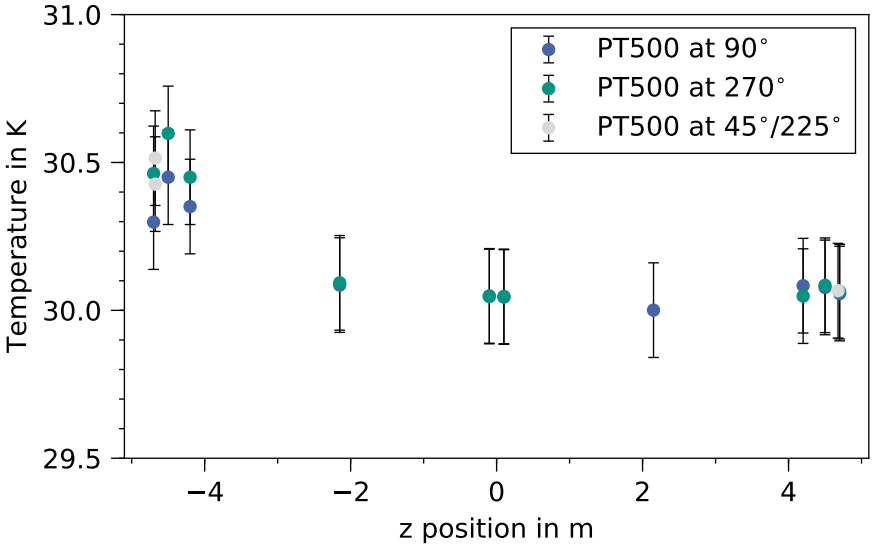

Figure 6.11.: Absolute temperature homogeneity of WGTS central beam tube at 30 K in one week of measurement time (spring 2018). The plot shows the mean temperature during the one week of analysed measurement time of the 22 working PT500 sensors at their position along the central WGTS beam tube ($z = 0$ middle of beamtube, positive z towards DPS, negative z towards rear section). The sensors marked in blue are mounted on top of the beam tube (90°), the sensors marked in green are mounted on the bottom of the beam tube (270°) and the sensors marked in grey are mounted on positions in between (45°/225°). The error bars are based on table A.1. A clear deviation of the temperature towards the rear end of the central beam tube is visible.

was underestimated beforehand and needs a correction to fulfil the WGTS temperature trueness requirements of the final-state distribution. This can be achieved by increasing the current through the PT500 sensors. Besides the trueness requirement also the homogeneity specifications of the WGTS cannot be kept with the new system, but this does not impact the physics analysis since it can be incorporated in the analysis as long as the inhomogeneity is stable over time. Indeed, this stability was demonstrated. Thanks to the Gantner modules, the stability per hour can now be calculated on a factor of ≈ 5 more data points due to the faster acquisition, which leads therefore to much more reliable results. The important stability requirements are exceeded by at least one order of magnitude which demonstrates the great performance of the WGTS cryo-system. The fact that these results were achieved in two independent weeks of measurements which are about one and a half years apart, shows the reproducibility of the performance. Important settings and handling conditions are well understood and even after increasing the WGTS temperature to 100 K for the ^{83m}Kr mode (see the following section), smooth and stable operating conditions at 30 K were re-established afterwards.

6.2.3. Stability and Homogeneity at 100 K

In order to operate the WGTS at 100 K, the neon in the two-phase cooling system has to be exchanged with argon. The two-phase cooling system of the WGTS is specified for vapour pressures between 1 and 11 bar, which corresponds to temperatures of 87-118 K for argon [Van64]. Since krypton condensates at pressures below the millibar regime (as applicable in the WGTS case) at 74 K [Lem70], argon is the ideal coolant for the WGTS gaseous ^{83m}Kr mode. The exchange of the neon by argon and the ramping of all WGTS cooling circuits to ^{83m}Kr mode temperatures is rather complex and takes about two days. The other way around, cooling down the WGTS from 100 K back to 30 K operation, takes three days[6]. The gaseous ^{83m}Kr measurement campaign in July 2017 (see chapter 5) was the first possibility to test these procedures, but also to investigate if the WGTS keeps its specifications with argon as two-phase coolant.

The specifications for the trueness of the temperature measurement (see equation 6.5), for the stability of the temperature of the central beam tube (see equation 6.2) and the DPS1 (see equation 6.3) and for the temperature homogeneity along the central beam tube (see equation 6.4) are listed above. In the following, it is investigated whether these specifications are kept for the 100 K operation of the WGTS for both the multiplexer-based and the Gantner module-based instrumentation of the PT500 sensors. Figure 6.12 gives an overview on the one week of analysed data from July 2017, in which the multiplexer-based system was still in use. The temperature behaviour of the Gantner module-based system at 100 K was tested for a time range of five days in January 2018 and as an example the temperature trend of this measurement of one of the central beam tube PT500 sensors is plotted in figure 6.13.

Temperature trueness: As mentioned in the previous section, a calibration of the PT500 sensors at 100 K is not possible since the capillaries for the vapour pressure measurement of the temperature (see figure 6.3) have been coupled thermally to the outer shield (liquid nitrogen) of the WGTS. This has been done in order to reduce the inhomogeneity along the central beam tube and a reduction by $\approx 50\,\%$ was achieved. Since argon freezes at liquid nitrogen temperatures at operational pressures > 1 bar [Lem70], a calibration of the PT500 sensors along the central beam tube is not possible in the 100 K mode. Thus, the uncalibrated uncertainty contributions have to be calculated. Some of them have already been discussed in [Gro11]. The full list can be found in table A.2 and is discussed in appendix A.2.1. For the non-calibrated

[6] Personal communication A. Jansen, Aug 30, 2018.

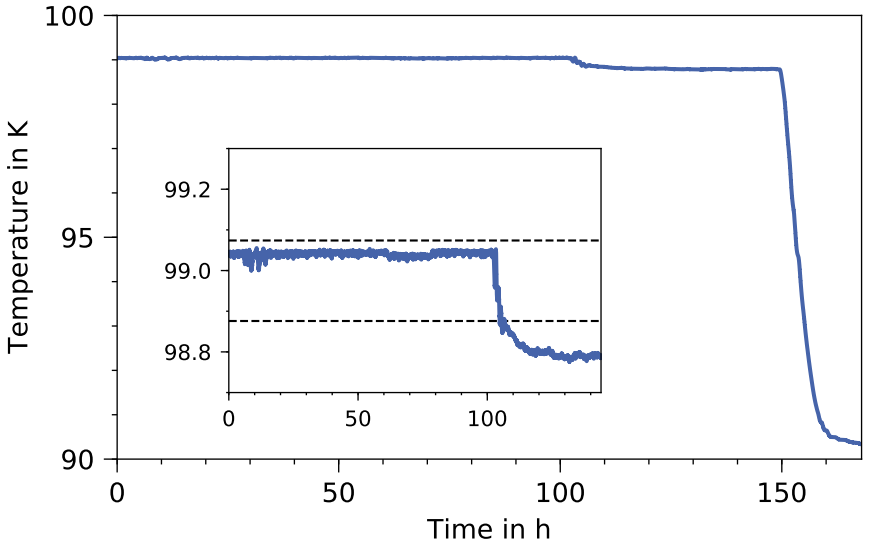

Figure 6.12.: WGTS temperature behaviour during ^{83m}Kr campaign. The graph shows the temperature trend of the central beam tube PT500 sensor RTP-3-5101, starting on July 4, 2017, 00:00 UTC time. The large and planned temperature drop of about 10 K at hour 150 was performed to measure the dependence of the ^{83m}Kr conversion electron rate on the temperature. This measurement is analysed in detail in section 6.2.4. The inset shows a close-up of the first six days of the measurement campaign. The smaller drop of 0.25 K between hour 100 and 110 occurs due to a large and unexpected temperature fluctuation of ±4 K in the gaseous helium circuit (see also figure 6.23). Due to the fluctuation, the two-phase system was forced into a new equilibrium state. As indicated by the two dashed lines, the stability requirement of ±0.1 % is not kept over the full six days, but it is kept if only intervals of one hour are investigated, which is the typical run length for ^{83m}Kr conversion line scans (see figure 6.14).

PT500 sensors in the old, multiplexer-based setup of July 2017 a temperature trueness of

$$|\Delta T|_{\text{true,100 K,old}} = 162.2\,\text{mK} \tag{6.14}$$

is achieved. For the new setup where the voltages are read out with Gantner modules, the instrumentation uncertainty increases and thus the trueness changes to (see table A.2 and appendix A.2.1

$$|\Delta T|_{\text{true,100 K,new}} = 274.5\,\text{mK}\ . \tag{6.15}$$

However, at 100 K the trueness does not play an equally important role as at 30 K. Since no neutrino mass data is taken at 100 K, the requirements on the temperature trueness from the calculation of the molecular final states (see section 4.2.17) is not relevant. The discrete energies of the ^{83m}Kr conversion electrons are not affected by the absolute temperature; only the widths of the conversion lines via Doppler broadening are. The line width is one of the fit parameters and the Gaussian Doppler part can be taken into account by the fitter, see section 5.4.9. Nevertheless, the value stated in equation 6.15 can be improved to the level of the old setup by increasing the current of the PT500 sensors to 500 µA. Then, again a trueness of 163.2 mK is achieved.

Temperature stability central beam tube: For the stability determination, the procedure is the same as for the 30 K measurements: the measurement time is split into one-hour intervals. For every working sensor of the central beam tube the relative stability

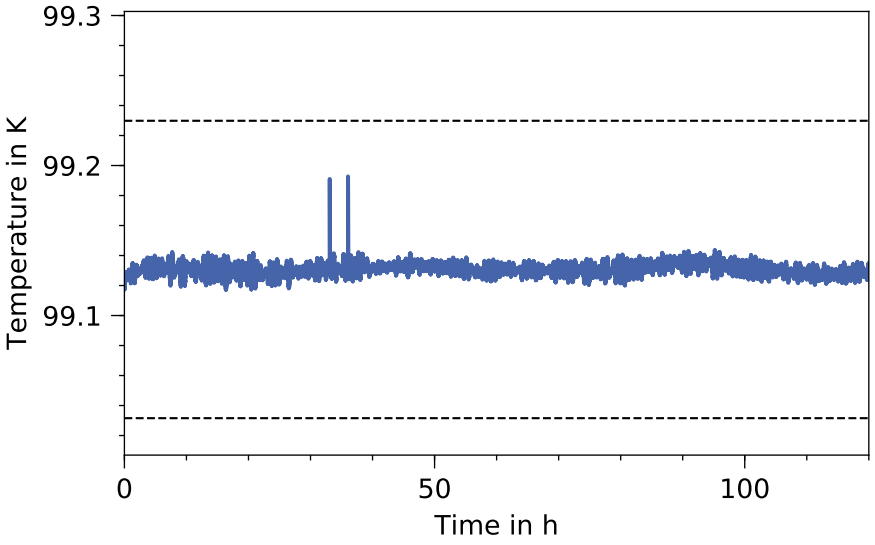

Figure 6.13.: WGTS temperature behaviour at 100 K in January 2018. The plot shows the temperature trend of the central beam tube PT500 sensor RTP-3-5101 for the five selected days in January 2018 used for the analysis presented in this section. During the five days, several read out failures occurred which had to be removed. Also the two spikes around between the hours 30 and 40 are probably linked to these read out failures. The dashed lines mark the ±0.1 % stability requirement. The selected PT500 sensor shows a stability of 4.5×10^{-5} over the five days of measurement. The other 21 working PT500 have similar stability values for that time range.

is calculated as the standard deviation divided by the mean over the interval. All relative stability values are filled into a histogram, which is shown for the multiplexer-based system in figure 6.14. The relative stability of the temperature for 90 % of the intervals is

$$\left|\frac{\Delta T}{T}\right|_{\mathrm{CB,100\,K,old}} < (5.4 \pm 0.4) \times 10^{-5}\,\frac{1}{\mathrm{h}}\,. \tag{6.16}$$

This is a factor of ≈ 18 better than the specification of 0.1 %. The temperature stability adds an uncertainty on the Doppler broadening calculation for the ^{83m}Kr conversion electron lines (see section 5.3). Due to the excellent stability, this influence of the temperature stability of the central beam tube on the measured line widths can be neglected (see section 5.4.9). However, in the gaseous ^{83m}Kr campaign in July 2017, only parts of the krypton decayed in the central beam tube (see figure 6.24). The temperature stability of the DPS1 and its influence on the line widths is therefore discussed further below.

In order to estimate the influence of the electronic devices and the cabling on the value presented in equation 6.16, a precision resistor of 150 Ω was mounted in the distribution pillar instead of one of the non-working PT500 sensors. The value of the resistor represents a temperature value of about 100 K. It is treated like the real temperature values from the PT500 sensors. A relative standard deviation of 3.6×10^{-6} per hour averaged over one week is calculated, indicating that the fluctuations of the electronics are only a small component of the stability value in equation 6.16. Since the fluctuations of the electronics are the ultimate limit of the temperature stability measurements, this means that there are some possibilities to improve the temperature stability determination further by a better adjustment and control of the heater elements mounted in the two-phase cooling tubes of the WGTS.

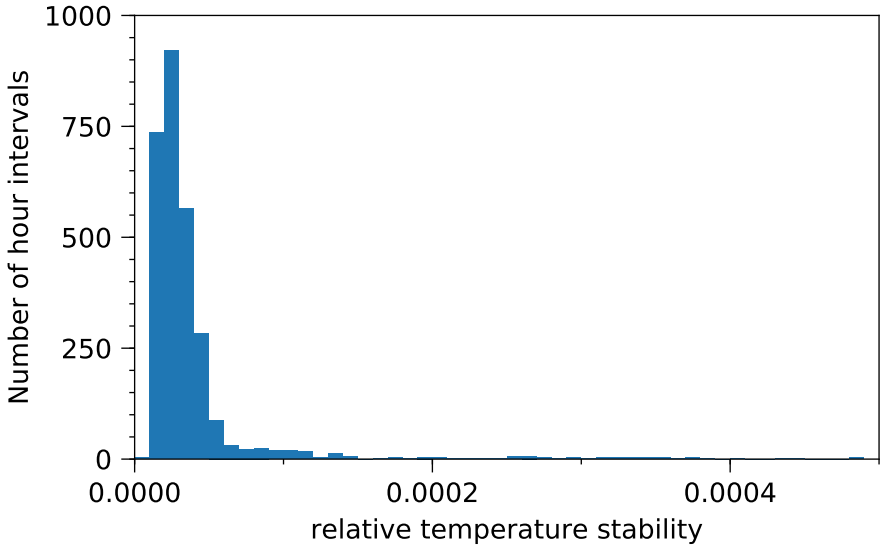

Figure 6.14.: Relative temperature stability of WGTS central beam tube during gaseous ^{83m}Kr campaign of July 2017. For the histogram, one-hour intervals of all working sensors of the central beam tube (not working: RTP-3-5104...07, -09) are taken. The time of the planned cool-down, starting in hour 149, is not included in this analysis, but the small drop of the temperature is part of the data set (see figure 6.12). Read-out failures have been removed. The maximum relative stability measured in one hour is 5.26×10^{-4}. The mean of the distribution is 3.9×10^{-5} with a standard deviation of 4.9×10^{-5}.

The temperature stability during the selected five days of WGTS operation at 100 K in January 2018 with the Gantner module-based system is estimated like above: for every working sensor of the 24 PT500 sensors along the central beam tube the five days are split into 120 one-hour intervals. For every one-hour interval, the relative temperature stability is calculated, which is the standard deviation of the interval divided by its mean. The standard deviations of all one-hour intervals are filled into a histogram, which is shown in figure 6.15. Based on this histogram the conclusion is drawn that the relative temperature stability for 90 % of the one-hour intervals is

$$\left|\frac{\Delta T}{T}\right|_{\mathrm{CB,100\,K,new}} < (4.9 \pm 0.4) \times 10^{-5}\,\frac{1}{\mathrm{h}}\,. \tag{6.17}$$

This result is comparable to the one stated in equation 6.16 for the ^{83m}Kr measurement campaign in July 2017. It is a factor of 20 better than the requirement (see equation 6.2).

A precision resistor of 150 Ω was mounted instead of one of the non-working PT500 sensors to estimate the influence of fluctuations in the electronic devices and the cabling on the stability value. The relative standard deviation of this precision resistor is 1.1×10^{-5} per hour in average for the analysed 5 days of measurement. Like for the 30 K measurement, the stability of the electronics of the Gantner module-based setup is worse than in the former, multiplexer-based setup.

Temperature stability DPS1: With 1 %/h, the stability requirement for the DPS1 is less stringent than the one for the central beam tube. The same analysis as for the

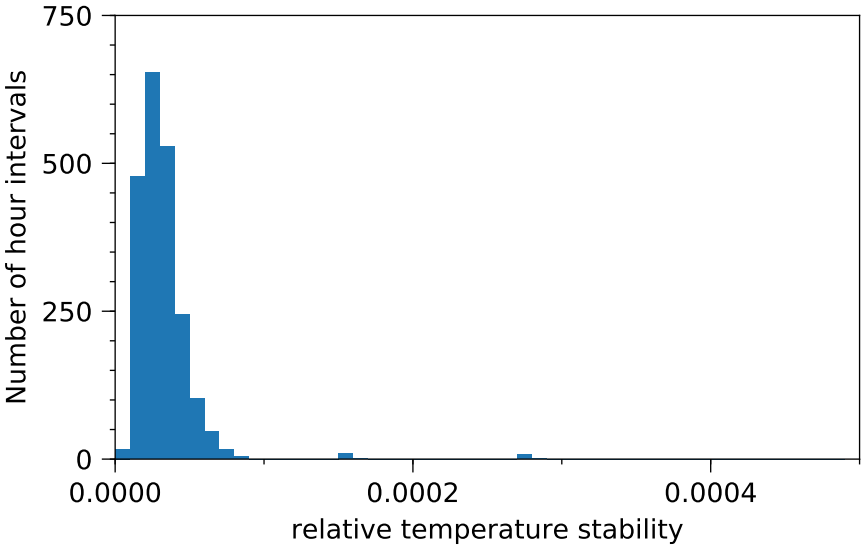

Figure 6.15.: Relative temperature stability of WGTS central beam tube at 100 K (January 2018). For the histogram, one-hour intervals of all working sensors of the central beam tube (not working: RTP-3-5103, -09) are taken for all five days. The relative temperature stability for every hour interval is calculated and filled into the histogram. Read out failures have been removed. The outliers at around 1.5×10^{-4} and at 2.8×10^{-4} occur to small spikes also visible in figure 6.13. The maximum relative stability measured in one hour is 2.83×10^{-4}. The mean of the distribution is 3.2×10^{-5} with a standard deviation of 2.3×10^{-5}. The bin size is 1.0×10^{-5}.

central beam tube sensors is done for the multiplexer-based system and the resulting histogram is shown in figure 6.16. The 90th percentile is

$$\left|\frac{\Delta T}{T}\right|_{\mathrm{DPS1-R/F,100\,K,old}} < (3.24 \pm 0.04) \times 10^{-4}\,\frac{1}{\mathrm{h}}\,, \tag{6.18}$$

which is a factor of 30 better than specified. Since in standard ^{83m}Kr operation of the WGTS the gas density in the DPS1 is already very low, it can be concluded that the temperature stability of the DPS1 has only a negligible influence on the line width of the ^{83m}Kr conversion electrons. The same conclusion holds for the dedicated ^{83m}Kr campaign in July 2017 which is described in chapter 5. Although there was no loop operation so that the ^{83m}Kr was distributed nearly equally in all WGTS sections (see figure 6.24), the excellent temperature stability of the DPS1 does not have a noticeable effect on the calculation of the Doppler broadening of the conversion lines (see section 5.3).

The temperature stability of the temperature sensors in the DPS1-R/F is investigated in the same way for the Gantner module-based setup: for every sensor, the five days of data-taking are split into one-hour intervals, for which the relative temperature stability as standard deviation divided by the mean is calculated. Each stability value is put into a histogram which is presented in figure 6.17. The DPS1-R/F sensors show a 90th percentile for the relative temperature stability of

$$\left|\frac{\Delta T}{T}\right|_{\mathrm{DPS1-R/F,100\,K,new}} < (5.43 \pm 0.04) \times 10^{-4}\,\frac{1}{\mathrm{h}}\,. \tag{6.19}$$

This is slightly worse than the result with the former, multiplexer-based voltage monitoring system during the ^{83m}Kr campaign in July 2017 (see equation 6.18).

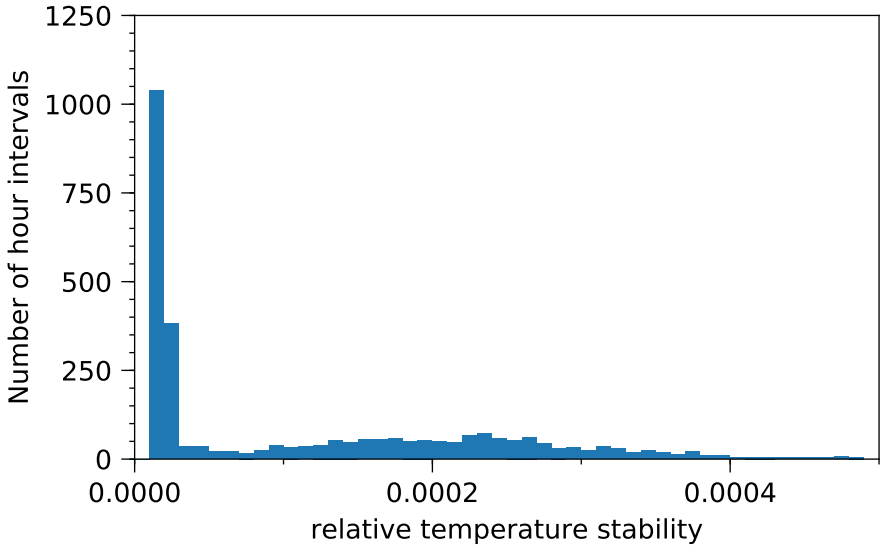

Figure 6.16.: Relative temperature stability of WGTS DPS1 during the gaseous ^{83m}Kr campaign of July 2017. For the histogram, one-hour intervals of all working sensors of the DPS1-R/F are taken. There was no broken sensor (see table 6.3 for a list of all DPS1 sensors). The time of the planned cool-down, starting in hour 149, is not included in this analysis. Instead of the small drop of temperature visible in the central beam tube sensor data between the hours 100 and 110 (see figure 6.12), the DPS1-R/F-1 sensors show, at that time, a fluctuation due to the instability in the gaseous helium circuit. While the DPS1-R-1 keeps its temperature level afterwards, the temperature in the DPS1-F-1 shows a drop like for the central beam tube sensors of about 0.15 K. The DPS1-R/F-2 are cooled by liquid nitrogen and therefore not affected by fluctuations in the gaseous helium circuit. Read out failures have been removed. The bin size is 1×10^{-5}. The maximum relative stability measured in one hour is 4.45×10^{-3}. The mean of the distribution is 1.5×10^{-5} with a standard deviation of 2.3×10^{-5}.

However, the result is still a factor of 18 better than the requirement, see equation 6.3. It should be noted that there are single one-hour intervals, in which the stability is very close to the requirement with a value of about 0.98 %. This underlines again that the value stated in equation 6.19 is more or less a rule of thumb, which stability value can be expected in future 100 K operation, but it is not valid for all times of KATRIN operation. The stability has to be re-calculated for every sensor and every run in future measurement programmes and should be a routine check among the data quality assessment procedures.

Temperature homogeneity: The homogeneity during the gaseous ^{83m}Kr measurements in July 2017 with the multiplexer-based instrumentation is plotted in figure 6.18. The difference between the maximum and the minimum value is a measure of the absolute inhomogeneity, which is (128.4 ± 229.4) mK. The comparably large uncertainty derived is based on table A.2. This corresponds to a relative inhomogeneity of

$$\left|\frac{\Delta T}{T}\right|_{\text{hom,100 K,old}} = (0.11 \pm 0.16)\,\% \ . \tag{6.20}$$

The relative inhomogeneity in the 100 K mode is by a factor of ≈ 15 smaller than in the 30 K mode (see equation 6.13). Especially the temperature increase towards the rear end of the WGTS is not visible at 100 K. As mentioned already in the previous section 6.2.2, a large inhomogeneity of ≈ 0.8 K was detected in the demonstrator measurements [Gro13]. Thus, it was decided to couple the capillaries of the vapour pressure bulbs (see figure 6.3) to the outer shield which is at liquid nitrogen tempera-

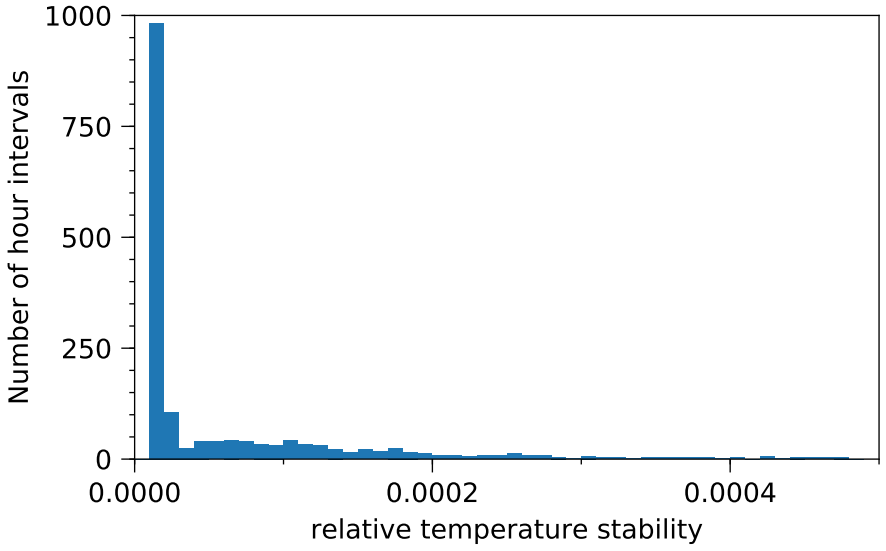

Figure 6.17.: Relative temperature stability of WGTS DPS1 at 100 K (January 2018). The histogram shows the relative temperature stability per hour of all DPS1-R/F temperature sensors for the five days of 100 K operation in January 2018. Read out failures have been removed. The worst stability recorded for the five consecutive days is 9.808×10^{-3}. The mean of the distribution is 2.43×10^{-4} with a standard deviation of 8.00×10^{-4}. The bin width is 1.0×10^{-6}.

tures of 77 K. This explains why the inhomogeneity is this much smaller in the 100 K mode than in the 30 K mode: At 30 K, the capillaries can still introduce some heat to the rear end of the WGTS, while at 100 K they cannot heat up the system any more and a much better homogeneity is the result. Although the demonstrator has not been driven in the 100 K mode, it is very likely that without the coupling of the capillaries to the liquid nitrogen shield also the 100 K mode of the WGTS would show an inhomogeneity. Therefore, these arrangements were a great success by eliminating the inhomogeneity for the ^{83m}Kr measurements and reducing the inhomogeneity for the standard tritium operation (see the previous section 6.2.2). However, the calibration at 100 K is no longer possible, which increases the uncertainties of the absolute temperature measurements in comparison to the calibrated PT500 sensors at 30 K significantly.

Figure 6.19 shows the mean temperatures of the PT500 sensors of the central beam tube during the five days of data-taking at 100 K in January 2018 with the Gantner module-based instrumentation. To determine the inhomogeneity along the beam tube, the minimum temperature value is subtracted from the maximum one. Divided by the mean of all 22 values, a relative inhomogeneity of

$$\left|\frac{\Delta T}{T}\right|_{\mathrm{hom,100\,K,new}} = (0.11 \pm 0.28)\,\% \tag{6.21}$$

is obtained. This result reproduces the one of the ^{83m}Kr campaign in July 2017 (see equation 6.20).

The analysis of the temperature data taken at 100 K during the gaseous ^{83m}Kr campaign in July 2017 and a week of measurements in January 2018 has again demonstrated the outstanding performance of the WGTS cryostat and its two-phase cooling system. While the temperature inhomogeneity along the central beam tube is reduced drastically in comparison to the 30 K mode, the stability both for the DPS1 and for the central beam

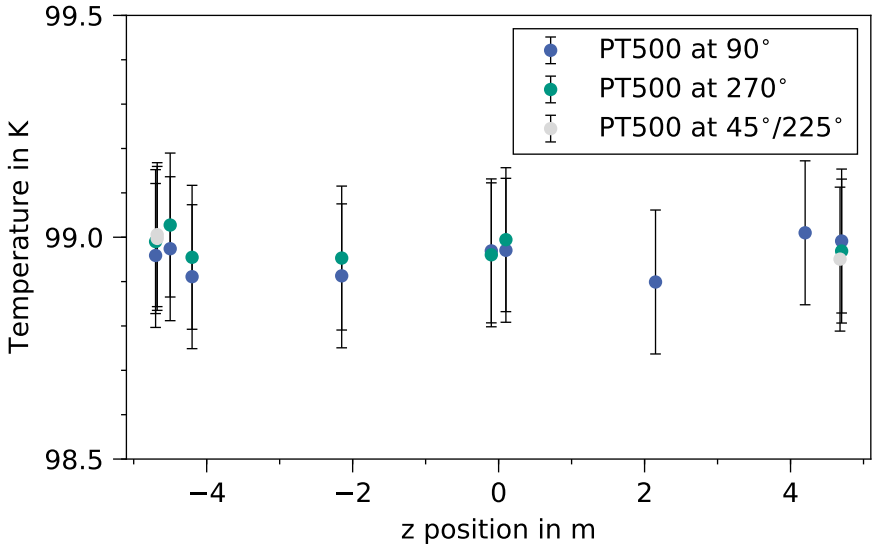

Figure 6.18.: Absolute temperature homogeneity of WGTS central beam tube during the gaseous ^{83m}Kr campaign of July 2017. The plot shows the mean temperature during the ^{83m}Kr campaign of the 19 working PT500 sensors at their positions along the central WGTS beam tube ($z = 0$ centre of beamtube, positive z towards DPS, negative z towards rear section). The cool-down of the WGTS at the end of the campaign (see figure 6.12) is excluded from the analysis. The sensors marked in blue are mounted on top of the beam tube (90°), the sensors marked in green are mounted on the bottom of the beam tube (270°) and the sensors marked in grey are mounted on positions in between (45°/225°). The error bars are based on table A.2.

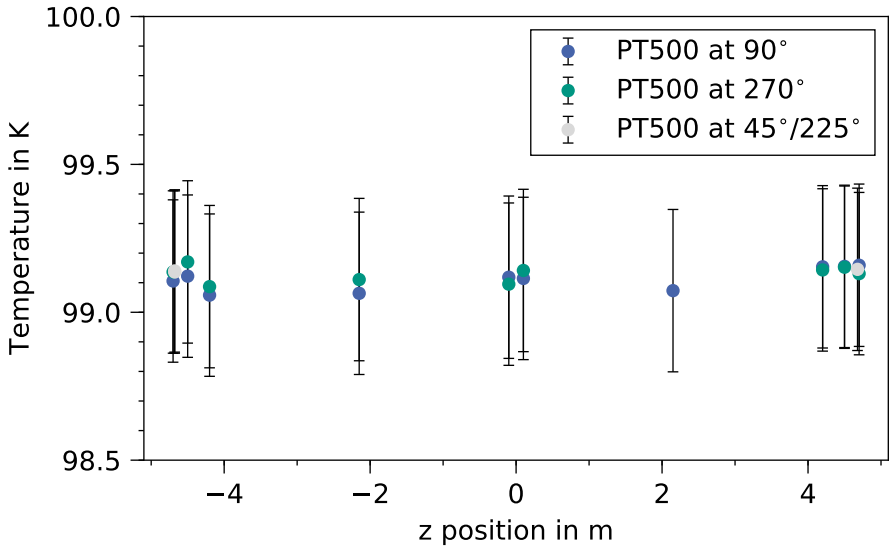

Figure 6.19.: Absolute temperature homogeneity of WGTS central beam tube at 100 K (January 2018). The plot shows the mean temperature of the 22 working PT500 sensors at their positions along the central WGTS beam tube ($z = 0$ middle of beamtube, positive z towards DPS, negative z towards rear section) during the five days of measurements at 100 K in January 2018. The sensors marked in blue are mounted on top of the beam tube (90°), the sensors marked in green are mounted on the bottom of the beam tube (270°) and the sensors marked in grey are mounted on positions in between (45°/225°). The error bars are based on table A.2.

Table 6.2.: ^{83m}Kr measurement during cool-down of WGTS – overview of WGTS temperatures. The table shows the maximal and minimal temperature during the ^{83m}Kr measurement with the WGTS cooling down. The last column shows the temperature difference. The values presented are the means over all sensors per section. Please note that the sensors 200-RTP-3-5104...07 and -09 were not working and are not included in the analysis.

WGTS section	KATRIN numbers	$T_{\max}$ (K)	$T_{\min}$ (K)	ΔT (K)
DPS1-R-2	200-RTP-3-1101...04	102.3	94.6	7.7
PP2-R	200-RTP-3-2101...02	100.2	93.3	6.9
DPS1-R-1	200-RTP-3-3101...06	101.7	92.1	9.6
PP1-R	200-RTP-3-6101...02	96.0	87.9	8.1
Central beam-tube	200-RTP-3-5101...24	98.8	94.5	4.3
PP1-F	200-RTP-3-4101...02	95.9	87.8	8.1
DPS1-F-1	200-RTP-3-7101...06	102.1	92.1	10.0
PP2-F	200-RTP-3-8101...02	100.0	92.8	7.2
DPS1-F-2	200-RTP-3-9101...04	102.6	94.8	7.8

tube is a factor of ≈ 20 better than specified. This reduces the influence of the temperature on the ^{83m}Kr spectrum to a minimum. The results of the stability are comparable to the 30 K measurements. The results for the former multiplexer-based instrumentation and the current Gantner module-based system do not show any noticeable deviations. The trueness of the Gantner module-based system can be improved by adjusting the current strength applied to the PT500 sensors. With this adjustment, nearly the same trueness as in the former system is achievable.

6.2.4. WGTS Temperature Influence on Detector Rate

During the ^{83m}Kr campaign in July 2017 (see chapter 5), a measurement to investigate the dependence of the ^{83m}Kr conversion electron rate on the WGTS temperature was performed with the gaseous Krypton source. Over a timespan of 4.5 hours, the WGTS temperature was decreased by 4 to 10 K depending on the WGTS section (see table 6.2). The high voltage of the main spectrometer was set to 30455 V, so that all ^{83m}Kr lines above the L_2-32 line (see table 5.2) contributed to the count rate at the focal plane detector, which was continuously monitored during the cool-down.

In a simplified picture, one can assume the ^{83m}Kr to form an ideal gas, so that the particle number density n should increase when the source temperature T is reduced:

$$n \propto \frac{1}{T} \,. \tag{6.22}$$

This behaviour can be seen qualitatively in figure 6.20: While the temperature decreases, the rate at the focal plane detector rises. To demonstrate the causal connection between the two parameters temperature and rate, a correlation analysis is presented in table 6.3, which shows a clear anticorrelation of the two parameters of $-0.73 \ldots -0.95$ depending on the sensors used and the cuts applied. However, the ^{83m}Kr conversion electron rate only increases from 10013 to 10225 cps (marked with the two dashed lines in figure 6.22), which equals a relative increase of 2.1 %. At the same time, the temperature is reduced by 4.4-9.8 % depending on the WGTS section. From equation 6.22 one would expect both being of the same magnitude.

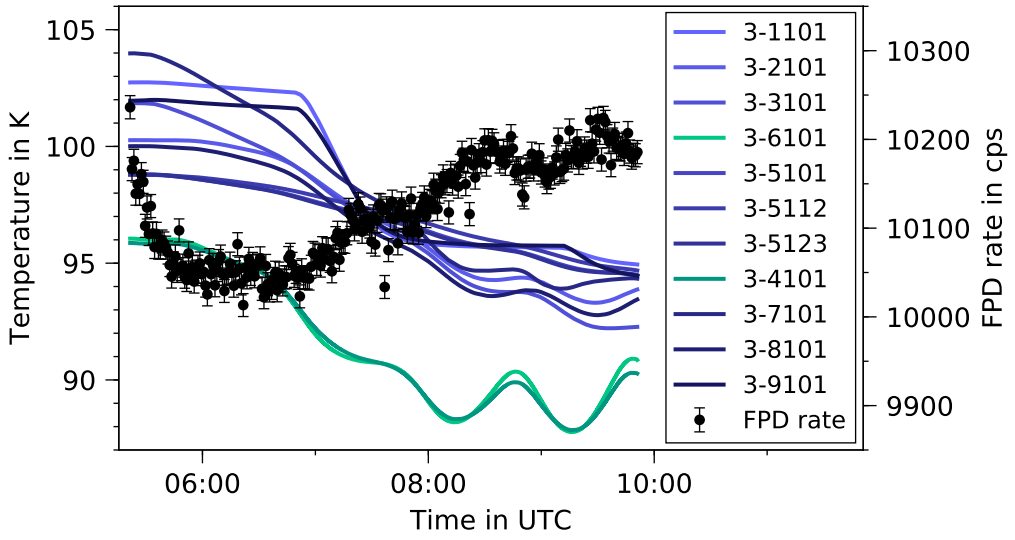

Figure 6.20.: ^{83m}Kr conversion electron rate dependence on WGTS temperature. The figure shows the ^{83m}Kr conversion electron rate measured with the focal plane detector (FPD) in 1 minute steps during the cool-down of the WGTS. Detailed information on the sensor position and the temperature differences in this measurement can be found in table 6.2. The sensors plotted with green lines show strong fluctuations, which are also visible in the rate. This effect is discussed in detail in the main text.

Table 6.3.: Correlation analysis of ^{83m}Kr and WGTS temperature. The table shows the Pearson correlation coefficient for the WGTS temperature and the observed ^{83m}Kr conversion electron rate when the WGTS is cooled down. A clear anticorrelation is visible as expected from equation 6.22. The presented correlation values are averaged over all sensors of a given WGTS section. ρ_0 denotes the correlation for the data without any cuts or shifts applied. In the fourth column, ρ_{cut} means that here the correlation coefficients are calculated without the first 20 data points of the ^{83m}Kr rate, where it is influenced by an unknown rate-decreasing effect (see main text and figure 6.20). In addition to the cut, in the last column the temperature values are shifted by 19 minutes. Then, the highest correlation values are achieved averaged over all sensors. For a deeper discussion of the applied shift, the reader is referred to the main text.

WGTS section	KATRIN numbers	ρ_0	ρ_{cut}	$\rho_{\text{cut,shift}}$
DPS1-R-2	200-RTP-3-1101...04	−0.813	−0.899	−0.923
PP2-R	200-RTP-3-2101...02	−0.864	−0.954	−0.955
DPS1-R-1	200-RTP-3-3101...06	−0.825	−0.941	−0.945
PP1-R	200-RTP-3-6101...02	−0.727	−0.837	−0.938
Central beam-tube	200-RTP-3-5101...24	−0.847	−0.942	−0.941
PP1-F	200-RTP-3-4101...02	−0.746	−0.856	−0.941
DPS1-F-1	200-RTP-3-7101...06	−0.796	−0.923	−0.944
PP2-F	200-RTP-3-8101...02	−0.853	−0.949	−0.954
DPS1-F-2	200-RTP-3-9101...04	−0.822	−0.908	−0.926

In order to find an explanation of this discrepancy, a closer look at the ^{83m}Kr conversion electron rate is necessary: at the beginning of the measurement, the rate drops significantly before it remains on the same level for about one hour. These one and a half hours at the beginning of the cool-down of the WGTS are obviously not correlated to the WGTS temperature: when the rate is decreasing for about half an hour, the temperature is still stable, and when the rate is stable at one level for about one hour, the temperature is already decreasing. Since after these initial one and a half hours the temperature and the rate are clearly correlated (see also table 6.3), a second effect has to be considered besides the temperature of the WGTS which lets the ^{83m}Kr conversion electron rate decrease. As soon as the cool-down of the WGTS starts, this decreasing effect is counterbalanced by the rate-increasing effect of the falling temperature, so that the rate is stable for one hour. After one and a half hour of measurement time, the rate-decreasing effect seems to end, so that then the rate follows clearly the temperature.

Several parameters can be identified which might cause the observed rate-decreasing effect. These shall be discussed briefly in the following:

Magnetic fields. If the source magnetic field strength decreases or the maximum magnetic field strength between the source and the detector increases, the acceptance angle of the decay electrons is reduced according to equation 3.5. A reduced acceptance angle causes a reduced rate at the detector. A significant decrease of the source magnetic field strength can already be ruled out due to the findings in section 6.1.

Retarding voltage. The voltage setpoint was kept constant during the measurement. However, if the voltage were to increase for some reason, the rate would decrease as soon as further ^{83m}Kr conversion lines are fully or partly blocked at the main spectrometer.

Reduced CPS temperature. If the CPS beam tube temperature is too high, so that the ^{83m}Kr pumping efficiency is not at 100 %, a drop in temperature could lead to a higher pumping efficiency and thus to a total rate decrease. However, this scenario is very unlikely because in the measurements performed before the cooling down of the WGTS, there were no hints that any ^{83m}Kr has reached the main spectrometer, so that the pumping efficiency of the CPS can be assumed to be 100 %.

Kr generator. Changes of the operational conditions of the ^{83m}Kr generator influence the rate. In particular, a rate decrease might result from changes in the outgasing rate inside the generator or if the setting of the regulating valve towards the WGTS is manipulated.

While the first three items can be checked easily since they are monitored with numerous sensors whose values are collected with ADEI (see section 3.3), the operational parameters of the ^{83m}Kr generator like the temperature or the status of the regulating valve were not recorded in a database. Figure 6.21 shows that the first three items can be ruled out as causing the rate-decreasing effect. Since the fourth item cannot be ruled out, the best explanation for the rate-decreasing effect is an irregularity in the operation of the gaseous ^{83m}Kr generator, but it cannot be investigated if the effect really ends after one and a half hours of the measurement.

However, one can try to estimate the real rate increase due to the temperature drop of the WGTS, which should be larger than the aforementioned 2.1 %, if it is really counterbalanced by a rate-decreasing effect of the same size in the first hour of cooling down. For doing this, the rate decrease is fitted with a straight line which is then extrapolated until the rate on the detector leaves its constant level and starts to rise again (see figure 6.22). With this estimation one ends up at a rate increase due to the cooling down of the WGTS of 8.7 %,

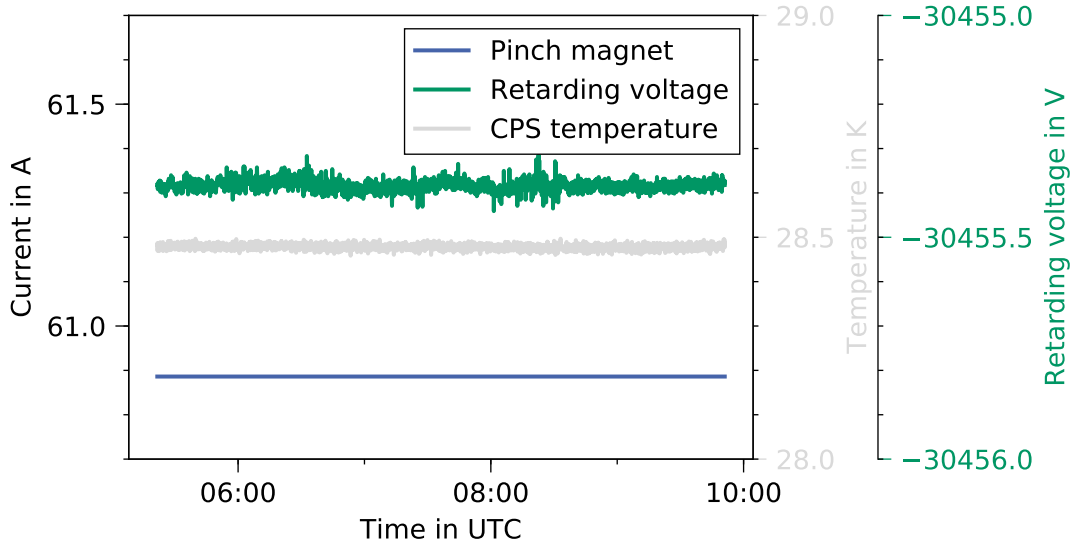

Figure 6.21.: Stability of selected beamline parameters during WGTS cool-down. The graph demonstrates the stability of the pinch magnetic field (shown is the current of the pinch magnet), the stability of the high voltage set point (read out via the high-precision voltage divider), and the stability of the CPS beam tube temperature. Since these three parameters are stable, they cannot be responsible for the observed rate decrease of the ^{83m}Kr, so that there must be some instability of the Kr generator, see the discussion in the main text.

which fits much better to the expectation of 4.4-9.8 % from the temperature decrease (see table 6.2).

Upon a deeper look on the second part of the measurement with the cooling-down of the WGTS, a structure in the ^{83m}Kr conversion electron rate can be seen which seems to be related to the structure visible in the temperature trend of nearly all temperature sensors, in particular in the trends of the sensors of the pump ports PP1-R/F (RTP-3-4101 and RTP-3-6101), see again figure 6.20. As shown in figure 6.23, this structure in the temperature is caused by an irregularity in the gaseous helium circuit of WGTS. Since the pump ports are cooled directly by the gaseous helium, here the effect is very clearly visible. The DPS1-R/F-1 are cooled by two-phase argon in the WGTS krypton mode. The argon circuit is connected to the gaseous helium circuit via a condenser (thermosiphon) which dampens the fluctuations. Also the two-phase cooling of the central beam tube (see figure 6.3) is connected to the gaseous helium circuit via a condenser, but here the fluctuations are further reduced due to the heating elements in the WGTS cooling system which counterbalance irregularities in the central beam tube operation. The DPS1-R/F-2 are not connected to the gaseous helium circuit and thus do not show these fluctuations.

Although these fluctuations should not occur during WGTS operation, in this particular measurement they can be used to investigate the time lag between the temperature sensor readings and the rate at the detector. The determination of this lag is essential for tritium operation: if there is a large time shift between temperature sensors and rates, this has to be considered in the analysis for the correct column density calculation. Based on simulations (see figure 6.24), it can be assumed that the ^{83m}Kr conversion electron rate is nearly uniform along the entire WGTS beam tube with 61 % of all decays in the WGTS taking place in the central beam tube and only 5.4 % in the pump ports PP1-R/F. However, the pump ports PP1-R/F show the largest temperature modulations of all sensors (see figure 6.20)

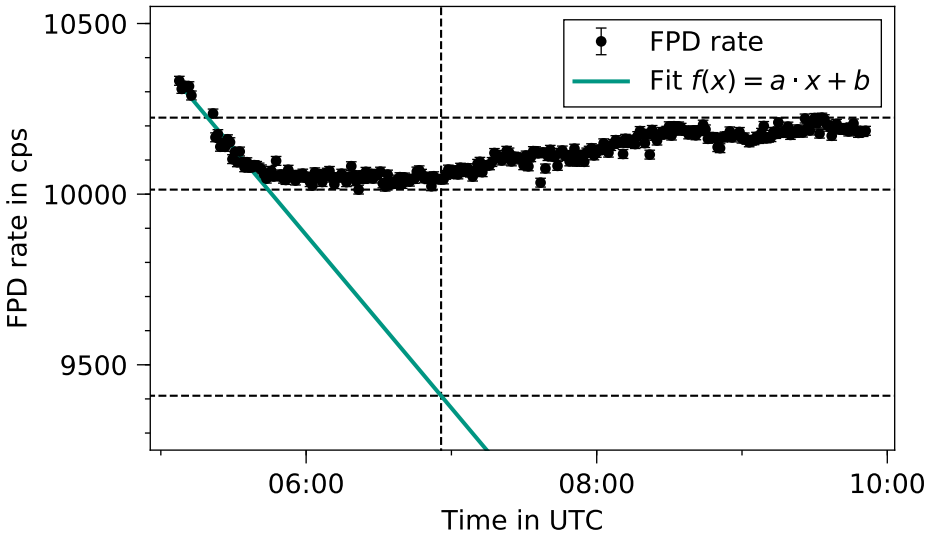

Figure 6.22.: Estimation of the actual ^{83m}Kr conversion electron rate increase due to WGTS cool-down. In comparison to figure 6.20, the rate was extended by one run before the actual start of the measurement, which already has the same settings and already shows the decreasing trend. The first 26 data points are fitted with a straight line which is then extrapolated. The fit result is $f(x) = (-0.141 \pm 0.007)\,\mathrm{cps\,s^{-1}} \cdot x + (2.11 \pm 0.10) \cdot 10^8\,\mathrm{cps}$. The two upper horizontal lines show the maximum and minimum rate if the decreasing effect is not considered and the third horizontal line shows the actual minimum rate, if the decreasing effect is extrapolated until the actual rate starts to increase again. Then, the minimal rate is 9409 cps.

with a difference of $\Delta T = 1.9\,\mathrm{K}$ for the first minimum (at 08:30 UTC, see figure 6.25) and the first maximum (09:00 UTC) and a difference of $\Delta T = 2.4\,\mathrm{K}$ between the second minimum (09:30 UTC) and the first maximum. This translates into a relative temperature change of 2.2 % and 2.7 % at 88 K, respectively. For the expected rate change due to the fluctuations in the pump ports PP1-R/F, these values have to be weighted with the 5.4 % of relative abundance. Then, a relative rate change of 0.12 % and 0.15 % is obtained. The relative rate changes which are observed (see figure 6.25) are 0.46 % and 0.71 %. The observation and the estimation based on the simulation in figure 6.25 agree quite well. It is obvious that the large temperature fluctuations in the pump ports PP1-R/F have a significant influence on the detected rate. Thus, the temperature trend of these two pump ports can be used to learn more about the time shift between temperature and detected rate.

The temperature sensors from the two pump ports and the rate are plotted in figure 6.25. A local maximum in the temperature should lead to a local minimum of the rate, so that it is clear how the temperature (or the rate) has to be shifted in time to achieve a match. It is found that the rate lags behind the temperature trend recorded by the sensors. The actual time shift is determined in two different ways: firstly, the first rate maximum is determined and used as fixed point where to shift the first temperature minimum. A shift of 14-18 minutes is found, see again figure 6.25. Secondly, the correlation between the pump port temperature sensors and the rate was calculated for different time shifts, and the maximum was found at 21-24 minutes. This second method is much more uncertain and it should be noted here that, if all WGTS sections are considered simultaneously, the maximum for this correlation analysis is found at 19 minutes (see table 6.3).

The obtained shift of ≈ 15 minutes thus reflects the time which a temperature fluctuation inside the cryogenic system needs to propagate into the gas column. It can be assumed that

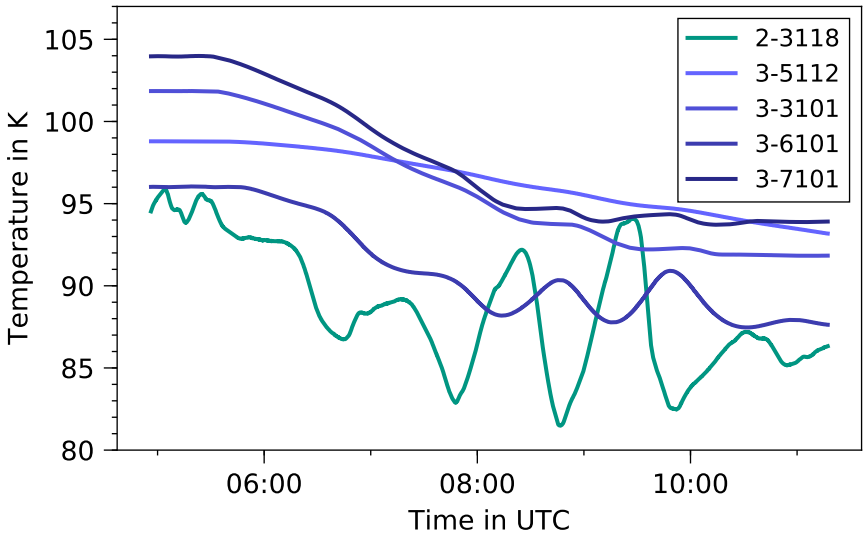

Figure 6.23.: Influence of the gaseous helium cooling cycle on the WGTS temperature. The gaseous helium for the inner shield of the WGTS is brought to cryogenic temperatures in a mixing process of gaseous helium at room temperature and liquid helium. Occurring turbulences lead to temperature fluctuations. During the discussed measurement with the WGTS being cooled down, such fluctuations with $\Delta T > 10\,\mathrm{K}$ happened in the gaseous helium circuit, recorded at the entrance of the gaseous helium circuit in the WGTS cryostat (sensor RTT-2-3118). After ≈ 20 minutes, the fluctuations reach the sensors at the WGTS beam tube. While the pump ports (represented by sensor RTP-3-6101) are directly cooled by the gaseous helium and show therefore also large fluctuations of $\Delta T \approx 5\,\mathrm{K}$, the two-phase cooling systems of the central beam tube (represented by sensor RTP-3-5112) and the DPS1-R/F-1 (represented by sensors RTP-3-3101/RTP-3-7101) are connected via thermosiphons to the gaseous helium circuit. Thus, the fluctuations are dampened strongly.

any modulation is dampened during the propagation. However, this time shift should be included in the analysis software to assure that the right values of temperature and detector rate are compared when the column density is calculated. In the discussed measurement, the time shift was measured at 100 K. In principle, the time shift can be different at 30 K. Furthermore, in future WGTS operation, the tritium and the krypton will be circulated in the loop system (see figure 3.3), so that the most important temperature sensors for the analysis are the ones of the central beam tube. Presumably, the time shift is also different for different WGTS sections. Since the time shift for the central beam tube sensors cannot be determined from the measurement because the fluctuations in the central beam tube sensors are too small, it is strongly recommended to repeat this measurement at both operational temperatures of the WGTS in loop operation.

Based on the results derived from the measurement during the krypton campaign in July 2017, the following procedure is proposed to get a better estimate of the time shift between the central beam tube sensors and the rate at 30 and 100 K:

- Before the cool-down of the WGTS starts, it should be guaranteed that the rate on the detector is stable and that all relevant parameters (magnetic fields, retarding voltage, injection pressure, temperatures, ...) are stabilised.
- The cool-down of the WGTS should not be monotonous, but interrupted by local excursions of the temperature artificially introduced to create well-defined points in time which can be used as markers to determine the time shift between temperature

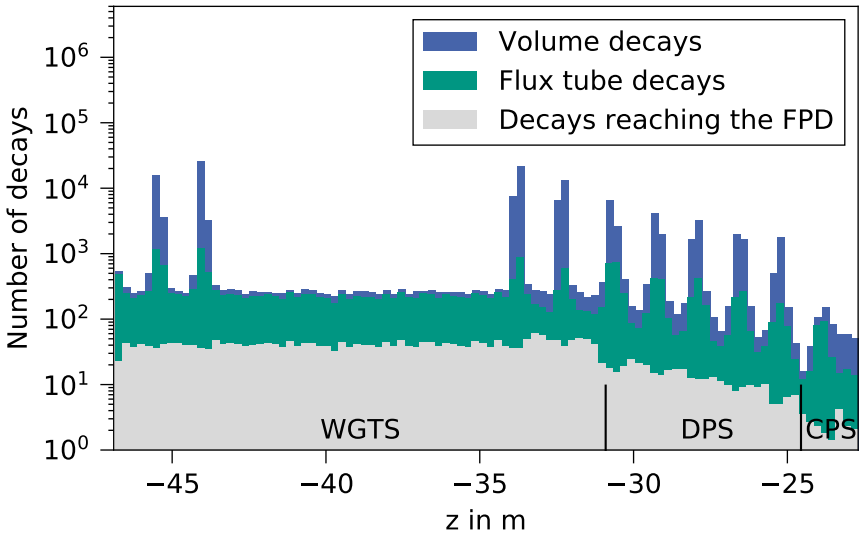

Figure 6.24.: Simulated ^{83m}Kr rate distribution in WGTS, DPS and CPS. The histogram shows the expected distribution of the ^{83m}Kr in the KATRIN source and transport section. The x-axis shows the z-component of the KATRIN coordinates ($z = 0$ at the middle of the main spectrometer). The distribution in the volume without any cuts is shown in blue. Most of the krypton is trapped in the pump port regions due to scattering off the walls. If only decays inside the flux tube are considered, the contribution from the pump port regions reduces drastically (green). Finally, also the acceptance angle of the electrons is taken into account to get the fraction of all decays which are actually counted at the detector (grey). Then, the rate distribution inside the WGTS is nearly flat. Simulation data kindly provided by F. Friedel.

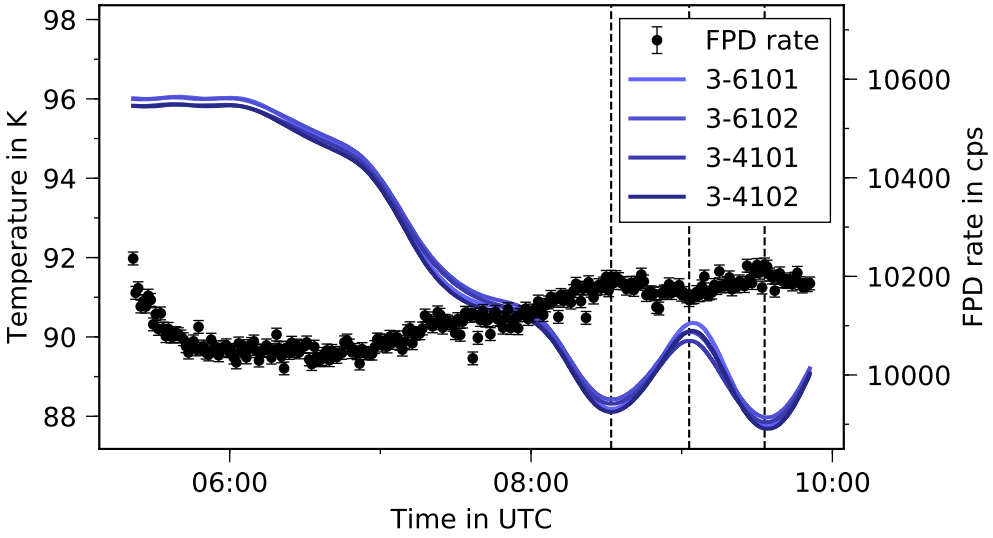

Figure 6.25.: Comparison of ^{83m}Kr rate and time-shifted WGTS temperature. In contrast to figure 6.20, the temperature trends of the four sensors of the pump ports PP1-R/F are shifted in time so that local maxima of the ^{83m}Kr rate match local minima of the temperature. Point of orientation is the first rate maximum at about 08:30 UTC. For all the three local extrema, time shifts between 14 and 18 minutes are obtained.

and rate. The discussed measurement has demonstrated that local maxima of 3 to 4 K (see figure 6.25) are sufficient to achieve a significant effect in the rate.

6.3. Conclusions

This section summarises the results of the analyses presented above. The following conclusions are drawn regarding the operation of the WGTS cryostat:

- The operation of the WGTS is stable. This is true for the temperature as well as for the magnetic field. The design parameters are surpassed by up to two orders of magnitude which underlines the excellent performance of the WGTS. Thus, the influence of both parameters on the neutrino mass estimate is minimised.
- While the axial uniformity of the magnetic field has still to be measured, the homogeneity of the central beam tube temperature was only demonstrated for the 100 K mode. For the 30 K operation, a sizeable inhomogeneity was detected. However, this can be tolerated since it can be implemented into the gas dynamics model. It should be noted here that the right conclusions were drawn from the WGTS demonstrator measurements [Gro13]: In order to reduce the inhomogeneity measured with the demonstrator setup, the vapour pressure capillaries were connected to the inner shield at 77 K. As demonstrated in the analyses presented in this chapter, this substantially reduced the inhomogeneity at 30 K and eliminated the inhomogeneity at 100 K.
- It should be kept in mind that the presented values on the temperature/magnetic field stability and temperature homogeneity can certainly serve as an indicator for longterm behaviour, but they are not valid in general. In such a complex cryostat as the WGTS, parameters can change for several reasons. Therefore, for neutrino mass analysis, the temperature and magnetic field stability have to be determined for every data-taking period anew.
- The change of the monitoring system of the PT500 voltages to Gantner modules made it necessary to re-evaluate the uncertainties involved into the temperature measurements. In this chapter and its associated appendix, measurement uncertainties for the old and the new system were calculated for both operational temperatures. These can now be used in the neutrino mass analysis in KATRIN standard operation. While the uncertainty on the temperature stability in both temperature modes is small, the uncertainty on the absolute value, the temperature trueness, does not keep the requirements. For the new temperature monitoring system with Gantner modules, some modifications are necessary in the future to reduce the uncertainty, e. g. by increasing the current through the PT500 sensors.
- The change of the PT500 voltage monitoring system was a success as the acquisition time of the temperature data could be reduced by a factor of 5. Now the temperature acquisition time is comparable to the ones of other KATRIN sensor data which facilitates the combined analysis.
- A new feature of the WGTS temperature system which was not known before was measured in the scope of this thesis. Based on the ^{83m}Kr data the time difference between a detection of a specific measurement point of a beam-tube temperature reading and the corresponding effect on the rate at the focal plane detector was measured to be around 16 min. Since the temperature is extremely stable, this time difference has normally no effect on the neutrino mass result when it is not taken into account in the analysis. However, sometimes there are fluctuations in the gaseous helium circuit which propagate to fluctuations in the beam tube temperature. Then it is important to implement the right time difference to compare the right data sets.

It is recommended to measure this time difference also at 30 K in loop operation to confirm the result.

- The analysed datasets have revealed that irregularities of the gaseous helium circuit may occur. These can lead to temperature changes in the central beam tube as well, although in a strongly damped way. Such a fluctuation occurring during a neutrino mass run could result in failing to comply with the stability requirement of the temperature. Thus, the neutrino mass measurement runs should be kept short (≈ 1 h) in order not to lose too much data in case of such a fluctuation occurring. Furthermore, the irregularities need to be monitored in the scope of the data quality screening which is part of the neutrino mass analysis chain.
- In some cases, the front part of the WGTS behaves differently than the rear part. For instance, during the first commissioning measurements in October 2016, the rear sensors showed an increase in the temperature whereas the front sensors did not. In the spring 2018 measurements it was the other way around: the front sensors showed a dip in the temperature trend which was not seen in the rear sensors. Both observations did not exceed the stability requirement. This behaviour is not fully understood yet, but probably linked to the software/data acquisition.

With this thesis, the specifications of the WGTS important for the neutrino mass measurements were tested experimentally. The WGTS cryostat is now fully characterised in its two operational modes at 30 K and 100 K. The influence of the WGTS operational parameters on the neutrino mass were proven to be small. Based on the results of the analyses above and the lessons learned during two years of WGTS operation, the cryostat is now ready for standard KATRIN operation.

7. Conclusions and Outlook

The discovery of neutrino oscillations forms irrefutable proof that neutrinos have a mass. This finding requires an extension of the Standard Model of Elementary Particles, opening a door towards new physics. However, the absolute neutrino mass scale could not be determined yet: It remains one of the fundamental questions of today's physics, as it is expected that neutrinos and their properties provide a key to the dark sector, the matter-antimatter asymmetry and other big questions. The neutrino mass scale can be accessed in three different ways: there are two indirect methods, involving complex models, based on observational cosmology and the search for neutrinoless double-beta decay, respectively. A direct method uses the model-independent measurement of the kinematic endpoint of beta decay or electron capture. All three approaches measure different combinations of effective neutrino masses.

The currently best limit for the effective electron antineutrino mass in a direct measurement was set by the Mainz and Troitsk Experiments at $m_\nu < 2\,\mathrm{eV}/c^2$ (95 % C. L.). Both experiments used tritium as a beta emitter. Tritium offers a comparatively high activity combined with one of the smallest known endpoint energies of all beta emitters at 18.6 keV. Both properties make it the ideal isotope for the neutrino mass search. Tritium is also used by the Karlsruhe Tritium Neutrino (KATRIN) experiment, the next-generation experiment to determine the effective electron antineutrino mass. KATRIN is designed for a neutrino mass sensitivity of $0.2\,\mathrm{eV}/c^2$ (90 % C. L.) and operated at the Tritium Laboratory Karlsruhe of Karlsruhe Institute of Technology (KIT) in Germany. Currently, the commissioning of KATRIN is being finalised and regular operations are planned to start in 2019.

The KATRIN beam line is 70 m long. Electrons are guided with magnetic fields from the high-luminosity windowless gaseous tritium source towards the main spectrometer, which acts as a MAC-E filter. The neutrino mass is imprinted as a tiny distortion on the integrated beta spectrum just below the kinematic endpoint. In order to measure this small deviation with a sensitivity of a factor of 10 better than the currently best limit, KATRIN has to both increase the statistics and decrease the systematic uncertainties by a factor of 100, since the observable is the neutrino mass squared, m_ν^2. The required statistics is achieved with a daily tritium throughput of 40 g which results in an activity of 10^{11} Bq inside the WGTS beam tube. In order to keep the tight systematic uncertainty budget, the operational parameters of KATRIN have to be stabilised on the ppm to per mille level.

In the thesis at hand, the KATRIN systematic uncertainties were critically reviewed and evaluated. As a result, the thesis offers a fully revised list of systematic uncertainties. For most of the systematic uncertainties, their influence on the final neutrino mass was quantified in ensemble tests. Where available, results from former works were updated and improved. Recent findings from the first tritium measurement campaign in 2018 were considered to achieve an up-to-date estimation of the systematic uncertainty budget of KATRIN. Five items, which are the final-state distribution, the energy loss function for

scattering processes of signal electrons in the source, the slope of the background rate, the ion-related systematic uncertainties, and the detector-related systematic uncertainties, still need a final quantification and corresponding investigations are ongoing. KATRIN performs significantly better than expected for some parameters, such as the high-voltage stability of the main spectrometer or the temperature stability of the WGTS, so that additional systematic effects which were not considered in the 2005 KATRIN Design Report are counterbalanced.

The in-depth evaluation of systematic effects has demonstrated that most of them are linked to the windowless gaseous tritium source in one way or another. Therefore, the WGTS was fully characterised in the second part of the thesis. The magnetic field stability of the cryostat was found to be $< 1.1 \times 10^{-5}\,\mathrm{h}^{-1}$, which is two orders of magnitude better than required. A similar result was found for the temperature stability of the central beam tube, which was measured to $(5 \pm 1) \times 10^{-5}\,\mathrm{h}^{-1}$ for the standard tritium operation at 30 K and $(5.4 \pm 0.4) \times 10^{-5}\,\mathrm{h}^{-1}$ for the gaseous ^{83m}Kr mode at 100 K. Both values are more than one order of magnitude better than the KATRIN Design Report requirement, underlining the outstanding performance of the WGTS. The temperature homogeneity at 30 K along the beam tube was found to be worse than demanded, but due to the near-to perfect stability, the inhomogeneity can be reliably included in the gas dynamics model. To complete the characterisation of the WGTS cryostat, the time it takes for a fluctuation measured in the cooling circuit to influence the column density inside the beam tube was measured to be 16 min with ^{83m}Kr at 100 K. This value has to be confirmed for tritium operation at 30 K and included in the analysis model.

The gaseous ^{83m}Kr mode of the WGTS is technically challenging, but is very important for the estimation of the plasma potential, which may arise from the beta-decay processes occurring in large numbers inside the source beam tube. In the scope of the work at hand, a dedicated measurement campaign with the full KATRIN beam line was proposed, planned and performed to test the gaseous ^{83m}Kr generator hardware and to set important calibration benchmarks before any hydrogen isotopologue was circulated through the WGTS. The measurement campaign was very successful. The full conversion electron spectrum of ^{83m}Kr was recorded, including Auger electron lines and the 9.4 keV transition. The measured conversion line positions are references for future KATRIN measurements with ^{83m}Kr, since they might shift due to work function changes in the WGTS as soon as tritium layers form on the inner surface. The conversion lines of the 9.4 keV transition were split according to the states of ionisation after the Auger cascade following the 32 keV transition. This splitting of the conversion lines allows to measure the change in the binding energy of the electrons in an ionised atom, which is an interplay of nuclear and atomic physics effects. To the best of knowledge, measurement results of this effect with ^{83m}Kr have been published only once before. These results could be confirmed, and for the first time values for the L_2 and L_3 lines have been derived. These results demonstrate the excellent capabilities of KATRIN in high-precision spectroscopy.

The measurement campaign also offered a first opportunity to test the linearity and stability of KATRIN's energy scale. It was found that the energy scale around the tritium endpoint is perfectly linear. A slight deviation was found at energies around the 9.4 keV transition, which has to be investigated further for the sterile neutrino measurement programme of KATRIN. The stability of the line positions was found to be better than 0.1 ppm in one week. This exceeds the requirement of the KATRIN Design Report by more than one order of magnitude and is the ultimate measurement of the energy scale stability as it is determined in situ.

To conclude, in the thesis at hand a major milestone of KATRIN on its way towards the first tritium measurement was achieved, which was the operation of the full setup for an entire week during the gaseous ^{83m}Kr campaign. Furthermore, the evaluation of systematic effects and the full characterisation of the WGTS are important for the planning of the regular tritium operation of KATRIN. Based on the findings in this thesis, an overview of the next steps can be derived:

- The remaining systematic effects, which could not be determined yet, have to be quantified soon. Especially the final-state distribution and the energy loss function are assumed to be two of the major contributions. The investigations are ongoing.
- In this thesis, the systematic uncertainties were investigated for the KATRIN Design Report conditions. At present, the background rate is a factor of 30-50 larger than estimated, but a final number, corresponding to a specific fiducial volume in the spectrometer, has not yet been defined by the collaboration. A number of measures to mitigate the impact of the elevated baseline background are currently under investigation. Since they comprise, among other suggestions, a broadening of the energy analysis window from 30 eV to 50 eV below the tritium spectral endpoint, a rather strong influence on some of the systematic uncertainties may be expected. Before regular tritium operation starts in 2019, optimised measurement settings balancing the statistical and systematic uncertainties have to be found to achieve the best KATRIN sensitivity possible.
- In 2018, the gaseous ^{83m}Kr measurements have been repeated in combination with loop operation and mixed with deuterium as the major carrier gas. Results for this measurement campaign are expected in the nearer future, providing an opportunity to detect a deuterium-related work function shift with regard to the results presented in the thesis at hand.

The regular operation of KATRIN starts in 2019 after more than 18 years of collaborative research and the neutrino mass as missing link in many fundamental questions of contemporary fields of physics will hopefully be found within the next five years.

A. Uncertainty Calculation of WGTS Beam Tube Temperature Measurement

Chapter 6 discusses WGTS temperature measurements in the 30 K and 100 K mode and investigates the fulfilment of the WGTS specifications and requirements for KATRIN. For both modes, two different uncertainty calculations are necessary, one for the old, multiplexer-based monitoring system of the WGTS beam tube temperature which was in use until the end of 2017, and one for the new, Gantner-module based monitoring system (see chapter 6.2.2 for details). While for the old temperature-monitoring system there are already uncertainty calculations in the literature [Gro11; Mar17a], there are no estimations for the new monitoring system available so far. In the following sections, the uncertainty of the absolute value and the uncertainty of the temperature stability are revised for the old system and calculated for the new system for 30 K (section A.1) and for 100 K (section A.2). Finally, the uncertainty of the PT1000 sensors in the DPS1-R/F is discussed in section A.3.

A.1. Uncertainty of the WGTS Mode at 30 K

For the 30 K mode it is possible to calibrate the PT500 sensors via vapour-pressure bulbs (see figure 6.3). The corresponding uncertainties of an absolute temperature measurement for the old and new temperature monitoring system are discussed in the following subsection A.1.1. For the determination of the temperature stability, the number of uncertainty contributions is reduced since only the relative temperature changes but not the absolute value is of interest. This is discussed in subsection A.1.2.

A.1.1. Temperature Trueness

Table A.1 lists all uncertainty contributions of the absolute measurement of the WGTS beam tube temperature with calibrated PT500 sensors at 30 K. Most of the contributions are taken from [Mar17a]. The main difference here is the modified consideration of the PT500 instrumentation and the PT500 sensor stability. All contributions are discussed in the following, for details the reader is referred to [Gro11; Mar17a].

PT500 instrumentation: The PT500 sensors are supplied with a well-defined current from a power supply (Keithley Model 6220 DC Current Source[1]) and at the same time the voltage is read out. In the former multiplexer-based read-out system, this was done with a Keithley Model 2701 ethernet-based DMM/Data Acquisition System[2]. Since

[1] see `https://de.tek.com/keithley-low-level-sensitive-and-specialty-instruments/keithley-ultra-sensitive-current-sources-seri` for the datasheet (accessed on August 17, 2018).

[2] see `https://de.tek.com/datasheet/2700-multimeter-data-acquisition-switch-systems/integra-series-technical-data-sheet` for the datasheet (accessed on July 18, 2018).

Table A.1.: Temperature trueness of WGTS PT500 sensors at 30 K. The table lists all contributions to the temperature trueness, that means to the absolute temperature measurement with calibrated sensors, of the PT500 sensors. The values are calculated for the former measurement system which was in use until the end of 2017 and for the new measurement system which is in use since then. In both cases, the instrumentation of the PT500 read out dominates the total uncertainty. Details on each item in the list can be found in the main text of this appendix, a short discussion of the uncertainties for KATRIN can be found in section 6.2.2.

Source of uncertainty	ΔT in mK
PT500 instrumentation (old)	49.8
PT500 instrumentation (new)	159.8
PT500 stability (old)	4.8
PT500 stability (new)	1.5
Vapour pressure instrumentation	1.2
Thermomolecular effect	0.2
Aerostatic systematic effects	0.2
Temperature gradient	0.3
Uncertainty of saturation vapor pressure curve	8.1
PT500 characteristic curve	0.4
Interpolation uncertainty	0.2
Combined uncertainty (old)	50.7
Combined uncertainty (new)	160.0

the beginning of 2018, the voltage read-out is done with Gantner modules[3]. The uncertainty of the voltage measurement $\Delta U/U$ and the uncertainty of the current supply $\Delta I/I$ directly translates into a temperature uncertainty via the resistance R of the PT500 sensors:

$$\frac{\Delta T}{T} = \frac{\Delta R}{R} = \sqrt{\left(\frac{\Delta I}{I}\right)^2 + \left(\frac{\Delta U}{U}\right)^2} \,. \tag{A.1}$$

The uncertainty on the current is calculated according to the data sheet for a current range of 2 mA and for a rectangular distribution with

$$\Delta I = \left(\frac{1}{3}(0.05\,\% \cdot I + 1\,\mu\mathrm{A})^2 + \frac{1}{3}(T_{\mathrm{oper}} - T_0)^2 \cdot (0.005\,\% \cdot I + 2 \cdot 10^{-2}\,\mu\mathrm{A})^2\right)^{\frac{1}{2}} \,. \tag{A.2}$$

I is the applied current value, T_{oper} the temperature at which the current supply is operating (35 °C) and T_0 is the reference temperature (28 °C). For the former, multiplexer-based setup a current of 500 µA and for the new Gantner-module based setup a current of 250 µA was applied. Thus, the relative uncertainties on the current in the old and new setup are

$$\left(\frac{\Delta I}{I}\right)_{\mathrm{old}} = 0.149\,\% \,, \tag{A.3}$$

$$\left(\frac{\Delta I}{I}\right)_{\mathrm{new}} = 0.265\,\% \,. \tag{A.4}$$

[3]The central beam tube sensors are connected to Gantner Q.bloxx A107, the DPS1-R/F-1 to Gantner Q.bloxx A105. See `www.gantner-instruments.com` (accessed on Jul 13, 2018) for more information.

The uncertainty of the voltage for the former, multiplexer-based setup is calculated according to the data sheet for a rectangular distribution via

$$\Delta U = \left(\frac{1}{3}(15\,\mathrm{ppm}\cdot U + 3\cdot 10^{-3}\,\mathrm{mV})^2 + \frac{1}{3}(T_{\mathrm{oper}} - T_0)^2\cdot(1\,\mathrm{ppm}\cdot U + 0.5\cdot 10^{-3}\,\mathrm{mV})^2\right)^{\frac{1}{2}} . \tag{A.5}$$

U denotes the voltage value and is estimated via $U = R \cdot I$ with I being the applied current and R being $10\,\Omega$, which is the typical resistance of a PT500 sensor at 30 K. The reference temperature T_0 for the digital multimeter is 24 °C, while the operational temperature is again 35 °C. Thus, the relative uncertainty of the voltage measurement with the multimeter is

$$\left(\frac{\Delta U}{U}\right)_{\mathrm{old}} = 0.073\,\% . \tag{A.6}$$

According to the data sheet of the Gantner modules, a maximum deviation of 20 µV for the applied measurement range of 100 mV has to be taken into account. Assuming a rectangular distribution, this value is lowered by factor of $1/\sqrt{3}$. With a current of 250 µA, a relative uncertainty of the voltage measurement of

$$\left(\frac{\Delta U}{U}\right)_{\mathrm{new}} = 0.462\,\% \tag{A.7}$$

is obtained.

According to equation A.1, the following instrumentation uncertainties for a temperature measurement at 30 K are calculated:

$$\Delta T_{\mathrm{instr.\ old}} = 49.8\,\mathrm{mK} , \tag{A.8}$$

$$\Delta T_{\mathrm{instr.\ new}} = 159.8\,\mathrm{mK} . \tag{A.9}$$

PT500 stability: The stability of the PT500 sensors has not been considered as an uncertainty contribution to the absolute temperature value so far in the cited literature. However, as the investigation in section 6.2.2 shows, the temperature values fluctuate over time, so that the stability has to be considered in the uncertainty budget. For all work presented in this thesis, the stability of the temperature is calculated as standard deviation over a time period of one hour. The value depends on the selected time interval, the sensor and on the temperature monitoring system (multiplexer-based vs. Gantner modules). Here, the stability estimations for the old and the new temperature monitoring system are used which are derived in section 6.2.2. If the relative values stated there are applied to 30 K, uncertainty contributions of

$$\Delta T_{\mathrm{stab.\ old}} = 4.8\,\mathrm{mK} , \tag{A.10}$$

$$\Delta T_{\mathrm{stab.\ new}} = 1.5\,\mathrm{mK} \tag{A.11}$$

are derived.

Vapour pressure instrumentation: The vapour pressure is read out with pressure transducers Cerabar S PMC71 from Endress+Hauser[4]. The accuracy of 0.05 % full scale of the range 0 to 4 bar is translated into a 1σ temperature uncertainty of

$$\Delta T_{\mathrm{vp\ instr.}} = 1.2\,\mathrm{mK} . \tag{A.12}$$

[4]The data sheet is available online at `https://www.de.endress.com/de/messgeraete-fuer-die-prozesstechnik/druck/Absolut-Relativdruck-Cerabar-PMC71` (accessed on August 17, 2018).

Thermomolecular effect: The thermomolecular effect describes pressure differences occurring if the pressure of a cryogenic system is measured at room temperature. This is the case at the WGTS, where the vapour pressure bulbs are at 30 K and the pressure transducers are at room temperature. Translated into temperature, an uncertainty contribution of

$$\Delta T_{\text{therm. mol.}} = 0.2\,\text{mK} \tag{A.13}$$

is obtained.

Aerostatic pressure differences: These systematic effects take density profiles in vertical sections of the vapour pressure capillaries into account and lead to an uncertainty contribution of

$$\Delta T_{\text{aerostatic}} = 0.2\,\text{mK}\ . \tag{A.14}$$

Temperature gradient: Temperature gradients inside the vapour pressure bulbs have to be taken into account with an uncertainty on the temperature of

$$\Delta T_{\text{temp. grad.}} = 0.3\,\text{mK}\ . \tag{A.15}$$

Uncertainty of saturation vapour pressure curve: The measured vapour pressure has to be translated into a temperature via a vapour pressure curve. The one used in the WGTS measurements is from NIST with a relative uncertainty of $\Delta p/p = 0.2\,\%$ [Lin05]. This equals a temperature uncertainty at 30 K of

$$\Delta T_{\text{vp curve}} = 8.1\,\text{mK}\ . \tag{A.16}$$

PT500 characteristic curve: The characteristic curve of the PT500 sensors translates the measured resistance into a temperature value and vice versa. The one implemented in the WGTS temperature monitoring software comes without any uncertainty value. Thus, the uncertainty was determined experimentally in [Mar17a]. The result is that the uncertainty contribution of the PT500 characteristic curve is

$$\Delta T_{\text{PT500 curve}} = 0.4\,\text{mK}\ . \tag{A.17}$$

Interpolation uncertainty: The characteristic curve of the PT500 is implemented in the WGTS temperature monitoring software with steps of 0.1 K. For temperatures in between, the software applies a linear interpolation. Since the curve is not perfectly linear, this interpolation introduces an uncertainty which is determined to be

$$\Delta T_{\text{interpol}} = 0.2\,\text{mK}\ . \tag{A.18}$$

All contributions are summed up quadratically to a total uncertainty on the absolute temperature measurement at 30 K of

$$\Delta T_{\text{tot old}} = 50.7\,\text{mK}\ , \tag{A.19}$$

$$\Delta T_{\text{tot new}} = 160.0\,\text{mK}\ . \tag{A.20}$$

If the current value is increased to 500 µA, the uncertainty on the PT500 instrumentation is decreased to 82 mK. Then, the total uncertainty reduces to 83 mK. This should be done in future measurements to satisfy the requirements of the final-state distribution.

A.1.2. Uncertainty of Temperature Stability

To calculate the uncertainty of the temperature stability, only two items from the list in table A.1 have to be considered; the uncertainty of the PT500 characteristic curve and its interpolation. These two contributions affect the translation from the resistance R to the temperature T and therefore introduce an uncertainty on the stability. Summing up both quadratically, an uncertainty of

$$\Delta T_{\mathrm{stab}} = 0.4\,\mathrm{mK} \tag{A.21}$$

is obtained. This is independent of the temperature monitoring system. It should be noted that the fluctuations caused by the electronic devices cannot be distinguished from the actual temperature fluctuations, but they are altogether considered by taking the standard deviation over a time range of one hour. However, there is a possibility to estimate the influence of the cabling and electronic devices on the temperature stability value: instead of a defect PT500 sensor, one precision resistance of $10\,\Omega$ is mounted and its measurement value is processed like the ones from the working PT500 sensors. $10\,\Omega$ equals a temperature of about 30 K. Taking the standard deviation over one hour of this resistance gives a measure of the contribution of the electronics to the stability value. At the same time, this is the minimum stability which can be achieved for the PT500 measurements. The precision resistor shows a stability of 2.1 mK per hour in average for the Gantner module-based monitoring system and a stability of 0.4 mK for the former multiplexer-based system.

A.2. Uncertainty of the WGTS Mode at 100 K

Since the capillaries of the vapour pressure bulbs (see figure 6.3) have been mounted to the outer shield of the WGTS, which is on a temperature of 77 K (liquid nitrogen), a calibration of the PT500 sensors in the 100 K mode of the WGTS is not possible. The coupling of the capillaries to the outer shield was necessary to reduce the inhomogeneity along the central beam tube (see section 6.2.3), but on the other hand, the coolant of the 100 K, two-phase argon, would freeze out at this temperature. Thus, the uncertainty on the absolute value is much larger and has different contributions than in the 30 K mode, which is discussed in more detail in the next section A.2.1. The uncertainty on the stability at 100 K is discussed in section A.2.2.

A.2.1. Temperature Trueness

The uncertainty on the non-calibrated measurement of the absolute WGTS temperature with the PT500 sensors at 100 K has been investigated already in the literature [Gro11]. However, these investigations have been done for an operational temperature of 120 K. This thesis gives an updated and more comprehensive uncertainty calculation for 100 K, which has been determined as a more viable operation temperature for the Krypton mode of the WGTS cryostat. All contributions to the total uncertainty on the absolute temperature value are listed in table A.2 and are discussed briefly in the following:

PT500 instrumentation: Like in section A.1.1, the uncertainty of the PT500 instrumentation has to be calculated for two different cases: the temperature monitoring system before 2018, in which the voltage was read out via a multiplexer-based digital multimeter, and for the new system based on Gantner modules for the voltage measurement, which was mounted at the beginning of 2018. The current supply of the PT500 is the same as for the 30 K case, so that for the uncertainty calculation of the current again equation A.2 applies. Since also the current values of 500 µA for the old and 250 µA for the new system are the same as for the 30 K mode, the relative uncertainties calculated in equations A.3 and A.4 can be taken here under the assumption of similar operational temperatures in the cabinets where the devices are mounted.

Table A.2.: Temperature trueness of WGTS PT500 sensors at 100 K. The table shows all uncertainty contributions to the absolute temperature measurement at 100 K with non-calibrated PT500 sensors. The contributions are calculated for the old measurement system (until end of 2017) and for the new one (since beginning of 2018). In both cases, the main contributions to the total uncertainty budget are the PT500 instrumentation, the sensor dispersion and the influence of the magnetic field.

Source of uncertainty	ΔT in mK
PT500 instrumentation (old)	148.9
PT500 instrumentation (new)	266.9
PT500 stability (old)	5.4
PT500 stability (new)	4.9
Sensor dispersion	0
Thermal cycling stability	3.0
Influence of magnetic field	64.0
Installation uncertainty	1.0
PT500 characteristic curve	0.4
Interpolation uncertainty	< 0.1
Combined uncertainty (old)	162.2
Combined uncertainty (new)	274.5

The uncertainty of the voltage measurement is calculated for the old setup according to equation A.5. At 100 K, the PT500 sensors have a resistance of approximately 150 Ω. Thus, the measured voltage of the PT500 sensors increases compared to the 30 K mode for a current of 500 µA to 75 mV. Hence, the relative uncertainty of the voltage becomes

$$\left(\frac{\Delta U}{U}\right)_{\text{old}} = 0.003\,\% \ . \tag{A.22}$$

For the new temperature monitoring system based on Gantner modules, the measurement range stays the same as in the 30 K mode, so that also the uncertainty of $\Delta U = 20\,\mu\text{V}/\sqrt{3}$ has to be applied here. Since the voltage has increased to 37.5 mV for a current of 250 µA, the relative voltage uncertainty decreases to

$$\left(\frac{\Delta U}{U}\right)_{\text{new}} = 0.031\,\% \ . \tag{A.23}$$

Using equation A.1 the relative uncertainties of the voltages and the currents are combined for the relative uncertainty on the temperature. Thus, the uncertainty due to the instrumentation of the PT500 sensors is for 100 K

$$\Delta T_{\text{instr. old}} = 148.9\,\text{mK} \ , \tag{A.24}$$

$$\Delta T_{\text{instr. new}} = 266.9\,\text{mK} \ . \tag{A.25}$$

PT500 stability: The stability of each PT500 sensor of the central beam tube has to be taken into account as uncertainty contribution. It is calculated as the standard deviation of the temperature over a time interval of one hour. Here, an averaged value is taken for the calculation of the total uncertainty budget, but it should be emphasised again that this contribution is normally sensor- and time-dependent. According to

the findings in section 6.2.3, the relative stability of the central beam tube values is better than $\Delta T/T = 5.4 \times 10^{-5}$ (see equation 6.16), so that an uncertainty of

$$\Delta T_{\text{stab. old}} = 5.4\,\text{mK} \tag{A.26}$$

on the absolute temperature value at 100 K for the multiplexer-based monitoring system is obtained. For the newly installed Gantner module system, a stability of

$$\Delta T_{\text{stab. new}} = 4.9\,\text{mK} \tag{A.27}$$

was measured in a measurement period of five days in January 2018.

Sensor dispersion: The PT500 sensors in use have slightly different lengths of their platinum wires. This means that also their characteristic curves differ slightly from each other. Besides the length, also mechanical stress or contaminations can have an influence on the characteristic curve of one single sensor. If now only one averaged characteristic curve was applied, an uncertainty which is called sensor dispersion would be introduced. Based on the data presented in [Gro11], the sensor dispersion is estimated for 100 K to be

$$\Delta T_{\text{sens. disp.}} = \frac{0.5\,\text{K}}{\sqrt{3}} = 288.7\,\text{mK}\ . \tag{A.28}$$

Since the values of the wire lengths are known, the sensor dispersion is corrected in the temperature monitoring and acquisition software. Thus, no uncertainty contribution remains.

Thermal cycling stability: In [Gro11], the PT500 sensors underwent a thermal cycle of five different temperatures: 273 K → 550 K → 77 K → 300 K → 273 K. It is demonstrated that the sensors do not reach the original resistance at 273 K after going through one such full cycle and an uncertainty on the non-calibrated sensor at 120 K of

$$\Delta T_{\text{thermal}} = 3\,\text{mK} \tag{A.29}$$

is assigned. The actual thermal cycles of the WGTS look a bit different: there are only three temperature levels, at which the sensors are operated, which are room temperature (during maintenance phases), 100 K (^{83m}Kr mode) and 30 K (tritium operation). A bake-out at 550 K is not possible due to technical reasons. However, the influence of temperature changes from 30 K to room temperature on the sensor performance cannot be investigated since all sensors are mounted and a direct comparison to a water triple point cell like in [Gro11] is no longer possible. For this reason, the value stated in equation A.29 is used further on. On the one hand, the maximum temperature difference in WGTS operation is smaller than the one applied in the thermal cycle in [Gro11], so that a smaller uncertainty is expected, but on the other hand, in the meantime several times the WGTS has be ramped up and down, so that a larger uncertainty can be assumed. In sum, the value in equation A.29 is the best estimation available.

Influence of magnetic field: The magnetic field influences the motion of the electrons inside the platinum wire of the PT500 sensors. Depending on the orientation of the sensors to the magnetic field lines, the measured resistance of the PT500 is gradually impeded. This effect was also investigated in [Gro11]. A magnetic field of 3.6 T at a temperature of 120 K leads to a shift of the temperature by 0.21 K with an uncertainty of 0.064 K. The shift can be corrected in the temperature monitoring and controlling software automatically. Based on [Gro11], the temperature shift can also be calculated for 100 K and for 2.52 T (the operational magnetic field value, 70 % of

the design value). It is the same as for 120 K and 3.6 T, so that the value from [Gro11] is still correct:

$$\Delta T_{\text{mag. field}} = 64\,\text{mK} \ . \tag{A.30}$$

Installation uncertainty: If the sensors heat up due to the current they carry or lose/gain heat due to conductive heat leaks; both effects have to be taken into account in the uncertainty budget. However, careful investigations in [Gro11] have shown that the installation uncertainties are small:

$$\Delta T_{\text{install}} = 1\,\text{mK} \ . \tag{A.31}$$

PT500 characteristic curve: For the determination of the uncertainty of the PT500 characteristic curve, in situ measurements were performed at 30 K (see section A.1.1). However, this is not possible at 100 K, since the PT500 sensors cannot be calibrated with the vapour pressure bulbs. There are no reasons to assume that the uncertainty at 100 K should be much larger than at 30 K, so that the same value is adopted here:

$$\Delta T_{\text{PT500curve}} = 0.4\,\text{mK} \ . \tag{A.32}$$

Interpolation uncertainty: The interpolation uncertainty is calculated for the temperature range of 98 to 102 K based on the equations presented in [Mar17a]. At temperatures around 100 K, the characteristic curve behaves more like a straight line, so that the uncertainty contribution of the linear interpolation decreases in comparison to 30 K to

$$\Delta T_{\text{interpol}} < 0.1\,\text{mK} \ . \tag{A.33}$$

All contributions are summed up quadratically to a total uncertainty on the absolute temperature measurement at 100 K of

$$\Delta T_{\text{tot old}} = 162.2\,\text{mK} \ , \tag{A.34}$$

$$\Delta T_{\text{tot new}} = 274.5\,\text{mK} \ . \tag{A.35}$$

If the PT500 sensors are in the new measurement system also supplied with 500 µA instead of 250 µA, the uncertainty on the instrumentation decreases to 150 mK, so that the total uncertainty is of nearly the same value as it was in the old, multiplexer-based system.

A.2.2. Uncertainty of Temperature Stability

For the uncertainty on the temperature stability, not all of the uncertainties listed in table A.2 have to be taken into account. Only those, which affect the translation from the measured resistance into the temperature are of interest, while the absolute temperature value and its uncertainty is not needed. Thus, only the uncertainties on the PT500 characteristic curve and its interpolation have to be taken into account. If they are summed up quadratically, a total uncertainty on the temperature stability at 100 K of

$$\Delta T_{\text{stab}} = 0.4\,\text{mK} \tag{A.36}$$

is obtained. Only the uncertainty of the PT500 curve itself contributes here. The value is independent of the monitoring system (multiplexer-based vs. Gantner modules). Like for the 30 K case (see section A.1.2), the influence of fluctuations of the electronic devices are part of the calculated stability value. However, there is also a precision resistance of 150 Ω mounted instead of one broken PT500 sensor, so that the influence of the electronics can be estimated based on the stability per hour of this resistance. The precision resistance shows a stability of 0.8 mK per hour for the Gantner module-based temperature monitoring system and a stability of 0.4 mK for the former multiplexer-based system. Both values are the smallest stability values which can be achieved in the measurements.

Table A.3.: Uncertainty of stability of WGTS DPS1-R/F PT1000 sensors. The table lists the uncertainty contributions for the stability analysis of the PT1000 sensors in the DPS1-R/F sections of the WGTS. There are only two contributions, from which the uncertainty on the PT1000 characteristic curve is by far the largest. The interpolation uncertainty is given for the two operating temperatures of 30 and 100 K.

Source of uncertainty	ΔT in mK
PT1000 characteristic curve	0.4
Interpolation uncertainty (30 K)	0.1
Interpolation uncertainty (100 K)	< 0.1
Combined uncertainty (30 K)	0.4
Combined uncertainty (100 K)	0.4

A.3. Uncertainty of Temperature Stability in DPS1-R/F

In contrast to the central beam tube, which is equipped with PT500 sensors, PT1000 sensors are mounted in the DPS1-R/F. For KATRIN operation and neutrino mass analysis, only their stability but not their absolute value is of interest. Therefore, only uncertainties connected to the characteristic curve have to be taken into account according to the discussions in the previous sections A.1.2 and A.2.2. These are the uncertainty on the characteristic curve itself and the uncertainty that is introduced due to the linear interpolation between the points of the characteristic curve. The uncertainties are listed for both temperature ranges of 28 to 32 K and for 98 to 100 K in table A.3. The total are obtained as

$$\Delta T_{\text{stab. } 30\,\text{K}} = 0.4\,\text{mK} \ , \tag{A.37}$$

$$\Delta T_{\text{stab. } 100\,\text{K}} = 0.4\,\text{mK} \ . \tag{A.38}$$

Bibliography

[Aar15] Aartsen, M. G. et al. (2015). Determining neutrino oscillation parameters from atmospheric muon neutrino disappearance with three years of IceCube DeepCore data. *Phys. Rev. D* **91**(7): 072004. DOI: 10.1103/PhysRevD.91.072004.

[Abd09] Abdurashitov, J. N. et al. (2009). Measurement of the solar neutrino capture rate with gallium metal. III. Results for the 2002-2007 data-taking period. *Phys. Rev. C* **80**(1): 015807. DOI: 10.1103/PhysRevC.80.015807.

[Abd17] Abdurashitov, D. N. et al. (2017). Electron Scattering on Hydrogen and Deuterium Molecules at 14-15 keV by the "Troitsk nu-Mass" Experiment. *Phys. Part. Nucl. Lett.* **14**(6): 892–899. DOI: 10.1134/S1547477117060024.

[Abe08] Abe, S. et al. (2008). Precision Measurement of Neutrino Oscillation Parameters with KamLAND. *Phys. Rev. Lett.* **100**(22): 259901. DOI: 10.1103/PhysRevLett.100.221803.

[Abe16a] Abe, K. et al. (2016a). Real-time supernova neutrino burst monitor at Super-Kamiokande. *Astropart. Phys.* **81**: 39–48. DOI: 10.1016/j.astropartphys.2016.04.003.

[Abe16b] Abe, K. et al. (2016b). Solar neutrino measurements in Super-Kamiokande-IV. *Phys. Rev. D* **94**(5): 052010. DOI: 10.1103/PhysRevD.94.052010.

[Abe16c] Abe, Y. et al. (2016c). Measurement of Θ_{13} in Double Chooz using neutron captures on hydrogen with novel background rejection techniques. *J. High Energy Phys.* **2016**: 163. DOI: 10.1007/JHEP01(2016)163.

[Abe17] Abe, K. et al. (2017). Measurement of neutrino and antineutrino oscillations by the T2K experiment including a new additional sample of ν_e interactions at the far detector. *Phys. Rev. D* **96**(9): 092006. DOI: 10.1103/PhysRevD.96.092006.

[Abe18] Abe, K. et al. (2018). Search for CP Violation in Neutrino and Antineutrino Oscillations by the T2K Experiment with 2.2×10^{21} Protons on Target. *Phys. Rev. Lett.* **121**(17): 171802. DOI: 10.1103/PhysRevLett.121.171802.

[Abo18] Abolfathi, B. et al. (2018). The Fourteenth Data Release of the Sloan Digital Sky Survey: First Spectroscopic Data from the Extended Baryon Oscillation Spectroscopic Survey and from the Second Phase of the Apache Point Observatory Galactic Evolution Experiment. *Astrophys. J. Suppl. Ser.* **235**(2). DOI: 10.3847/1538-4365/aa9e8a.

[Acc16a] Acciarri, R. et al. (2016a). Long-Baseline Neutrino Facility (LBNF) and Deep Underground Neutrino Experiment (DUNE) Conceptual Design Report Volume 1: The LBNF and DUNE Projects. *arXiv pre-print*: 1601.05471. URL: https://arxiv.org/abs/1601.05471.

[Acc16b] Acciarri, R. et al. (2016b). Long-Baseline Neutrino Facility (LBNF) and Deep Underground Neutrino Experiment (DUNE) Conceptual Design Report Volume 2: The Physics Program for DUNE at LBNF. *arXiv pre-print*: 1512.06148. URL: https://arxiv.org/abs/1512.06148.

[Acc98] Acciarri, M. et al. (1998). Determination of the number of light neutrino species from single photon production at LEP. *Phys. Lett. B* **431**(1-2): 199–208. DOI: 10.1016/S0370-2693(98)00519-X.

[Ace18] Acero, M. A. et al. (2018). New constraints on oscillation parameters from ν_e appearance and ν_μ disappearance in the NOvA experiment. *Phys. Rev. D* **98**(3): 032012. DOI: 10.1103/PhysRevD.98.032012.

[Ada16] Adam, R. et al. (2016). Planck 2015 results - I. Overview of products AND scientific results. *Astron. Astrophys.* **594**: A1. DOI: 10.1051/0004-6361/201527101.

[Ada17a] Adamson, P. et al. (2017a). Constraints on Oscillation Parameters from ν_e Appearance and ν_μ Disappearance in NOvA. *Phys. Rev. Lett.* **118**(23): 231801. DOI: 10.1103/PhysRevLett.118.231801.

[Ada17b] Adamson, P. et al. (2017b). Measurement of the Neutrino Mixing Angle θ_{23} in NOvA. *Phys. Rev. Lett.* **118**(15): 151802. DOI: 10.1103/PhysRevLett.118.151802.

[Ade16] Ade, P. A. R. et al. (2016). Planck 2015 results - XIII. Cosmological parameters. *Astron. Astrophys.* **594**: A13. DOI: 10.1051/0004-6361/201525830.

[Adh17] Adhikari, R. et al. (2017). A White Paper on keV sterile neutrino Dark Matter. *J. Cosmol. Astropart. Phys.* **2017**(01): 025. DOI: 10.1088/1475-7516/2017/01/025.

[Agh18] Aghanim, N. et al. (2018). Planck 2018 results. VI. Cosmological parameters. *arxiv pre-print*: 1807.06209. URL: https://arxiv.org/abs/1807.06209.

[Ago18] Agostini, M. et al. (2018). Improved Limit on Neutrinoless Double-β Decay of ^{76}Ge from GERDA Phase II. *Phys. Rev. Lett.* **120**(13): 132503. DOI: 10.1103/PhysRevLett.120.132503.

[Agu10] Aguilar-Arevalo, A. A. et al. (2010). Event Excess in the MiniBooNE Search for $\bar{\nu}_\mu \to \bar{\nu}_e$ Oscillations. *Phys. Rev. Lett.* **105**(18): 181801. DOI: 10.1103/PhysRevLett.105.181801.

[Aha13] Aharmim, B. et al. (2013). Combined analysis of all three phases of solar neutrino data from the Sudbury Neutrino Observatory. *Phys. Rev. C* **88**(2): 025501. DOI: 10.1103/PhysRevC.88.025501.

[Ahm01] Ahmad, Q. R. et al. (2001). Measurement of the Rate of $\nu_e + d \to p + p + e^-$ Interactions Produced by ^8B Solar Neutrinos at the Sudbury Neutrino Observatory. *Phys. Rev. Lett.* **87**(7): 071301. DOI: 10.1103/PhysRevLett.87.071301.

[Ald18] Alduino, C. et al. (2018). First Results from CUORE: A Search for Lepton Number Violation via $0\nu\beta\beta$ Decay of ^{130}Te. *Phys. Rev. Lett.* **120**(13): 132501. DOI: 10.1103/PhysRevLett.120.132501.

[Ali01] Alitalo, S. et al. (2001). The valence photoelectron satellite spectra of Kr and Xe. *J. Electron Spectrosc. Relat. Phenom.* **114-116**: 141–146. DOI: 10.1016/S0368-2048(00)00277-2.

[Alt05] Altmann, M. et al. (2005). Complete results for five years of GNO solar neutrino observations. *Phys. Lett. B* **616**(3-4): 174–190. DOI: 10.1016/j.physletb.2005.04.068.

[Alt18] Altenmüller, K. et al. (2018). Silicon drift detector prototypes for the keV-scale sterile neutrino search with TRISTAN. *Nucl. Instrum. Methods Phys. Res., Sect. A (in press)*. DOI: 10.1016/j.nima.2017.12.026.

[Ams15] Amsbaugh, J. et al. (2015). Focal-plane detector system for the KATRIN experiment. *Nucl. Instrum. Methods Phys. Res. A* **778**: 40–60. DOI: 10.1016/j.nima.2014.12.116.

[An16a] An, F. P. et al. (2016a). New measurement of Θ_{13} via neutron capture on hydrogen at Daya Bay. *Phys. Rev. D* **93**(7): 072011. DOI: 10.1103/PhysRevD.93.072011.

[An16b] An, F. et al. (2016b). Neutrino physics with JUNO. *J. Phys. G* **43**(3): 030401. DOI: 10.1088/0954-3899/43/3/030401.

[An17] An, F. P. et al. (2017). Measurement of electron antineutrino oscillation based on 1230 days of operation of the Daya Bay experiment. *Phys. Rev. D* **95**(7): 072006. DOI: 10.1103/PhysRevD.95.072006.

[Ang05] Angrik, J. et al. (2005). KATRIN Design Report 2004. *Wissenschaftliche Berichte Forschungszentrum Karlsruhe* **7090**.

[Arc18] Arcadi, G. et al. (2018). Tritium beta decay with additional emission of new light bosons. *arxiv pre-print*: 1811.03530. URL: https://arxiv.org/abs/1811.03530.

[Are16] Arenz, M. et al. (2016). Commissioning of the vacuum system of the KATRIN Main Spectrometer. *J. Instrum.* **11**: P04011. DOI: 10.1088/1748-0221/11/04/P04011.

[Are17] Arenz, M. (2017). *Production and PAC studies of ^{83}Rb/^{83m}Kr solid state calibration sources for the KATRIN experiment*. PhD thesis. Rheinische Friedrich-Wilhelms-Universität Bonn. URL: http://hss.ulb.uni-bonn.de/2017/4930/4930.htm.

[Are18a] Arenz, M. et al. (2018a). Calibration of high voltages at the ppm level by the difference of ^{83m}Kr conversion electron lines at the KATRIN experiment. *Eur. Phys. J. C* **78**: 368. DOI: 10.1140/epjc/s10052-018-5832-y.

[Are18b] Arenz, M. et al. (2018b). First transmission of electrons and ions through the KATRIN beamline. *J. Instrum.* **13**(04): P04020. DOI: 10.1088/1748-0221/13/04/P04020.

[Are18c] Arenz, M. et al. (2018c). The KATRIN superconducting magnets: overview and first performance results. *J. Instrum.* **13**(08): T08005. DOI: 10.1088/1748-0221/13/08/T08005.

[Ase00] Aseev, V. et al. (2000). Energy loss of 18 keV electrons in gaseous T_2 and quench condensed D_2 films. *Eur. Phys. J. D* **10**: 39–52. DOI: 10.1007/s100530050525.

[Ase11] Aseev, V. N. et al. (2011). Upper limit on the electron antineutrino mass from the Troitsk experiment. *Phys. Rev. D* **84**(11): 112003. DOI: 10.1103/PhysRevD.84.112003.

[Ash17] Ashtari Esfahani, A. et al. (2017). Determining the neutrino mass with cyclotron radiation emission spectroscopy - Project 8. *J. Phys. G: Nucl. Phys.* **44**(5). DOI: 10.1088/1361-6471/aa5b4f.

[Asn15] Asner, D. M. et al. (2015). Single-Electron Detection and Spectroscopy via Relativistic Cyclotron Radiation. *Phys. Rev. Lett.* **114**(16): 162501. DOI: 10.1103/PhysRevLett.114.162501.

[Bab12] Babutzka, M. et al. (2012). Monitoring of the operating parameters of the KATRIN Windowless Gaseous Tritium Source. *New J. Phys.* **14**(103046). DOI: 10.1088/1367-2630/14/10/103046.

[Bab14] Babutzka, M. (2014). *Design and development for the Rearsection of the KATRIN experiment*. PhD thesis. Karlsruhe Institute of Technology. URL: https://publikationen.bibliothek.kit.edu/1000045598.

[Bah01] Bahcall, J. N., Pinsonneault, M. H., and Basu, S. (2001). Solar models: current epoch and time dependences, neutrinos, and helioseismological properties. *Astrophys. J.* **555**(2): 990–1012. DOI: 10.1086/321493.

[Bar14] Barry, J., Heeck, J., and Rodejohann, W. (2014). Sterile neutrinos and right-handed currents in KATRIN. *J. High Energy Phys.* **2014**: 081. DOI: 10.1007/JHEP07(2014)081.

[Bar16a] Barinov, V. et al. (2016). BEST sensitivity to O(1) eV sterile neutrino. *Phys. Rev. D* **93**(7): 073002. DOI: 10.1103/PhysRevD.93.073002.

[Bar16b] Barrett, J. P. (2016). *A Spatially Resolved Study of the KATRIN Main Spectrometer Using a Novel Fast Multipole Method*. PhD thesis. Massachusetts Institute of Technology. URL: https://dspace.mit.edu/handle/1721.1/114314.

[Bau13a] Bauer, S. (2013). *Energy calibration and stability monitoring of the KATRIN experiment*. PhD thesis. Westfälische Wilhelms-Universität Münster. URL: https://miami.uni-muenster.de/Record/da3d6759-9202-4b68-bb80-711f52b208d8.

[Bau13b] Bauer, S. et al. (2013). Next generation KATRIN high precision voltage divider for voltages up to 65kV. *J. Instrum.* **8**: P10026. DOI: 10.1088/1748-0221/8/10/P10026.

[Bea80] Beamson, G., Porter, H. Q., and Turner, D. W. (1980). The collimating and magnifying properties of a superconducting field photoelectron spectrometer. *J. Phys. E: Sci. Instrum.* **13**(1): 64–66. DOI: 10.1088/0022-3735/13/1/018.

[Bec96] Becquerel, H. (1896). Sur les radiations invisible émises par les corps phosphorescents. *Comptes Rendus* **122**: 501–503.

[Beh17a] Behrens, J. (2017). *Design and commissioning of a mono-energetic photoelectron source and active background reduction by magnetic pulse at the KATRIN experiment*. PhD thesis. Westfälische Wilhelms-Universität Münster. URL: https://www.katrin.kit.edu/publikationen/phd_behrens.pdf.

[Beh17b] Behrens, J. et al. (2017). A pulsed, mono-energetic and angular-selective UV photo-electron source for the commissioning of the KATRIN experiment. *Eur. Phys. J. C* **77**: 410. DOI: 10.1140/epjc/s10052-017-4972-9.

[Bel08] Belesev, A. I. et al. (2008). Investigation of Space-Charge Effects in Gaseous Tritium as a Source of Distortions of the Beta Spectrum Observed in the

Troitsk Neutrino-Mass Experiment. *Phys. At. Nucl.* **71**(3). DOI: 10.1134/S1063778808030046.

[Bel11] Bellini, G. et al. (2011). Precision Measurement of the ^{7}Be Solar Neutrino Interaction Rate in Borexino. *Phys. Rev. Lett.* **107**(14): 141302. DOI: 10.1103/PhysRevLett.107.141302.

[Ber71] Bergkvist, K.-E. (1971). On Some Atomic Effects in the Tritium β-Spectrum. *Phys. Scr.* **4**(23). DOI: 10.1088/0031-8949/4/1-2/004.

[Bet34] Bethe, H. and Peierls, R. (1934). The "Neutrino". *Nature* **133**: 532. DOI: 10.1038/133532a0.

[Bet38] Bethe, H. A. and Critchfield, C. L. (1938). The Formation of Deuterons by Proton Combination. *Phys. Rev.* **54**(4): 248. DOI: 10.1103/PhysRev.54.248.

[Bil10] Bilenky, S. (2010). *Introduction to the Physics of Massive and Mixed Neutrinos.* Lect. Notes Phys. 817. Springer, Berlin, Heidelberg. DOI: 10.1007/978-3-642-14043-3.

[Blo18] Block, F. (2018). *Characterisation of the Background in the KATRIN Experiment.* MA thesis. Karlsruhe Institute of Technology. URL: http://www.katrin.kit.edu/publikationen/mth_fblock.pdf.

[Bod11] Bode, T. (2011). *Experimentelle Untersuchung der thermischen Eigenschaften der KATRIN-Tritiumquelle am WGTS-Demonstrator.* Diploma thesis. Karlsruhe Institute of Technology.

[Bod15] Bodine, L. I., Parno, D. S., and Robertson, R. G. H. (2015). Assessment of molecular effects on neutrino mass measurements from tritium β decay. *Phys. Rev. C* **91**(035505). DOI: 10.1103/PhysRevC.91.035505.

[Boh32] Bohr, N. (1932). Faraday lecture. Chemistry and the quantum theory of atomic constitution. Delivered on May 8th, 1930. *J. Chem. Soc.* **0**: 349–384. DOI: 10.1039/JR9320000349.

[Bon11] Bonn, J. et al. (2011). The KATRIN sensitivity to the neutrino mass and to right-handed currents in beta decay. *Phys. Lett. B* **703**(3): 310–312. DOI: 10.1016/j.physletb.2011.08.005.

[Bon99] Bonn, J. et al. (1999). A high resolution electrostatic time-of-flight spectrometer with adiabatic magnetic collimation. *Nucl. Instrum. Methods Phys. Res.* **421**(1-2): 256–265. DOI: 10.1016/S0168-9002(98)01263-7.

[Bor11] Bornschein, B. (2011). Between Fusion and Cosmology - The Future of the Tritium Laboratory Karlsruhe. *Fusion Sci. Technol.* **60**(3): 1088–1091. DOI: 10.13182/FST11-A12604.

[Bra04] Bragg, W. H. (1904). On the absorption of α rays, and on the classification of the α rays from radium. *Philos. Mag.* **8**(48). DOI: 10.1080/14786440409463245.

[Cal06] Caló, A. et al. (2006). The Kr valence photoelectron satellite lines in the photon energy region below the 3d threshold. *J. Phys. B: At., Mol. Opt. Phys.* **39**(20): 4169–4177. DOI: 10.1088/0953-4075/39/20/015.

[Car73] Carlson, T. A. and Nestor, C. W. (1973). Calculation of Electron Shake-Off Probabilities as the Result of X-Ray Photoionization of the Rare Gases. *Phys. Rev. A* **8**(6): 2887. DOI: 10.1103/PhysRevA.8.2887.

[Cha14] Chadwick, J. (1914). Intensitätsverteilung im magnetischen Spectrum der β-Strahlen von Radium B + C. *Verhandl. Dtsc. Phys. Ges.* **16**: 383.

[Cha71] Chang, C. C. (1971). Auger Electron Spectroscopy. *Surf. Sci.* **25**(1): 53–79. DOI: 10.1016/0039-6028(71)90210-X.

[Chi10] Chilingaryan, S. et al. (2010). Advanced data extraction infrastructure: Web based system for management of time series data. *J. Phys. Conf. Ser.* **219**(4): 042034. DOI: 10.1088/1742-6596/219/4/042034.

[Cho16] Choi, J. H. et al. (2016). Observation of Energy and Baseline Dependent Reactor Antineutrino Disappearance in the RENO Experiment. *Phys. Rev. Lett.* **116**(21): 211801. DOI: 10.1103/PhysRevLett.116.211801.

[Chr64] Christenson, J. H. et al. (1964). Evidence for the 2π decay of the K_2^0 meson. *Phys. Rev. Lett.* **13**(4): 138. DOI: 10.1103/PhysRevLett.13.138.

[Cle98] Cleveland, B. T. et al. (1998). Measurement of the Solar Electron Neutrino Flux with the Homestake Chlorine Detector. *Astrophys. J.* **496**(1): 505–526. DOI: 10.1086/305343.

[Cor14] Corona, T. (2014). *Methodology and application of high performance electrostatic field simulation in the KATRIN experiment*. PhD thesis. University of North Carolina at Chapel Hill. URL: https://cdr.lib.unc.edu/record/uuid:6f44a9c2-f053-404a-b726-b960d5772619.

[Cow56] Cowan, C. L. et al. (1956). Detection of the Free Neutrino: a Confirmation. *Science* **124**(3212). DOI: 10.1126/science.124.3212.103.

[Cra57] Crawford, F. S. et al. (1957). Detection of Parity Nonconservation in Λ Decay. *Phys. Rev.* **108**(4): 1102. DOI: 10.1103/PhysRev.108.1102.

[Cue16] Cuesta, A. J., Niro, V., and Verde, L. (2016). Neutrino mass limits: Robust information from the power spectrum of galaxy surveys. *Phys. Dark Universe* **13**: 77–86. DOI: 10.1016/j.dark.2016.04.005.

[Dan62] Danby, G. et al. (1962). Observation of High-Energy Neutrino Reactions and the Existence of Two Kinds of Neutrinos. *Phys. Rev. Lett.* **9**(36). DOI: 10.1103/PhysRevLett.9.36.

[Dav68] Davis, R., Harmer, D. S., and Hoffman, K. C. (1968). Search for Neutrinos from the Sun. *Phys. Rev. Lett.* **20**(21): 1205–1209. DOI: 10.1103/PhysRevLett.20.1205.

[De 82] De Rújula, A. and Lusignoli, M. (1982). Calorimetric measurements of ^{163}Holmium decay as tools to determine the electron neutrino mass. *Phys. Lett. B* **118**(4-6): 429–434. DOI: 10.1016/0370-2693(82)90218-0.

[Dec90a] Decamp, D. et al. (1990). A precise determination of the number of families with light neutrinos and of the Z boson partial widths. *Phys. Lett. B* **235**(3-4): 399–411. DOI: 10.1016/0370-2693(90)91984-J.

[Dec90b] Decman, D. J. and Stoeffl, W. (1990). Atomic Electron Binding Energies of Multiply Charged Krypton Ions by Internal-Conversion-Electron Spectroscopy. *Phys. Rev. Lett.* **64**(23). DOI: 10.1103/PhysRevLett.64.2767.

[Def17] Deffert, M. (2017). *Simulation of the global beamline alignment of the KATRIN experiment*. MA thesis. Karlsruhe Institute of Technology. URL: http://www.katrin.kit.edu/publikationen/mth_Marco_Deffert.pdf.

[Den17] Dentler, M. et al. (2017). Sterile neutrinos or flux uncertainties? - Status of the reactor anti-neutrino anomaly. *J. High Energy Phys.* **2017**: 099. DOI: 10.1007/JHEP11(2017)099.

[Di 16] Di Valentino, E. et al. (2016). Cosmological limits on neutrino unknowns versus low redshift priors. *Phys. Rev. D* **93**(8): 083527. DOI: 10.1103/PhysRevD.93.083527.

[Dos06] Doss, N. et al. (2006). Molecular effects in investigations of tritium molecule β decay endpoint experiments. *Phys. Rev. C* **73**(2): 025502. DOI: 10.1103/PhysRevC.73.025502.

[Dos07] Doss, N. (2007). *Calculated final state probability distributions for T_2 β-decay measurements.* PhD thesis. University College London.

[Due11] Duerr, M., Lindner, M., and Merle, A. (2011). On the quantitative impact of the Schechter-Valle theorem. *J. High Energy Phys.* **2011**: 91. DOI: 10.1007/JHEP06(2011)091.

[Dyb19] Dyba, S. (2019). *PhD thesis in preparation.* PhD thesis. Westfälische Wilhelms-Universität Münster.

[Eic08] Eichelhardt, F. et al. (2008). First Tritium Results of the KATRIN Test Experiment Trap. *Fusion Sci. Technol.* **54**(2): 615–618. DOI: 10.13182/FST08-A1890.

[Ell17] Ellinger, E. et al. (2017). Monitoring the KATRIN source properties within the beamline. *J. Phys. Conf. Ser.* **888**(1): 012229. DOI: 10.1088/1742-6596/888/1/012229.

[Ell27] Ellis, C. D. and Wooster, W. A. (1927). The Average Energy of Disintegration of Radium E. *Proc. Roy. Soc. London* **A117**(776). DOI: 10.1098/rspa.1927.0168.

[Eng17] Engel, J. and Menéndez, J. (2017). Status and future of nuclear matrix elements for neutrinoless double-beta decay: a review. *Rep. Prog. Phys.* **80**(4). DOI: 10.1088/1361-6633/aa5bc5.

[Eng64] Englert, F. and Brout, R. (1964). Broken Symmetry and the Mass of Gauge Vector Mesons. *Phys. Rev. Lett.* **13**(9): 321. DOI: 10.1103/PhysRevLett.13.321.

[Erh14] Erhard, M. et al. (2014). High-voltage monitoring with a solenoid retarding spectrometer at the KATRIN experiment. *J. Instrum.* **9**: P06022. DOI: 10.1088/1748-0221/9/06/P06022.

[Erh16] Erhard, M. (2016). *Influence of the magnetic field on the transmission characteristics and the neutrino mass systematic of the KATRIN experiment.* PhD thesis. Karlsruhe Institute of Technology. URL: https://publikationen.bibliothek.kit.edu/1000065003.

[Erh18] Erhard, M. et al. (2018). Technical design and commissioning of the KATRIN large-volume air coil system. *J. Instrum.* **13**: P02003. DOI: 10.1088/1748-0221/13/02/P02003.

[Eri87] Eriksson, B. et al. (1987). The high energy excited shake-up electron spectra of krypton. *J. Phys. Colloques* **48**(C9): 531–534. DOI: 10.1051/jphyscol:1987987.

[Esm12] Esmaili, A. and Peres, O. L. G. (2012). KATRIN sensitivity to sterile neutrino mass in the shadow of lightest neutrino mass. *Phys. Rev. D* **85**(11): 117301. DOI: 10.1103/PhysRevD.85.117301.

[Est17] Esteban, I. et al. (2017). Updated fit to three neutrino mixing: exploring the accelerator-reactor complementary. *J. High Energy Phys.* **2017**: 087. DOI: 10.1007/JHEP01(2017)087.

[Fer34] Fermi, E. (1934). Versuch einer Theorie der β-Strahlen. *Z. Phys.* **88**(3-4). DOI: 10.1007/BF01351864.

[Fis11] Fischer, S. et al. (2011). Monitoring of Tritium Purity During Long-Term Circulation in the KATRIN Test Experiment LOOPINO Using Laser Raman Spectroscopy. *Fusion Sci. Technol.* **60**(3): 925–930. DOI: 10.13182/FST11-A12567.

[Fis14] Fischer, S. (2014). *Commissioning of the KATRIN Raman system and durability studies of optical coatings in glove box and tritium atmospheres.* PhD thesis. Karlsruhe Institute of Technology. URL: https://publikationen.bibliothek.kit.edu/1000043697.

[Fog02] Fogli, G. L. et al. (2002). Getting the most from the statistical analysis of solar neutrino oscillations. *Phys. Rev. D* **66**(5): 053010. DOI: 10.1103/PhysRevD.66.053010.

[For11] Formaggio, J. A. and Barrett, J. (2011). Resolving the reactor neutrino anomaly with the KATRIN neutrino experiment. *Phys. Lett. B* **706**(1): 68–71. DOI: 10.1016/j.physletb.2011.10.069.

[För17] Förstner, E. (2017). *Optimization of the KATRIN rear wall for a keV-scale sterile neutrino search.* BA thesis. Karlsruhe Institute of Technology.

[Frä10] Fränkle, F. (2010). *Background Investigations of the KATRIN Pre-Spectrometer.* PhD thesis. Karlsruhe Institute of Technology. URL: https://publikationen.bibliothek.kit.edu/1000019392.

[Frä11] Fränkle, F. et al. (2011). Radon induced background processes in the KATRIN pre-spectrometer. *Astropart. Phys.* **35**(3): 128–134. DOI: 10.1016/j.astropartphys.2011.06.009.

[Frä14] Fränkle, F. et al. (2014). Penning discharge in the KATRIN pre-spectrometer. *J. Instrum.* **9**: P07028. DOI: 10.1088/1748-0221/9/07/P07028.

[Frä17] Fränkle, F. (2017). Background processes in the KATRIN main spectrometer. *J. Phys. Conf. Ser.* **888**(1): 012070. DOI: 10.1088/1742-6596/888/1/012070.

[Fuk98] Fukuda, Y. et al. (1998). Evidence for Oscillation of Atmospheric Neutrinos. *Phys. Rev. Lett.* **81**(8): 1562. DOI: 10.1103/PhysRevLett.81.1562.

[Fur15] Furse, D. L. (2015). *Techniques for Direct Neutrino Mass Measurement Utilizing Tritium β-Decay.* PhD thesis. Massachusetts Institute of Technology. URL: https://dspace.mit.edu/handle/1721.1/99313.

[Fur17] Furse, D. et al. (2017). Kassiopeia: a modern, extensible C++ particle tracking package. *New J. Phys.* **19**: 053012. DOI: 10.1088/1367-2630/aa6950.

[Fur39] Furry, W. H. (1939). On Transition Probabilities in Double Beta-Disintegration. *Phys. Rev.* **56**(12): 1184. DOI: 10.1103/PhysRev.56.1184.

[Gan13] Gando, A. et al. (2013). Reactor on-off antineutrino measurement with KamLAND. *Phys. Rev. D* **88**(3): 033001. DOI: 10.1103/PhysRevD.88.033001.

[Gan16] Gando, A. et al. (2016). Search for Majorana Neutrinos Near the Inverted Mass Hierarchy Region with KamLAND-Zen. *Phys. Rev. Lett.* **117**(8): 082503. DOI: 10.1103/PhysRevLett.117.082503.

[Gar16] Gariazzo, S. et al. (2016). Light sterile neutrinos. *J. Phys. G: Nucl. Part. Phys.* **43**(3): 033001. DOI: 10.1088/0954-3899/43/3/033001.

[Gar57] Garwin, R. L., Lederman, L. M., and Weinrich, M. (1957). Observations of the Failure of Conservation of Parity and Charge Conjugation in Meson Decays: the Magnetic Moment of the Free Muon. *Phys. Rev.* **105**(4): 1415. DOI: 10.1103/PhysRev.105.1415.

[Gas17] Gastaldo, L. et al. (2017). The electron capture in ^{163}Ho experiment - ECHo. *Eur. Phys. J. Spec. Top.* **226**(8): 1623–1694. DOI: 10.1140/epjst/e2017-70071-y.

[Gav15] Gavrin, V. et al. (2015). Current status of new SAGE project with ^{51}Cr neutrino source. *Phys. Part. Nucl.* **46**(2): 131–137. DOI: 10.1134/S1063779615020100.

[Ger17] Gershon, T. and Gligorov, V. V. (2017). *CP* violation in the *B* system. *Rep. Prog. Phys.* **80**(4): 046201. DOI: 10.1088/1361-6633/aa5514.

[Gia17] Giachero, A. et al. (2017). Measuring the electron neutrino mass with improved sensitivity: the HOLMES experiment. *J. Instrum.* **12**: C02046. DOI: 10.1088/1748-0221/12/02/C02046.

[Gil10] Gil, W. et al. (2010). The Cryogenic Pumping Section of the KATRIN Experiment. *IEEE Trans. Appl. Supercond.* **20**(3): 316–319. DOI: 10.1109/TASC.2009.2038581.

[Giu11] Giunti, C. and Laveder, M. (2011). Statistical significance of the gallium anomaly. *Phys. Rev. C* **83**(6): 065504. DOI: 10.1103/PhysRevC.83.065504.

[Gla61] Glashow, S. L. (1961). Partial-symmetries of weak interactions. *Nucl. Phys.* **22**(4): 579–588. DOI: 10.1016/0029-5582(61)90469-2.

[Glü13] Glück, F. et al. (2013). Electromagnetic design of the large-volume air coil system of the KATRIN experiment. *New J. Phys.* **15**(083025). DOI: 10.1088/1367-2630/15/8/083025.

[Goe35] Goeppert-Mayer, M. (1935). Double Beta-Disintegration. *Phys. Rev.* **48**(6): 512. DOI: 10.1103/PhysRev.48.512.

[Gol58] Goldhaber, M., Grodzins, L., and Sunyar, A. W. (1958). Helicity of Neutrinos. *Phys. Rev.* **109**(3): 1015–1017. DOI: 10.1103/PhysRev.109.1015.

[Gör14] Görhardt, S. (2014). *Background Reduction Methods and Vacuum Technology at the KATRIN Spectrometers*. PhD thesis. Karlsruhe Institute of Technology. URL: https://publikationen.bibliothek.kit.edu/1000038050.

[Gri69] Gribov, V. and Pontecorvo, B. (1969). Neutrino astronomy and lepton charge. *Phys. Lett. B* **28**(7). DOI: 10.1016/0370-2693(69)90525-5.

[Gro08] Grohmann, S. et al. (2008). Cryogenic design of the KATRIN source cryostat. *AIP Conference Proceedings* **985**: 1277. DOI: 10.1063/1.2908483.

[Gro09] Grohmann, S. (2009). Stability analyses of the beam tube cooling system in the KATRIN source cryostat. *Cryogenics* **49**: 413–420. DOI: 10.1016/j.cryogenics.2009.06.001.

[Gro11] Grohmann, S. et al. (2011). Precise temperature measurement at 30 K in the KATRIN source cryostat. *Cryogenics* **51**: 438–445. DOI: 10.1016/j.cryogenics.2011.05.001.

[Gro13] Grohmann, S. et al. (2013). The thermal behaviour of the tritium source in KATRIN. *Cryogenics* **55-56**: 5–11. DOI: 10.1016/j.cryogenics.2013.01.001.

[Gro15] Groh, S. (2015). *Modeling of the response function and measurement of transmission properties of the KATRIN experiment*. PhD thesis. Karlsruhe Institute of Technology. URL: https://publikationen.bibliothek.kit.edu/1000046546.

[Hac15] Hackenjos, M. (2015). *Die differentielle Pumpstrecke des KATRIN-Experiments - Inbetriebnahme und Charakterisierung des supraleitenden Magnetsystems*. MA thesis. Karlsruhe Institute of Technology. URL: http://www.katrin.kit.edu/publikationen/MaT_Hackenjos.pdf.

[Hac17] Hackenjos, M. (2017). *KATRIN "First Light" - Commissioning and Modelling of the Beamline*. PhD thesis. Karlsruhe Institute of Technology. URL: https://publikationen.bibliothek.kit.edu/1000078933.

[Han17] Hannen, V. et al. (2017). Deconvolution of the energy loss function of the KATRIN experiment. *Astropart. Phys.* **89**: 30–38. DOI: 10.1016/j.astropartphys.2017.01.010.

[Har15] Harms, F. (2015). *Characterization and Minimization of Background Processes in the KATRIN Main Spectrometer*. PhD thesis. Karlsruhe Institute of Technology. URL: https://publikationen.bibliothek.kit.edu/1000050027.

[Hei18] Heizmann, F. (2018). *Analysis tools and methods for tritium data taking with the KATRIN experiment*. PhD thesis. Karlsruhe Institute of Technology.

[Hig64a] Higgs, P. W. (1964a). Broken symmetries, massless particles and gauge fields. *Phys. Lett.* **12**(2): 132–133. DOI: 10.1016/0031-9163(64)91136-9.

[Hig64b] Higgs, P. W. (1964b). Broken Symmetries and the Masses of Gauge Bosons. *Phys. Rev. Lett.* **13**(16): 508. DOI: 10.1103/PhysRevLett.13.508.

[Hil11] Hillen, B. (2011). *Untersuchung von Methoden zur Unterdrückung des Spektrometeruntergrunds beim KATRIN Experiment*. PhD thesis. Westfälische Wilhelms-Universität Münster. URL: http://repositorium.uni-muenster.de/document/miami/1c6278eb-3176-4658-b37c-8133a3b12e3b/diss_hillen.pdf.

[Hil17] Hilk, D. (2017). *Electric field simulations and electric dipole investigations at the KATRIN main spectrometer*. PhD thesis. Karlsruhe Institute of Technology. URL: https://publikationen.bibliothek.kit.edu/1000065869.

[Hir88] Hirata, K. et al. (1988). Experimental study of the atmospheric neutrino flux. *Phys. Lett. B* **205**(2-3): 416–420. DOI: 10.1016/0370-2693(88)91690-5.

[Höt12] Hötzel, M. (2012). *Simulation and analysis of source-related effects for KATRIN*. PhD thesis. Karlsruhe Institute of Technology. URL: https://publikationen.bibliothek.kit.edu/1000031259.

[How04] Howe, M. A. et al. (2004). Sudbury Neutrino Observatory Neutral Current Detector Acquisition Software Overview. *IEEE Trans. Nucl. Sci.* **51**(3): 878–883. DOI: 10.1109/TNS.2004.829527.

[Hub19] Huber, A. (2019). *PhD thesis in preparation.* PhD thesis. Karlsruhe Institute of Technology.

[Jan15] Jansen, A. (2015). *The cryogenic pumping section of the KATRIN Experiment - Design studies and Experiments for the commissioning.* PhD thesis. Karlsruhe Institute of Technology. URL: https://publikationen.bibliothek.kit.edu/1000047146.

[Jan17] Janka, H. T. (2017). *Handbook of Supernovae.* Ed. by A. W. Alsabti and P. Murdin. Springer International Publishing AG. Chap. Neutrino Emission from Supernovae: 1575–1604. DOI: 10.1007/978-3-319-20794-0_4-1.

[Jon96] Jonsell, S. and Monkhorst, H. J. (1996). Effects from Changes in the Final State Spectrum on the Neutrino Mass Determination from T_2 Beta Decay Experiments. *Phys. Rev. Lett.* **76**(24): 4476. DOI: 10.1103/PhysRevLett.76.4476.

[Käf12] Käfer, W. (2012). *Sensitivity studies for the KATRIN experiment.* PhD thesis. Karlsruhe Institute of Technology. URL: https://publikationen.bibliothek.kit.edu/1000026021.

[Kat12] Katz, U. F. and Spiering, C. (2012). High-energy neutrino astrophysics: Status and perspectives. *Prog. Part. Nucl. Phys.* **67**(3): 651–704. DOI: 10.1016/j.ppnp.2011.12.001.

[Kaz08] Kazachenko, O. et al. (2008). Tritium Processing Loop for KATRIN Experiment. *Fusion Sci. Technol.* **54**(1): 67–70. DOI: 10.13182/FST08-A1766.

[Kel20] Kellerer, J. (2020). *PhD thesis in preparation.* PhD thesis. Karlsruhe Institute of Technology.

[Kib67] Kibble, T. W. B. (1967). Symmetry Breaking in Non-Abelian Gauge Theories. *Phys. Rev.* **155**(5): 1554. DOI: 10.1103/PhysRev.155.1554.

[Kik96] Kikas, A. et al. (1996). High-resolution study of the correlation satellites in photoelectron spectra of the rare gases. *J. Electron Spectrosc. Relat. Phenom.* **77**(3): 241–266. DOI: 10.1016/0368-2048(95)02552-9.

[Kir99] Kirsten, T. et al. (1999). GALLEX solar neutrino results and status of GNO. *Nucl. Phys. B Proc. Suppl.* **77**(1-3): 26–34. DOI: 10.1016/S0920-5632(99)00389-8.

[Kle14] Kleesiek, M. (2014). *A Data-Analysis and Sensitivity-Optimization Framework for the KATRIN Experiment.* PhD thesis. Karlsruhe Institute of Technology. URL: https://publikationen.bibliothek.kit.edu/1000043301.

[Kle18a] Kleesiek, M. et al. (2018). β-Decay Spectrum, Response Function and Statistical Model for Neutrino Mass Measurements with the KATRIN Experiment. *Eur. Phys. J. C (submitted for publication).* URL: https://arxiv.org/pdf/1806.00369.pdf.

[Kle18b] Klein, M. (2018). *Tritium ions in KATRIN: blocking, removal and detection.* PhD thesis. Karlsruhe Institute of Technology.

[Kob73] Kobayashi, M. and Maskawa, T. (1973). CP-Violation in the Renormalizable Theory of Weak Interaction. *Progr. Theoret. Phys.* **49**(2): 652–657. DOI: 10.1143/PTP.49.652.

[Kod01] Kodama, K. et al. (2001). Observation of tau neutrino interactions. *Phys. Lett. B* **504**(3). DOI: 10.1016/S0370-2693(01)00307-0.

[Kon47] Konopinski, E. J. (1947). H^3 and the Mass of the Neutrino. *Phys. Rev.* **72**(6): 518. DOI: 10.1103/PhysRev.72.518.2.

[Kor16] Korzeczek, M. (2016). *eV- & keV-sterile neutrino studies with KATRIN*. MA thesis. Karlsruhe Institute of Technology. URL: http://www.katrin.kit.edu/publikationen/MKorz-MA-eV-keV%20sterile%20Neutrinos.pdf.

[Kos12] Kosmider, A. (2012). *Tritium Retention Techniques in the KATRIN Transport Section and Commissioning of its DPS2-F Cryostat*. PhD thesis. Karlsruhe Institute of Technology. URL: https://publikationen.bibliothek.kit.edu/1000028959.

[Kov92] Kovalík, A. et al. (1992). The K and LMX Auger spectra of krypton from the ^{83}Rb decay. *J. Electron Spectrosc. Relat. Phenom.* **58**(1-2): 49–66. DOI: 10.1016/0368-2048(92)80006-T.

[Kra03] Kraus, C. (2003). *Messungen und Gesamtanalyse zur Neutrinomasse am Mainzer Tritium-β-Experiment*. PhD thesis. Johannes-Gutenberg-Universität Mainz. URL: https://www.katrin.kit.edu/publikationen/phd-christine_kraus.pdf.

[Kra05] Kraus, C. et al. (2005). Final results from phase II of the Mainz neutrino mass search in tritium β decay. *Eur. Phys. J. C* **40**(4): 447–468. DOI: 10.1140/epjc/s2005-02139-7.

[Kra16] Kraus, M. (2016). *Energy-scale systematics at the KATRIN main spectrometer*. PhD thesis. Karlsruhe Institute of Technology. URL: https://publikationen.bibliothek.kit.edu/1000054447.

[Kro14] Krochin, A. (2014). *Untersuchungen zum Einfluss des Verhältnisses von Ortho-Paratritium auf die Neutrinomassensensitivitä bei KATRIN*. BA thesis. Karlsruhe Institute of Technology.

[Kuc16] Kuckert, L. (2016). *The windowless gaseous tritium source of the KATRIN experiment - Characterisation of gas dynamical and plasma properties*. PhD thesis. Karlsruhe Institute of Technology. URL: https://publikationen.bibliothek.kit.edu/1000065077.

[Kuc18] Kuckert, L. et al. (2018). Modelling of gas dynamical properties of the KATRIN tritium source and implications for the neutrino mass measurement. *Vacuum* **158**: 195–205. DOI: 10.1016/j.vacuum.2018.09.036.

[Kur36] Kurie, F. N. D., Richardson, J. R., and Paxton, H. C. (1936). The Radiations Emitted from Artificially Produced Radioactive Substances. I. The Upper Limits and Shapes of the β-Ray Spectra from Several Elements. *Phys. Rev.* **49**(5): 368. DOI: 10.1103/PhysRev.49.368.

[Lan57] Landau, L. (1957). On the conservation laws for weak interactions. *Nucl. Phys.* **3**(1): 127–131. DOI: 10.1016/B978-0-444-88081-9.50006-0.

[Lee56] Lee, T. D. and Yang, C. N. (1956). Question of Parity Conservation in Weak Interactions. *Phys. Rev.* **104**(1). DOI: 10.1103/PhysRev.104.254.

[Lee57] Lee, T. D. and Yang, C. N. (1957). Parity Nonconservation and a Two-Component Theory of the Neutrino. *Phys. Rev.* **105**(5). DOI: 10.1103/PhysRev.105.1671.

[Lei14] Leiber, B. (2014). *Investigations of background due to secondary electron emission in the KATRIN-experiment.* PhD thesis. Karlsruhe Institute of Technology. URL: https://publikationen.bibliothek.kit.edu/1000042415.

[Lem70] Leming, C. W. and Pollack, G. L. (1970). Sublimation Pressures of Solid Ar, Kr, and Xe. *Phys. Rev. B* **2**(8): 3323. DOI: 10.1103/PhysRevB.2.3323.

[Les12] Lesgourgues, J. and Pastor, S. (2012). Neutrino Mass from Cosmology. *Adv. High Energy Phys.* **2012**: 608515. DOI: 10.1155/2012/608515.

[Let18] Letnev, J. et al. (2018). Technical design and commissioning of a sensor net for fine-meshed measuring of the magnetic field at the KATRIN spectrometer. *J. Instrum.* **13**: T08010. DOI: 10.1088/1748-0221/13/08/T08010.

[Lin05] Linstrom, P. J. and W. G. Mallard, eds. (2005). *NIST Chemistry Webbook, NIST Standard Reference Database Number 69.* Gaithersburg, MD 20899: National Institute of Standards and Technology. URL: webbook.nist.gov.

[Liu87] Liu, J. W. (1987). Total cross sections for high-energy electron scattering by H_2 ($^1\Sigma_g^+$), N_2 ($^1\Sigma_g^+$), and O_2 ($^3\Sigma_g^-$). *Phys. Rev. A* **35**(2): 591. DOI: 10.1103/PhysRevA.35.591.

[Lor02] Loredo, T. J. and Lamb, D. Q. (2002). Bayesian analysis of neutrinos observed from supernova SN 1987 A. *Phys. Rev. D* **65**(6): 063002. DOI: 10.1103/PhysRevD.65.063002.

[Luc00] Lucas, L. L. and Unterweger, M. P. (2000). Comprehensive Review and Critical Evaluation of the Half-Life of Tritium. *J. Res. Nat. Inst. Stand. Technol.* **105**(4): 541. DOI: 10.6028/jres.105.043.

[Luk12] Lukić, S. et al. (2012). Measurement of the gas-flow reduction factor of the KATRIN DPS2-F differential pumping section. *Vacuum* **86**(8): 1126–1133. DOI: 10.1016/j.vacuum.2011.10.017.

[Mac16] Machatschek, M. (2016). *Simulation of the ^{83m}Kr Mode of the Tritium Source of the KATRIN Experiment.* MA thesis. Karlsruhe Institute of Technology. URL: http://www.katrin.kit.edu/publikationen/mth-machatschek.pdf.

[Mac19] Machatschek, M. (2019). *PhD thesis in preparation.* PhD thesis. Karlsruhe Institute of Technology.

[Mak62] Maki, Z., Nakagawa, M., and Sakata, S. (1962). Remarks on the Unified Model of Elementary Particles. *Progr. Theoret. Phys.* **28**(5). DOI: 10.1143/PTP.28.870.

[Man91] Manson, S. T., Theodosiou, C. E., and Inokuti, M. (1991). Spectral and electron-collision properties of atomic ions. II. Inner-shell properties. *Phys. Rev. A* **43**(9): 4688. DOI: 10.1103/PhysRevA.43.4688.

[Mar17a] Marsteller, A. (2017). *Measurement of Temperature Stability and Homogeneity of the KATRIN WGTS Cryostat.* MA thesis. Karlsruhe Institute of Technology. URL: http://www.katrin.kit.edu/publikationen/mth_marsteller.pdf.

[Mar17b] Martin, E. L. (2017). *Electron Detection Systems for KATRIN Detector and Spectrometer Section*. PhD thesis. University of Washington. URL: https://digital.lib.washington.edu/researchworks/handle/1773/40285.

[Mei23] Meitner, L. (1923). Über eine mögliche Deutung des kontinuierlichen β-Strahlenspektrums. *Z. Phys.* **19**. DOI: 10.1007/BF01327566.

[Mei30] Meitner, L. and Orthmann, W. (1930). Über eine absolute Bestimmung der Energie der primären β-Strahlen von Radium E. *Z. Phys.* **60**(3-4). DOI: 10.1007/BF01339819.

[Mer12] Mertens, S. (2012). *Study of Background Processes in the Electrostatic Spectrometers of the KATRIN Experiment*. PhD thesis. Karlsruhe Institute of Technology. URL: https://publikationen.bibliothek.kit.edu/1000027058.

[Mer15a] Mertens, S. et al. (2015a). Sensitivity of next-generation tritium beta-decay experiments for keV-scale sterile neutrinos. *J. Cosmol. Astropart. Phys.* **02**(020). DOI: 10.1088/1475-7516/2015/02/020.

[Mer15b] Mertens, S. et al. (2015b). Wavelet approach to search for sterile neutrinos in tritium β-decay spectra. *Phys. Rev. D* **91**(4): 042005. DOI: 10.1103/PhysRevD.91.042005.

[Mik86] Mikheyev, S. P. and Smirnov, A. Y. (1986). Resonant Amplification of ν Oscillations in Matter and Solar-Neutrino Spectroscopy. *Il Nuovo Cimento* **9C**(1). DOI: 10.1007/BF02508049.

[Moh75] Mohapatra, R. N. and Pati, J. C. (1975). "Natural" left-right symmetry. *Phys. Rev. D* **11**(9): 2558. DOI: 10.1103/PhysRevD.11.2558.

[Mon09] Monreal, B. and Formaggio, J. A. (2009). Relativistic cyclotron radiation detection of tritium decay electrons as a new technique for measuring the neutrino mass. *Phys. Rev. D* **80**(5): 051301. DOI: 10.1103/PhysRevD.80.051301.

[Mye15] Myers, E. G. et al. (2015). Atomic Masses of Tritium and Helium-3. *Phys. Rev. Lett.* **114**(013003). DOI: 10.1103/PhysRevLett.114.013003.

[Osi01] Osipowicz, A. et al. (2001). KATRIN: A next generation tritium beta decay experiment with sub-eV sensitivity for the electron neutrino mass. Letter of intent. *Wissenschaftliche Berichte Forschungszentrum Karlsruhe* **6691**.

[Osi12] Osipowicz, A. et al. (2012). A mobile magnetic sensor unit for the KATRIN main spectrometer. *J. Instrum.* **7**: T06002. DOI: 10.1088/1748-0221/7/06/T06002.

[Ott08] Otten, E. and Weinheimer, C. (2008). Neutrino mass limit from tritium β decay. *Rep. Prog. Phys.* **71**. DOI: 10.1088/0034-4885/71/8/086201.

[Par16] Parke, S. and Ross-Lonergan, M. (2016). Unitarity and the three flavor neutrino mixing matrix. *Phys. Rev. D* **93**(11): 113009. DOI: 10.1103/PhysRevD.93.113009.

[Päs15] Päs, H. and Rodejohann, W. (2015). Neutrinoless double beta decay. *New J. Phys.* **17**: 115010. DOI: 10.1088/1367-2630/17/11/115010.

[Pau30] Pauli, W. (1930). In : *Wissenschaftlicher Briefwechsel mit Bohr, Einstein, Heisenberg u.a. Band II: 1930-1939 / Scientific Correspondence with Bohr,*

Einstein, Heisenberg a. o. Volume II: 1930-1939. Ed. by K. v. Meyenn. Springer, Berlin, Heidelberg, 1985. DOI: 10.1007/978-3-540-78801-0.

[Per75] Perl, M. L. et al. (1975). Evidence for Anomalous Lepton Production in $e^+ - e^-$ Annihilation. *Phys. Rev. Lett.* **35**(22). DOI: 10.1103/PhysRevLett.35.1489.

[Pic92] Picard, A. et al. (1992). Precision measurement of the conversion electron spectrum of ^{83m}Kr with a solenoid retarding spectrometer. *Z. Physik A - Hadrons and Nuclei* **342**(71). DOI: 10.1007/BF01294491.

[Pon58] Pontecorvo, B. (1958). Inverse beta processes and nonconservation of lepton charge. *J. Exp. Theor. Phys.* **34**(1): 172–173.

[Pon68] Pontecorvo, B. (1968). Neutrino experiments and the problem of conservation of leptonic charge. *J. Exp. Theor. Phys.* **26**(5): 984–988.

[Pon83] Pontecorvo, B. (1983). Pages in the development of neutrino physics. *Sov. Phys. Usp.* **26**(12): 1087. DOI: 10.1070/PU1983v026n12ABEH004586.

[Pra11] Prall, M. (2011). *Background Reduction of the KATRIN Spectrometers: Transmission Function of the Pre-Spectrometer and Systematic Tests of the Main-Spectrometer Wire Electrode*. PhD thesis. Westfälische Wilhelms-Universität Münster. URL: https://www.researchgate.net/publication/238418212_Transmission_Function_of_the_Pre-Spectrometer_and_Systematic_Tests_of_the_Main-Spectrometer_Wire_Electrode_PHD_thesis.

[Pra12] Prall, M. et al. (2012). The KATRIN pre-spectrometer at reduced filter energy. *New J. Phys.* **14**: 073054. DOI: 10.1088/1367-2630/14/7/073054.

[Pri15] Priester, F., Sturm, M., and Bornschein, B. (2015). Commissioning and detailed results of KATRIN inner loop tritium processing system at Tritium Laboratory Karlsruhe. *Vacuum* **116**: 42–47. DOI: 10.1016/j.vacuum.2015.02.030.

[Qia15] Qian, X. and Vogel, P. (2015). Neutrino mass hierarchy. *Prog. Part. Nucl. Phys.* **83**: 1–30. DOI: 10.1016/j.ppnp.2015.05.002.

[Ran17] Ranitzsch, P. C.-O. et al. (2017). Characterization of the ^{163}Ho Electron Capture Spectrum: A Step Towards the Electron Neutrino Mass Determination. *Phys. Rev. Lett.* **119**(12): 122501. DOI: 10.1103/PhysRevLett.119.122501.

[Rei13] Reich, J. (2013). *Magnetic Field Inhomogeneities and Their Influence on Transmission and Background at the KATRIN Main Spectrometer*. PhD thesis. Karlsruhe Institute of Technology. URL: https://publikationen.bibliothek.kit.edu/1000033076.

[Rei19] Reiling, C. (2019). *Master's thesis in preparation*. MA thesis. Karlsruhe Institute of Technology.

[Rei53] Reines, F. and C. L. Cowan, J. (1953). Detection of the Free Neutrino. *Phys. Rev.* **92**(3): 830. DOI: 10.1103/PhysRev.92.830.

[Ren11] Renschler, P. (2011). *Monte Carlo simulations of low-energy electrons in silicon*. PhD thesis. Karlsruhe Institute of Technology. URL: https://publikationen.bibliothek.kit.edu/1000024959.

[Res19] Rest, O. (2019). *PhD thesis in preparation*. PhD thesis. Westfälische Wilhelms-Universität Münster.

[Rii11] Riis, A. S. and Hannestad, S. (2011). Detecting sterile neutrinos with KATRIN like experiments. *J. Cosmol. Astropart. Phys.* **2011**: 011. DOI: 10.1088/1475-7516/2011/02/011.

[Rob88] Robertson, R. G. H. and Knapp, D. A. (1988). Direct measurements of neutrino mass. *Ann. Rev. Nucl. Part. Sci.* **38**: 185–215. DOI: 10.1146/annurev.ns.38.120188.001153.

[Rob91] Robertson, R. G. H. et al. (1991). Limit on $\bar{\nu}_e$ Mass from Observation of the β Decay of Molecular Tritium. *Phys. Rev. Lett.* **67**(8). DOI: 10.1103/PhysRevLett.67.957.

[Rod18] Rodenbeck, C. (2018). *Calibration and Monitoring of KATRIN's Precision High Voltage System with First ^{83m}Kr Measurements.* MA thesis. Karlsruhe Institute of Technology.

[Rod21] Rodenbeck, C. (2021). *PhD thesis in preparation.* PhD thesis. Westfälische Wilhelms-Universität Münster.

[Röl15] Röllig, M. (2015). *Tritium analytics by beta induced X-ray spectrometry.* PhD thesis. Karlsruhe Institute of Technology. URL: https://publikationen.bibliothek.kit.edu/1000054050.

[Röt19] Röttele, C. (2019). *PhD thesis in preparation.* PhD thesis. Karlsruhe Institute of Technology.

[Ryš92] Ryšavý, M. and Dragoun, O. (1992). What Can we Learn from the Internal-Conversion Electron Spectra of Multiply Charged Krypton Ions? *Europhys. Lett.* **17**(4): 303–308. DOI: 10.1209/0295-5075/17/4/004.

[Sac20] Sack, R. (2020). *PhD thesis in preparation.* PhD thesis. Westfälische Wilhelms-Universität Münster.

[Sae00] Saenz, A., Jonsell, S., and Froelich, P. (2000). Improved Molecular Final-State Distribution of HeT^+ for the β-Decay Process of T_2. *Phys. Rev. Lett.* **84**(2): 242. DOI: 10.1103/PhysRevLett.84.242.

[Sak67] Sakharov, A. D. (1967). Violation of CP invariance, C asymmetry, and baryon asymmetry of the universe. *J. Exp. Theor. Phys. Let.* **5**(1): 32–35.

[Sal57] Salam, A. (1957). On parity conservation and neutrino mass. *Il Nuovo Cimento* **5**(1): 299–301. DOI: 10.1007/BF02812841.

[Sal68] Salam, A. (1968). Weak and electromagnetic interactions. *Proceedings of the Eight Nobel Symposium May 19-25, 1968*: 367–377.

[Sch08] Schmitt, U. (2008). *Entwicklung eines Monitordetektors für das KATRIN-Experiment.* PhD thesis. Universität Karlsruhe. URL: https://publikationen.bibliothek.kit.edu/1000010172.

[Sch13a] Schlösser, M. (2013). *Accurate calibration of the Raman system for the Karlsruhe Tritium Neutrino Experiment.* PhD thesis. Karlsruhe Institute of Technology. URL: https://publikationen.bibliothek.kit.edu/1000034967.

[Sch13b] Schlösser, M. et al. (2013a). Accurate calibration of the laser Raman system for the Karlsruhe Tritium Neutrino Experiment. *J. Mol. Struct.* **1044**: 61–66. DOI: 10.1016/j.molstruc.2012.11.022.

[Sch13c] Schlösser, M. et al. (2013b). In-Line Calibration of Raman Systems for Analysis of Gas Mixtures of Hydrogen Isotopologues with Sub-Percent Accuracy. *Anal. Chem.* **85**: 2739–2745. DOI: 10.1021/ac3032433.

[Sch14] Schwarz, J. (2014). *The Detector System of the KATRIN Experiment - Implementation and First Measurements with the Spectrometer*. PhD thesis. Karlsruhe Institute of Technology. URL: https://publikationen.bibliothek.kit.edu/1000042772.

[Sch16] Schönung, K. (2016). *Development of a Rear Wall for the KATRIN Rear Section and investigation of tritium compatibility of Rear Section components*. PhD thesis. Karlsruhe Institute of Technology. URL: https://publikationen.bibliothek.kit.edu/1000056077.

[Sch19] Schlüter, L. (2019). *Master's thesis in preparation*. MA thesis. Technische Universität München.

[Sch20] Schimpf, L. (2020). *PhD thesis in preparation*. PhD thesis. Karlsruhe Institute of Technology.

[Sch57] Schopper, H. (1957). Circular polarization of γ-rays: Further proof for parity failure in β decay. *Philos. Mag.* **2**(17). DOI: 10.1080/14786435708242717.

[Sen18] Sentkerestiová, J. et al. (2018). Gaseous ^{83m}Kr generator for KATRIN. *J. Instrum.* **13**: P04018. DOI: 10.1088/1748-0221/13/04/P04018.

[Sig17] Sigl, G. (2017). *Astroparticle Physics: Theory and Phenomenology*. Vol. 1. Atlantis Studies in Astroparticle Physics and Cosmology. Atlantis Press, Paris. DOI: 10.2991/978-94-6239-243-4.

[Sle13] Slezák, M. et al. (2013). Electron line shape of the KATRIN monitor spectrometer. *J. Instrum.* **8**: T12002. DOI: 10.1088/1748-0221/8/12/T12002.

[Sle15] Slezák, M. (2015). *Monitoring of the energy scale in the KATRIN neutrino experiment*. PhD thesis. Czech Academy of Sciences. URL: https://www.katrin.kit.edu/publikationen/phd-Martin_Slezak.pdf.

[Spe74] Spears, D. P., Fischbeck, H. J., and Carlson, T. A. (1974). Satellite structure in the x-ray photoelectron spectra of rare gases and alkali-metal halides. *Phys. Rev. A* **9**(4): 1603. DOI: 10.1103/PhysRevA.9.1603.

[Spr87] Springer, P. T., Bennett, C. L., and Baisden, P. A. (1987). Measurement of the neutrino mass using the inner bremsstrahlung emitted in the electron-capture decay of ^{163}Ho. *Phys. Rev. A* **35**(2): 679. DOI: 10.1103/PhysRevA.35.679.

[Ste17] Steinbrink, N. M. N. et al. (2017). Statistical sensitivity on right-handed currents in presence of eV scale sterile neutrinos with KATRIN. *J. Cosmol. Astropart. Phys.* **2017**: 015. DOI: 10.1088/1475-7516/2017/06/015.

[Sto95] Stoeffl, W. and Decman, D. J. (1995). Anomalous Structure in the Beta Decay of Gaseous Molecular Tritium. *Phys. Rev. Lett.* **75**(18): 3237. DOI: 10.1103/PhysRevLett.75.3237.

[Stu10a] Sturm, M. (2010). *Aufbau und Test des Inner-Loop-Systems der Tritiumquelle von KATRIN*. PhD thesis. Karlsruhe Institute of Technology. URL: https://publikationen.bibliothek.kit.edu/1000019355.

[Stu10b] Sturm, M. et al. (2010). Monitoring of All Hydrogen Isotopologues at Tritium Laboratory Karlsruhe Using Raman Spectroscopy. *Laser Physics* **20**(2): 493–507. DOI: 10.1134/S1054660X10030163.

[Stu47] Stull, D. R. (1947). Vapor Pressure of Pure Substances - Inorganic Compounds. *Ind. Eng. Chem.* **39**(4): 540–550. DOI: 10.1021/ie50448a023.

[Sve88] Svensson, S. et al. (1988). Electron shake-up and correlation satellites and continuum shake-off distributions in x-ray photoelectron spectra of the rare gas atoms. *J. Electron Spectrosc. Relat. Phenom.* **47**: 327–384. DOI: 10.1016/0368-2048(88)85020-5.

[Tan18] Tanabashi, M. et al. (2018). Review of Particle Physics. *Phys. Rev. D* **98**(3): 030001. DOI: 10.1103/PhysRevD.98.030001. URL: http://pdg.lbl.gov/.

[Thü07] Thümmler, T. (2007). *Präzisionsüberwachung und Kalibration der Hochspannung für das KATRIN-Experiment.* PhD thesis. Westfälische Wilhelms-Universität Münster. URL: http://repositorium.uni-muenster.de/document/miami/0e96c5e3-6f06-489e-a73f-5859fbe9cae7/diss_thuemmler.pdf.

[Thü09] Thümmler, T., Marx, R., and Weinheimer, C. (2009). Precision high voltage divider for the KATRIN experiment. *New J. Phys.* **11**: 103007. DOI: 10.1088/1367-2630/11/10/103007.

[Tro18] Trost, N. (2018). *Modeling and measurement of Rydberg-State mediated Background at the KATRIN Main Spectrometer.* PhD thesis. Karlsruhe Institute of Technology.

[Ubi09] Ubieto-Díaz, M. et al. (2009). A broad-band FT-ICR Penning trap system for KATRIN. *Int. J. Mass Spectrom.* **288**(1-3): 1–5. DOI: 10.1016/j.ijms.2009.07.003.

[Val09] Valerius, K. (2009). *Spectrometer-related background processes and their suppression in the KATRIN experiment.* PhD thesis. Westfälische Wilhelms-Universität Münster. URL: http://repositorium.uni-muenster.de/document/miami/93137705-73f4-404a-a438-09d487cbff63/diss_valerius.pdf.

[Van64] Van Itterbeek, A. et al. (1964). Vapour pressure of liquid argon. *Physica* **30**: 2119–2122.

[Vén14] Vénos, D. et al. (2014). Gaseous source of ^{83m}Kr conversion electrons for the neutrino experiment KATRIN. *J. Inst.* **9**(12). DOI: 10.1088/1748-0221/9/12/P12010.

[Vén18] Vénos, D. et al. (2018). Properties of ^{83m}Kr conversion electrons and their use in the KATRIN experiment. *J. Instrum.* **13**: T02012. DOI: 10.1088/1748-0221/13/02/T02012.

[Wal13] Wall, B. L. (2013). *Karlsruhe Tritium Experiment: Detector System Commissioning and In-Situ PIN-Diode Array Dead-Layer Measurement.* PhD thesis. University of Washington. URL: https://digital.lib.washington.edu/researchworks/handle/1773/22845.

[Wan13] Wandkowsky, N. et al. (2013). Validation of a model for radon-induced background processes in electrostatic spectrometers. *J. Phys. G: Nucl. Part. Phys.* **40**(8): 085102. DOI: 10.1088/0954-3899/40/8/085102.

[War91] Wark, D. L. et al. (1991). Correspondence of electron spectra from photoionization and nuclear internal conversion. *Phys. Rev. Lett.* **67**(17): 2291. DOI: 10.1103/PhysRevLett.67.2291.

[Wei35] Weizsäcker, C. F. v. (1935). Zur Theorie der Kernmassen. *Z. Phys.* **96**(7-8): 431–458. DOI: 10.1007/BF01337700.

[Wei67] Weinberg, S. (1967). A Model of Leptons. *Phys. Rev. Lett.* **19**(21). DOI: 10.1103/PhysRevLett.19.1264.

[Wie16] Wierman, K. J. (2016). *Studies of charge accumulation in the KATRIN main spectrometer*. PhD thesis. University of North Carolina at Chapel Hill.

[Wil87] Wilkerson, J. F. et al. (1987). Limit on $\bar{\nu}_e$ Mass from Free-Molecular-Tritium Beta Decay. *Phys. Rev. Lett.* **58**(20): 2023. DOI: 10.1103/PhysRevLett.58.2023.

[Wol78] Wolfenstein, L. (1978). Neutrino oscillations in matter. *Phys. Rev. D* **17**(9). DOI: 10.1103/PhysRevD.17.2369.

[Wu57] Wu, C. S. et al. (1957). Experimental Test of Parity Conservation in Beta Decay. *Phys. Rev.* **105**(4): 1413. DOI: 10.1103/PhysRev.105.1413.

[Yec17] Yeche, C. et al. (2017). Constraints on neutrino masses from Lyman-alpha forest power spectrum with BOSS and XQ-100. *J. Cosmol. Astropart. Phys.* **2017**(06): 047. DOI: 10.1088/1475-7516/2017/06/047.

[Zac15] Zacher, M. (2015). *High-field electrodes design and an angular-selective photoelectron source for the KATRIN spectrometers*. PhD thesis. Westfälische Wilhelms-Universität Münster.

[Zbo11] Zboril, M. (2011). *Solid electron sources for the energy scale monitoring in the KATRIN experiment*. PhD thesis. Westfälische Wilhelms-Universität Münster. URL: http://repositorium.uni-muenster.de/document/miami/79b74253-2dcd-493b-a08d-4eeb5a10b8c1/diss_zboril.pdf.

[Zbo13] Zboril, M. et al. (2013). Ultra-stable implanted ^{83}Rb/^{83m}Kr electron sources for the energy scale monitoring in the KATRIN experiment. *J. Instrum.* **8**: P03009. DOI: 10.1088/1748-0221/8/03/P03009.

[Zel17] Zeller, G. (2017). *Development of a calibration procedure and calculation of the uncertainty budget for the KATRIN laser Raman system*. MA thesis. Karlsruhe Institute of Technology. URL: http://www.katrin.kit.edu/publikationen/mth-Zeller.pdf.

[Zha12] Zhang, S. W., Ji, G. Z., and Han, J. (2012). The Positional and Angular Distribution of Molecules Flowing through Cylindrical Tube in Free Molecular Flow. *Phys. Procedia* **32**: 513–524. DOI: 10.1016/j.phpro.2012.03.595.

[Zie13] Ziegler, S. (2013). *Die Extraktion der Energieverlustfunktion beim KATRIN Experiment*. Diploma thesis. Karlsruhe Institute of Technology. URL: http://www.katrin.kit.edu/publikationen/dth_-_Ziegler.pdf.

[Zub11] Zuber, K. (2011). *Neutrino Physics*. 2nd ed. CRC Press, Boca Raton, London, New York.

Acknowledgements

Zum Schluss möchte ich bei allen bedanken, die zum Gelingen dieser Arbeit beigetragen haben. Insbesondere danken möchte ich:

- Prof. Dr. Guido Drexlin für die Möglichkeit, diese Doktorarbeit zu schreiben, seine Unterstützung und Förderung seit Bachelorarbeitszeiten und für seine guten Vorlesungen, die bei mir das Interesse an Astroteilchenphysik und KATRIN geweckt haben.
- Prof. Dr. Ulrich Husemann für die Übernahme des Korreferats und den wertvollen Blick von außen.
- Dr. Kathrin Valerius für ihre Betreuung und Unterstützung während der Promotionszeit, ihre wertschätzende und zutrauende Art der Führung und für die Erkenntnis, dass Laufen gehen doch gar nicht so langweilig ist, wie ich vorher immer dachte.
- Dr. Alexander Jansen für die Organisation der WGTS-Inbetriebnahme und der Krypton-Messphase.
- Allen Beteiligten an der Krypton-Messphase 2017, insbesondere Drahoslav Vénos, Jana Sentkerestiová, Martin Slezák, Martin Ryšavý und Ottokar Dragoun für die Vorbereitung des Krypton-Generators, die Diskussion der Messergebnisse und die Bereitstellung von Theoriewerten für die Analyse.
- Dem WGTS-Team (Heike Bolz, Dr. Moritz Hackenjos, Florian Heizmann, Dr. Alexander Jansen, Benedikt Kuffner, Steffen Lichter, Alexander Marsteller) für die schöne und lehrreiche Zeit im Labor.
- Moritz Machatschek für seine Korrekturen des Krypton-Kapitels, seine Hilfe mit dem Krypton-Fitter und die gute und unkomplizierte Zusammenarbeit in der Lehre.
- Allen Kollegen und Kolleginnen, die mir beim Zusammentragen der Systematiken geholfen, Effekte mit mir diskutiert und Teile des Kapitels Korrektur gelesen haben.
- Steffen Lichter und Rolf Rinderspacher für die Bereitstellung der CAD-Zeichnungen.
- Meinen Zimmerkollegen Johannes Antoni, Anton Huber, Fabian Leven und Moritz Machatschek für eine allzeit gute Atmosphäre im Büro.
- Fabian Block, Dominik Hinz und Jonas Kellerer für die Unterstützung in der Lehre im letzten Semester.
- Florian Heizmann für seine Hilfe bei Programmier- und Computerproblemen, eine legendäre Posterpreisverleihung in kurzen Hosen auf der Neutrinokonferenz und das Teilen von so manchem Doppelzimmer.
- Dr. Marco Kleesiek für seine Hilfe per Mail, obwohl er gar nicht mehr am Institut arbeitet.

- Den Sekretärinnen Marion Behechti, Diana Fellner, Katharina Fischer, Anna Friedrich, Brigitte Gering, Barbara Lepold und Eva Porter für die immer freundliche Unterstützung bei Verwaltungsvorgängen jeglicher Art.
- Thomas Csabo für das zweimalige schnelle Bereitstellen eines Ersatzlaptops während der Schreibphase.
- Andreas Pargner für seine Freundschaft, die gute Zusammenarbeit in verschiedenen Gremien und die gemeinsame Vorbereitung auf den 1. Februar.
- Der Graduiertenschule KSETA für die Möglichkeit, einen Blick über den Tellerrand der eigenen Arbeitsgruppe zu werfen, für die Finanzierung vieler Dienstreisen und Dr. Irmgard Langbein für die gute Zusammenarbeit während meiner Zeit als Doktorandenvertreter.
- Allen BaMaDiDoNawis für den guten Zusammenhalt und die gemeinsamen Aktivitäten außerhalb der alltäglichen Arbeit.
- Klaus Mehret für einen privaten Fotokurs, vertrauensvolle Gespräche und abwechslungsreiche Mittagspausen.
- Allen Korrekturlesern und -leserinnen.
- Allen Kollegen und Kolleginnen am ETP, IKP, TLK und der ganzen KATRIN-Kollaboration für die gute Arbeitsatmosphäre.

Meinen Eltern, meiner Familie und meinen Freunden danke ich für das Verständnis, dass ich in der Schreibphase nicht immer so Kontakt halten konnte, wie ich das sonst mache. Zuletzt danke ich meiner Frau für ihre Ermunterungen in Phasen voller Selbstzweifel und für ihre Geduld gerade gegen Ende des Schreibens.